

Technical Matter Wave Optics

Imaging devices for Bose condensed matter waves -
an aberration analysis in space and time



TECHNISCHE
UNIVERSITÄT
DARMSTADT

Vom Fachbereich Physik
der Technischen Universität Darmstadt

zur Erlangung des Grades
eines Doktors der Naturwissenschaften (Dr. rer. nat.)

genehmigte Dissertation von
Jan Teske

ERSTGUTACHTER: Prof. Dr. Reinhold Walser
ZWEITGUTACHTER: Prof. Dr. Enno Giese

Darmstadt 2023
D 17

“Wenn es so wäre, dass die Bedingungen allein die Zukunft vorgeben, wären wir jegliche Verantwortung, jedes Gefühl für Schuld, jedes Gewissen los. So einfach ist es aber nicht. Die Hauptsache kommt immer noch; sie bleibt zu tun.”

- Anne Weber, *Annette, Ein Heldinnen-Epos* -

Jan Teske:

Technical Matter Wave Optics
Imaging devices for Bose condensed matter waves -
an aberration analysis in space and time

ERSTGUTACHTER: Prof. Dr. Reinhold Walser

ZWEITGUTACHTER: Prof. Dr. Enno Giese

TAG DER PRÜFUNG: 10. Juli 2023

DARMSTADT, Technische Universität Darmstadt

Jahr der Veröffentlichung der Dissertation auf TUprints: 2023

URN: urn:nbn:de:tuda-tuprints-243260

Veröffentlicht unter CC BY-NC-ND 4.0 International

Namensnennung - nicht kommerziell - keine Bearbeitung

<https://creativecommons.org/licenses/>



ABSTRACT

Cold atomic gases are the ultimate quantum sensors. Embedded in a matter-wave interferometer, they provide a platform for high-precision sensing of accelerations and rotations probing fundamental physical questions. As in all optical instruments, these devices require careful modeling. Sources of possible aberrations need to be quantified and optimized to guarantee the best possible performance. This applies in particular to high-demanding experiments in microgravity with low repetition rates.

In this thesis, we present a theoretical (3+1)d aberration analysis of expanded Bose-Einstein condensates. We demonstrate that the Bogoliubov modes of the scaled mean-field equation serve as good basis states to obtain the corresponding aberration coefficients. Introducing the Stringari polynomials, we describe density and phase variations in terms of a multipole decomposition analogous to the Zernike wavefront analysis in classical optics.

We apply our aberration analysis to Bose-Einstein condensates on magnetic chip traps. We obtain the trapping potential using magnetic field simulations with finite wire elements. Using the multipole expansion, we characterize the anharmonic contributions of the Ioffe-Pritchard type Zeeman potential. Used as a matter-wave lens for delta-kick collimation, we determine the wavefront aberrations in terms of “Seidel-diagrams”. Supported by (3+1)d Gross-Pitaevskii simulations we study mean-field interactions during long expansion times.

Matter-wave interferometry with Bose-Einstein condensates can also be performed in guiding potentials. One of the building blocks are toroidal condensates in a ring-shaped geometry. The required light field patterns are obtained by using the effect of conical refraction or with programmable digital micromirror devices. For the former, we study equilibrium properties and compare them with experimental data. We investigate the collective excitations in the two-dimensional ring-shaped condensate. Our result is compared to the numerical results of the Bogoliubov-de Gennes equations. The latter is used to find signatures in the excitation spectrum during the topological transition from simply connected harmonic to multiply connected ring traps. Changing the topology dynamically leads to radial excitations of the condensate. We propose a damping mechanism based on feedback measurements to control the motion within the toroidal ring.

ZUSAMMENFASSUNG

Kalte atomare Gase sind die ultimativen Quantensensoren. Eingebettet in ein Materiewelleninterferometer bieten sie eine Plattform für die hochpräzise Erfassung von Beschleunigungen und Rotationen, mit der fundamentale physikalische Fragen untersucht werden können. Wie bei allen optischen Instrumenten müssen auch diese Geräte sorgfältig modelliert werden. Die Quellen möglicher Aberrationen müssen quantifiziert und optimiert werden, um die bestmögliche Leistung zu gewährleisten. Dies gilt insbesondere für anspruchsvolle Experimente, die in Mikrogravitation mit niedrigen Wiederholungsraten durchgeführt werden.

In dieser Arbeit präsentieren wir eine theoretische $(3+1)$ d-Aberrationsanalyse von expandierten Bose-Einstein-Kondensaten. Wir zeigen, dass die Bogoliubov-Moden der skalierten klassischen Feldgleichung als gute Basiszustände dienen, um die entsprechenden Aberrationskoeffizienten zu erhalten. Durch die Einführung der Stringari-Polynome beschreiben wir Dichte- und Phasenvariationen mit Hilfe einer Multipolzerlegung, die der Zernike-Wellenfrontanalyse in der klassischen Optik entspricht.

Wir wenden unsere Aberrationsanalyse auf Bose-Einstein-Kondensate in magnetischen Chip-Fallen an. Wir erhalten das Fallenpotential durch Magnetfeldsimulationen mit finiten Drahtelementen. Mit Hilfe der Multipolentwicklung charakterisieren wir die anharmonischen Beiträge des Zeeman-Potentials vom Ioffe-Pritchard-Typ. Bei Verwendung als Materiewellenlinse für Delta-Kick-Kollimation bestimmen wir die Wellenfrontaberrationen in Form von Seidel-Diagrammen. Mit Hilfe von $(3+1)$ d Gross-Pitaevskii-Simulationen untersuchen wir die Dichte-Wechselwirkung bei langen Expansionszeiten.

Materiewellen-Interferometrie mit Bose-Einstein-Kondensaten kann auch in leitenden Potentialen durchgeführt werden. Einer der Bausteine sind toroidale Kondensate in einer ringförmigen Geometrie. Die erforderlichen Lichtfeldmuster werden durch Nutzung des Effekts der konischen Brechung oder mit programmierbaren digitalen Mikrospiegeln erzielt. Für erstere untersuchen wir Gleichgewichtseigenschaften und vergleichen sie mit experimentellen Daten. Wir untersuchen die kollektiven Anregungen in zweidimensionalen ringförmigen Kondensaten. Unsere Ergebnisse werden mit numerischen Ergebnissen der Bogoliubov-de Gennes-Gleichungen verglichen. Letztere werden verwendet, um Signaturen im Anregungsspektrum während des topologischen Übergangs von einfach verbundenen harmonischen zu mehrfach verbundenen Ringfallen zu finden. Die dynamische Änderung der Topologie führt zu radialen Anregungen des Kondensats. Wir schlagen einen Dämpfungsmechanismus vor, der auf Rückkopplungsmessungen beruht, um die Bewegung in der toroidalen Ringfalle zu kontrollieren.

CONTENTS

1	INTRODUCTION	1
2	MAGNETIC CHIP TRAPS	5
2.1	Static magnetic fields	5
2.1.1	Maxwell's equations	5
2.1.2	Biot-Savart Law	6
2.2	Zeeman potential	6
2.2.1	Zeeman effect	6
2.2.2	Alkali atoms	7
2.2.3	Adiabatic approximation	7
2.3	Trapping geometries	8
2.3.1	Linear waveguide	8
2.3.2	Z- and U- shaped traps	9
2.4	QUANTUS II chip	9
2.4.1	Chip model	9
2.4.2	Finite wires	10
2.4.3	Harmonic approximation	10
2.4.4	Release trap	12
2.4.5	Magnetic lens	15
3	CLASSICAL DESCRIPTION OF ATOMIC MATTER WAVES	17
3.1	Principle of least action	17
3.2	Hamilton dynamics	18
3.3	Canonical transformation	19
3.3.1	Ballistic expansion	20
3.3.2	Harmonic oscillator	21
3.4	Scaling transformation	21
4	CONCEPTS OF COLD ATOMIC GASES	25
4.1	Dilute gases at low temperatures	25
4.2	Model for interactions	25
4.2.1	Elastic scattering for neutral atoms	26
4.2.2	Pseudo potential	28
4.3	Weakly interacting Bose gas	28
4.3.1	Mean-field approximation for Bosons	29
4.3.2	Gross-Pitaevskii equation	29
4.3.3	Thomas-Fermi approximation	30
4.4	Hydrodynamic field equations	34
4.4.1	Scaling solution of the Euler equation	35
4.4.2	Hydrodynamic sound wave excitations	36
4.5	Linearization of the Gross-Pitaevskii equation	37
4.5.1	Bogoliubov - de Gennes equations	38
4.5.2	Density and phase amplitudes	39

5	WIGNER REPRESENTATION OF INTERACTING BOSE-EINSTEIN CONDENSATES	41
5.1	Wigner distribution	41
5.2	Thomas-Fermi Wigner function	42
5.2.1	One-dimensional harmonic oscillator	42
5.2.2	Three-dimensional harmonic oscillator	48
6	WAVEFRONT ABERRATION OF EXPANDING BOSE-EINSTEIN CONDENSATES	51
6.1	Gross-Pitaevskii equation in adaptive scales	51
6.2	Aberration analysis in linear response	53
7	EFFICIENT MULTIPOLE REPRESENTATION FOR MATTER-WAVE OPTICS	55
7.1	Trapping potentials	55
7.1.1	Optical dipole potentials	55
7.1.2	Zeeman potential	56
7.2	Multipole expansion with Stringari polynomials	56
7.3	Numerical evaluation	58
7.4	Example potentials	59
7.4.1	3d isotropic harmonic oscillator potential	59
7.4.2	Anisotropic harmonic oscillator potential	59
7.4.3	Magnetic Zeeman potential of an atom chip	61
7.4.4	Laguerre-Gaussian dipole potential	61
7.5	Ground state density distributions	63
7.5.1	3d isotropic harmonic oscillator potential	64
7.5.2	3d anisotropic harmonic oscillator potential	69
8	COLDEST CLOUDS IN UNIVERSE	75
8.1	Delta-kick collimation using adaptive scales	75
8.2	Condensate in the release trap	78
8.2.1	Ground state density distribution	78
8.2.2	Collective excitations	81
8.3	Ballistic expansion: pre lens	87
8.4	Delta-kick collimation with magnetic chip traps	90
8.4.1	Characterization of the magnetic lens	90
8.4.2	Optimal lens time	90
8.4.3	Wavefront aberrations	91
8.4.4	Momentum kicks	93
8.4.5	Momentum width	94
8.5	Ballistic expansion: post lens	95
9	TOPOLOGICAL DEFORMATION OF BOSE-EINSTEIN CONDENSATES IN OPTICAL DIPOLE TRAPS	99
9.1	Optical dipole traps	99
9.2	Ring geometries with dipole optical potential	101
9.2.1	Conical refraction	101
9.2.2	Digital micromirror devices	105
9.3	Bose-Einstein condensate in a quasi-two-dimensional harmonic ring potential	105
9.3.1	Effective Gross-Pitaevskii equation	106
9.3.2	Linear response analysis	107
9.4	Collective excitations during topology change	110
9.4.1	Definition of transition potential	110
9.4.2	Discussion of excitation spectrum	111

9.5	Damping with feedback	112
10	CONCLUSION AND OUTLOOK	119
A	WAVE PACKET DYNAMICS	121
A.1	Schrödinger propagation	121
A.2	Gross-Pitaevskii propagation	122
B	OBSERVABLES IN SCALED REFERENCE FRAME	125
B.1	Position	125
B.2	Momentum	126
B.3	Correlations	126
C	TIME OF FLIGHT SERIES	127
D	PROPERTIES OF SPHERICAL HARMONICS	131
D.1	General relations	131
D.2	Multipole expansion	131
D.3	Products of spherical harmonics	132
D.4	Visual representation	132
E	JACOBI POLYNOMIALS	133
F	FOURIER REPRESENTATION OF WAVE FUNCTIONS	137
F.1	Discrete Fourier Transform	137
F.2	Representation of the 3D discrete wave function	138
F.3	Evaluation of the kinetic energy	138
F.4	Radial Fourier grid	139
G	GROSS-PITAEVSKII EQUATION IN DIMENSIONLESS UNITS	141
H	HARTREE-FOCK-BOGOLIUBOV-SELF-ENERGY OPERATOR	143
H.1	Mathematical properties	143
H.2	Numerical treatment of the Bogoliubov equations	144
I	ANGULAR MOMENTUM FILTERING ON CARTESIAN GRIDS	145
J	BOGOLIUBOV MODES QUANTUS II RELEASE TRAP	147
K	STATIONARY STATES IN EXTERNAL POTENTIALS	159
K.1	Non-rotational single-component BEC	159
K.2	Non-rotational multi-component BEC	160
L	TIME-EVOLUTION OF WAVE FUNCTION	161
L.1	Runge-Kutta integrator	161
L.2	Split operator	162
M	COORDINATE SYSTEMS	165
M.1	Rotation matrices	165
M.2	Finite rotations	166
M.3	Rotation of angular momentum states	166
M.4	Rotation of multipole coefficients	166

Contents

BIBLIOGRAPHY	169
PUBLICATIONS	180
CONFERENCE CONTRIBUTIONS	182
DANKSAGUNG	184

1 INTRODUCTION

In 1934 Frits Zernike introduced the orthogonal “Kreisflächenpolynome” [1] to describe the optical path difference between light waves and a spherical reference wavefront. Understanding the phase differences and minimizing the optical aberrations laid the base for the first phase-contrast microscope [2] for which he was awarded the Nobel Prize in Physics 1953. Nowadays, the Zernike polynomials are widely used in optical system design as a standard description of imperfections in optical imaging [3]. As they are a complete orthogonal basis set, any wavefront distortion can be described as a linear combination of these polynomials. The corresponding expansion coefficients then refer to a specific type of wavefront aberration such as defocus, astigmatism, coma, spherical aberration, and higher-order aberrations [4].

Balancing aberrations is also relevant for optical imaging with electron microscopes [5–7]. In contrast to visible light, massive particles, such as electrons, atoms, and even larger molecules [8], have a much smaller de Broglie wavelength, $\lambda_{dB} = h/p$ [9], and therefore a possible higher resolving power with resolutions of $\sim 1 \text{ \AA}$. Besides probing structures at atomic length scales, matter waves that travel on two or more different paths can form an atom interferometer [10, 11]. The resulting interference pattern, which depends on the phase shift, can be used to study various fundamental scientific questions like tests of the Einstein equivalence principle [12], probing the quantum superposition on macroscopic scales [13] and the search for dark matter candidates [14] and gravitational waves [15, 16]. Being very sensitive to accelerations and rotations, atom interferometry could be used for inertial sensing, replacing commercial laser gyroscopes, and satellite navigation in space [17].

The proposed experiments are typically light-pulse atom interferometers [18]. Beam splitters and mirrors are based on the atom-light interaction in standing laser light waves [19–23]. Depending on the pulse time, the gained velocity recoils lead to splitting or recombination of the atom cloud, analogous to their mechanical counterpart in classical light interferometers. A sketch of a typical time sequence for a Mach-Zehnder type atom interferometer is shown in figure 1.1.

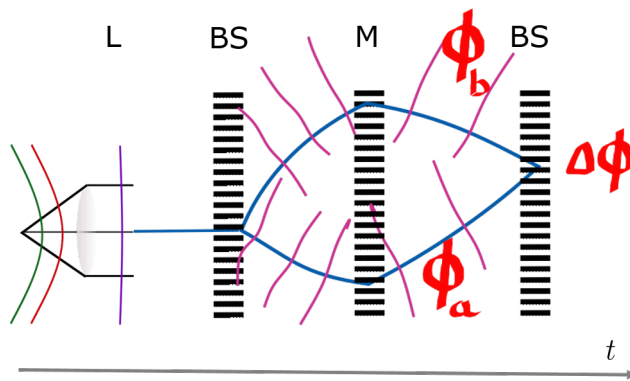


Figure 1.1: Time sequence in a light-pulse atom interferometer. Optical elements: collimating matter-wave lens (L), first beam splitter (BS) pulse by two counter-propagating laser beams, mirror (M) pulse to invert the motion, second beam splitter (BS) pulse for recombination. Path-dependent phases $\phi_{a,b}$ are accumulated in the interferometer arms.

The potential of atomic matter waves as quantum sensors is fully exploited in weightlessness as sensitivity scales quadratically with the interrogation time [24]. Microgravity environments on

earth have been mimicked in atomic fountains [13, 25], drop towers [26, 27] as well as in parabolic flights [28, 29], allowing interferometer times of several seconds. In another approach magnetic forces are used for gravity compensation, levitating the atoms in space [30]. Moreover, milestones for future space applications have been demonstrated on a sounding rocket bringing the first Bose-Einstein condensate to space [31, 32] and on the International Space Station (ISS) having the first Bose-Einstein condensate in Earth's orbit [33, 34].

Common to all μg -interferometric measurements with Bose-Einstein condensates are long expansion times to reduce mean-field interaction as well as to increase the sensitivity of the interferometer. Atomic lenses ((L) in figure 1.1) [35–37] are used to reduce wave packet spreading. The collimated condensate wave function defines the input state for the beam splitter laser pulses that split and recombine the atomic wave packet. As in classical optics, these lenses cause undesired aberrations in the form of additional phase contributions. Hence it is crucial to understand the actual shape of the condensate's phase as it determines the interference patterns at the end of the interferometer [38]. Inspired by Zernike, we adapt his approach for analyzing these aberrations in the world of matter waves.

The major part of this work¹ was done in collaboration with the QUANTUS² (*QUANT*engase *Unter Schwerelosigkeit*) project. The QUANTUS' experimental setups are miniaturized to fit in a drop capsule that is launched at the drop tower facility ZARM (*Zentrum für Angewandte Raumfahrttechnologie und Mikrogravitation*) in Bremen which provides up to 4.7 s free fall time. The initial QUANTUS I project created the first Bose-Einstein condensate in microgravity conditions [26, 39] and realized atom interferometry with long expansion times [27]. The follow-up project QUANTUS II pursues long-term goals such as dual species interferometry with rubidium and potassium. In addition, the scientific findings helped to realize the BEC apparatus for the MAIUS (*MAteriewellenInterferometer Unter Schwerelosigkeit*) rocket mission and the planned BECCAL (*Bose-Einstein Condensate and Cold Atom Laboratory*) project on the ISS. Due to the high technical efforts and various other experiments which are performed at ZARM, the QUANTUS collaboration has performed about 1000 drops in total [40], underlining the need for precision modeling and numerical simulations.

The interferometric measurements discussed so far are performed in free space. Another approach uses guiding potential to build atomic wave guides [41–44]. The coherent and superfluid properties of Bose-Einstein condensates [45, 46] make them also favorable to study persistent flows [47] in exotic potential landscapes. The latter is investigated in the research topic called ATOMTRONICS (*Atom Electronics*) [44] which highlights the analogy to superconductivity in electronic circuits. At TU Darmstadt G. Birkl and his group³ are developing new techniques utilizing digital micro-optics to study ultra-cold atoms in innovative trapping geometries [48]. One of the building blocks are toroidal ring traps that can serve as storage rings but also can be used for interferometric measurements. We study various properties of toroidal Bose-Einstein condensates in the last part of this thesis.

This thesis is organized as follows: In chapter 2, we review the theoretical basics of trapping neutral atoms with magnetic fields and introduce the magnetic chip model that is used in current QUANTUS II experiments. From experimental currents, we deduce trapping potentials that are analyzed and applied in the ongoing thesis. In chapter 3 we briefly repeat the basic concepts of classical mechanics that are important for a semi-classical description of atomic matter waves. We introduce canonical transformations that are required to describe the atomic distributions in a co-expanding frame [49, 50]. In chapter 4, we discuss the major concepts for cold atomic gases and

¹Supported by the German Space Agency (DLR) with funds provided by the Federal Ministry for Economic Affairs and Energy (BMWi) due to enactment of the German Bundestag under grant numbers DLR 50WM1957 and 50WM2250E

²<https://quantus-projects.de/>

³https://www.iap.tu-darmstadt.de/apq/research_apq/atomics_apq/index.en.jsp

Bose-Einstein condensates. We present our results on the momentum widths in the Thomas-Fermi approximation [51]. Based on that, we provide a Thomas-Fermi Wigner function description that can be used as a phase-space representation of interacting condensates in chapter 5. In chapter 6, we formulate a framework and the equation of motion that describe possible aberrations for expanding Bose-Einstein condensates that are perturbed by non-harmonic potentials. These potentials are investigated in chapter 7 in terms of a multipole expansion with physical hydrodynamical basis functions. We apply the latter to characterize aberrations in a single-lens delta-kick collimation sequence in chapter 8. In the last part of this work, chapter 9, we investigate static and dynamical properties of toroidal ring traps and present our findings for the topological deformation from a simply to a multiple connected trap. We summarize the results and provide an outlook in chapter 10.

2 MAGNETIC CHIP TRAPS

The miniaturization of complex wire structures produces tiny magnetic field configurations that can be used for trapping, cooling, and manipulating ultra-cold atoms. As atomic chip traps can be used to scale down the size of experimental setups, they have become very popular in various micro-gravity facilities, for example at the drop tower ZARM [26, 27] or in the Cold Atom Lab on the ISS [34].

In this chapter, we review the basic concepts for magnetic chip traps. We start by introducing Maxwell's equations for static magnetic fields and derive the Biot-Savart law [52]. For trapping neutral atoms in a static magnetic field, we need to consider the interaction of the atom's magnetic dipole moment with the external magnetic field [53]. If the external field strength is small compared to the hyperfine structure of the atoms, the energy shift of the magnetic sublevels is described by the Zeeman effect [54]. In the limit of slow atomic motion one finds the Zeeman potential, which is proportional to the modulus of the magnetic induction. We briefly discuss simple wire geometries that allow the trapping of neutral atoms in three spatial dimensions. We conclude by introducing an actual model of the QUANTUS II atom chip [55, 56] and present different trapping geometries that we use in this thesis.

2.1 STATIC MAGNETIC FIELDS

2.1.1 MAXWELL'S EQUATIONS

The time-independent Maxwell's equations [52] for the magnetic induction $\mathbf{B}(\mathbf{r})$ read

$$\nabla \cdot \mathbf{B} = 0, \quad \nabla \times \mathbf{B} = \mu_0 \mathbf{j}. \quad (2.1)$$

While there are no magnetic charges, Amperè's law links the circulation of the magnetic induction to stationary current density \mathbf{j} , with μ_0 being the magnetic constant of the vacuum. Besides the magnetic induction \mathbf{B} , it is useful to introduce the magnetic vector potential \mathbf{A}

$$\nabla \times \mathbf{A} = \mathbf{B}. \quad (2.2)$$

The vector potential is not uniquely defined, as one can add a curl-free field to \mathbf{A} without changing the magnetic induction. Within the Coulomb gauge

$$\nabla \cdot \mathbf{A} = 0, \quad (2.3)$$

one finds with the Maxwell equations (2.1) the following Poisson equation for the vector potential

$$\Delta \mathbf{A} = -\mu_0 \mathbf{j}. \quad (2.4)$$

In a volume free of any currents the vector potential and the magnetic induction are both satisfying the Laplace equation

$$\Delta \mathbf{A} = 0, \quad \Delta \mathbf{B} = 0. \quad (2.5)$$

As the vector fields in equation (2.5) are harmonic functions, they do not have any stable minima or maxima [57]. However, as discussed in the next section 2.2 the Zeeman potential depends on

2 Magnetic chip traps

the strength of the magnetic induction, $B(\mathbf{r}) = |\mathbf{B}(\mathbf{r})|$. Wing's theorem states that there are no local maxima for the magnetic induction field strength which limits the available magnetic substates that can be used for trapping neutral atoms [58, 59].

2.1.2 BIOT-SAVART LAW

The Poisson equation (2.4) is solved by the Green's function

$$\mathbf{A}(\mathbf{r}) = \frac{\mu_0}{4\pi} \int \frac{\mathbf{j}(\mathbf{r}')}{|\mathbf{r} - \mathbf{r}'|} d^3r'. \quad (2.6)$$

Evaluating the curl of equation (2.6), one finds the relation to the magnetic induction

$$\mathbf{B}(\mathbf{r}) = \frac{\mu_0}{4\pi} \int \frac{\mathbf{j}(\mathbf{r}') \times (\mathbf{r} - \mathbf{r}')}{|\mathbf{r} - \mathbf{r}'|^3} d^3r'. \quad (2.7)$$

Assuming that the current density consists of infinitesimally thin wires which carry the current I , one may replace $\mathbf{j} d^3r'$ the volume integral in equation (2.7) by the line integral $I d\mathbf{r}'$, with the line element $d\mathbf{r}'$. In doing so, one finds the Biot-Savart law

$$\mathbf{B}(\mathbf{r}) = \frac{\mu_0}{4\pi} I \int \frac{d\mathbf{r}' \times (\mathbf{r} - \mathbf{r}')}{|\mathbf{r} - \mathbf{r}'|^3}. \quad (2.8)$$

2.2 ZEEMAN POTENTIAL

2.2.1 ZEEMAN EFFECT

The Zeeman effect describes the energy shift of the atomic energy levels in the presence of an external magnetic induction \mathbf{B} , which interacts with all the different magnetic moments of the atom. The interaction with a magnetic dipole $\hat{\boldsymbol{\mu}}$ is described by the Hamilton operator of the form

$$\hat{H}_1 = -\hat{\boldsymbol{\mu}} \cdot \mathbf{B}. \quad (2.9)$$

The total magnetic moment operator $\hat{\boldsymbol{\mu}}$ of an atom is given by

$$\hat{\boldsymbol{\mu}} = -\frac{\mu_B}{\hbar} \left(g_s \hat{\mathbf{S}} + g_L \hat{\mathbf{L}} - \frac{m_e}{m_p} g_I \hat{\mathbf{I}} \right), \quad (2.10)$$

where the operators $\hat{\mathbf{L}}$, $\hat{\mathbf{S}}$ are referring to the total orbital angular momentum and the total spin of the electrons with the corresponding Landé factors being $g_s \approx 2$, $g_L = 1$. $\hat{\mathbf{I}}$ denotes the total angular momentum of the nuclear spin with g -factor g_I . The fundamental constant

$$\mu_B = \frac{e\hbar}{2m_e}, \quad (2.11)$$

is the Bohr magneton. The last term in equation (2.10) consists of the ratio of the electron and proton masses, $m_e/m_p \ll 1$, and is neglected in the ongoing discussion. For alkali atoms (cf. section 2.2.2) in their ground state, the valence electron is an s -state and therefore does not possess a fine structure splitting as $L = 0$ and equation (2.9) simplifies to

$$\hat{H}_1 = 2\mu_B B \hat{S}_z / \hbar, \quad (2.12)$$

for a magnetic induction orientated along the z -axis $\mathbf{B} = B\mathbf{e}_z$ [53].

The unperturbed Hamilton operator that represents the interaction of the nuclear magnetic moment with the electron spin is

$$\hat{H}_0 = A\hat{\mathbf{I}} \cdot \hat{\mathbf{S}}, \quad (2.13)$$

whereas the c-number A can be found in [53]. To diagonalize \hat{H}_0 , one introduces the total angular momentum of the atom

$$\hat{\mathbf{F}} = \hat{\mathbf{S}} + \hat{\mathbf{I}}, \quad (2.14)$$

and the coupled basis states $\{|(S, I); F, m_F\rangle\}$ that consist of the common eigenstates of the operators $\hat{\mathbf{S}}^2, \hat{\mathbf{I}}^2, \hat{\mathbf{F}}^2, F_z$. If the magnetic interaction is smaller than the hyperfine splitting, we can use the eigenstates of \hat{H}_0 to determine the energy shift in first-order perturbation theory

$$E_{F, m_F} = \langle (S, I); F, m_F | \hat{H}_1 | (S, I); F, m_F \rangle = \mu_B m_F g_F B, \quad (2.15)$$

with the Landé factor

$$g_F = \frac{F(F+1) + S(S+1) - I(I+1)}{F(F+1)}. \quad (2.16)$$

For magnetic induction strengths that are comparable with the energy of the hyperfine splitting, one needs to diagonalize the total Hamilton operator $\hat{H}_0 + \hat{H}_1$. For angular momenta of $F = I \pm \frac{1}{2}$, one finds the Breit-Rabi formula [60] that describes the transition from a weak (Zeeman regime) to a strong external field (Paschen-Back regime).

2.2.2 ALKALI ATOMS

Cold atom experiments are mainly performed with bosonic and/or fermionic alkali atoms due to their favorable atomic properties that are required for laser cooling and trapping. They have one valence electron outside filled shells and behave as simple hydrogen-like atoms. The state of the valence electron is characterized by the ket $|n((LS), J, I), F, m_F\rangle$. Figure 2.1 shows the relevant level scheme of the ground state $n^2S_{1/2}$ as well as the first optical transitions to the excited states $n^2P_{1/2}, n^2P_{3/2}$ for alkali metals with nuclear spin $I = 3/2$. Without the external magnetic field the magnetic substates m_F are energetically degenerate. More detailed hyperfine structures, spectroscopic data of the D1 and D2 transition lines as well as some of the collision properties of different alkali atoms are collected in [61]. The data for ^{87}Rb is summarized in [62]. Properties for different Potassium isotopes are provided in [63] and the references therein.

The total nuclear spin for ^{87}Rb and for ^{41}K is $I = 3/2$. Hence, the total spin is either $F = 1$ or $F = 2$ and the Landé factors (2.16) become $g_1 = -1/2$ and $g_2 = 1/2$ respectively. Therefore, for both atomic species, the magnetic sub-states $|F = 1, m_F = -1\rangle, |F = 2, m_F = 2\rangle$ and $|F = 2, m_F = 1\rangle$ are weak-field seekers which can be trapped in static magnetic fields.

2.2.3 ADIABATIC APPROXIMATION

The energy shifts in equation (2.15) for the eigenstates $|F, m_F\rangle$ may be interpreted as an external potential $U(\mathbf{r})$ when $B(\mathbf{r})$ is spatially dependent. As the atoms are moving through this potential, they experience a temporal change of the magnetic induction. As long as the change is small compared to the typical time scales of the atom's motion, the atom remains in its hyperfine state. This can be expressed by the adiabatic condition

$$\left| \frac{d}{dt} \frac{\mathbf{B}}{|\mathbf{B}|} \right| \ll \omega_L, \quad (2.17)$$

where the time scale is set by the Larmor frequency $\omega_L = g_F \mu_B |\mathbf{B}| / \hbar$.

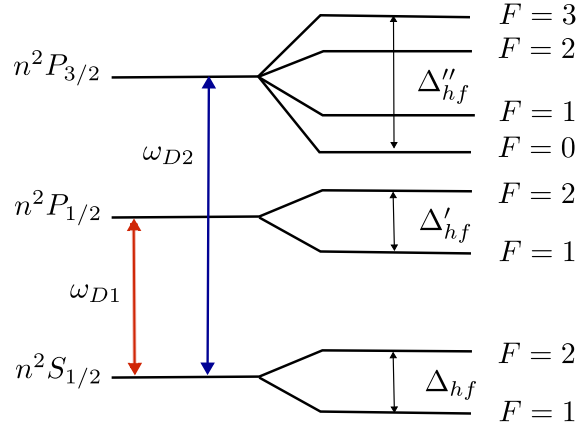


Figure 2.1: Level scheme for alkali metals with nuclear angular momentum $I = 3/2$. Optical transitions to the $D1$ and $D2$ lines. Hyperfine splittings in the different angular momentum manifolds Δ_{hf} , Δ'_{hf} , Δ''_{hf}

As long as the adiabatic criterion (2.17) is fulfilled, atoms are trapped in a Zeeman potential

$$U(\mathbf{r}, t) = \mu_B m_F g_F B(\mathbf{r}, t), \quad B(\mathbf{r}, t) = |\mathbf{B}(\mathbf{r}, t)|. \quad (2.18)$$

For $m_F g_F > 0$, the potential is always positive and atoms are trapped in a local field minimum of B . Therefore, these states are called weak-field seekers. On the other hand, high-field seekers, $m_F g_F < 0$ would be trapped in a local maximum. As discussed in Wing's theorem, local maxima do not exist in free space, and therefore only low-field seeking states are trapped with the Zeeman potential (2.18). For a region where B is very small or becomes zero, atoms may be transferred to another hyperfine state. When the sign of m_F changes or $m_F = 0$, the atoms are lost from the trap which is known as Majorana spin-flip losses [64].

2.3 TRAPPING GEOMETRIES

In this section, we briefly discuss different wire geometries, that are used for trapping and manipulating neutral atoms. We also like to mention that more advanced trapping geometries, e.g. lattices and guiding structures, are feasible using atom chips [65, 66].

2.3.1 LINEAR WAVEGUIDE

The simplest confinement is achieved by superposing the magnetic induction of a single wire carrying a current I and homogeneous bias field being perpendicular to the conductor

$$\mathbf{B}(\mathbf{r}) = B_{\text{bias}} \mathbf{e}_x + \frac{I \mu_0}{2\pi(x^2 + y^2)} (-y \mathbf{e}_x + x \mathbf{e}_y). \quad (2.19)$$

The magnetic induction vanishes at $x_0 = 0, y_0 = I \mu_0 / (2\pi B_{\text{bias}})$. To avoid Majorana flips in the trap centers, one uses an additional offset field, parallel to the waveguide axis. Close to the minimum, one finds the harmonic waveguide approximation

$$B(\mathbf{r}) = \sqrt{b^2 r^2 + B_{\text{off}}^2} \approx B_{\text{off}} + \frac{1}{2} b^2 r^2 / B_{\text{off}}. \quad (2.20)$$

2.3.2 Z- AND U- SHAPED TRAPS

A waveguide just provides trapping in the radial direction. The axial confinement depends on the actual shape of the finite wire endings. For a planar geometry, the wire endings can bend either in the same (U shape) or in opposite directions (Z shape). While the U-shaped wire creates a quadrupole trap, the Z-trap confines the atoms in an elongated three-dimensional Ioffe-Pritchard type potential which is non-zero in the trap center [67–70].

2.4 QUANTUS II CHIP

The QUANTUS II chip is the successor of the QUANTUS I chip that was used successfully in drop tower experiments to create a Bose-Einstein condensate in free fall experiments as well as to perform atom interferometry in microgravity [26, 27]. The more recent model was developed to create a high-flux source of Bose-condensed atoms that can be used for matter-wave interferometry in the drop tower’s catapult mode. In addition, the chip was also designed to trap potassium as a second Bosonic species [55].

2.4.1 CHIP MODEL

The atom chip that is used in this thesis (cf. figure 2.2) is designed in a three-layer structure providing several possible trapping configurations. In combination with a magnetic bias field, created by three pairs of Helmholtz coils, a wide range of different trapping potentials, e.g. magneto-optical trap, evaporation trap, and magnetic lenses, are available. The first layer holds the largest mesoscopic structures. The U-shaped wires form a quadrupole field that is used for the three-dimensional magneto-optical trap (MOT). The second layer, the base chip (BC), and the third layer, the science chip (SC), consist of 4 and 5 wires, respectively, which intersect with one central orthogonal wire [56]. In the following, we regard the active conductors on the base as well as on

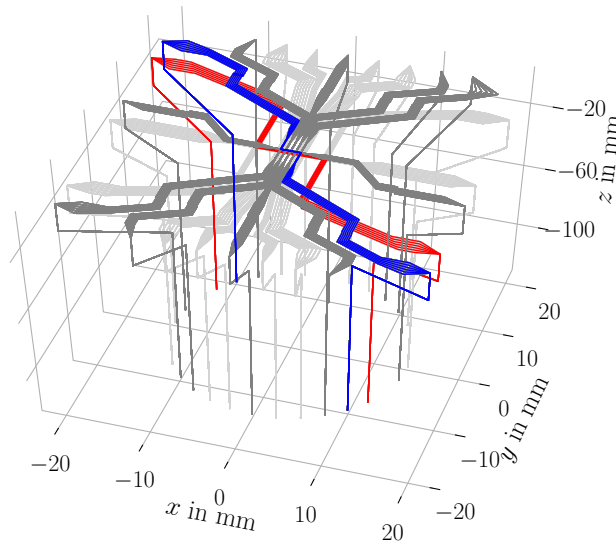


Figure 2.2: QUANTUS II atom chip model [55, 56]. Light-gray wires belong to base chip structure. Gray wires belong to science chip structure. Active conductors in Z-trap configuration in blue (science chip) and red (base chip) colors. Helmholtz coils for the homogeneous field are not depicted.

the science chip in Z-trap configuration which are marked as red and blue in figure 2.2. Both are creating an Ioffe-Pritchard type trapping potential, that is used for releasing (section 2.4.4) and

2 Magnetic chip traps

collimating the condensate (section 2.4.5). The field is superposed by a magnetic bias field created by pairs of Helmholtz coils.

2.4.2 FINITE WIRES

The magnetic induction field for the atom chip is modeled by using finite wire elements that describe the shape of the actual wire for the specified chip geometry. For the atomic waveguide in equation (2.19), we have considered the magnetic induction of an infinite wire. For modeling more complicated structures, we use finite wires with lengths $l_i = |\mathbf{r}_{2,i} - \mathbf{r}_{1,i}|$ that point into the directions $\mathbf{w}_i = (\mathbf{r}_{2,i} - \mathbf{r}_{1,i})/l_i$ and carry a steady current I_i (cf. figure 2.3). We compute the magnetic induction for a single finite wire element using the law of Biot-Savart (2.8). For the parametrization of one wire $\mathbf{r}'(s) = \mathbf{r}_1 + \mathbf{w}s$, $s \in [0, 1]$, one finds

$$\mathbf{B}(\mathbf{r}) = \frac{\mu_0 I}{4\pi r} \frac{\mathbf{e}_1 \times \mathbf{w}}{1 - (\mathbf{e}_1 \cdot \mathbf{w})^2} (\mathbf{e}_2 - \mathbf{e}_1) \cdot \mathbf{w}, \quad (2.21)$$

where the unit vectors \mathbf{e}_2 , (\mathbf{e}_1) are pointing from the conductor's end (start) to the observation point \mathbf{r} and $r = |\mathbf{r} - \mathbf{r}_1|$ denotes the distance to the start of the wire element \mathbf{r}_1 . As Maxwell's equations are linear, the total magnetic induction field for N wires is determined by the sum of all individual fields

$$\mathbf{B}(\mathbf{r}) = \sum_{i=1}^N \mathbf{B}_i(\mathbf{r}) = \frac{\mu_0}{4\pi} \sum_{i=1}^N \frac{I_i}{r_i} \frac{\mathbf{e}_{1,i} \times \mathbf{w}_i}{1 - (\mathbf{e}_{1,i} \cdot \mathbf{w}_i)^2} (\mathbf{e}_{2,i} - \mathbf{e}_{1,i}) \cdot \mathbf{w}_i. \quad (2.22)$$

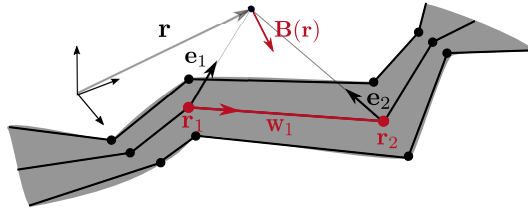


Figure 2.3: Magnetic induction $\mathbf{B}(\mathbf{r})$ at an observation point \mathbf{r} created by a current in the finite wire element pointing in direction \mathbf{w}_1 .

2.4.3 HARMONIC APPROXIMATION

A sketch of the chip coordinate system is shown in figure 2.4. The chip surface lies in the x - y plane, whereas the y -coordinate points into the direction of gravity when the chip is mounted in the drop capsule. To describe the dynamics of ultra-cold gases within the resulting Zeeman potential (2.18), it is convenient to use a coordinate system that fits the atom's center of mass motion. In particular, the minimum of the potential is typically located at a position that is much larger than the typical extent of the atomic cloud.

In general, transformations between two coordinate systems (cf. appendix M) may be considered as either active or passive transformations. From the active point of view, the object is rotated in a fixed coordinate system. In a passive rotation, the object remains fixed while the coordinate system is rotated. The relation for the Zeeman potential between old, chip coordinates \mathbf{r} and new center of mass coordinates \mathbf{r}' is

$$\mathbf{r} = \mathbf{R}\mathbf{r}' + \mathbf{a}, \quad (2.23)$$

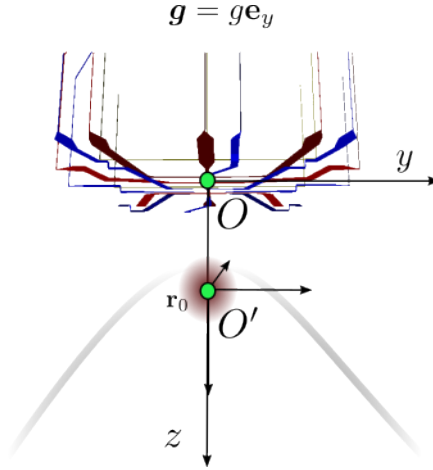


Figure 2.4: Sketch of coordinate system referring to the atomic chip. O refers to the origin defined by the wire geometry. O' refers to the potential minimum aligned with the principle axis of the Hesse matrix K . Gravity points into $\mathbf{g} = g\mathbf{e}_y$ direction.

where R denotes an orthogonal rotation matrix and \mathbf{a} is a translation vector. The value of potential must be equal at the same point regardless of which coordinate system is used

$$U'(\mathbf{r}') = U(\mathbf{r}). \quad (2.24)$$

As the location of the potential determines the center of mass position of the trapped atoms, we are usually interested in the location of the potential minimum $U(\mathbf{r}_0) = U_0$, which is found numerically using standard optimization algorithms [71]. Therein, we do a Taylor expansion up to the second order to obtain the quadratic approximation

$$U(\mathbf{r}) = U_0 + \frac{1}{2}(\mathbf{r} - \mathbf{r}_0)^\top K(\mathbf{r} - \mathbf{r}_0) + \dots \quad (2.25)$$

The real, symmetric Hesse matrix K defines the stiffness as well as the orientation of the trap. For the Zeeman potential (2.18), one finds

$$K_{ij} = \mu_B m_F g_F \frac{\partial^2 B(\mathbf{r}_0)}{\partial x_i \partial x_j}. \quad (2.26)$$

The main axes of the potential are obtained from the eigenvalue equation

$$KR = Kk, \quad k = \text{diag}(k_1, k_2, k_3), \quad (2.27)$$

which defines the 3×3 rotation matrix in equation (2.23) and the corresponding Euler or Tait-Bryan angles. The definition of the rotation matrices and angles are described in appendix M.1. In our case, the rotation matrix R refers to a passive rotation, where the chip object is fixed and the coordinate system changes. As a convention, we refer the lowest eigenvalue to the first axis, the x -direction. Knowing the mass M of the trapped atomic species, the trap trapping-frequencies are obtained

$$\nu_i = \frac{1}{2\pi} \sqrt{\frac{k_i}{M}}, \quad (2.28)$$

by using the eigenvalues k_i from equation (2.27). If not stated explicitly otherwise, we are using the center of mass frame of the Bose-Einstein condensate, whose principle axis is aligned to the release trap axis.

2 Magnetic chip traps

2.4.4 RELEASE TRAP

The release trap configuration is the final stage before the condensate is released to free space to perform matter-wave interferometry with long expansion times. Hence, it is crucial to understand the final state of the condensate in the trap for further explorations. Before the release, there is a sequence of forced evaporation cooling to create a Bose-Einstein condensate and a transport moving the condensate away from the chip surface. During the transport, trap frequencies are decreased to decompress the Bose-condensed gas and to reduce the mean-field energy. The sequence has been optimized to minimize center of mass and quadrupole oscillations via methods of reverse engineering [72]. In addition, controlled quadrupole excitations and a timed release depending on the oscillation phase are used for a lower expansion rate in a specific direction [37]. The set of currents that are used in [37] is summarized in table 2.1.

wires	current
science chip	2.0 A
base chip	6.0 A
x-coils	0.1 A
y-coils	-0.374 31 A
z-coils	0.0 A

Table 2.1: Applied currents to the atom chip to create the release trap.

Cross-sections of the magnetic field strength for the release trap at a mesoscopic length scale are depicted in figure 2.5. Therein, the origin of the coordinate corresponds to the center of

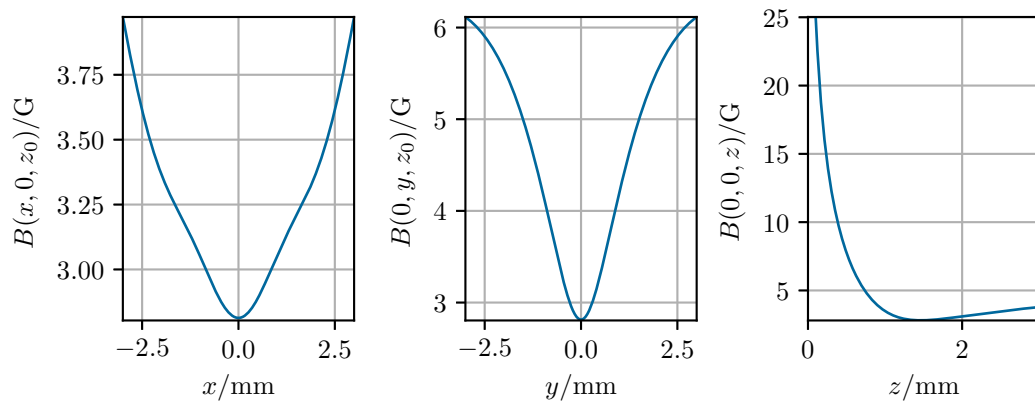


Figure 2.5: One-dimensional cross-sections of the magnetic induction field strength $B(\mathbf{r})$ for the so-called release trap configuration. Currents as in table 2.1. Field minimum at $\mathbf{r}_0 = (0, 0, 1462) \mu\text{m}$.

the atom chip as sketched in figure 2.4. The minimum of magnetic inductions is at $\mathbf{r}_0 = (0, 0, 1462) \mu\text{m}$. Hence, the atoms are located at the center of the atom chip with a displacement in z -direction. After having determined the modulus of the magnetic induction, we can calculate the Zeeman potential $U(\mathbf{r})$ (2.18), where we used the magnetic $|F = 2, m_F = 2\rangle$ substate for alkali atoms. Two-dimensional cross-sections in each plane are shown in figure 2.6. In contrast to figure 2.5, we evaluate the potential in the trap minimum and at a microscopic length scale that covers the spatial extent of the atoms. The typical length scales are set by the thermal de Broglie

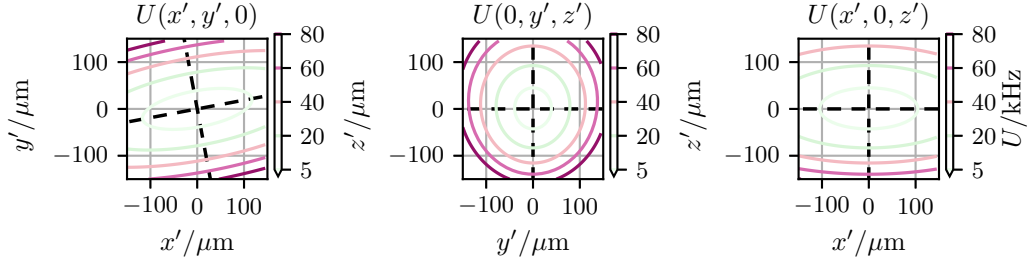


Figure 2.6: Two-dimensional cross-sections of the release trap Zeeman potential for the $|F = 2, m_F = 2\rangle$ magnetic substate. Coordinates are shifted towards the trap minimum. Principle axis of the spring constant K (2.27) marked as black - - -. The constant energy shift is set to zero, $U_0 = 0$.

wavelength, the harmonic oscillator wavelength, and the Thomas-Fermi size of an interacting condensate (cf. section 4.3.3). In addition, we recognize that the equipotential lines in the x - y plane are rotated by an angle γ with respect to chip coordinates. To determine the length scales, the trapping frequencies, as well as the Tait-Bryan angles, we evaluate the Hesse matrix in equation (2.26) and use the masses of the alkali atoms ^{87}Rb and ^{41}K . The trap parameters of the harmonic approximation are shown in table 2.2. For a large condensate consisting of 10^5 ^{87}Rb atoms, we

parameter	symbol	value
spring constant	k	$(709, 6685, 5210) \text{ kHz mm}^{-2}$
frequencies ^{87}Rb	ν_{Rb}	$(9.08, 27.88, 24.61) \text{ Hz}$
frequencies ^{41}K	ν_{K}	$(13.23, 40.41, 35.86) \text{ Hz}$
trap minimum	\mathbf{r}_0	$(0, 0, 1462) \mu\text{m}$
Tait-Bryan angles (xyz)	α, β, γ	$(0, 0, 9.7)^\circ$

Table 2.2: Physical parameters of the QUANTUS II release trap. Spring constants and trap frequencies are corresponding to the magnetic substate $|F = 2, m_F = 2\rangle$.

find in section 4.3.3 that the maximal extent of the condensed cloud is $r_{\text{max}} \approx 25.5 \mu\text{m}$, (cf. figure 4.1). Within this length scale, the harmonic approximation matches the Zeeman potential quite well as shown in figure 2.7. The potential is evaluated using the coordinate transformation in equation (2.23), with $\mathbf{a} = \mathbf{r}_0$ such that the coordinate system is aligned with the principle axis of the Hesse matrix. We provide a more detailed analysis of the release trap potential in chapter 7.1 in terms of a multipole decomposition and in chapter 8 when we analyze a sequence of delta-kick collimation.

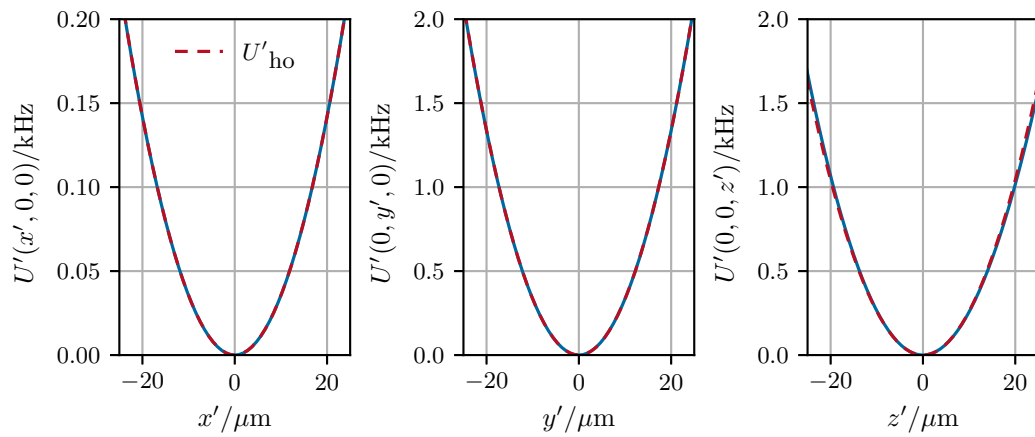


Figure 2.7: One-dimensional cross-sections of the release trap Zeeman potential and its harmonic approximation (red - - -). Coordinate axes are aligned with the principle axis of the harmonic approximation. The constant energy shift is set to zero, $U_0 = 0$.

2.4.5 MAGNETIC LENS

The magnetic lens is based on the release trap configuration, meaning that shape and frequencies are adjusted for optimal collimation. As the magnetic lens is also used in the Z-shape configuration the magnetic field strength does not differ much from the release trap configuration as shown in figure 2.8. As the currents in science chip as well as in the base chip are reduced, the field strength and curvature of the magnetic lens are smaller compared to the release trap. The set of currents

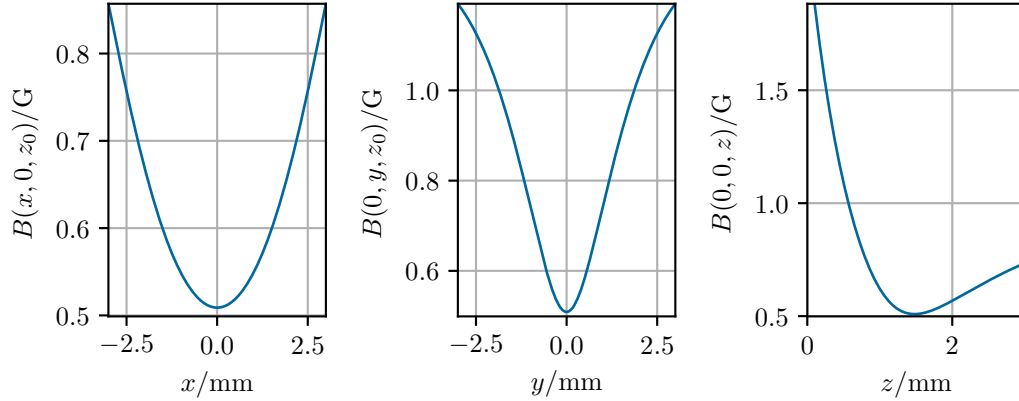


Figure 2.8: Cross-sections of the magnetic induction field strength $B(\mathbf{r})$ for the magnetic lens configuration. Currents as in table 2.3.

for the magnetic lens is shown in the table 2.3. As the magnetic lens is applied after a certain

wires	current
science chip	0.0 A
base chip	1.828 A
x-coils	0.1 A
y-coils	-0.075 428 3 A
z-coils	0.0 A

Table 2.3: Applied currents to the atom chip to create the magnetic lens.

expansion time of the condensate, we need to consider a larger length scale, $r_{\max} \approx 100 \mu\text{m}$, when we evaluated the Zeeman potential for the atoms. The potential for the $|F = 2, m_F = 2\rangle$ state is shown in figures 2.9 and 2.10. The atom chip model provides the parameters of the harmonic approximation in the table 2.4. We note that the trap minimum of the lens differs by $\Delta z = 17 \mu\text{m}$ (cf. table 2.4) with respect to the minimum of the release trap. As discussed in chapter 8, a deviation of the trap minimum for the center of mass position leads to an additional momentum kick. However, the offset is chosen on purpose as an additional center of mass velocity is observed experimentally which is compensated by the spatial position of the lens [38, 73]. The shape of the magnetic lens is almost cylindrical $\omega_y \approx \omega_z$ which can be used for collimation of the atomic ensemble in at least two directions. The velocity spread in the third direction may be reduced by shaping the corresponding quadrupole mode [37].

2 Magnetic chip traps

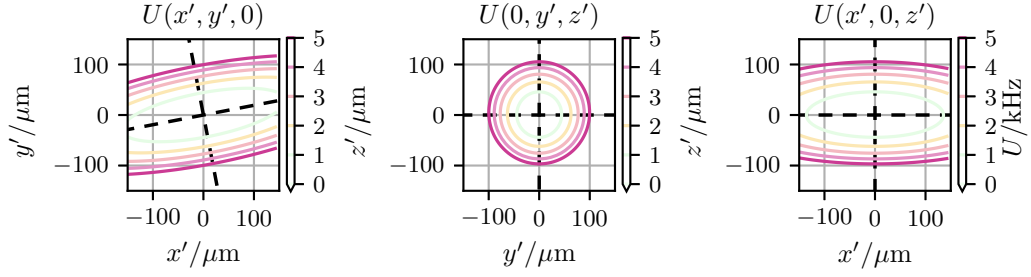


Figure 2.9: Two-dimensional cross-sections of the magnetic lens potential for the $|F = 2, m_F = 2\rangle$ magnetic substate. Coordinates are shifted towards the trap minimum. Principle axis of the string constant K (2.27) marked as black - - -. The constant energy shift is set to zero, $U_0 = 0$.

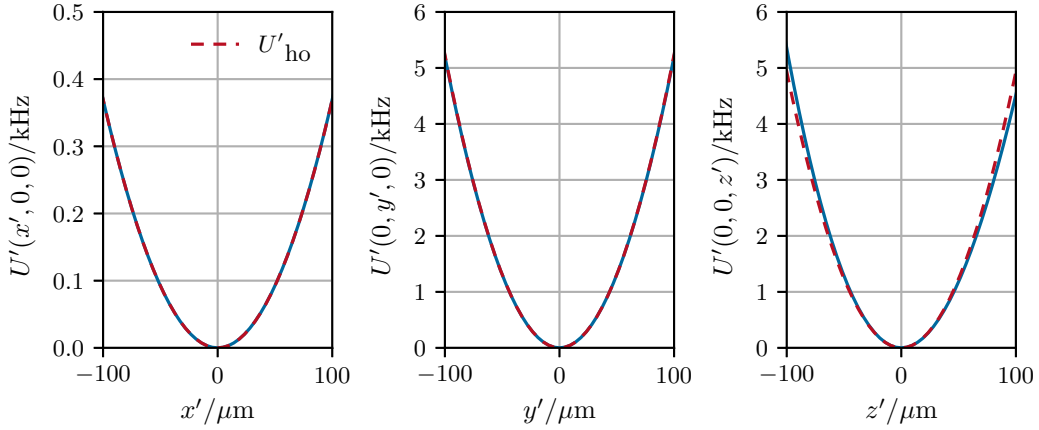


Figure 2.10: One-dimensional cross-sections of the magnetic lens potential and its harmonic approximation (red - - -). Coordinate axes are aligned with the principle axis of the harmonic approximation. The constant energy shift is set to zero, $U_0 = 0$.

parameter	symbol	value
spring constant	k	$(75, 978, 975) \text{ kHz mm}^{-2}$
frequencies ^{87}Rb	ν_{Rb}	$(2.96, 10.66, 10.65) \text{ Hz}$
frequencies ^{41}K	ν_{K}	$(4.31, 15.53, 15.51) \text{ Hz}$
trap minimum	r_0	$(0, 0, 1479) \mu\text{m}$
Tait-Bryan angles (XYZ)	α, β, γ	$(0, 0, 9.3)^\circ$

Table 2.4: Physical parameters of the QUANTUS II magnetic lens. Spring constants and trap frequencies are corresponding to the magnetic substate $|F = 2, m_F = 2\rangle$.

3 CLASSICAL DESCRIPTION OF ATOMIC MATTER WAVES

For an ideal gas, the either classical or quantum phase-space distribution function factorizes to an effective single-particle distribution function whose dynamic is described by a classical or quantum Liouville-von Neumann equation respectively [74]. If the Hamiltonian of the system is at most quadratic in position and momentum, the time-evolution of the quantum system coincides with its classical counterpart [75]. Therefore, it is often sufficient and insightful to study the trajectories of a classical single particle in phase space. In this chapter, we will briefly introduce the basic concepts of classical mechanics [76–78]. We recap the principle of least action and Hamilton’s equation of motion. Afterward, we discuss the concept of canonical transformations as they play a major role in an efficient description of Bose-condensed gas in quadratic potentials [49, 50, 79].

3.1 PRINCIPLE OF LEAST ACTION

The state of a classical system in configuration space with N particles in d spatial dimensions is characterized by its generalized coordinates and velocities

$$(\mathbf{q}, \dot{\mathbf{q}}) = (q_1, \dots, q_f; \dot{q}_1, \dots, \dot{q}_f), \quad f = Nd. \quad (3.1)$$

To obtain the equations of motion for classical particles, we formulate Hamilton’s principle of least action which states that the action functional,

$$S[\mathbf{q}] = \int_{t_0}^{t_1} L(\mathbf{q}, \dot{\mathbf{q}}) dt, \quad (3.2)$$

becomes stationary for the actual path of the motion. The action $S[\mathbf{q}]$ is defined by the integral of the Lagrange function

$$L(\mathbf{q}, \dot{\mathbf{q}}) = T - U, \quad (3.3)$$

over the time interval (t_0, t_1) . T and U are the kinetic and potential energy of the system. For a stationary point, the variation of the integral for fixed t_0 and t_1 is zero

$$\delta S = 0. \quad (3.4)$$

The change of the action is then given by

$$\delta S = \int_{t_0}^{t_1} \sum_{i=1}^f \left(\frac{\partial L}{\partial q_i} \delta q_i + \frac{\partial L}{\partial \dot{q}_i} \delta \dot{q}_i \right) dt. \quad (3.5)$$

Applying partial integration on the second term on the right-hand side and demanding that the variations at the endpoints are vanishing, $\delta q_i(t_0) = \delta q_i(t_1) = 0$, one finds

$$\delta S = \int_{t_0}^{t_1} \sum_{i=1}^f \left(\frac{\partial L}{\partial q_i} - \frac{d}{dt} \frac{\partial L}{\partial \dot{q}_i} \right) \delta q_i dt. \quad (3.6)$$

3 Classical description of atomic matter waves

According to the least action principle, equation (3.4) is satisfied when all terms of the sum are vanishing simultaneously. Therefore, the integrand has to be zero and we arrive at the Euler-Lagrange equations

$$\frac{d}{dt} \frac{\partial L}{\partial \dot{q}_i} = \frac{\partial L}{\partial q_i}, \quad (3.7)$$

that describe the dynamics of a conservative system.

3.2 HAMILTON DYNAMICS

An alternative formulation of classical mechanics is the Hamiltonian description in terms of two first-order differential equations of the two independent variables (\mathbf{q}, \mathbf{p}) , with conjugate momenta that are defined as

$$p_i = \frac{\partial L}{\partial \dot{q}_i}. \quad (3.8)$$

Though physics is unaltered in the new formalism, it is useful to provide a framework for theoretical extensions such as the Hamilton-Jacobi theory in classical mechanics or the Hamilton formulation of quantum mechanics and field theory. Mathematically we switch from coordinates $(\mathbf{q}, \dot{\mathbf{q}}, t)$ to $(\mathbf{q}, \mathbf{p}, t)$ by a Legendre transformation with respect to the velocities $\dot{\mathbf{q}}$. We write the Lagrangian in its differential form

$$\begin{aligned} dL &= \sum_{i=1}^f \left(\frac{\partial L}{\partial q_i} dq_i + \frac{\partial L}{\partial \dot{q}_i} d\dot{q}_i \right) + \frac{\partial L}{\partial t} dt \\ &= \sum_{i=1}^f (\dot{p}_i dq_i + p_i d\dot{q}_i) + \frac{\partial L}{\partial t} dt. \end{aligned} \quad (3.9)$$

In the first line within the brackets, we recognize the generalized momenta defined in equation (3.8). For the second term, we used the Euler-Lagrange equation. The Legendre transformation is generated by the Hamilton function

$$H(\mathbf{q}, \mathbf{p}, t) = \sum_{i=1}^f p_i \dot{q}_i - L, \quad (3.10)$$

which is a function of \mathbf{q}, \mathbf{p} and t . One can write the Hamilton function in its differential form

$$dH = \sum_{i=1}^f (-\dot{p}_i dq_i + \dot{q}_i dp_i) - \partial_t L dt. \quad (3.11)$$

using equation (3.9). Comparing the equation (3.11) with

$$dH = \sum_{i=1}^f \left(\frac{\partial H}{\partial p_i} dp_i + \frac{\partial H}{\partial q_i} dq_i \right) + \frac{\partial H}{\partial t} dt, \quad (3.12)$$

and using the differential form of the Lagrange function in equation (3.9), one finds the following set of equations

$$\dot{q}_i = \frac{\partial H}{\partial p_i}, \quad \dot{p}_i = -\frac{\partial H}{\partial q_i}, \quad \frac{\partial L}{\partial t} = -\frac{\partial H}{\partial t}, \quad (3.13)$$

which are the Hamilton's equations of motion, replacing the Euler-Lagrange equations.

3.3 CANONICAL TRANSFORMATION

In the Lagrangian description, the Euler-Lagrange equations are invariant under a so-called point transformation

$$Q_i = Q_i(\mathbf{q}, t), \quad (3.14)$$

where we have introduced a new coordinate Q_i that is a function of the old generalized coordinates and may depend explicitly on time t . The strength of the Hamilton formalism is the treatment of coordinates and momenta as independent variables. Therefore a much wider class of transformations

$$Q_i = Q_i(\mathbf{q}, \mathbf{p}, t), \quad P_i = P_i(\mathbf{q}, \mathbf{p}, t), \quad (3.15)$$

to new coordinates, Q_i and P_i , are allowed as they may depend on the old phase space coordinates and explicitly on time. \mathbf{Q} and \mathbf{P} are called canonical variables, and the transformation from (\mathbf{q}, \mathbf{p}) to (\mathbf{Q}, \mathbf{P}) is said to be a canonical transformation with respect to a new Hamilton function $K(\mathbf{Q}, \mathbf{P}, t)$ such that the equations of motion are of the form

$$\dot{Q}_i = \frac{\partial K}{\partial P_i}, \quad \dot{P}_i = -\frac{\partial K}{\partial Q_i}. \quad (3.16)$$

To derive a relation between old coordinates and momenta and the new ones, we express the Lagrange functions $L(\mathbf{q}, \dot{\mathbf{q}})$ and $L'(\mathbf{Q}, \dot{\mathbf{Q}})$ in their differential form

$$p_i dq_i - H dt = P_i dQ_i - K dt + dF. \quad (3.17)$$

They differ by a total differential dF that does not alter the equations of motion. Assuming that $F = F(\mathbf{q}, \mathbf{Q}, t)$ is a function of old and new coordinates and time, the differential takes the form

$$dF = \frac{\partial F}{\partial q_i} dq_i + \frac{\partial F}{\partial Q_i} dQ_i + \frac{\partial F}{\partial t} dt. \quad (3.18)$$

Comparing equation (3.17) with equation (3.18) one finds the following relation

$$p_i = \frac{\partial F}{\partial q_i}, \quad P_i = -\frac{\partial F}{\partial Q_i}, \quad K = H + \frac{\partial F}{\partial t}. \quad (3.19)$$

F is called the generating function and defines the coordinate transformation from one set of canonical variables to another one. In general, there are four basic types of generating functions being related to each other by a Legendre transformation. Their properties are summarized in table 3.1.

Generating function	Relation to coordinates and momenta
$F = F_1(q, Q, t)$	$p_i = \partial F_1 / \partial q_i, \quad P_i = -\partial F_1 / \partial Q_i$
$F = F_2(q, P, t) - Q_i P_i$	$p_i = \partial F_2 / \partial q_i, \quad Q_i = \partial F_2 / \partial P_i$
$F = F_3(P, Q, t) + q_i p_i$	$q_i = -\partial F_3 / \partial p_i, \quad P_i = -\partial F_3 / \partial Q_i$
$F = F_4(p, P, t) + q_i p_i - Q_i P_i$	$q_i = \partial F_4 / \partial p_i, \quad Q_i = \partial F_4 / \partial P_i$

Table 3.1: Properties of the four basic generating functions for canonical transformations

3 Classical description of atomic matter waves

A special generating function is found when the new Hamilton function $K = 0$ vanishes. Let $S = S(\mathbf{q}, \mathbf{P}, t)$ be the corresponding generating function with $p_i = \partial_{q_i} S$ (cf. table 3.1). Then S must satisfy the so-called Hamilton-Jacobi equation

$$H\left(q_i, \frac{\partial S}{\partial q_i}\right) + \frac{\partial S}{\partial t} = 0. \quad (3.20)$$

For a general Hamilton function, a complete solution of the Hamilton-Jacobi equation is not available. However, if the Hamilton function is of the form

$$H = H_0 + H_1, \quad (3.21)$$

where the dynamics of H_0 is known and H_1 is a small perturbation, the generating of H_0 can be used to study the transformed Hamiltonian $K = H_1$ in perturbation theory [80]. Ideally, the canonical variables of $K(\mathbf{Q}, \mathbf{P}, t)$ show less time dependence than the original phase-space coordinates. The latter becomes important for numerical studies over long periods. Hence, canonical coordinate transformations are required to study the dynamics of cold gases on macroscopic time scales and large distances [81].

3.3.1 BALLISTIC EXPANSION

The simplest system is the free-moving point particle. In the absence of the external potential, the Hamilton function is merely

$$H_0 = \frac{\mathbf{p}^2}{2M}, \quad (3.22)$$

the kinetic energy. According to the Hamilton equations (3.13), the equations of motion are

$$\dot{\mathbf{q}} = \frac{\mathbf{p}}{M}, \quad \dot{\mathbf{p}} = 0. \quad (3.23)$$

Including the initial conditions the general solution reads

$$\begin{pmatrix} \mathbf{q}(t) \\ \mathbf{p}(t) \end{pmatrix} = \underbrace{\begin{pmatrix} \mathbb{1} & \frac{1}{M}(t - t_0) \\ 0 & \mathbf{p}_0 \end{pmatrix}}_{G_0(t, t_0)} \begin{pmatrix} \mathbf{q}_0 \\ \mathbf{p}_0 \end{pmatrix}. \quad (3.24)$$

where $G_0(t, t_0)$ is the transfer matrix of the free particle. To obtain the generating function for the free particle Hamiltonian, one considers the inverse transformation with G_0^{-1} of equation (3.24) which defines the canonical variables $\mathbf{q}_0 = \mathbf{Q}$, $\mathbf{p}_0 = \mathbf{P}$. Let $S_0(\mathbf{q}, \mathbf{Q}, t)$ be the generating function depending on old and new coordinates. Using the corresponding relations in table 3.1, one finds

$$S_0(\mathbf{q}, \mathbf{Q}, t) = \frac{M}{2} \frac{(\mathbf{Q} - \mathbf{q})^2}{t - t_0}, \quad (3.25)$$

which transforms the system to

$$K = H_0 + \partial_t S_0 = 0. \quad (3.26)$$

3.3.2 HARMONIC OSCILLATOR

One of the most important systems is the harmonic oscillator. The Hamilton function reads

$$H_{\text{HO}} = \frac{\mathbf{p}^2}{2M} + \frac{1}{2} \mathbf{q}^\top \mathbf{K} \mathbf{q}, \quad (3.27)$$

where the real symmetric matrix \mathbf{K} describes the stiffness of the trap. For a particle with mass M , one finds the trapping matrix $\Omega^2 = \mathbf{K}/M$. The Hamilton's equations are

$$\dot{\mathbf{q}} = \frac{\mathbf{p}}{M}, \quad \dot{\mathbf{p}} = -M\Omega^2 \mathbf{q}. \quad (3.28)$$

The transfer function for the harmonic oscillator is given by

$$\begin{pmatrix} \mathbf{q}(t) \\ \mathbf{p}(t) \end{pmatrix} = \underbrace{\begin{pmatrix} \cos \Omega t & (M\Omega)^{-1} \sin \Omega t \\ -M\Omega \sin \Omega t & \cos \Omega t \end{pmatrix}}_{\mathbf{G}_{\text{HO}}(t, t_0)} \begin{pmatrix} \mathbf{q}_0 \\ \mathbf{p}_0 \end{pmatrix}, \quad (3.29)$$

representing a rotation in phase space. As described in the previous section, we can look for the corresponding generating function, that solves the Hamilton-Jacobi equation. It reads

$$S_{\text{HO}}(\mathbf{q}, \mathbf{Q}, t) = \frac{M\Omega}{2 \sin \Omega t} [(\mathbf{q}^2 + \mathbf{Q}^2) \cos \Omega t - 2\mathbf{q}\mathbf{Q}]. \quad (3.30)$$

It is worth noting that the generating functions for the free particle S_0 in equation (3.25) and for the harmonic oscillator S_{HO} in equation (3.30) coincide with the Green's functions for the corresponding single-particle Schrödinger equations. In particular, this statement holds as long as the time evolution is generated by a quadratic Hamilton operator. This can be formalized in terms of the quantum action principle and quantum canonical transformation [82, 83].

3.4 SCALING TRANSFORMATION

In this section, we discuss the Hamilton function

$$H(\mathbf{r}, \mathbf{p}, t) = \frac{\mathbf{p}^2}{2M} + \frac{M}{2} [\mathbf{r} - \mathbf{r}_0(t)]^\top \Omega^2(t) [\mathbf{r} - \mathbf{r}_0(t)] + \mathbf{F}^\top \mathbf{r} + U_1(\mathbf{r}, t), \quad (3.31)$$

for a general time-dependent harmonic oscillator, that may have changing frequencies $\Omega^2(t)$ and a changing spatial position $\mathbf{r}_0(t)$. In addition, we have included a constant force \mathbf{F} acting on the atoms as well as a small perturbation $U_1(\mathbf{r}, t)$ to the harmonic oscillator. The time-dependent quadratic system ($\mathbf{F} = U_1 = 0$) has been heavily studied in classical as well as in quantum mechanics. In particular for constructing Lewis-Riesenfeld invariants [84–86], that map the motion of the quantum particle to a set of ordinary differential equations.

In order to solve the mechanical problem, one considers the following canonical transformation

$$\begin{pmatrix} \boldsymbol{\xi} \\ \boldsymbol{\pi} \end{pmatrix} = \begin{pmatrix} \Lambda^{-1} & 0 \\ -M\dot{\Lambda}^\top & \Lambda^\top \end{pmatrix} \begin{pmatrix} \mathbf{r} - \boldsymbol{\eta}(t) \\ \mathbf{p} - M\dot{\boldsymbol{\eta}}(t) \end{pmatrix}, \quad (3.32)$$

with time-dependent function $\boldsymbol{\eta}(t)$ and a time-dependent 3×3 matrix $\Lambda(t)$ with initial value $\Lambda(t_0) = \mathbb{1}$, $\dot{\Lambda}(t_0) = 0$. As the Λ -matrix acts as a rescaling of the original position coordinate, the

3 Classical description of atomic matter waves

transformation is a so-called scaling transformation with adaptive scales to the new phase-space coordinates $(\boldsymbol{\xi}, \boldsymbol{\pi})$. The transformed Hamilton function with respect to the new coordinates reads

$$H'(\boldsymbol{\xi}, \boldsymbol{\pi}, t) = H(\mathbf{r}, \mathbf{p}, t) + \partial_t S(\mathbf{r}, \boldsymbol{\pi}, t), \quad (3.33)$$

with Hamilton's equations of motion

$$\dot{\boldsymbol{\xi}} = \frac{\partial H'}{\partial \boldsymbol{\pi}}, \quad \dot{\boldsymbol{\pi}} = -\frac{\partial H'}{\partial \boldsymbol{\xi}}. \quad (3.34)$$

The generating function $S(\mathbf{r}, \boldsymbol{\pi}, t)$ depends on the old position and new momentum variables such that

$$\boldsymbol{\xi} = \frac{\partial S}{\partial \boldsymbol{\pi}}, \quad \mathbf{p} = \frac{\partial S}{\partial \mathbf{r}}. \quad (3.35)$$

After integrating these equations using the relation between the old and new coordinates in (3.32), one finds the generating function for the scaling transformation

$$\begin{aligned} S(\mathbf{r}, \boldsymbol{\pi}, t) &= \frac{M}{2} [\mathbf{r} - \boldsymbol{\eta}(t)]^\top \dot{\Lambda} \Lambda^{-1} [\mathbf{r} - \boldsymbol{\eta}(t)] \\ &\quad + M \mathbf{r}^\top \dot{\boldsymbol{\eta}}(t) + \boldsymbol{\pi}^\top \Lambda^{-1} [\mathbf{r} - \boldsymbol{\eta}(t)] \\ &\quad + s(t), \end{aligned} \quad (3.36)$$

where $s(t)$ denotes some time-dependent function, that does not depend on the phase space coordinates. Using equation (3.33) the new Hamilton function becomes

$$\begin{aligned} H'(\boldsymbol{\xi}, \boldsymbol{\pi}) &= \frac{1}{2M} \boldsymbol{\pi}^\top M^{-1} \boldsymbol{\pi} + U_1(\Lambda \boldsymbol{\xi} + \boldsymbol{\eta}, t) \\ &\quad + \frac{M}{2} \boldsymbol{\xi}^\top \left[\Lambda^\top \ddot{\Lambda} + \Lambda^\top \Omega^2(t) \Lambda \right] \boldsymbol{\xi} \\ &\quad + M \boldsymbol{\xi}^\top \Lambda^\top [\ddot{\boldsymbol{\eta}} + \Omega^2(t)(\boldsymbol{\eta} - \mathbf{r}_0) + \mathbf{F}/M] \\ &\quad + M \frac{d}{dt}(\boldsymbol{\eta} \dot{\boldsymbol{\eta}}) - L + \dot{s}, \end{aligned} \quad (3.37)$$

where we have introduced the Lagrange function

$$L(\boldsymbol{\eta}, \dot{\boldsymbol{\eta}}, t) = \frac{M}{2} \dot{\boldsymbol{\eta}}^2 - \mathbf{F}^\top \boldsymbol{\eta} - \frac{M}{2} (\boldsymbol{\eta} - \mathbf{r}_0)^\top \Omega^2(t) (\boldsymbol{\eta} - \mathbf{r}_0), \quad (3.38)$$

and the time-dependent mass matrix

$$\mathbf{M} = \Lambda^\top \Lambda, \quad (3.39)$$

in the kinetic energy of H' . The last line defines the action variable which reads

$$s(t) = \int_{t_0}^t L(\boldsymbol{\eta}, \dot{\boldsymbol{\eta}}, t') dt' - M[\boldsymbol{\eta}(t) \dot{\boldsymbol{\eta}}(t) - \boldsymbol{\eta}(t_0) \dot{\boldsymbol{\eta}}(t_0)]. \quad (3.40)$$

Further, one demands that the coordinates $\boldsymbol{\eta}(t)$ follow the Newton equation

$$\ddot{\boldsymbol{\eta}} = -\Omega^2(t)(\boldsymbol{\eta} - \mathbf{r}_0) - \mathbf{F}/M, \quad (3.41)$$

in the time-dependent harmonic oscillator potential and the constant force. To simplify the second line being quadratic in the coordinate $\boldsymbol{\xi}$, one can specify a matrix differential equation for the adaptive scales $\Lambda(t)$, depending on the further treatment of the system.

FREE-PARTICLE If one chooses the matrix differential equation to be

$$\ddot{\Lambda} + \Omega^2(t)\Lambda = 0, \quad (3.42)$$

the Hamilton function in equation (3.37) is transformed to a free-particle system with time-dependent mass, for a vanishing perturbation $U_1 = 0$ and constant force $\mathbf{F} = 0$.

HARMONIC OSCILLATOR Besides the free-particle solution, one can transform the system to a time-independent harmonic oscillator by choosing the following non-linear matrix differential equation

$$\Lambda^\top \left[\ddot{\Lambda} + \Omega^2(t)\Lambda \right] = f(\Lambda)\Omega^2(0), \quad (3.43)$$

where f is a scalar function of the time-dependent scales. The explicit form depends on the spatial dimension as well as the shape of the trapping matrix $\Omega^2(t)$.

For a non-interacting, single particle in a one-dimensional harmonic oscillator, one recovers the famous Ermakov-Pinney [87, 88] equation

$$\ddot{\lambda} + \omega^2(t)\lambda = \omega_0^2\lambda^{-3}, \quad (3.44)$$

which arises naturally when constructing Lewis-Riesenfeld [84] invariants for the time-dependent harmonic oscillator. For a wave packet solution (cf. appendix A) of the time-dependent Schrödinger equation, $\lambda(t)$ corresponds to the width or position uncertainty. $\eta(t)$ describes the classical position of the Gaussian having a momentum of $M\dot{\eta}$ [85].

4 CONCEPTS OF COLD ATOMIC GASES

In this chapter, we review the basic concepts of cold atomic gases. In particular, we focus on the physics of a Bose-condensed gas, which provides a coherent atomic source for matter-wave optics. In ultra-cold gases, the interparticle interaction is strongly influenced by the collision properties in the low-energy regime for small relative momenta. We introduce important scattering properties such as the phase shift and the s-wave scattering length. Afterwards, we derive the classical field equation for Bosons by modeling the state of the condensate as a multimode coherent state that is macroscopically occupied. We present our results for the d-dimensional Thomas-Fermi approximation, which we use in chapter 5 to calculate the single-particle Wigner function [51]. We conclude by introducing the scaling solutions for the classical Euler equation which we require for (3+1)d-dimensional simulations with long expansion times in chapter 8.

4.1 DILUTE GASES AT LOW TEMPERATURES

We consider an N particle system with atoms of mass M . From the classical point of view, we can assign to each particle a position in configuration space \mathbf{r} and momentum $\mathbf{p} = M\mathbf{v}$ in momentum space where \mathbf{v} is the velocity of the atom. For matter waves, we associate to the momentum $\mathbf{p} = \hbar\mathbf{k}$ a de Broglie wavelength $\lambda_{\text{dB}} = 2\pi/k$ [9], where $k = |\mathbf{k}|$ is a wavenumber. For a thermal gas, one can define a thermal de Broglie wavelength

$$\lambda_{\text{th}} = \left(\frac{2\pi\hbar^2}{Mk_B T} \right)^{1/2}, \quad (4.1)$$

at a temperature T . The length λ_{th} describes the position uncertainty associated with the thermal momentum distribution. Quantum effects become visible when the phase space density is

$$n\lambda_{\text{th}}^3 \lesssim 1, \quad (4.2)$$

that is when the size of the atomic wave packets is comparable to the interparticle distance [89].

4.2 MODEL FOR INTERACTIONS

For dilute gases at low temperatures, the atoms move slowly at large distances from each other and interact pairwise via a van-der Waals-like potential. Slowly means that the thermal de Broglie wavelength is much larger than the range of the interaction potential $\lambda_{\text{th}}r_0 \gg 1$ or in terms of the wavenumber for the relative particle motion

$$kr_0 \ll 1. \quad (4.3)$$

In this low-energy collision regime, the asymptotic wave function ($r \gg r_0$) becomes independent of the details of the interaction potential as the short-range physics is not resolved. Instead, one introduces the concepts of the phase shift and the associated scattering length to describe the collisional properties of the quantum gas [90].

4.2.1 ELASTIC SCATTERING FOR NEUTRAL ATOMS

In time-independent scattering theory [91, 92] the asymptotic wave function at large distances may be written in terms

$$\psi_k(r, \theta) = \psi_{\text{in}} + \psi_{\text{sc}} \underset{r \rightarrow \infty}{\simeq} e^{ikr \cos \vartheta} + f(\vartheta) \frac{e^{ikr}}{r}, \quad (4.4)$$

of an incident plane wave, traveling in the z -direction, and a scattered, outgoing spherical wave. The prefactor $f(\vartheta)$ is the scattering amplitude representing the probability for scattering at an angle ϑ .

To describe the scattering process for neutral atoms in a spherical symmetric central potential $V(|\mathbf{r}_1 - \mathbf{r}_2|)$, it is convenient to introduce the center of mass

$$\mathbf{R} = \frac{M_1 \mathbf{r}_1 + M_2 \mathbf{r}_2}{M_1 + M_2}, \quad (4.5)$$

and the relative position coordinates

$$\mathbf{r} = \mathbf{r}_1 - \mathbf{r}_2. \quad (4.6)$$

In these coordinates the total wave function separates as

$$\Psi(\mathbf{R}, \mathbf{r}) = \psi_{\text{com}}(\mathbf{R})\psi(\mathbf{r}), \quad (4.7)$$

where the center of mass wave function is a constant, while the wave function for the relative motion obeys the single-particle Schrödinger equation

$$\left[\frac{\hat{p}_r^2}{2\tilde{\mu}} + \frac{\hat{L}^2}{2\tilde{\mu}r^2} + V(r) \right] \psi(\mathbf{r}) = E\psi(\mathbf{r}), \quad (4.8)$$

for a particle with reduced mass

$$\tilde{\mu} = \frac{M_1 M_2}{M_1 + M_2}. \quad (4.9)$$

The kinetic energy in position representation is written terms of the radial momentum

$$\hat{p}_r = -i\hbar \frac{1}{r} \frac{\partial}{\partial r} (r \cdot), \quad (4.10)$$

as well as the angular momentum operator

$$\hat{L}^2 = -\hbar^2 \left[\frac{1}{\sin \vartheta} \frac{\partial}{\partial \vartheta} \left(\sin \vartheta \frac{\partial}{\partial \vartheta} \right) + \frac{1}{\sin^2 \vartheta} \frac{\partial^2}{\partial \varphi^2} \right]. \quad (4.11)$$

The general solution for a particle in a central potential

$$\psi_k(\mathbf{r}) = \sum_{l=0}^{\infty} \sum_{m=-l}^l c_{lm} R_{lm}(r, k) Y_{lm}(\vartheta, \varphi) \quad (4.12)$$

$$= \sum_{l=0}^{\infty} (2l+1)! c_l R_l(r, k) P_l(\cos \vartheta), \quad (4.13)$$

is a linear combination of radial R_{lm} and angular Y_{lm} eigenfunctions, known as a partial wave expansion [93]. In equation (4.13), we have exploited the azimuthal independence of the scattering

solutions by choosing the incident wave vector in z -direction. P_l are the Legendre polynomials. The radial functions are the eigenfunctions of the radial Schrödinger equation

$$\left[-\frac{\hbar^2}{2\tilde{\mu}} \left(\frac{d^2}{dr^2} + \frac{2}{r} \frac{d}{dr} \right) + V_{\text{eff}}(r) \right] R_l(r, k) = E_{kl} R_l(r, k), \quad (4.14)$$

with an effective potential

$$V_{\text{eff}}(r) = V(r) + V_{\text{rot}}(r) = V(r) + \frac{\hbar^2 l(l+1)}{2\tilde{\mu} r^2}, \quad (4.15)$$

that consists of the central potential $V(r)$ and the centrifugal barrier $V_{\text{rot}}(r)$.

For large distances beyond the effective range of the interactions potential ($r \gg r_0$) the solution of equation (4.14) must coincide with the free Schrödinger equation which consists of spherical Bessel and spherical von-Neumann functions [90]. Regarding large distances in the far field zone, $r \rightarrow \infty$, the functions have the asymptotic behavior

$$R_l(r, k) \xrightarrow{r \rightarrow \infty} \frac{1}{kr} \sin(kr + \eta_l - l\pi/2), \quad (4.16)$$

where η_l represents the collisional phase shift, containing the physical information of the scattering process.

The partial wave expansion of the scattering amplitude

$$f(\vartheta) = \sum_{l=0}^{\infty} (2l+1) f_l(k) P_l(\cos \vartheta), \quad f_l(k) = \frac{e^{2i\eta_l} - 1}{2ik}, \quad (4.17)$$

connects the amplitudes f_l to the scattering phase shift η_l by combining equations (4.4), (4.16) and (4.13).

For cold atoms at low energies $kr \ll 1$, we are particularly interested in the limit $k \rightarrow 0$. For typical parameters of alkali atoms, the centrifugal barrier allows only s -wave scattering with angular momentum of $l = 0$. The short-range, low-energy expansion of the scattering phase

$$k\eta_0 = -\frac{1}{a_s} + \mathcal{O}(k^2), \quad (4.18)$$

leads to the definition of the s -wave scattering length a_s . For the scattering wave function of the colliding atoms, one finds in the low-energy limit

$$R_0(r) = 1 - \frac{a_s}{r}, \quad (4.19)$$

and the scattering observables, such as the scattering amplitude, the differential, and the total cross-section are given by

$$f_0 = -a_s, \quad \frac{d\sigma}{d\Omega} = |f_0|^2 = a_s^2, \quad \sigma = \int |f_0|^2 d^2\Omega = 4\pi a_s^2. \quad (4.20)$$

So far we discussed only the collisions of distinguishable particles, for example, atoms in different internal states or atoms that belong to different species. For identical Bosons or Fermions in the same spin state, the wave function for the relative motion must be either symmetric or anti-symmetric. One finds for the asymptotic wave function

$$\psi \underset{r \rightarrow \infty}{\simeq} (e^{ikz} \pm e^{-ikz}) + [f(\vartheta) \pm f(\vartheta - \pi)] \frac{e^{ikr}}{r}, \quad (4.21)$$

where $+$ ($-$) is used for bosonic (fermionic) atoms. Equation (4.21) leads to an enhanced scattering amplitude for Bosons and a vanishing s-wave scattering length for the fermionic counterpart.

4.2.2 PSEUDO POTENTIAL

In the ongoing thesis, we are not working with the exact interaction potential of the different alkali atoms. In general, $V(r)$ is very difficult to calculate to the required precision level. In addition, the mean-field treatment (cf. 4.3.1) of a Bose-condensed gas relies on the convergence of the Born approximation, which is not provided for a potential with a hard repulsive core [94, 95].

The key idea is to replace the exact interaction potential with a so-called pseudo potential [96], which is treatable by the Born approximation and which reproduces the same low-energy scattering properties such as the scattering length (4.18). The potential operator which satisfies these conditions may be written

$$V(\mathbf{r})\psi(r) = g\delta(\mathbf{r})\left\{\frac{\partial}{\partial r}[r\psi(\mathbf{r})]\right\}, \quad (4.22)$$

in terms of a Dirac delta distribution and a regularizing operator. The coupling constant

$$g = \frac{4\pi\hbar^2 a_s}{M}, \quad (4.23)$$

contains the s-wave scattering length. For a wave function that is regularly close to $r = 0$, the pseudo-potential is merely a contact interaction potential

$$V(\mathbf{r}) = g\delta(\mathbf{r}). \quad (4.24)$$

4.3 WEAKLY INTERACTING BOSE GAS

The many-body Hamilton operator for Bosons trapped in an external potential with pairwise two-particle interactions reads as

$$\begin{aligned} \hat{H} = & \int \int \hat{\Psi}^\dagger(\mathbf{r}') \langle \mathbf{r}' | \hat{T} + \hat{U} | \mathbf{r} \rangle \hat{\Psi}(\mathbf{r}) d^3r' d^3r \\ & + \frac{1}{2} \int \int \int \int \hat{\Psi}^\dagger(\mathbf{r}'_1) \hat{\Psi}^\dagger(\mathbf{r}'_2) \langle \mathbf{r}'_1 \mathbf{r}'_2 | \hat{V} | \mathbf{r}_1 \mathbf{r}_2 \rangle \hat{\Psi}(\mathbf{r}_2) \hat{\Psi}(\mathbf{r}_1) d^3r'_1 d^3r'_2 d^3r_1 d^3r_2, \end{aligned} \quad (4.25)$$

where \hat{T} and \hat{U} are single-particle operators representing the kinetic, as well as the potential energy, and \hat{V} is the two-particle operator describing the interactions between the atoms [90]. If the interatomic potential is approximated by a contact potential (4.24), one can simplify equation (4.25) to

$$\hat{H} = \int \hat{\Psi}^\dagger(\mathbf{r}) \left[-\frac{\hbar^2}{2M} \nabla^2 + U(\mathbf{r}) \right] \hat{\Psi}(\mathbf{r}) d^3r + \frac{g}{2} \int \hat{\Psi}^\dagger(\mathbf{r}) \hat{\Psi}^\dagger(\mathbf{r}) \hat{\Psi}(\mathbf{r}) \hat{\Psi}(\mathbf{r}) d^3r. \quad (4.26)$$

The field operators $\hat{\Psi}^\dagger$ ($\hat{\Psi}$) create (annihilate) bosonic particles at a position \mathbf{r} in Fock space

$$\hat{\Psi}^\dagger(\mathbf{r}) |0\rangle = |\mathbf{r}\rangle, \quad (4.27)$$

obeying the following commutation relationships

$$[\hat{\Psi}(\mathbf{r}), \hat{\Psi}^\dagger(\mathbf{r}')] = \delta(\mathbf{r} - \mathbf{r}'), \quad [\hat{\Psi}(\mathbf{r}), \hat{\Psi}(\mathbf{r}')] = 0. \quad (4.28)$$

A general many-particle states may be expanded in the Fock basis

$$|\Psi\rangle = \sum_{N=0}^{\infty} \int |\mathbf{r}_1 \dots \mathbf{r}_N\rangle \langle \mathbf{r}_1 \dots \mathbf{r}_N | \Psi \rangle_N d^{3N}r, \quad (4.29)$$

with many-particle amplitudes $\Psi(\mathbf{r}_1, \dots, \mathbf{r}_N) = \langle \mathbf{r}_1 \dots \mathbf{r}_N | \Psi \rangle_N$. One obtains the equation of motion from the Lagrangian formulation

$$\mathcal{L}[\Psi, \dot{\Psi}] = \langle \Psi(t) | i\hbar\partial_t - \hat{H} | \Psi(t) \rangle, \quad (4.30)$$

with the canonical momentum $\pi = \delta\mathcal{L}/\delta\dot{\Psi} = i\Psi^*$. Using the Hamilton formulation with $\dot{\pi} = \delta\mathcal{L}/\delta\Psi$, one recovers the Schrödinger equation in Fock space

$$i\partial_t |\Psi(t)\rangle = \hat{H} |\Psi(t)\rangle. \quad (4.31)$$

4.3.1 MEAN-FIELD APPROXIMATION FOR BOSONS

In general, it is impossible to solve the many-body Schrödinger equation (4.31) in most cases. However, in a Bose-Einstein condensate the atoms occupy the same quantum states macroscopically, and one can approximate the general state of the systems

$$\hat{\Psi}(\mathbf{r}) |\Psi\rangle_c = \Psi(\mathbf{r}) |\Psi\rangle_c, \quad (4.32)$$

by a coherent state $|\Psi\rangle_c$. The eigenvalue $\Psi(\mathbf{r})$ is often called the macroscopic wave function or order parameter for the ordered, coherent state of Bosons. A coherent state has not a well-defined number of particles but the fractional uncertainty, $\Delta N/N$, tends to zero for a large number of particles in the same mode. One can associate a modulus as well as a well-defined phase to the complex field which corresponds to a spontaneous symmetry breaking of the phase of the many-particle system [97, 98].

4.3.2 GROSS-PITAEVSKII EQUATION

From the coherent-state approximation, one derives mean-field equations using variational principles. This leads to the Hartree-Fock equations for a Bose condensate [97]. Using the Hamilton operator with the contact interaction (4.26), the Lagrangian field equation for the condensate becomes

$$\mathcal{L} = i\hbar\Psi^*\partial_t\Psi - \mathcal{E}, \quad (4.33)$$

with the energy density

$$\mathcal{E}(\mathbf{r}, t) = \frac{|\hbar\nabla\Psi|^2}{2M} + U|\Psi|^2 + \frac{g}{2}|\Psi|^4. \quad (4.34)$$

Inserting (4.33) into the Euler-Lagrange equations

$$\frac{d}{dt} \frac{\delta\mathcal{L}}{\delta\dot{\Psi}^*} = \frac{\delta\mathcal{L}}{\delta\Psi^*}, \quad (4.35)$$

one obtains the time-dependent Gross-Pitaevskii equation

$$i\partial_t\Psi(\mathbf{r}, t) = \left[-\frac{\hbar^2\nabla^2}{2M} + U(\mathbf{r}, t) + g|\Psi|^2 \right] \Psi(\mathbf{r}, t), \quad (4.36)$$

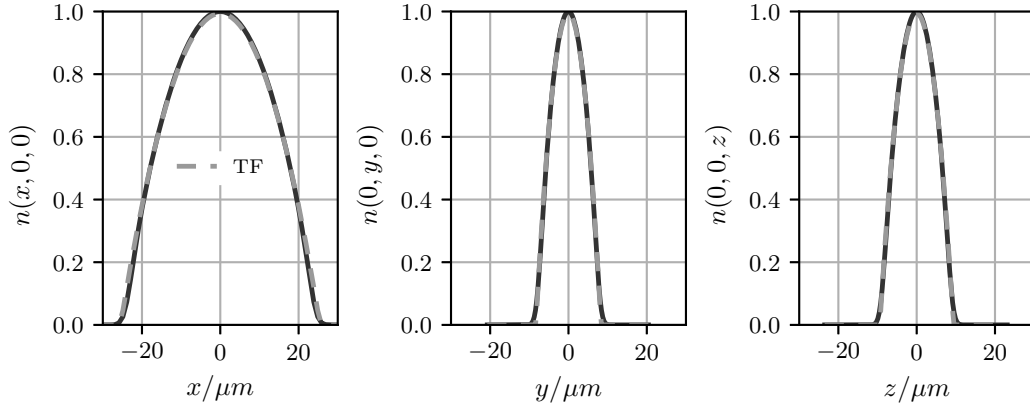


Figure 4.1: Cross-sections of the atomic density $n(x, y, z)$ versus position in each spatial direction. --- lines correspond to the Thomas-Fermi approximation n_{TF} . We have used 10^5 ^{87}Rb atoms in a harmonic trap with frequencies as in table 2.2. The Thomas-Fermi radii are $\mathbf{r}_{\text{TF}} = (25.5, 8.3, 9.4)\mu\text{m}$ with chemical potential $\mu_{\text{TF}} = 25.3 \hbar\omega_x$. Density scaled to the maximal value.

which has the form of a non-linear Schrödinger equation. In a static external potential $U = U(\mathbf{r})$, one finds the stationary Gross-Pitaevskii equation

$$\left[-\frac{\hbar^2 \nabla^2}{2M} + U + g|\Psi|^2 \right] \Psi = \mu \Psi, \quad (4.37)$$

by making the ansatz $\Psi(\mathbf{r}, t) = \Psi(\mathbf{r}) \exp(-i\mu t/\hbar)$ for the time-dependent field where μ denotes the chemical potential of the ground state [45].

4.3.3 THOMAS-FERMI APPROXIMATION

In the limit of large repulsive interactions, one may neglect the quantum kinetic energy in the stationary Gross-Pitaevskii (4.37)

$$[U(\mathbf{r}) + gn_{\text{TF}}(\mathbf{r}) - \mu] \Psi_{\text{TF}}(\mathbf{r}) = 0, \quad (4.38)$$

which as known as the Thomas-Fermi approximation [99–101]. Equation (4.38) admits the algebraic solution for the condensate density

$$n_{\text{TF}}(\mathbf{r}) = \begin{cases} \frac{\mu - U(\mathbf{r})}{g}, & \mu - U(\mathbf{r}) \geq 0, \\ 0 & \text{else,} \end{cases} \quad (4.39)$$

and the corresponding wave function $\Psi_{\text{TF}} = \sqrt{n_{\text{TF}}}$. In [51], we have considered the Thomas-Fermi field for a general harmonic oscillator potential

$$U = \frac{M}{2} \mathbf{r}^\top \Omega^2 \mathbf{r}, \quad (4.40)$$

in d spatial dimensions. The trap frequencies $\omega_i > 0$ are the entries of the diagonal eigenvalue matrix

$$\Omega^2 \mathbf{R} = \mathbf{R} \omega^2. \quad (4.41)$$

From the geometrical average of the frequencies $\bar{\omega} = (\omega_1 \cdots \omega_d)^{\frac{1}{d}}$ one can define the length of the harmonic oscillator $\bar{a} = \sqrt{\hbar/M\bar{\omega}}$ as the primary length scale for the non-interacting condensed Bose gas. In figure 4.1 we depict the atomic ground state density obtained by solving the stationary Gross-Pitaevskii equation in a three-dimensional harmonic potential. The analytic Thomas-Fermi density shows good agreement with the numerical solution for the given number of ^{87}Rb atoms.

To cope with the physical anisotropy of the potential in the Cartesian lab frame $\mathbf{r} = (x_1, \dots, x_d)$, it is useful to introduce a rotated, scaled frame with new coordinates defined $\mathbf{r}' = (x'_1, \dots, x'_d)$ by

$$\mathbf{r} \equiv \mathbf{R}\mathbf{S}\mathbf{r}', \quad (4.42)$$

introducing the scaling transformation $\mathbf{S} = \sqrt{2\mu/M\omega^2}$. For each direction, the scale factors are determined by the Thomas-Fermi radii $r_{\text{TF},i} \equiv \sqrt{2\mu/M\omega_i^2}$. It is also relevant to introduce the averaged radial condensate extent $r_{\text{TF}} \equiv \sqrt{2\mu/M\bar{\omega}^2}$ as a secondary global length scale or the strongly interacting condensate. The particle normalization of the fields links the dimensional lab-coordinates amplitude $\Psi(\mathbf{r})$ to the dimensionless amplitude $\Psi'(\mathbf{r}')$ in the scaled coordinates by

$$\Psi'(\mathbf{r}') \equiv r_{\text{TF}}^{\frac{d}{2}} \Psi(\mathbf{r}). \quad (4.43)$$

In d -dimensional spherical coordinates [102], the hyper-radius $r' = \sqrt{\mathbf{r}'^2}$ is given by the Euclidean norm. The differential solid angle $d^{d-1}\Omega$, is obtained from the Cartesian volume element $d^d x' = r'^{d-1} dr' d^{d-1}\Omega$ and encompasses a total solid angle of $\Omega_d = 2\pi^{\frac{d}{2}}/\Gamma(\frac{d}{2})$ where $\Gamma(\cdot)$ denotes the Gamma function. With these definitions, one finds a compact expression for the non-vanishing field

$$\Psi'_{\text{TF}}(\mathbf{r}') = \sqrt{\mathbf{n}} \sqrt{1 - r'^2}, \quad \sqrt{\mathbf{n}} = \sqrt{\frac{\mu r_{\text{TF}}^d}{g}}, \quad (4.44)$$

within the Thomas-Fermi volume defined by equation (4.39). Here, the parameter \mathbf{n} denotes the ratio between chemical potential and internal energy and is proportional to the total particle number.

An ensemble with fixed particle number N defines the chemical potential $\mu(N)$ implicitly by

$$N = \int_{V_{\text{TF}}} n_{\text{TF}}(\mathbf{r}) d^d r = \mathbf{n} \Omega_d \int_0^1 r'^{d-1} (1 - r'^2) dr'. \quad (4.45)$$

Evaluating the hyperradial integral, the chemical potential as a function of particle number is then given by

$$\mu(N) = \hbar\bar{\omega} \left[\kappa \frac{d(d+2)}{4(2\pi)^{\frac{d}{2}}} \Gamma\left(\frac{d}{2}\right) \right]^{\frac{2}{d+2}}, \quad \kappa = \frac{gN}{\bar{a}^d \hbar\bar{\omega}}. \quad (4.46)$$

Thus, the chemical potential exhibits a characteristic algebraic dependence on the geometric dimension, the potential shape, and the internal energy κ is given in energy units of the harmonic oscillator $\hbar\bar{\omega}$.

In figure 4.2, we depict the density of the Gross-Pitaevskii state n' , as well as the Thomas-Fermi density n'_{TF} at equal chemical potential $\mu = 14.12 \hbar\bar{\omega}$ in different spatial dimensions. This implies different coupling constants κ for each dimension d according to (4.46). The inset magnifies the region around r_{TF} , where the approximation exhibits the characteristic first-order discontinuity.

Besides the position density, one can also evaluate the momentum distribution of the Thomas-Fermi field using the definition of the Fourier transform

$$\tilde{\Psi}(\mathbf{k}) = \int_{-\infty}^{\infty} \frac{e^{-i\mathbf{k}\mathbf{r}}}{(2\pi)^{\frac{d}{2}}} \Psi(\mathbf{r}) d^d r, \quad \mathbf{k} = \mathbf{p}/\hbar, \quad (4.47)$$

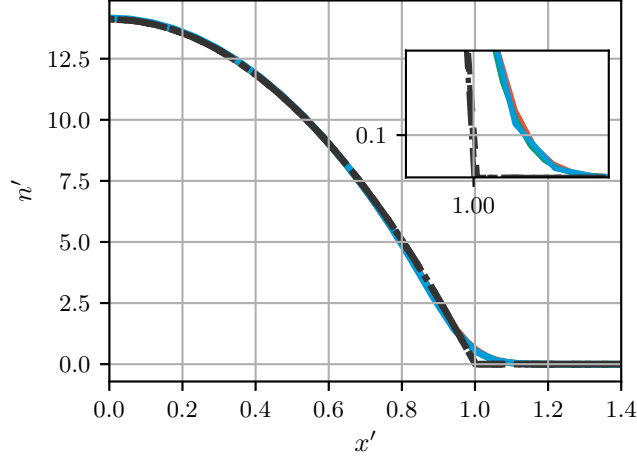


Figure 4.2: Ground-state position density versus Cartesian coordinate x' in a d -dimensional harmonic potential in dimensionless units: Gross-Pitaevskii solution with $d = 1$, $n'(x')$ (red —), $d = 2$, $n'(x', 0)$ (green —), $d = 3$, $n'(x', 0, 0)$ (blue —) and Thomas-Fermi density with $d = 1$, $n'_{\text{TF}}(x')$ (---), $d = 2$, $n'_{\text{TF}}(x', 0)$ (-·-·-), $d = 3$, $n'_{\text{TF}}(x', 0, 0)$ (·····). We have chosen different coupling constants $\kappa = 100$ ($d = 1$), $\kappa = 625.96$ ($d = 2$) and $\kappa = 3547.62$ ($d = 3$) in each dimension to obtain the same chemical potential $\mu_{\text{TF}} = 14.12 \hbar\bar{\omega}$. The inset shows a close-up view of the Thomas-Fermi region.

in d spatial dimensions. According to (4.43), one can define a dimensionless Fourier amplitude and density

$$\tilde{\Psi}(\mathbf{k}) = r_{\text{TF}}^{\frac{d}{2}} \tilde{\Psi}'(\mathbf{k}'), \quad (4.48a)$$

$$\tilde{n}'(\mathbf{k}') = |\tilde{\Psi}'(\mathbf{k}')|^2, \quad (4.48b)$$

with scaled Cartesian wave vectors

$$\mathbf{k}' = \text{SR}^{\top} \mathbf{k}. \quad (4.49)$$

All things considered, the dimensionless Fourier transform to the Thomas-Fermi field reads

$$\tilde{\Psi}'_{\text{TF}}(\mathbf{k}') = \sqrt{\mathbf{n}} \int_{V_{\text{TF}}} \frac{e^{-i\mathbf{k}' \cdot \mathbf{r}'}}{(2\pi)^{\frac{d}{2}}} \sqrt{1 - r'^2} d^d r'. \quad (4.50)$$

In hyper-spherical coordinates, the integral over the hyper-angles factorizes and evaluates to

$$o_d(k' r') \equiv \int_{S_{\text{TF}}} \frac{e^{-i\mathbf{k}' \cdot \mathbf{r}'}}{(2\pi)^{\frac{d}{2}}} d^{d-1} \Omega = \frac{J_{\frac{d}{2}-1}(k' r')}{(k' r')^{\frac{d}{2}-1}}, \quad (4.51)$$

with J_d being the Bessel function of the first kind of order d [103]. The remaining radial integral also admits a closed-form solution

$$\tilde{\Psi}'_{\text{TF}}(\mathbf{k}') = \sqrt{\mathbf{n}} \int_0^1 r'^{d-1} \sqrt{1 - r'^2} o_d(k' r') dr' = \sqrt{\mathbf{n}} \sqrt{\frac{\pi}{2}} o_{d+3}(k'). \quad (4.52)$$

It is interesting to present this result with the original physical Cartesian wave-vectors

$$\tilde{\Psi}(\mathbf{k}) = r_{\text{TF}}^{\frac{d}{2}} \sqrt{\mathbf{n}} \sqrt{\frac{\pi}{2}} o_{d+3} \left(\sqrt{\mathbf{k}^{\top} \frac{2\mu}{M\Omega^2} \mathbf{k}} \right), \quad (4.53)$$

which demonstrates that the diagonalization (4.41) is not required to obtain the Fourier amplitude of the Thomas-Fermi field in the anisotropic oscillator in d dimensions. In particular, for the most relevant three-dimensional case $d = 3$, our result agrees with [101]. In figure 4.3, we show the momentum spectra of the numerical Gross-Pitaevskii field and the analytical Thomas-Fermi solution (4.53). As a guide to the eye, we have added algebraic k'^{-d-2} (see equation (4.54)) and exponential $e^{-k'/2}$ envelopes to match the asymptotic behavior for large wavenumbers.

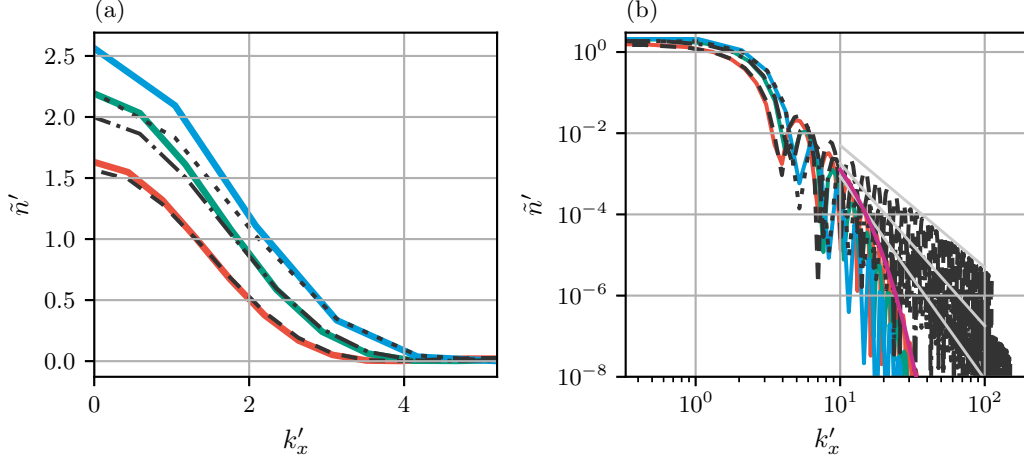


Figure 4.3: (a) Ground-state Fourier density versus scaled Cartesian wavenumber k'_x in a d -dimensional harmonic potential in dimensionless units: Gross-Pitaevskii density for $d = 1$, $\tilde{n}'(k'_x)$ (red —), $d = 2$, $\tilde{n}'(k'_x, 0)$ (green —), $d = 3$, $\tilde{n}'(k'_x, 0, 0)$ (blue —) and Thomas-Fermi density for $d = 1$, $\tilde{n}'_{\text{TF}}(k'_x)$ (---), $d = 2$, $\tilde{n}'_{\text{TF}}(k'_x, 0)$ (-·-·-), $d = 3$, $\tilde{n}'_{\text{TF}}(k'_x, 0, 0)$ (·····). (b) The double logarithmic plot shows the high-energy algebraic decay $\sim k'^{-d-2}$ (gray —) of $\tilde{n}'_{\text{TF}}(k')$, and an exponential $\sim e^{-k'/2}$ decay (magenta —) for the numerical Gross-Pitaevskii density. Fourier densities are all normalized to one.

To foster physical interpretation and to choose suitable numerical grids in simulations of the Gross-Pitaevskii equation, it is important to understand the high energy behavior of the Fourier amplitude. From the asymptotic representation of the Bessel functions, one finds a periodic oscillation with algebraic decay

$$\tilde{\Psi}'_{\text{TF}}(\mathbf{k}' \rightarrow \infty) \sim \sqrt{\mathbf{n}} \frac{\sin(k' - d\frac{\pi}{4})}{k'^{\frac{d+2}{2}}}. \quad (4.54)$$

For small wave vectors, the Fourier amplitude stays regular and approaches

$$\tilde{\Psi}'_{\text{TF}}(\mathbf{k}' \rightarrow 0) \sim \frac{\sqrt{\mathbf{n}}}{2^{\frac{d+2}{2}} \Gamma(\frac{d+3}{2})}. \quad (4.55)$$

The Heisenberg uncertainty principle of quantum physics and the uncertainty relation of harmonic analysis [104]

$$\Delta r \Delta k \geq \frac{d}{2}, \quad (4.56)$$

are connected by the de Broglie relation $p = \hbar k$ [9]. It provides the basis for the rule-of-thumb estimate of a minimal width, i. e., the standard deviation of the Thomas-Fermi field in k -space

$$\Delta k_{\text{TF}}^{\text{H}} \geq \frac{d}{2r_{\text{TF}}}. \quad (4.57)$$

	Solid angle	Bessel zero	Rayleigh width	Heisenberg width	%
d	Ω_d	k'_1	$\Delta k_{\text{TF}}^{\text{R}}$	$\Delta k_{\text{TF}}^{\text{H}}$	β
1	2	3.83	$0.38 \mu\text{m}^{-1}$	$0.05 \mu\text{m}^{-1}$	0.98
2	2π	4.49	$0.45 \mu\text{m}^{-1}$	$0.10 \mu\text{m}^{-1}$	0.95
3	4π	5.14	$0.51 \mu\text{m}^{-1}$	$0.15 \mu\text{m}^{-1}$	0.93

Table 4.1: Widths in k space according to the Rayleigh and Heisenberg criterion for an explicit Thomas-Fermi radius of $r_{\text{TF}} = 10 \mu\text{m}$.

If the Thomas-Fermi radius is a measure of the position width $\Delta r = r_{\text{TF}}$. Alternatively, we can specify a width of the Thomas-Fermi field (4.53) according to the Rayleigh criterion

$$\Delta k_{\text{TF}}^{\text{R}} = \frac{k'_1}{r_{\text{TF}}}, \quad (4.58)$$

by the first root of the Bessel function $J_{\frac{d+1}{2}}(k'_1) = 0$. Then, the fraction of atoms

$$\beta \equiv N^{-1} \int_{-\infty}^{\infty} \theta(k'_1 - q') |\tilde{\Psi}_{\text{TF}}(\mathbf{q}')|^2 d^d q', \quad (4.59)$$

measures the localization of the spectrum for wave numbers $q' \leq k'_1$. In table 4.1, we have summarized these parameters as a function of the spatial dimension d for a given Thomas-Fermi radius.

4.4 HYDRODYNAMIC FIELD EQUATIONS

In the hydrodynamic formulation of a Bose-Einstein condensate, the classical complex Gross-Pitaevskii wave function is written in terms of the two real hydrodynamical variables, the density of the condensates $n(\mathbf{r}, t)$ and its phase $\phi(\mathbf{r}, t)$,

$$\Psi(\mathbf{r}, t) = \sqrt{n} e^{i\phi}, \quad \Psi^*(\mathbf{r}, t) = \sqrt{n} e^{-i\phi}, \quad (4.60)$$

also known as a Madelung transform. Inserting the equations (4.60) into the Lagrange density (4.33) one finds

$$\mathcal{L} = i \frac{\hbar}{2} \dot{n} - n \hbar \dot{\phi} - \mathcal{E}, \quad (4.61)$$

with the energy density expressed in terms of velocity and density

$$\mathcal{E}(\mathbf{r}, t) = \frac{Mv^2}{2} n + \frac{(\hbar \nabla \sqrt{n})^2}{2M} + Un + \frac{g}{2} n^2. \quad (4.62)$$

The first term in the energy density consists of the classical kinetic energy with velocity \mathbf{v} . It is usually defined by the particle-current density

$$\mathbf{j} = \frac{\hbar}{M} \Im\{\Psi^* \nabla \Psi\} = n \frac{\hbar}{M} \nabla \phi = n \mathbf{v}, \quad (4.63)$$

$$\mathbf{v} = \frac{\hbar}{M} \nabla \phi, \quad (4.64)$$

where the velocity field is proportional to the gradient of the phase. The second term in (4.62) is purely quantum and corresponds to the localization energy of the wave function. The equations of motion are determined by the Euler-Lagrange equations

$$\frac{d}{dt} \frac{\delta L}{\delta \dot{\phi}} = \frac{\delta L}{\delta \phi}, \quad (4.65a)$$

$$\frac{d}{dt} \frac{\delta L}{\delta \dot{n}} = \frac{\delta L}{\delta n}. \quad (4.65b)$$

Applying equation (4.65a) and using the definition of local velocity (4.64) and particle current density (4.63), one finds the continuity equation for the particle density

$$\dot{n} + \nabla \cdot \mathbf{j} = 0, \quad (4.66)$$

as a consequence of particle number conservation of the Bose-Einstein condensate. Equation (4.65b) leads to an Euler equation for a fluid

$$-\hbar \dot{\phi} = \frac{M \mathbf{v}^2}{2} + U + gn - \frac{\hbar^2}{2M} \frac{\Delta \sqrt{n}}{\sqrt{n}}, \quad (4.67)$$

with an additional quantum pressure due to the localization energy. Equation (4.66) and (4.67) are equivalent to the Gross-Pitaevskii equation (4.36) connected by the Madelung transformation in equation (4.60).

4.4.1 SCALING SOLUTION OF THE EULER EQUATION

If one neglects the quantum pressure in the Euler equation (4.67), one recovers the Thomas-Fermi density (4.39) as the stationary solution. An analytic solution of the hydrodynamic Euler (4.67) and continuity equation (4.66) can be found within a time-dependent harmonic oscillator potential [105]

$$U(\mathbf{r}, t) = \frac{M}{2} \mathbf{r}^\top \Omega^2(t) \mathbf{r}. \quad (4.68)$$

In section 3.4, we have discussed that a change of phase space coordinates by a canonical transformation simplifies the equations of motion for a classical particle in a harmonic oscillator with time-dependent frequencies. As the initial Thomas-Fermi density itself is quadratic in its spatial shape, the Thomas-Fermi density obeys the following scaling ansatz [105]

$$n_{\text{TF}}(\mathbf{r}, t) = |\Lambda(t)|^{-1} n_0(\Lambda^{-1}(t) \mathbf{r}), \quad (4.69)$$

where n_0 denotes the initial density in the harmonic trap (4.39). Inserting the (4.69) into the continuity equation (4.66), one finds the corresponding phase evolution [49, 50, 79]

$$\hbar \phi(\mathbf{r}, t) = \frac{\mathbf{r}^\top \mathbf{p}_\lambda}{2} - \beta(t), \quad \mathbf{p}_\lambda = M \mathbf{v}_\lambda, \quad \beta(t) = \int^t \mu / |\Lambda(t')| dt', \quad (4.70)$$

where the velocity field (4.64) of the superfluid is given by

$$\mathbf{v}_\lambda = \dot{\Lambda} \Lambda^{-1} \mathbf{r}. \quad (4.71)$$

In order to determine the unknown $\Lambda(t)$, one inserts the Thomas-Fermi density (4.39) into equation (4.67) neglecting the quantum pressure. One finds that the scales fulfill the second-order matrix differential equation

$$\Lambda^\top(t) \left[\ddot{\Lambda}(t) + \Omega^2(t)\Lambda(t) \right] = \frac{\Omega^2(0)}{|\Lambda(t)|}. \quad (4.72)$$

Comparing equation (4.72) with the differential equation (3.43), one finds that $f(\Lambda) = |\Lambda(t)|^{-1}$ as a consequence of the mean-field interactions within the quantum fluid. The nonlinear differential equation can be used for the ballistic expansion for $\Omega^2(t) = 0$, when the condensate is released from the trap. In addition, for small amplitude oscillations, one finds modes that correspond to the excitation spectrum in the hydrodynamic regime [49, 106].

4.4.2 HYDRODYNAMIC SOUND WAVE EXCITATIONS

Hydrodynamic sound waves are found considering density and phase perturbations, n_1 , ϕ_1

$$n(\mathbf{r}, t) = n_{\text{TF}}(\mathbf{r}) + n_1(\mathbf{r}, t), \quad (4.73)$$

$$\phi(\mathbf{r}, t) = \phi_0(t) + \phi_1(\mathbf{r}, t), \quad (4.74)$$

around the stationary Thomas-Fermi density $n_{\text{TF}}(\mathbf{r})$ which oscillates with the uniform phase $\phi_0(t) = \mu t / \hbar$ [107, 108]. One can expand the Lagrangian (4.61) for the hydrodynamic variables up to second order in n_1 and ϕ_1

$$\mathcal{L} = -n_1 \hbar \dot{\phi}_1 - \frac{n_{\text{TF}}}{2M} (\hbar \nabla \phi_1)^2 - \frac{g}{2} n_1^2. \quad (4.75)$$

Using the Euler-Lagrange equations, one finds the coupled differential equations

$$\hbar \dot{\phi}_1 = -g n_1, \quad \dot{n}_1 = -\frac{\hbar}{M} \nabla (n_{\text{TF}} \nabla \phi_1), \quad (4.76)$$

describing the hydrodynamic excitations. The set of first-order differential equations can be rewritten as a wave equation for either the density n_1

$$\ddot{n}_1 = \nabla (c^2 \nabla n_1), \quad (4.77)$$

or phase perturbations respectively. Equation (4.77) describes the propagation of sound waves with the local sound velocity

$$c(\mathbf{r}) = \sqrt{g n_{\text{TF}}(\mathbf{r}) / M}, \quad (4.78)$$

which depends on the spatially varying Thomas-Fermi density. One seeks stationary solutions of equation (4.77) by making the ansatz

$$n_1(\mathbf{r}, t) = \bar{n}_1(\mathbf{r}) e^{-i\omega t} + \text{c.c.}, \quad (4.79)$$

where the positive frequency components $\bar{n}_1(\mathbf{r})$ are solutions of the differential equation

$$\omega^2 \bar{n}_1 = -\nabla (c^2 \nabla \bar{n}_1). \quad (4.80)$$

SOUND WAVES IN 3D SPHERICAL SYMMETRIC TRAP

One can find analytical solutions of equation (4.80) for some external trapping potentials and for the homogeneous condensate. For spherical symmetric traps $U(\mathbf{r}) = U(r)$, equation (4.80) becomes

$$\omega^2 \bar{n}_1 = \left(\frac{U'}{M} \partial_r + 2gn_{\text{TF}} \hat{T} \right) \bar{n}_1, \quad (4.81)$$

with $U' = dU/dr$ and the operator

$$\hat{T} = \frac{\hat{p}_r^2}{2M} + \frac{\hat{L}^2}{2Mr^2}. \quad (4.82)$$

\hat{L}^2 is the square of the angular momentum operator (4.11) and \hat{p}_r denotes the radial momentum operator (4.10) with $\hbar = 1$. The most general solution of equation (4.81) is a linear combination of the form $\bar{n}_1(\mathbf{r}) = R_l(r) Y_{lm}(\vartheta, \varphi)$ consisting of radial functions $R_l(r)$ and angular momentum eigenfunctions $Y_{lm}(\vartheta, \varphi)$ (cf. equation (4.12)). The radial function R_l is determined by the equation

$$\omega^2 R_l(r) = \frac{U' R_l'}{M} + 2gn_{\text{TF}} \left[\frac{\hat{p}_r^2}{2M} + \frac{l(l+1)}{2Mr^2} \right] R_l. \quad (4.83)$$

For the isotropic harmonic potential $U = M \frac{\omega_0^2}{2} r^2$, the ansatz $R_l(r) = x^{l/2} F_l(x)$, with new radial coordinate $x = \tilde{r}^2 = (r/r_{\text{TF}})^2$, transform equation (4.83) to the hypergeometrical differential equation

$$x(1-x)F_l'' + \left[\frac{2l+3}{2} - \frac{2l+5}{2}x \right] F_l' + \frac{\lambda-l}{2} F_l = 0, \quad \lambda = \omega^2/\omega_0^2, \quad (4.84)$$

[103]. Regular solutions of (4.84) are the Jacobi polynomials $J_n^{(l+1/2, 0)}(1-2\tilde{r}^2)$ [109, 110]. The eigenfrequencies of the systems, expressed in terms of principle quantum number n and angular momentum l , are given by

$$\omega(n, l) = \omega_0 \sqrt{2n^2 + 2nl + 3n + l}. \quad (4.85)$$

Besides the three-dimensional harmonic trap, there exist analytic solutions for the isotropic two and one-dimensional harmonic trap. They become relevant in highly deformed traps which can reduce the degrees of freedom in the system [107]. There exists also solutions for the three-dimensional axial symmetric [111] and for the general triaxially anisotropic parabolic potential [112]. For the latter, the eigenfunctions are finite polynomials and the corresponding energies can be labeled in terms of three integer quantum numbers.

4.5 LINEARIZATION OF THE GROSS-PITAEVSKII EQUATION

In section 4.4.2, we have already studied the response of the density and the phase of the condensate with respect to small perturbations around the steady Thomas-Fermi ground state density. For inhomogeneous systems that also include particle-like excitations, one needs to linearize the Gross-Pitaevskii equation (4.36) around the stationary solution (4.37). The linear response of the non-linear equation is used to prove that the stationary solutions are stable with respect to small perturbations. Moreover, one can study the excitation spectrum which is useful to interpret experimental imperfections.

4.5.1 BOGOLIUBOV - DE GENNES EQUATIONS

We assume that the trapping potential in equation (4.37) is slightly modified by a time-dependent perturbation

$$U(\mathbf{r}, t) = U_0(\mathbf{r}) + U_1(\mathbf{r}, t). \quad (4.86)$$

If U_1 is assumed to be small, one can linearize (4.36) in terms of the small perturbation Ψ_1 by inserting the following ansatz

$$\Psi(\mathbf{r}, t) = e^{-i\mu t/\hbar}[\Psi_0(\mathbf{r}) + \Psi_1(\mathbf{r}, t)]. \quad (4.87)$$

Neglecting the second orders in Ψ_1 and U_1 , one finds the linear equation

$$i\hbar\partial_t\mathcal{X}(t) = \Sigma^B\mathcal{X}(t) + \mathcal{S}(t). \quad (4.88)$$

for the two-component vector $\mathcal{X} = (\Psi_1, \Psi_1^*)^\top$ with the source term $\mathcal{S} = (U_1\Psi_0, -U_1\Psi_0^*)^\top$ and the linear Hartree-Fock-Bogoliubov self-energy operator

$$\Sigma^B = -\frac{\hbar^2\nabla^2}{2M}\sigma_3 + \begin{pmatrix} \mathcal{V}_B & \mathcal{M} \\ -\mathcal{M}^* & -\mathcal{V}_B^* \end{pmatrix}, \quad \sigma_3 = \begin{pmatrix} 1 & 0 \\ 0 & -1 \end{pmatrix}, \quad (4.89)$$

$$\mathcal{V}_B = U + 2g|\Psi_0|^2 - \mu, \quad \mathcal{M} = g\Psi_0^2. \quad (4.90)$$

The mathematical properties of the non-hermitian operator Σ^B are discussed in detail in [97, 113] and are summarized in the appendix H. One finds that the spectrum has a real-valued spectrum of pairwise positive and negative eigenvalues

$$\Sigma^B W_{k,\pm} = \pm E_k W_{k,\pm}, \quad E_k > 0, \quad (4.91)$$

where the positive right eigenvectors $W_{k,+} = (u_k, v_k)^\top$ contain the particle and hole-like mode functions $u_k(\mathbf{r}), v_k(\mathbf{r})$ which are normalized as

$$\int |u_k(\mathbf{r})|^2 - |v_k(\mathbf{r})|^2 d^3r = 1. \quad (4.92)$$

In the literature, the eigenvalue problem (4.91) is known as the Bogoliubov - de Gennes equations [114, 115] equations, though Pitaevskii applied them first to non-uniform systems. In addition, the operator Σ^B has an eigenvector $P = (\Psi_0, -\Psi_0^*)^\top$ with doubly degenerate zero eigenvalue

$$\Sigma^B P = 0, \quad (4.93)$$

as the energy is unaltered for a change in the global phase of the condensate wave function [46].

Equation (4.88) has the formal solution

$$\mathcal{X}(t) = e^{-it\Sigma^B/\hbar}\mathcal{X}(0) + \frac{e^{-it\Sigma^B/\hbar}}{i\hbar} \int_0^t e^{is\Sigma^B/\hbar}\mathcal{S}(s) ds. \quad (4.94)$$

Using the completeness relation for the Bogoliubov basis (H.11), one finds for an initial vanishing perturbation $\mathcal{X}(0) = 0$,

$$\begin{aligned}\mathcal{X}(t) &= \frac{W'}{i\hbar} \int_0^t e^{-iE'(t-s)/\hbar} \sigma_3^{(n-1)} \mathcal{S}'(s) ds \\ &+ \frac{1}{i\hbar} \int_0^t [iQ\mathcal{S}_N(s) - iP\mathcal{S}_\Phi(s)] ds \\ &- \frac{1}{i\hbar} \int_0^t (t-s) \frac{iP\mathcal{S}_N(s)}{\mathfrak{M}} ds,\end{aligned}\quad (4.95)$$

where we have introduced the amplitudes,

$$\mathcal{S}' = W'^\dagger \sigma_3^{(n-1)} \mathcal{S}, \quad \mathcal{S}_N = P^\dagger \sigma_3 \mathcal{S}, \quad \mathcal{S}_\Phi = Q^\dagger \sigma_3 \mathcal{S}. \quad (4.96)$$

4.5.2 DENSITY AND PHASE AMPLITUDES

In order to connect the perturbations Ψ_1 of the complex field with experimental observables, we can use the Madelung transform (4.60)

$$\Psi(\mathbf{r}, t) = \Psi_0(\mathbf{r}) + \Psi_1(\mathbf{r}, t) = \sqrt{n_0(\mathbf{r}) + n_1(\mathbf{r}, t)} e^{i\phi_1(\mathbf{r}, t)}. \quad (4.97)$$

If the density $n_1 \ll n_0$ and phase perturbation $\phi_1 \ll 1$ are small compared to their initial values, one can linearize (4.97) as,

$$\Psi(\mathbf{r}, t) \approx \Psi_0 \left(1 + i\phi_1 + \frac{n_1}{2n_0} \right) = \Psi_0 + i\phi_1 \sqrt{n_0} + \frac{n_1}{2\sqrt{n_0}}. \quad (4.98)$$

The complex-valued perturbation field Ψ_1 is then determined by

$$\Psi_1(\mathbf{r}, t) = \frac{n_1}{2\sqrt{n_0}} + i\phi_1 \sqrt{n_0}. \quad (4.99)$$

Thus density and phase aberrations are related to the real and imaginary part of Ψ_1 . We can express (4.99) in terms of density and phase

$$\begin{aligned}\phi_1 &= \frac{\Im[\Psi_1]}{\sqrt{n_0}} = \frac{1}{2i\sqrt{n_0}} (\Psi_1 - \Psi_1^*), \\ n_1 &= 2\sqrt{n_0} \Re[\Psi_1] = \sqrt{n_0} (\Psi_1 + \Psi_1^*),\end{aligned}\quad (4.100)$$

which consists of a rotation in the complex plane and a squeezing transformation in the amplitude direction.

5 WIGNER REPRESENTATION OF INTERACTING BOSE-EINSTEIN CONDENSATES

In this chapter, we discuss the properties of the single-particle Wigner function for an interacting Bose-Einstein condensate. In particular, we demonstrate the effect of mean-field interaction on the phase-space distribution. Afterward, we find a suitable approximation of the Thomas-Fermi Wigner function in a one-dimensional harmonic oscillator potential. The latter is useful to illustrate the time evolution using the exact scaling solution for the ballistic expansion and reducing the velocity width with delta-kick collimation.

5.1 WIGNER DISTRIBUTION

The Wigner function [75, 116] is a powerful concept in optics and wave mechanics to describe partially and fully coherent optical as well as matter waves. It is defined in d -dimension space

$$W(\mathbf{r}, \mathbf{k}) = \int_{-\infty}^{\infty} \frac{e^{-i\mathbf{k}\boldsymbol{\xi}/\hbar}}{(2\pi)^d} \rho(\mathbf{r}, \boldsymbol{\xi}) d^d \boldsymbol{\xi}, \quad (5.1)$$

as the Fourier transform of the coherence function

$$\rho(\mathbf{r}, \boldsymbol{\xi}) = \Psi^*(\mathbf{r} - \boldsymbol{\xi}/2)\Psi(\mathbf{r} + \boldsymbol{\xi}/2). \quad (5.2)$$

For the classical Gross-Pitaevskii field, the coherence function $\rho(\mathbf{r}, \mathbf{r}')$ is just the single-particle density matrix [117]

$$\rho(\mathbf{r}, \mathbf{r}') = \langle \Psi^\dagger(\mathbf{r})\Psi(\mathbf{r}') \rangle. \quad (5.3)$$

As the Fourier transformation is unitary, the Wigner function contains the same physical information as the single-particle density matrix. From equation (5.1), one can determine the position and Fourier densities

$$|\tilde{\psi}(\mathbf{k})|^2 = \int_{-\infty}^{\infty} W(\mathbf{r}, \mathbf{k}) d^d r, \quad (5.4a)$$

$$|\psi(\mathbf{r})|^2 = \int_{-\infty}^{\infty} W(\mathbf{r}, \mathbf{k}) d^d k, \quad (5.4b)$$

which are the marginal distributions of the Wigner function. The Wigner function is only a quasi-probability distribution, as it can acquire negative values. This is not a bug, but the central feature of interference of waves in phase space.

If the physical system is described by an Hamilton operator $H = T + U$, the time-evolution of the ($d = 3$) Wigner function $W = W(\mathbf{r}, \mathbf{p}, t)$ is described by a quantum Liouville-von Neumann equation

$$[\partial_t + \frac{1}{M}\mathbf{p} \cdot \nabla - (\nabla U) \cdot \partial_{\mathbf{p}}]W = \sum_{l=1}^{\infty} \frac{(-1)^l}{(2l+1)!} \left(\frac{\hbar}{2}\right)^{2l} \sum_{|\mathbf{m}|=2l+1} (\nabla^{|\mathbf{m}}|U) \partial_{\mathbf{p}}^{|\mathbf{m}}|W, \quad (5.5)$$

using $\mathbf{m} = (m_1, m_2, m_3)$ and the norm $|\mathbf{m}| = m_1 + m_2 + m_3$ as an abbreviation. The left-hand side of equation (5.5) describes the classical transport, whereas the right-hand side contains quantum corrections of the order $\mathcal{O}(\hbar^{2l})$. By taking the limit $\hbar \rightarrow 0$, one recovers the classical limit which is also known as the truncated Wigner approach [118, 119]. For external potentials whose third and higher derivatives vanish, the quantum Liouville equation coincides with its classical counterpart. Although the time evolution of the quantum state moves alongside the classical trajectories, its quantumness is still encoded in the initial Wigner function. Widely used examples are the ballistic expansion and the evolution in a harmonic oscillator potential, which we introduced in sections 3.3.1 and 3.3.2. .

As discussed in chapter 4.4.1, the correct scaling laws in a time-dependent quadratic potential for the Thomas-Fermi field are obtained by using the scaling coordinate transformation (3.32) described in chapter 3.4. The time-dependence for the scales for the interacting Thomas-Fermi density is given by equation (4.72). Hence, the dynamic for a Thomas-Fermi Wigner function is described by

$$W(\mathbf{r}, \mathbf{p}, t) = W'(\boldsymbol{\xi}(t), \boldsymbol{\pi}(t), 0), \quad (5.6)$$

where $W'(\boldsymbol{\xi}, \boldsymbol{\pi}, 0)$ represents the Wigner function of the initial state, but with time-dependent coordinates $(\boldsymbol{\xi}(t), \boldsymbol{\pi}(t))$. In [119] only a Gaussian ansatz was considered which disregards the quantum nature of the interacting Gross-Pitaevskii field as discussed in the following.

5.2 THOMAS-FERMI WIGNER FUNCTION

5.2.1 ONE-DIMENSIONAL HARMONIC OSCILLATOR

For a chemical potential, $\mu \gg 1$ we expect the mean-field Wigner function to differ from the Gaussian Wigner function

$$W(x, p) = \frac{1}{\hbar\pi} e^{-2H(x,p)/(\hbar\omega)}, \quad H(x, p) = \frac{p^2}{2M} + \frac{M}{2} \omega^2 x^2, \quad (5.7)$$

of the one-dimensional harmonic oscillator ground state [75]. As the Thomas-Fermi field for the interacting condensate is a good approximation for the interacting condensate, we look for its Wigner representation in phase space.

In the following, we use our results from chapter 4.3.3. where we have introduced the Thomas-Fermi size $x_{\text{TF}} = \sqrt{2\mu/(M\omega^2)}$ to define the dimensionless phase space coordinates as

$$(x', k') = (x/x_{\text{TF}}, k x_{\text{TF}}). \quad (5.8)$$

Further, we use the dimensionless Thomas-Fermi field (4.44) to evaluate the coherence function

$$\rho'_{\text{TF}}(x', \xi') = \mathbf{n} \left[(1 - x'^2)^2 - (1 + x'^2) \frac{\xi'^2}{2} + \frac{\xi'^4}{16} \right]^{\frac{1}{2}}, \quad (5.9)$$

that was defined in equation (5.2). In equation (5.9) the coordinates are in the range of $|x'| < 1$ and $|\xi'| < \xi'_+(x') \equiv 2(1 - |x'|)$. The coherence function vanishes otherwise. $\xi'_+(x')$ defines the upper and lower limit of the Fourier integral (5.1) and leads to the Thomas-Fermi Wigner function

$$W'_{\text{TF}}(x', k') = \int_{-\xi'_+(x')}^{\xi'_+(x')} \frac{e^{-ik'\xi'}}{2\pi} \rho'_{\text{TF}}(x', \xi') d\xi'. \quad (5.10)$$

The Fourier-integral (5.10) can be evaluated by numerical quadrature and is shown in figure 5.1. In the Thomas-Fermi regime $\mu \gg \hbar\omega$, the mean-field pressure increases the spatial size of the

condensates beyond the harmonic oscillator size, $r_{\text{TF}} \gg \sqrt{\hbar/(M\omega)}$, but squeezes the distribution in the k -direction reciprocally. The negative domains in the Wigner function that appear for non-Gaussian states can be seen clearly by dark-blue stripes in the color-coded density plot.

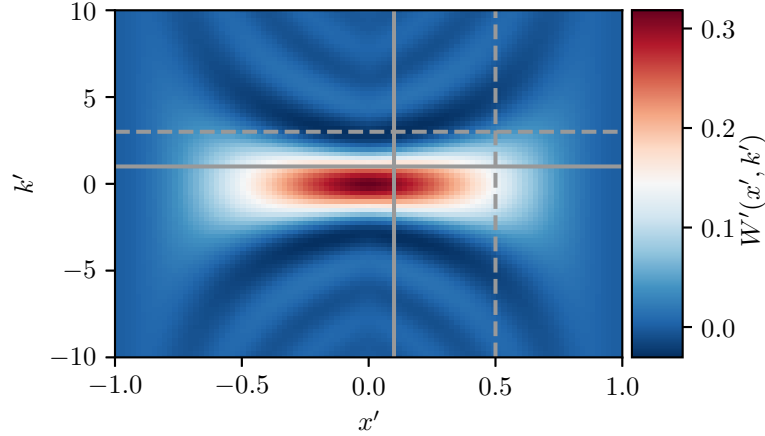


Figure 5.1: Color-coded density plot of the numerically calculated Thomas-Fermi Wigner function $W'_{\text{TF}}(x', k')$ for an one-dimensional harmonic oscillator in phase-space. Cross-sections along the phase-space coordinates $x' = \{0.1, 0.5\}$ and $k' = \{1.0, 3.0\}$ are marked by the gray lines (—, - - -) and are depicted in the figures 5.3 and 5.4. The parameters are $\kappa = 100$ (4.46) and $\mu_{\text{TF}} = 14.12 \hbar\omega$.

We have already compared the numerical exact Gross-Pitaevskii field with the Thomas-Fermi approximation in position space in figure 4.2 and reciprocal space in 4.3. In figure 5.2 (a), we depict the full phase-space representation of the numerical Gross-Pitaevskii field with strong interaction. Indeed, the two-dimensional phase-space density plot exhibits the same qualitative appearance as in figure 5.1 for the Thomas-Fermi Wigner function. However, the more detailed cross-section plots in the figures 5.3, 5.4 and highlights the deviations between the Wigner functions of the Gross-Pitaevskii, the Thomas-Fermi field as well as the factorizing ansatz (5.14) of the coherence function as discussed in the following paragraph. The limit for weak interaction, $\mu = 0.54 \hbar\omega$, is shown in subfigure 5.2 (b) where we almost recover the positive Gaussian phase-space distribution in equation (5.7) of a harmonic oscillator ground state for zero interaction.

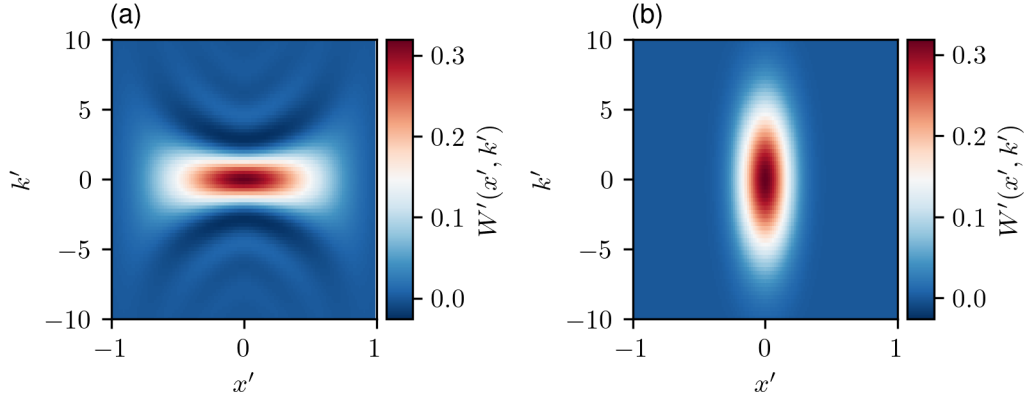


Figure 5.2: Color-coded density plot of the Gross-Pitaevskii Wigner function $W'(x', k')$ for the ground state in an one-dimensional harmonic potential. In subfigure (a), we have strong interaction $\kappa = 100$, $\mu = 14.11 \hbar\omega$ and weak interaction $\kappa = 0.1$, $\mu = 0.54 \hbar\omega$ in subfigure (b). In (b) dimensionless coordinates are with respect to the Thomas-Fermi size determined by the chemical potential in (a).

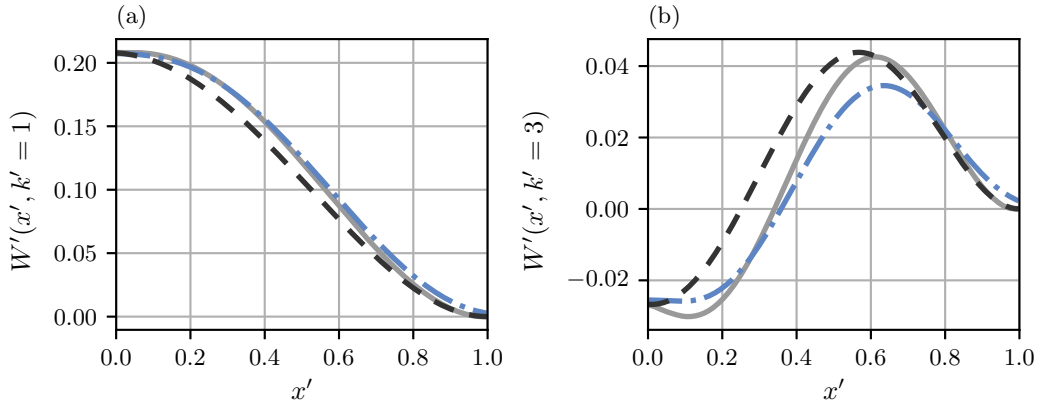


Figure 5.3: Cross-section of the Wigner function versus x' for fixed wave-number k' for the one-dimensional harmonic oscillator. Comparison of Thomas-Fermi approximation $W'_{\text{TF}}(x', k')$ (gray —), with the Gross-Pitaevskii Wigner function $W'(x', k')$ (blue - · - ·) and the factorizing approach $W'_{\text{TF}}(x', k')$ in equation (5.14) (black - - -). We have chosen the same parameters as in figure 5.1: (a) $k' = 1.0$, (b) $k' = 3.0$.

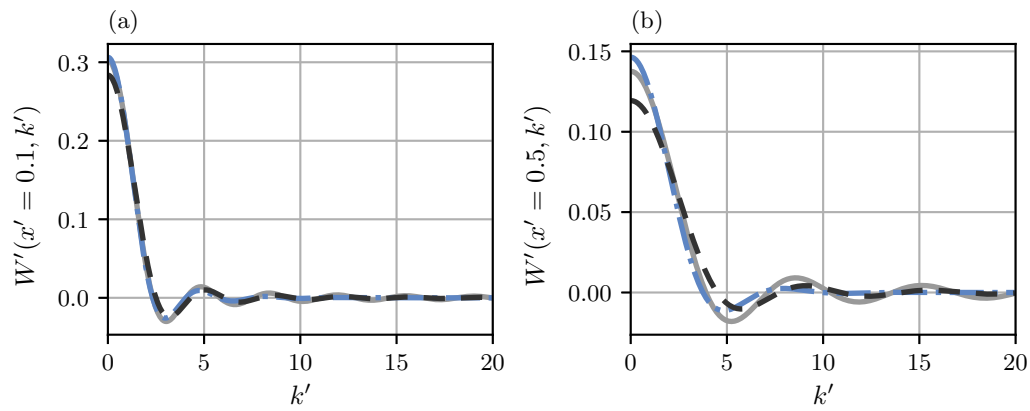


Figure 5.4: Cross-section of the Wigner function versus k' for fixed position x' for the one-dimensional harmonic oscillator. Comparison of Thomas-Fermi approximation $W'_{\text{TF}}(x', k')$ (gray —), with the Gross-Pitaevskii Wigner function $W'(x', k')$ (blue - · -) and the factorizing approach $W'_{\text{TF}}(x', k')$ (5.14) (black - - -). We have chosen the same parameters as in figure 5.1: (a) $x' = 0.1$, (b) $x' = 0.5$.

FACTORIZING THE COHERENCE FUNCTION Despite the functional simplicity of the Thomas-Fermi Wigner function, we have not succeeded in finding closed-form expression for the one-dimensional harmonic oscillator. Therefore, we consider a physical factorization ansatz for the coherence function (5.9)

$$\rho'_{\text{TF}}(x', \xi') = n'_{\text{TF}}(x') \chi\left(\frac{\xi'}{\eta(x')}\right), \quad (5.11)$$

where the factors consist of the position Thomas-Fermi density

$$n'_{\text{TF}}(x') = \rho'(x, 0) = \mathbf{n}(1 - x'^2), \quad (5.12)$$

as well as

$$\chi(\xi') = \frac{\rho'(0, \xi)}{\rho'(0, 0)} = 1 - \frac{\xi'^2}{4}, \quad (5.13)$$

that includes an unspecified x -dependent scale $\eta(x)$. With a suitable scale, the factorized coherence function $\rho'_{\text{TF}}(x', \xi')$ in equation (5.11) has the same support in phase space as the full coherence function (5.9). By choosing this scale as $\eta(x') = \xi'_+(x')/2$, one obtains the Wigner function as

$$W'_{\text{TF}}(x', k') = n'_{\text{TF}}(x') \frac{2 j_1[k' \xi'_+(x')]}{\pi k'}, \quad (5.14)$$

where j_1 is the spherical Bessel function of order one. Equation (5.14) matches the numerical simulations quite well for various values of x and k as regarded in figures 5.3 and 5.4. Further, the factorized Wigner function (5.14) features the correct marginal distribution (5.4b)

$$n'_{\text{TF}}(x') = n'_{\text{TF}}(x') \geq 0, \quad (5.15)$$

for the position density. For the marginal distribution in k -space, one finds

$$\tilde{n}'_{\text{TF}}(k') = \frac{\mathbf{n}}{\pi k'^4} [2k' \text{Si}(2k') + \cos 2k' - k' \sin 2k' - 1] \geq 0, \quad (5.16)$$

where Si denotes the sine-integral [103]. The Fourier density $\tilde{n}'_{\text{TF}}(k')$ is shown in figure 5.5. In contrast to the analytical result in equation (4.52), it lacks the nodal structure and shows some deviations for small values of k' . Nevertheless, it is positive and exhibits the same algebraic asymptotic behavior $\tilde{n}'_{\text{TF}}(k' \rightarrow \infty) \sim \mathbf{n}k'^{-3}$, as in equation (4.54).

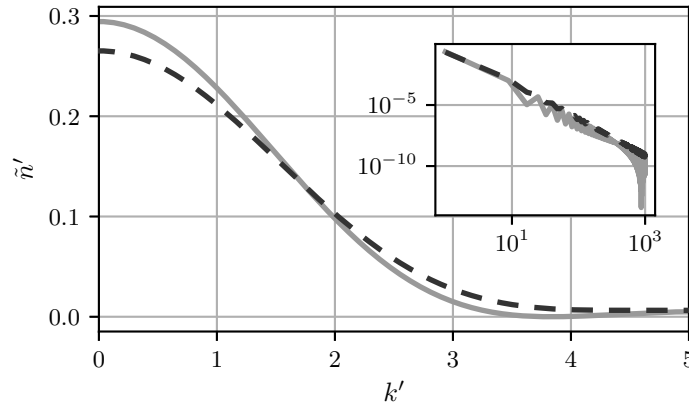


Figure 5.5: Fourier density $\tilde{n}'_{\text{TF}}(k')$ of the Thomas-Fermi approximation versus wave-number k' in a one-dimensional oscillator (4.52) (—) and $\tilde{n}'_{\text{TF}}(k')$ of the factorized Wigner function (5.16) (- - -). The double logarithmic inset displays the algebraic decay for large k' .

BALLISTIC EXPANSION In the previous section, we have found a suitable approximation of the Thomas-Fermi Wigner function $W_{\text{TF}}(x, k)$ (5.14). Using the scaling ansatz for the time-evolution in equation (5.6), we can study the ballistic expansion of a one-dimensional Bose-Einstein condensate in phase space. For a wave packet, the scales in equation (3.32) are obtained by the Ermakov-Pinney equation [87, 88], $\ddot{\lambda} = \omega^2 \lambda^{-p}$, with $p = 2$ for the interacting and $p = 3$ for the non-interacting wave packet (cf. equations (3.44) and (4.72)). For the latter one finds the analytic form $\lambda(t) = \sqrt{1 + \omega^2 t^2}$, which corresponds to the correct time-dependence of the width of a spreading wave packet (cf. appendix (A.8)) [120].

In figure 5.6, we show the shearing of the Wigner function during the ballistic expansion for the Gross-Pitaevskii wave function (a), the Thomas-Fermi Wigner function $W_{\text{TF}}(\xi(t), \pi(t))$ with time-dependent coordinates (b), and for the non-interacting Gaussian wave packet (c). For short

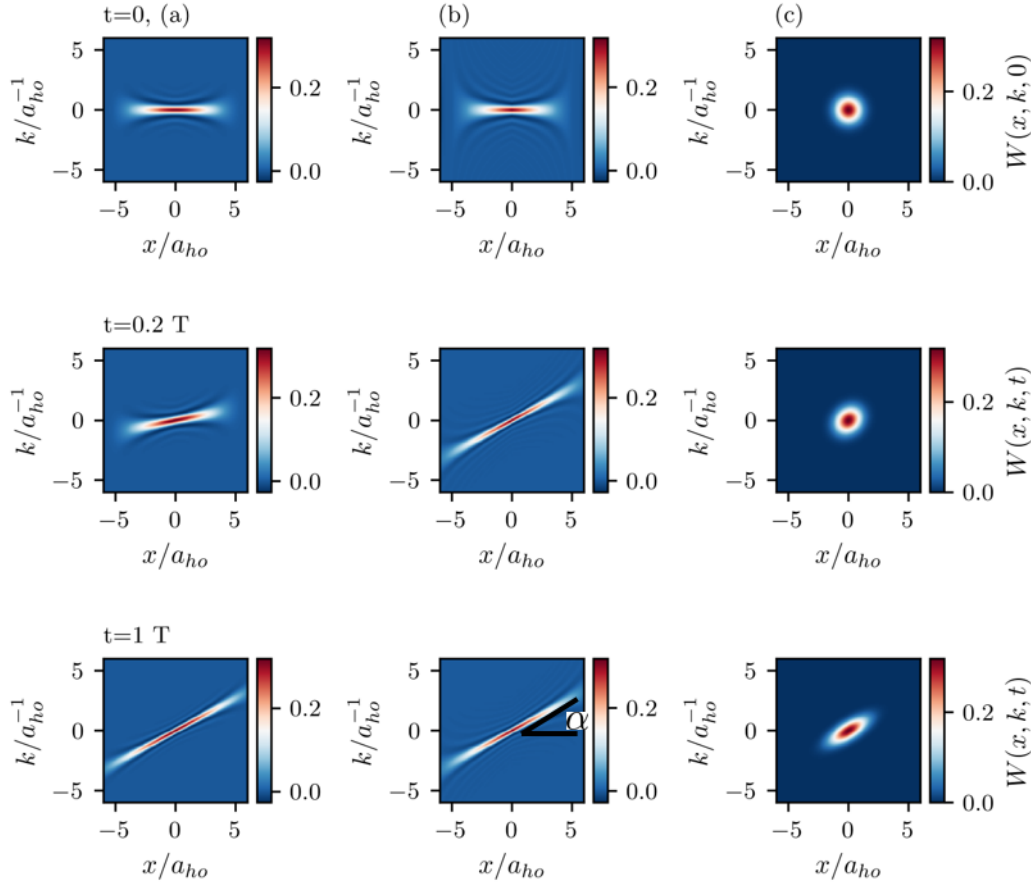


Figure 5.6: Shearing of the Wigner phase-space distribution during the ballistic expansion at three different times. Columns (a): Wigner function of the Gross-Pitaevskii field, $\kappa = 100$, $\mu = 14.11 \hbar\omega$ (b): Thomas-Fermi Wigner function $W_{\text{TF}}(x, k)$. (c) non-interacting $\kappa = 0$ Gaussian wave packet. Sketch of the shearing angle α at $t = 1 T$ in (b).

expansion ($t = 0.2 T$, $T \equiv 1/\omega$), we see qualitative differences in the shearing behavior for the interacting (a), (b), and the non-interacting limit (c), due to the different extents of the distribution in position as well as in momentum spaces. For the latter more k -values are distributed at higher momenta. At the same, the distribution has a smaller extent in the position direction, resulting in a different shearing angle at small expansion times, $t = 0.2 T$.

DELTA-KICK COLLIMATION Delta-kick collimation is used to narrow the momentum width of an atomic ensemble. It consists of a two-step protocol: 1) a free expansion of the atomic wave

packet, and 2) a short application of a harmonic potential that acts as a matter-wave lens. The method can be visualized using the Wigner representation in phase space. As mentioned in 3.3.1 and demonstrated in the previous section, the ballistic expansion corresponds to shearing of the Wigner function by an angle α (cf. figure 5.6). The application of the harmonic potential rotates the phase space distribution by an angle β that ideally corresponds to the shearing angle as $\beta = -\alpha$. Afterward, the Wigner function is aligned with x -coordinate axis such that the momentum width is smaller than the width of the initial distribution, $\Delta p^2(t) < \Delta p^2(0)$. As one can connect a thermodynamic temperature to a momentum width, $\Delta p^2 \propto k_B T/2$, the method is also sometimes called delta-kick cooling.

In terms of the Thomas-Fermi scaling solution (4.69), (4.70) and the coordinate transformation (3.32), one finds for the variance of the one-dimensional momentum using equation (B.11),

$$\Delta p^2(t) = \frac{1}{\lambda^2} \Delta \pi^2 + M \dot{\lambda}^2 \Delta \xi^2 + 2M \frac{\dot{\lambda}}{\lambda} (\langle \pi \xi \rangle - \langle \pi \rangle \langle \xi \rangle). \quad (5.17)$$

Here, $\Delta \pi^2 = \Delta p^2(0)$ and $\Delta \xi^2 = \Delta x^2(0)$ denote the initial variance of the trapped condensate in momentum and position respectively. As the scale $\lambda(t) > 0$, one finds the minimal velocity for $\dot{\lambda} = 0$, with $\Delta p^2(t) < \Delta p^2(0)$ [120]. The latter is illustrated in figure 5.7. The change

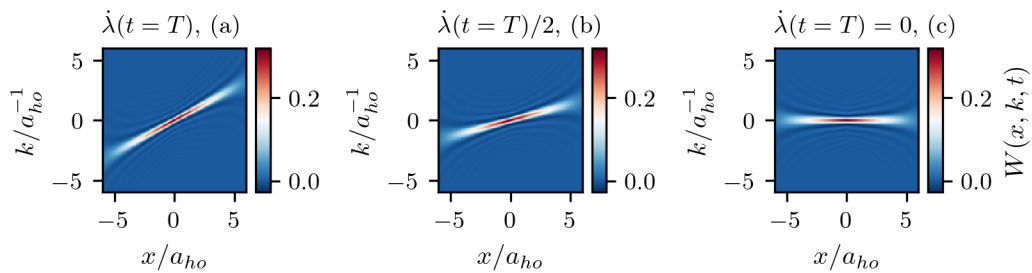


Figure 5.7: Illustration of delta-kick collimation using the Thomas-Fermi Wigner function W_{TF} (5.14) for different values of $\dot{\lambda}(t)$.

instantaneous change of $\dot{\lambda}$ corresponds to different rotation angles of the Thomas-Fermi Wigner function with minimal velocity spread in subfigure (c).

5.2.2 THREE-DIMENSIONAL HARMONIC OSCILLATOR

So far we have only discussed the Thomas-Fermi Wigner function in two-dimensional phase space. In [51], we investigated similar approximations for the six-dimensional Wigner function. As discussed in section 4.3.3, we have considered an anisotropic tilted harmonic oscillator and defined the coordinate transformation (4.42) between lab- and body-fixed scaled coordinates. In turn, this induces a relation between the field amplitudes in the two frames (4.43). For the Wigner representation, this transformation reads

$$W'(\mathbf{r}', \mathbf{k}') \equiv W(\mathbf{r}, \mathbf{k}). \quad (5.18)$$

In the body-fixed scaled coordinates, the Thomas-Fermi field (4.44) becomes an isotropic s -wave. Thus, the complexity of the Wigner function is reduced, $W'_{TF}(\mathbf{r}', \mathbf{k}') = W'_{TF}(r', k', \mathbf{r}' \cdot \mathbf{k}')$, as it must depend only on the three rotation invariant scalars [121], $r' = |\mathbf{r}'|$, $k' = |\mathbf{k}'|$ and the scalar

product $\mathbf{r}' \cdot \mathbf{k}' = r' k' \cos \vartheta_k$ with enclosed angle $\vartheta_k = \angle(\mathbf{r}', \mathbf{k}')$. This rotation invariance can be also seen directly in the coherence function

$$\rho'_{\text{TF}}(\mathbf{r}', \boldsymbol{\xi}') = n \sqrt{\left(1 - r'^2 - \frac{\xi'^2}{4}\right)^2 - (\mathbf{r}' \cdot \boldsymbol{\xi}')^2}. \quad (5.19)$$

In figure 5.8, we have depicted a two-dimensional cross-section (x', k'_x) of the six-dimensional Thomas-Fermi Wigner function for an isotropic three-dimensional harmonic oscillator potential using numerical quadrature.

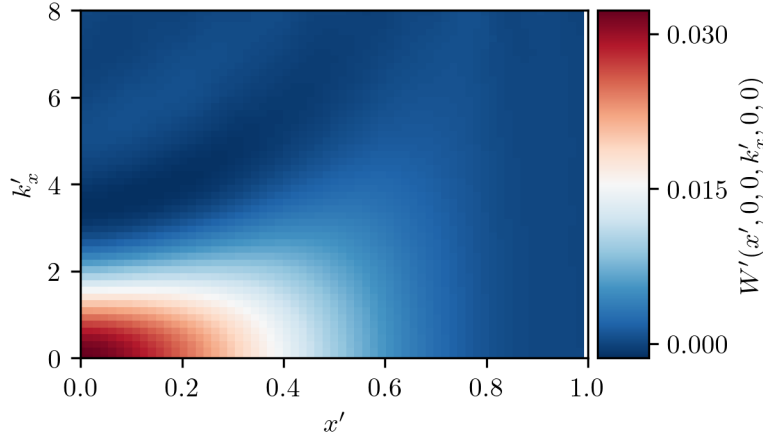


Figure 5.8: Color-coded two-dimensional cross-section of the six-dimensional Cartesian Thomas-Fermi Wigner function $W'_{\text{TF}}(x', 0, 0, k'_x, 0, 0)$ for the isotropic three-dimensional harmonic oscillator in phase space.

If the integration variable $\boldsymbol{\xi}'$ is expressed in spherical coordinates (ξ', θ, ϕ) with \mathbf{r}' aligned with the z' -direction and $\mathbf{k}' \in x'$ - z' plane, then $\theta = \angle(\mathbf{r}', \boldsymbol{\xi}')$ denotes the polar angle. The coherence function $\rho'_{\text{TF}}(r', \xi', \theta)$

$$\rho'_{\text{TF}} = n \left[\left(1 - r'^2 - \frac{\xi'^2}{4}\right)^2 - (r' \xi' \cos \theta)^2 \right]^{\frac{1}{2}}, \quad (5.20)$$

$$\xi'(r', \theta) \equiv 2 \left(\sqrt{1 - r'^2 \sin^2 \theta} - r' |\cos \theta| \right), \quad (5.21)$$

is finite only, when $r' < 1$ and $\xi' < \xi'(r', \theta)$. Exploiting the axial-symmetry of the coherence function yields the Wigner function as

$$W'_{\text{TF}}(r', k', \theta_k) = \int_0^\pi d\theta \sin \theta \int_0^{\xi'(r', \theta)} d\xi' \xi'^2 J_0(k'_x \xi'_x) \frac{e^{-ik'_z \xi'_z}}{(2\pi)^2} \rho'_{\text{TF}}(r', \xi', \theta), \quad (5.22)$$

where $k'_x = k' \sin \theta_k$, $k'_z = k' \cos \theta_k$ and $\xi'_x = \xi' \sin \theta$, $\xi'_z = \xi' \cos \theta$. So far we have not found any simplification of the integral in equation (5.22). Neglecting the angular dependence in the coherence function by a similar factorization ansatz as in the previous section is possible but leads to significant deviations from the numerical solution [51].

6 WAVEFRONT ABERRATION OF EXPANDING BOSE-EINSTEIN CONDENSATES

In classical optics, it is very convenient to analyze the deformation of the wavefront in terms of suitable basis functions. The expansion coefficients for the wavefront are then related to specific types of aberrations in the optical system. For circular pupil shapes, Zernike polynomials are a convenient choice as they represent a complete orthogonal set.

In this chapter, we show that the Bogliubov basis functions introduced in chapter 4.5 are a suitable basis to describe the aberrations for the condensate wave function. In particular, this statement remains true regarding condensates in quadratic time-dependent potentials including the free expansion. Approximations to the numerical Bogoliubov functions in form of hydrodynamic polynomials have been used for example in [122–126] to characterize phase fluctuations in highly elongated condensates.

6.1 GROSS-PITAEVSKII EQUATION IN ADAPTIVE SCALES

So far we have discussed the classical motion of a single particle 3.4 as well as the motion for a fluid with mean-field pressure in time-dependent harmonic trapping potentials by using a coordinate scaling transformation. One can apply the same ansatz for the exact time-dependent Gross-Pitaevskii equation (4.36) which leads to the affine transformation of the Gross-Pitaevskii mean-field wave function [49, 50, 79],

$$\Psi(\mathbf{r}, t) = e^{iS(\mathbf{r}, t)/\hbar} \psi(\Lambda^{-1}[\mathbf{r} - \boldsymbol{\eta}(t)], t) |\Lambda|^{-\frac{1}{2}}, \quad (6.1)$$

where the local action is given by

$$S(\mathbf{r}, t) = \frac{M}{2} [\mathbf{r} - \boldsymbol{\eta}(t)]^\top \dot{\Lambda} \Lambda^{-1} [\mathbf{r} - \boldsymbol{\eta}(t)] + M \mathbf{r}^\top \dot{\boldsymbol{\eta}}(t) + s(t) - \beta(t). \quad (6.2)$$

The scales $\Lambda(t)$ obey the matrix differential equation (4.72) as in the Thomas-Fermi limit. The center of mass coordinates $\boldsymbol{\eta}(t)$ follow the Newton equation (3.41) which in free fall reduces to a time-dependent harmonic oscillator equation. The global phases $s(t)$, $\beta(t)$ are defined in the equations (3.40) and (4.70). Therein, the chemical potential μ is obtained by the stationary Gross-Pitaevskii equation (4.37).

By inserting the ansatz (6.1) into the time-dependent Gross-Pitaevskii equation (4.36), one finds a new equation of motion for the transformed wave function $\psi(\boldsymbol{\xi}, t)$ with respect to the new coordinates $\boldsymbol{\xi}$,

$$i\hbar \partial_t \psi(\boldsymbol{\xi}, t) = -\frac{\hbar^2}{2M} \nabla_{\boldsymbol{\xi}}^\top M^{-1} \nabla_{\boldsymbol{\xi}} \psi + \frac{1}{|\Lambda|} \left(\frac{M}{2} \boldsymbol{\xi}^\top \Omega^2(0) \boldsymbol{\xi} + g|\psi|^2 - \mu \right) \psi + U_1(\Lambda \boldsymbol{\xi} + \boldsymbol{\eta}, t) \psi, \quad (6.3)$$

where we have defined the mass-matrix $M = \Lambda^\top \Lambda$ in equation (3.39). Equation (6.3) is now the optimal Gross-Pitaevskii equation to describe the motion of the condensate, as it takes into account

the Kohn-Dobson harmonic potential theorem [127, 128], where the center mass motion decouples from the condensate's wave function and the time-dependence of the oscillator frequencies $\Omega^2(t)$.

In the following, we introduce the scaling approximation of the Gross-Pitaevskii field. Therefore, we rewrite the transformed Gross-Pitaevskii equation (6.3) as

$$i\hbar\partial_t\psi = |\Lambda|^{-1}[H_0 + H_1(\psi)]\psi + [H_2(t) + H_3(t)]\psi. \quad (6.4)$$

The first two terms on the right-hand side are defined by the time-independent Gross-Pitaevskii operator

$$H_0 = -\frac{\hbar^2}{2M}\nabla_{\boldsymbol{\xi}}^2 + \frac{M}{2}\boldsymbol{\xi}^\top\Omega^2(0)\boldsymbol{\xi} + g|\psi_0|^2 - \mu, \quad (6.5)$$

and a non-linear perturbation

$$H_1(\psi) = g(|\psi|^2 - |\psi_0|^2), \quad (6.6)$$

that depends on the non-linear response of the Gross-Pitaevskii field during the time evolution. It is easy to see that $H_0 + H_1$ represents the usual time-dependent Gross-Pitaevskii equation for the transformed wave function $\psi(\boldsymbol{\xi}, t)$. Moreover, we define a kinetic energy perturbation

$$H_2(t) = -\frac{\hbar^2}{2M}\nabla_{\boldsymbol{\xi}}^\top\delta\mathbf{M}^{-1}(t)\nabla_{\boldsymbol{\xi}}, \quad (6.7)$$

with a time-dependent ‘‘mass difference’’ matrix

$$\delta\mathbf{M}^{-1}(t) = \mathbf{M}^{-1}(t) - |\Lambda(t)|^{-1}. \quad (6.8)$$

The last contribution arises from any residual anharmonicities

$$H_3(t) = U_1(\Lambda\boldsymbol{\xi} + \boldsymbol{\eta}, t), \quad (6.9)$$

of the external potential which vanishes during a ballistic expansion. We note that if at $t_0 = 0$ all perturbations are equal to zero, $H_1 = H_2 = H_3 = 0$, the macroscopic wave function of the condensate satisfies the stationary Gross-Pitaevskii equation

$$H_0\psi_0 = 0. \quad (6.10)$$

In the strongly interacting regime, the kinetic perturbation H_2 is usually small compared to the energetic contributions in $H_0 + H_1$. Thus for a harmonic potential, when $H_3 = 0$, the time evolution of the condensate wave function is completely determined by the scales $\Lambda(t)$ and position coordinates $\boldsymbol{\eta}(t)$ as $\partial_t\psi \approx 0$. Thus, we obtain

$$\Psi_s(\mathbf{r}, t) = e^{iS(\mathbf{r}, t)/\hbar}\psi_0(\Lambda^{-1}[\mathbf{r} - \boldsymbol{\eta}(t)])|\Lambda|^{-\frac{1}{2}}, \quad (6.11)$$

the so-called scaling approximation of the Gross-Pitaevskii field in time-dependent harmonic traps. We emphasize that we use in equation (6.11), the exact ground state solution and not the analytic Thomas-Fermi field ψ_{TF} which would also neglect the kinetic energy in H_0 . If the scaling approximation has high fidelity with the exact Gross-Pitaevskii solution, one can directly evaluate important quantities such as the expectation values

$$(\mathbf{r}_0, \mathbf{p}_0) = (\langle\mathbf{r}\rangle, \langle\mathbf{p}\rangle), \quad (6.12)$$

and covariance matrices

$$\Sigma_{\mathbf{r}} = \langle (\mathbf{r} - \mathbf{r}_0) \otimes (\mathbf{r} - \mathbf{r}_0) \rangle, \quad \Sigma_{\mathbf{p}} = \langle (\mathbf{p} - \mathbf{p}_0) \otimes (\mathbf{p} - \mathbf{p}_0) \rangle, \quad (6.13)$$

in either position or momentum space by solving the ordinary differential equations (4.72), (3.41), and evaluating the stationary ground state wave function once (cf. appendix B and [79]).

The wave function Ψ_s in equation (6.11) is often used for approximation schemes that estimate the time evolution in quadratic potentials [26, 27]. We use the scaling approximation as the matter-wave analog to the paraxial solution in classical ray and wave optics [129]. For the latter, one defines aberrations in optical systems as optical path differences between the actual to the reference wavefront from the paraxial approximation. Hence, the aberrated complex wave function reads

$$\delta\Psi_{\mathbf{r}}(\mathbf{r}, t) = \Psi(\mathbf{r}, t) - \Psi_s(\mathbf{r}, t) = e^{iS(\mathbf{r}, t)/\hbar} |\Lambda|^{-\frac{1}{2}} \psi_1(\boldsymbol{\xi}, t), \quad (6.14)$$

with

$$\psi_1(\boldsymbol{\xi}, t) = \psi(\boldsymbol{\xi}, t) - \psi_0(\boldsymbol{\xi}). \quad (6.15)$$

The deviations in (6.14) include the intrinsic kinetic energy perturbation H_2 that is neglected in the scaling approximation as well as non-quadratic contributions of the external potential H_3 .

6.2 ABERRATION ANALYSIS IN LINEAR RESPONSE

In the previous section, we have defined a reference wave function in equation (6.14) that can be used for an aberration analysis of interacting Bose-Einstein condensates. As the time-dependence of the field $\psi(\boldsymbol{\xi}, t)$ is considered to be small, $\partial_t \psi \approx 0$, we analyze the deviations to the scaling approximation in linear response. As in section 4.5, we linearize equation (6.4) around the stationary solution using the ansatz as in equation (6.15),

$$\psi(\boldsymbol{\xi}, t) = \psi_0(\boldsymbol{\xi}) + \psi_1(\boldsymbol{\xi}, t). \quad (6.16)$$

Neglecting terms of the order ψ_1^2 , $H_2\psi_1$ and $H_3\psi_1$, one finds for the two-component vector $\chi(\boldsymbol{\xi}, t) = (\psi_1, \psi_1^*)^\top$,

$$i\hbar\partial_t\chi(\boldsymbol{\xi}, t) = |\Lambda|^{-1}\Sigma^{\text{B}}\chi + \mathcal{S}, \quad (6.17)$$

where the Bogoliubov operator was defined in equation (4.89) and the source term reads

$$\mathcal{S}(\boldsymbol{\xi}, t) = \{[H_2(t) + H_3(t)]\psi_0(\boldsymbol{\xi}), -[H_2(t) + H_3(t)]\psi_0^*(\boldsymbol{\xi})\}^\top. \quad (6.18)$$

Equation (6.17) can now formally be solved by expanding the fields in terms of the Bogoliubov basis functions of the initially trapped condensate. Hence, we state that by comparing (6.17) with equation (4.88), the deviations to the scaling approximation (6.14) are well described by the

Bogoliubov basis function for the initially trapped condensate and whose time-evolution is given by equation (6.17). Comparing (6.17) with equation (4.88), we find for the distorted complex field

$$\begin{aligned}
 \chi(t) = & W' e^{-iE'\tau(t)/\hbar} \sigma_3^{(n-1)} \chi'(0) \\
 & - \tau(t) \frac{iP\delta N}{\mathfrak{M}} \\
 & + iQ\delta N - iP\delta\Phi \\
 & + \frac{W'}{i\hbar} \int_0^t e^{-iE'[\tau(t)-\tau(s)]/\hbar} \sigma_3^{(n-1)} \mathcal{S}'(s) ds \\
 & + \frac{1}{i\hbar} \int_0^t [iQ\mathcal{S}_N(s) - iP\mathcal{S}_\Phi(s)] ds \\
 & - \frac{1}{i\hbar} \int_0^t [\tau(t) - \tau(s)] \frac{iPS_N(s)}{\mathfrak{M}} ds,
 \end{aligned} \tag{6.19}$$

with amplitudes defined in equation (4.96) and [113],

$$\chi' = W'^{\dagger} \sigma_3 \chi, \quad \delta N = P^{\dagger} \sigma_3 \chi, \quad \delta\Phi = Q^{\dagger} \sigma_3 \chi. \tag{6.20}$$

In addition, we introduced the new time variable

$$\tau(t) = \int_0^t |\Lambda(t')|^{-1} dt'. \tag{6.21}$$

Equation (6.19) describes all deviations to the scaling approximation (6.11) in linear response. The first three terms arise if the initial state exhibits non-quadratic density or phase perturbations at $t = 0$. The last three summands correspond to the source term (6.18) which includes the kinetic energy perturbation H_3 as well as the appearance of time-dependent anharmonic potentials. Hence, we state that most deviations are well described by the Bogoliubov basis function for the initially trapped condensate. From equation (6.19), one can extract the density and phase deviations, (n_1, ϕ_1) using the relations to complex fields (ψ_1, ψ_1^*) in equation (4.100). Instead of recalculating the required modes and amplitudes for each separate problem, we approximate the Bogoliubov problem with known basis functions obtained from the hydrodynamic formulation in section 4.4.2. In the following chapters, we apply these in terms of a multipole expansion of known trapping potential 7.4. Moreover, we use the partial wave expansion to characterize the properties of the condensate. In particular, we study the phase evolution for delta-kick collimation 8.4.3 with magnetic chip traps analog Zernike's description of classical wavefront aberrations.

7

EFFICIENT MULTIPOLE REPRESENTATION FOR MATTER-WAVE OPTICS

In this chapter, we present a multipole analysis for an efficient description of matter-wave optics with Bose-Einstein condensates in three-dimensional space. For this purpose, we characterize external potentials obtained by magnetic chip traps and Laguerre-Gaussian beams in terms of expansion coefficients and polynomial basis functions. We conclude by studying an efficient interpolation scheme for different density distributions.

7.1 TRAPPING POTENTIALS

Cold atoms may be trapped or guided in either optical dipole or Zeeman potentials. Furthermore, the method of phase imprinting maps [130] the shape of the external potential onto the phase of the atomic wave packet. Thus, as the shape of the potential defines the shape and evolution of the condensate's density and phase, it is vital to characterize the potential for high-precision matter-wave optics.

7.1.1 OPTICAL DIPOLE POTENTIALS

Conservative optical potentials are typically created by laser light far detuned from the atomic resonance

$$U_D(\mathbf{r}) = U_0 e^{-\theta(\mathbf{r})}, \quad (7.1)$$

with constant amplitude $U_0 = \hbar|\Omega_0|^2/(4\Delta)$. Here, $\Delta = \omega_L - \omega_0$ describes the laser detuning and Ω_0 is the Rabi frequency. If the laser is red-detuned $\Delta < 0$ with respect to the atomic transition, the dipole potential is negative and the atoms are attracted into the light field. For blue detuning, $\Delta > 0$, the atoms are repelled from the light field (cf. equation (9.10)). Therefore, the potential minimum corresponds to minimal intensity [131]. We have summarized more details about the physical mechanisms in chapter 9.

For a single Laguerre-Gaussian beam, the exponent in equation (7.1) has the spatial dependence

$$\theta(\mathbf{r}) = 2\frac{x^2 + y^2}{w(z)^2} + \ln\left(1 + \frac{z^2}{z_R^2}\right) \approx 2\frac{x^2 + y^2}{w(z)^2} + \frac{z^2}{z_R^2}, \quad (7.2)$$

where the Rayleigh range $z_R = \pi w_0^2/\lambda_L$, is typically much larger than the extension of the condensate wave packet. $\lambda_L = 2\pi/k_L$ denotes the laser wavelength and $w(z) = w_0\sqrt{1 + z^2/z_R^2}$ is the beam waist. Figure 7.1 shows the isolines of equal energy of an optical dipole potential created by a single Laguerre-Gaussian beam. The chosen parameters are similar to [132], where the dipole potential acts as an optical lens to perform matter-wave optics in the time domain. For a large Rayleigh range ($z_R \gg z$), the potential is of cylindrical shape with very weak confinement in the longitudinal direction.

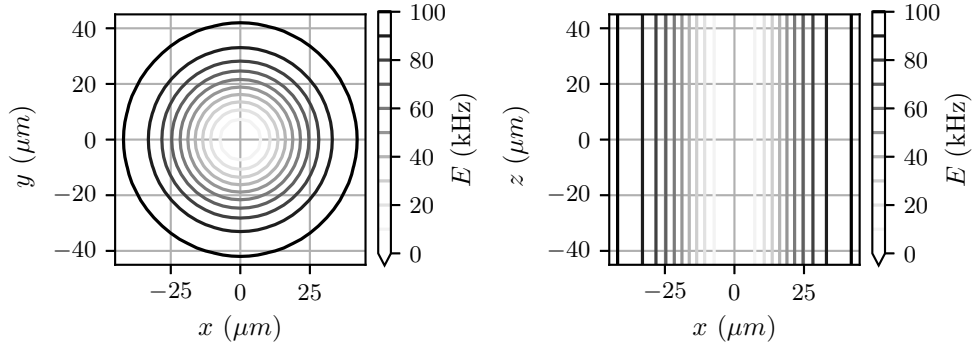


Figure 7.1: Isolines of an optical dipole potential generated by a single Laguerre-Gaussian beam. Parameters used as in [132]. Trap depth for laser power of 60 mW, $|U_0|/h = 5\mu K k_B/h$, Rayleigh range $z_R = 3.2$ mm, $w_0 = 33$ μm , trapping frequencies $\nu_{\text{Rb}} \approx (211, 211, 1.5)$ Hz.

7.1.2 ZEEMAN POTENTIAL

Besides optical dipole potentials, we consider Zeeman potentials (2.18) that have been introduced in chapter 2. In figure 7.2 we depict the isolines of equal energy of the release trap potential, discussed in section 2.4.4. In contrast to figure 2.5, we have shifted the coordinate system by the value of the trap minimum, $\mathbf{a} = \mathbf{r}_0$, but have not included any rotations. The tilt in the x-y plane corresponds to the rotation angle $\gamma = 9.7^\circ$ in table 2.2.

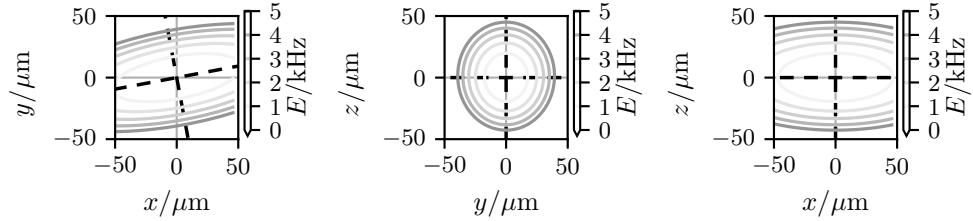


Figure 7.2: Contour lines of a magnetic Zeeman potential generated by the Z-wire structures of an atomic chip trap. Parameters as in table 2.1 and 2.2. The principle axis of the ellipsoid obtained by the Hesse matrix (2.26), are marked as - - - lines.

7.2 MULTIPOLE EXPANSION WITH STRINGARI POLYNOMIALS

The three-dimensional trapping potentials discussed above can be approximated by a Taylor expansion around \mathbf{r}_0 (7.3)

$$U(\mathbf{r}) = U_0 + (\mathbf{r} - \mathbf{r}_0)^\top \nabla U(\mathbf{r}_0) + \frac{1}{2!} (\mathbf{r} - \mathbf{r}_0)^\top \nabla^2 U(\mathbf{r}_0) (\mathbf{r} - \mathbf{r}_0) + \dots \quad (7.3)$$

$$= \sum_{n=0}^{\infty} \sum_{l=0}^{\infty} \sum_{m=-l}^l U_{nlm} \langle \mathbf{r} | nlm \rangle, \quad (7.4)$$

or in a multipole expansion (7.4). The Taylor polynomial (7.3) is useful for extracting the trapping frequencies in the second-order coefficients. However, the Taylor monomials $x^r y^s z^t$ are not well

suitable for efficient approximation schemes. Therefore, we introduce orthonormal basis functions in spherical coordinates $\mathbf{r} = (r, \vartheta, \varphi)$,

$$\langle \mathbf{r} | nlm \rangle = S_{nlm}(\mathbf{r}) = S_{nl}(r) Y_{lm}(\vartheta, \varphi), \quad \langle n'l'm' | nlm \rangle = \delta_{n,n'} \delta_{l,l'} \delta_{m,m'}, \quad (7.5)$$

that consist of spherical harmonics $Y_{lm}(\vartheta, \varphi)$ and radial polynomials $S_{nl}(r)$. The latter, we name Stringari's polynomials because they appear naturally as sound wave excitations of a Bose-Einstein condensate in an isotropic three-dimensional harmonic oscillator potential (cf. section 4.4.2) [109, 133]. The Stringari polynomials

$$\begin{aligned} S_{nl}(r) &= \mathcal{N}_{nl} \tilde{r}^l J_n^{(l+1/2,0)}(1 - 2\tilde{r}^2), \quad \tilde{r} = r/R, \\ N_{nl} &= [(4n + 2l + 3)/R^3]^{1/2}, \end{aligned} \quad (7.6)$$

consist explicitly of Jacobi polynomials $J_n^{(l+1/2,0)}(1 - 2\tilde{r}^2)$ with quadratic dependence of the radial coordinate. The constant \mathcal{N}_{nl} is chosen such as the polynomials are orthonormal on the interval $0 \leq r \leq R$ (cf. appendix E)

$$\int_0^R r^2 S_{n'l}(r) S_{nl}(r) dr = \delta_{n,n'}. \quad (7.7)$$

Therefore, the expansion coefficients in (7.4) are given by

$$U_{nlm} = \langle nlm | U \rangle = \int_V S_{nlm}^*(\mathbf{r}) U(\mathbf{r}) d^3r, \quad (7.8)$$

with spherical volume $V = 4\pi R^3/3$. For the trapping potentials, we usually choose R to be of the order of typical atomic length scales.

Alternatively, it is useful to introduce the logarithm of the exponential which is also called the cumulant generating function [134]. This is particularly useful for Gaussian functions as the series terminates after the second order. The general multipole expansion for an exponential of the form (7.1) is then given by

$$\theta(\mathbf{r}) = -\log \frac{U(\mathbf{r})}{U_0} = \sum_{n=0}^{\infty} \sum_{l=0}^{\infty} \sum_{m=-l}^l \theta_{nlm} \langle \mathbf{r} | nlm \rangle. \quad (7.9)$$

SPECTRAL POWERS In the next sections, we analyze the potentials and the cumulants in terms of this multipole expansion. However, to visualize and compress the information stored in the complex expansion coefficients n_{nlm} , θ_{nlm} , we recap how the multipole expansion coefficients transform under a rotation of the coordinate system. We consider a coordinate transformation $\mathbf{r}' = \mathbf{R}\mathbf{r}$, where \mathbf{R} denotes an orthogonal rotation matrix $\mathbf{R}\mathbf{R}^\top = \mathbb{1}$. In both frames, the values of the potential must be equal

$$\langle \mathbf{r} | U \rangle = \langle \mathbf{r}' | U' \rangle = \sum_{nlm'} \langle \mathbf{r}' | nlm' \rangle U'_{nlm'}. \quad (7.10)$$

The coefficients in the new reference frame $U'_{nlm'}$ are given by

$$U'_{nlm'} = \sum_{m=-l}^l D_{m'm}^{(l)}(\mathbf{R}) U_{nlm}, \quad (7.11)$$

where the $D_{m'm}^{(l)}(\mathbf{R}) = \langle lm' | \hat{R} | lm \rangle$ are the Wigner D-matrices as the matrix representation of the rotation operator in the angular momentum basis [93, 135, 136], (cf. appendix M.3). Using the unitarity of the rotation operator, $\hat{R}\hat{R}^\dagger = \hat{R}^\dagger\hat{R} = \mathbb{1}$, as well the orthonormality of the Stringari polynomials (7.5), we specify rotational invariant measures such as the total power

$$P(U) = \int_V |U(\mathbf{r})|^2 d^3r = \sum_{nlm} |U_{nlm}|^2. \quad (7.12)$$

Moreover, we define the marginals P_{nl} , P_l as well as the relative fractional powers p_{nl} as

$$P_{nl}(U) = \sum_m |U_{nlm}|^2, \quad P_l(U) = \sum_n P_{nl}(U) \quad p_{nl}(U) = \frac{P_{nl}(U)}{P(U)}. \quad (7.13)$$

Thus, the relative fractional powers sum to $\sum_{nl} p_{nl} = 1$.

7.3 NUMERICAL EVALUATION

While the multipole coefficients for the quadratic harmonic oscillator potential may be evaluated analytically using the scalar product in equation (7.8), we are using a least-square evaluation [71] when the potential is represented on a numerical grid. As the discretized Stringari polynomials are non-orthogonal basis functions, we introduce the finite complex scalar product

$$(a|b) = \sum_{\mathbf{r}_j \in V} \mathcal{V} a^*(\mathbf{r}_j) b(\mathbf{r}_j) = \mathbf{a}^\dagger \mathbf{b}, \quad (7.14)$$

with discrete position coordinates $\{\mathbf{r}_j\}$, the measure of the Cartesian volume element $\mathcal{V} = \Delta x \Delta y \Delta z$ and its norm $\|\mathbf{a}\| = \sqrt{(a|a)}$. Hence, the distance of the squared residuals is given by

$$\varepsilon = \|\mathbf{S}\mathbf{u} - \mathbf{U}\|^2. \quad (7.15)$$

Here, we have introduced the complex coefficient vector $\mathbf{u} = \{U_{nlm}\}$, the values of the discrete target potential $\mathbf{U} = \{U(\mathbf{r}_j)\}$ and the complex matrix $\mathbf{S} = \{S_{nlm}(\mathbf{r}_j)\}$ that contains the discrete set of the finite Stringari basis functions. One finds the least square minimizer

$$\partial\varepsilon/\partial\mathbf{u}^* = 0, \quad (7.16)$$

by setting the derivative to zero which leads to the best estimate

$$\mathbf{u} = (\mathbf{S}^\dagger \mathbf{S})^{-1} \mathbf{S}^\dagger \mathbf{U}. \quad (7.17)$$

In the following, we will examine some popular trapping potentials using this multipole decomposition. We discuss several cases of the harmonic oscillator potential with different symmetries. Afterward, we discuss the multipole expansion of the optical dipole potential with a Laguerre-Gaussian beam and the Zeeman potential obtained by the chip model from section 2.4.

As the potentials are approximated as polynomials, we are free to choose the radius R of the spherical volume that defines the interval where we evaluated the Stringaris. For the potentials, we choose R to be of the order of typical atomic length scales.

7.4 EXAMPLE POTENTIALS

7.4.1 3D ISOTROPIC HARMONIC OSCILLATOR POTENTIAL

The isotropic harmonic oscillator potential, characterized by the stiffness parameter k ,

$$U(\mathbf{r}) = \frac{k}{2}r^2 = \sum_{n=0}^1 U_{n00} \langle \mathbf{r} | n00 \rangle = u_c \left(\frac{3}{5} \langle \mathbf{r} | 000 \rangle - \sqrt{\frac{12}{175}} \langle \mathbf{r} | 100 \rangle \right), \quad (7.18)$$

is invariant under rotations. Thus, only the monopoles $l = 0$ in equation (7.4) are present. For a Stringari S_{n00} of order n , the polynomial is of the order r^{2n} . Thus the Stringari-polynomials (7.6) with $n < 2$ suffice to parametrize a harmonic oscillator trap. The expansion coefficients U_{nlm} are given in terms of a dimensional factor [$\text{J m}^{3/2}$]

$$u_c = \frac{M\omega_0^2}{2} R^2 \sqrt{V}, \quad (7.19)$$

considering the harmonic oscillator energy and the volume of a sphere with radius R . As only s-waves are contributing, we can directly calculate the total and the fractional powers

$$P(U) = \frac{3}{7}u_c^2, \quad p_{00}(U) = \frac{21}{25} = 0.84, \quad p_{10}(U) = \frac{4}{25} = 0.16. \quad (7.20)$$

7.4.2 ANISOTROPIC HARMONIC OSCILLATOR POTENTIAL

PROLATE OR OBLATE SPHEROIDAL HARMONIC POTENTIAL

For a prolate or oblate spheroidal harmonic oscillator, the potential is characterized by two angular frequencies ω_{\perp} and ω_{\parallel} , but it is still rotational symmetric around the z -axis

$$U(\mathbf{r}) = \frac{k_{\perp}}{2}(x^2 + y^2 + \alpha^2 z^2). \quad (7.21)$$

The anisotropy is measured by $\alpha^2 = k_{\parallel}/k_{\perp}$. In contrast to the isotropic oscillator, one needs also a quadrupole within the multipole expansion

$$\begin{aligned} U_{000} &= \frac{2 + \alpha^2}{5}u_c, & U_{100} &= -\frac{4 + 2\alpha^2}{\sqrt{525}}u_c, \\ U_{020} &= -\frac{2 - 2\alpha^2}{\sqrt{105}}u_c, & u_c &= \frac{M\omega_{\perp}^2}{2}R^2\sqrt{V}. \end{aligned} \quad (7.22)$$

Using the coefficients in (7.22) we can evaluate

$$\begin{aligned} P(U) &= \frac{(8 + 4\alpha^2 + 3\alpha^4)}{35}u_c^2, & p_{00}(U) &= \frac{7}{5} \frac{(2 + \alpha^2)^2}{8 + 4\alpha^2 + 3\alpha^4}, \\ p_{10}(U) &= \frac{4}{15} \frac{(2 + \alpha^2)^2}{(8 + 4\alpha^2 + 3\alpha^4)}, & p_{02}(U) &= \frac{4}{3} \frac{(1 - \alpha^2)}{(8 + 4\alpha^2 + 3\alpha^4)}, \end{aligned} \quad (7.23)$$

the angular powers for the cylindrical symmetric oscillator potential. It is noteworthy that this expansion encompasses degenerate traps with vanishing z -confinement $\alpha = 0$, as well as the isotropic trap (7.18) with $\alpha = 1$. The former becomes relevant, for very large Rayleigh lengths z_R in equation (7.2) which exhibits very small confinement in the z -direction.

TILTED ANISOTROPIC HARMONIC OSCILLATOR POTENTIAL

We consider a general oscillator potential in a coordinate system, e.g. the coordinates of an atomic chip trap, where the potential minimum is at position \mathbf{r}_0 . Hence, the harmonic approximation of the potential reads

$$\begin{aligned} U(\mathbf{r}) &= \frac{1}{2}(\mathbf{r} - \mathbf{r}_0)^T \mathbf{K}(\mathbf{r} - \mathbf{r}_0) \\ &= \frac{1}{2}\mathbf{r}_0^T \mathbf{K} \mathbf{r}_0 - \mathbf{r}_0^T \mathbf{K} \mathbf{r} + \frac{1}{2}\mathbf{r}^T \mathbf{K} \mathbf{r} \\ &= U^{(0)} + U^{(1)}(\mathbf{r}) + U^{(2)}(\mathbf{r}). \end{aligned} \quad (7.24)$$

In the last line of equation (7.24) we sort it into different homogeneous potentials of the order r^n , $U^{(n)}(\mathbf{r})$. In order to determine the coefficients, we write the Cartesian position vectors in (7.24) in terms of the three spherical basis vectors $\{\mathbf{e}_1, \mathbf{e}_0, \mathbf{e}_{-1}\}$,

$$\mathbf{r} = \sum_{m=-1}^1 q_m \mathbf{e}^m = \sum_{m=-1}^1 q^m \mathbf{e}_m, \quad m \in \{\pm 1, 0\}, \quad (7.25)$$

whereas the spherical and Cartesian basis vectors are connected by

$$\mathbf{e}_{\pm 1} = \frac{\mp \mathbf{e}_x - i \mathbf{e}_y}{\sqrt{2}}, \quad \mathbf{e}_0 = \mathbf{e}_z. \quad (7.26)$$

In equation (7.25), we introduced also the dual basis $\{\mathbf{e}^1, \mathbf{e}^0, \mathbf{e}^{-1}\}$ with

$$\mathbf{e}^m = (-1)^m \mathbf{e}_{-m} = \mathbf{e}_m^*, \quad (7.27)$$

$$\mathbf{e}_n \mathbf{e}^m = \mathbf{e}_n \mathbf{e}_m^* = \delta_{n,m}. \quad (7.28)$$

with the standard complex scalar product. The covariant components $q_m = (4\pi/3)^{1/2} \mathcal{R}_{1m}(\mathbf{r}) = r T_m^{(1)}(\hat{\mathbf{r}})$ are the regular solid harmonics \mathcal{R}_{1m} , that may be rewritten in terms of a spherical tensor $T_m^{(1)}(\hat{\mathbf{r}})$ of rank 1 with a unit vector $\hat{\mathbf{r}}$ [137]. The dipole coefficients for $U^{(1)}$ in equation (7.24) are then given by the spherical components of the vector \mathbf{r}_0

$$U^{(1)}(\mathbf{r}) = r \sum_{m=-1}^1 U_{1m}^{(1)} T_m^{(1)}(\hat{\mathbf{r}}), \quad U_{1m}^{(1)} = - \sum_{s=-1}^1 q_{0,s}^* \mathbf{K}_{ms}. \quad (7.29)$$

The second order contribution $U^{(2)}$ in equation (7.24) contains a product of two spherical tensors that can be simplified using the Clebsch-Gordan expansion

$$T_{m_1}^{(l_1)}(\hat{\mathbf{r}}) T_{m_2}^{(l_2)}(\hat{\mathbf{r}}) = \sum_{l=|l_1-l_2|}^{l_1+l_2} \sum_{m=-l}^l C(l_1 l_2 l; m_1 m_2 m) T_m^{(l)}(\hat{\mathbf{r}}), \quad (7.30)$$

with Clebsch-Gordan coefficients $C(l_1 l_2 l; m_1 m_2 m) = \langle l_1 m_1 l_2 m_2 | l m \rangle$ [93]. Hence, we can rewrite $U^{(2)}(\mathbf{r})$ as

$$U^{(2)}(\mathbf{r}) = \sum_{r,s=-1}^1 \frac{1}{2} (-1)^s q_r q_{(-s)} \mathbf{K}_{rs} = \frac{r^2}{2} \sum_{l=0}^2 \sum_{m=-2}^2 U_{lm}^{(2)} T_m^{(l)}(\hat{\mathbf{r}}), \quad (7.31)$$

with multipole coefficients that contain the matrix elements of \mathbf{K} in the spherical basis and Clebsch-Gordan coefficients

$$U_{lm}^{(2)} = \sum_{r,s=-1}^1 (-1)^s C(11l; r(-s)m) K_{rs}. \quad (7.32)$$

For the remaining radial part, one can use the results from the expansion of isotropic oscillator 7.4.1 in terms of the Stringari polynomials with $l = 0$. The total power in equation (7.12) of $U^{(2)}$ evaluates to

$$P(U^{(2)}) = 9 \frac{2 \operatorname{tr} \mathbf{K}^2 + \operatorname{tr} \mathbf{K}^2}{35 \operatorname{tr} \mathbf{K}^2} u^2, \quad u = \frac{\operatorname{tr} \mathbf{K}}{6} R^2 \sqrt{V}. \quad (7.33)$$

7.4.3 MAGNETIC ZEEMAN POTENTIAL OF AN ATOM CHIP

For the Zeeman potential (2.18) we use the finite wire model of the atom chip discussed in chapter 2.4. We use the multipole expansion (7.4) to evaluate the chip potential, as well as its harmonic approximation. For comparison, we extract also the multipoles of the cumulant in equation (7.9). The results are summarized in figure 7.3 where we show the relative fractional angular powers p_{nl} for the harmonic approximation $p_{nl}(U_{\text{ho}})$ (a), the full Zeeman potential $p_{nl}(U_z)$ (b) and the cumulant $p_{nl}(\theta)$ (c). In each case we have used the same number of basis functions, replacing the infinite sums in equation (7.4) and (7.9) with finite sums

$$U(\mathbf{r}) = \sum_{n=0}^{n_{\max}} \sum_{l=0}^{l_{\max}} \sum_{m=-l}^l U_{nlm} \langle \mathbf{r} | nlm \rangle, \quad (7.34)$$

$$\theta(\mathbf{r}) = \sum_{n=0}^{n_{\max}} \sum_{l=0}^{l_{\max}} \sum_{m=-l}^l \theta_{nlm} \langle \mathbf{r} | nlm \rangle. \quad (7.35)$$

The multipole expansion is performed at the position of the trap minimum \mathbf{r}_0 shifting the position vector in equation (7.24) by $\mathbf{r} = \mathbf{r}' + \mathbf{r}_0$. The latter implies a vanishing dipole component $U^{(1)}(\mathbf{r}, \mathbf{r}_0) = 0$ for the harmonic approximation. To calculate the cumulant, the potential is shifted by a positive constant to avoid artificial anomalies when taking the logarithm of the potential at the origin.

As discussed in the previous section 7.4.2, the anisotropic harmonic oscillator potential exhibits just two monopoles ($l = 0$) and one quadrupole contribution ($l = 2$) validated in subfigure 7.3 (a). For a Z-wire trap configuration, one finds particular multipoles in the dipole ($l = 1$) as well as in the octupole ($l = 3$), (b). The latter corresponds to the mostly cubic anharmonicity for distances closer to the chip surface when the strength of the magnetic induction diverges (cf. figure 2.5). The dipole moment reflects that the position of the trap minimum does not match the center of mass position of the trap. Hence, the Zeeman potential causes an additional momentum kick to the atomic distribution when applied as a magnetic lens for delta-kick collimation. Multipoles of higher order $l > 3$ are decaying rapidly. In addition, we find that the expansion of the cumulant converges more slowly for the given number of basis functions due to the logarithmic character of equation (7.9), see subfigure 7.3 (c).

7.4.4 LAGUERRE-GAUSSIAN DIPOLE POTENTIAL

The harmonic approximation of equation (7.2), corresponds to the spheroidal trapping potential in equation (7.21) with stiffness

$$k_{\perp} = \frac{4U_0}{w_0^2}, \quad k_{\parallel} = \frac{2U_0}{z_R^2}, \quad (7.36)$$

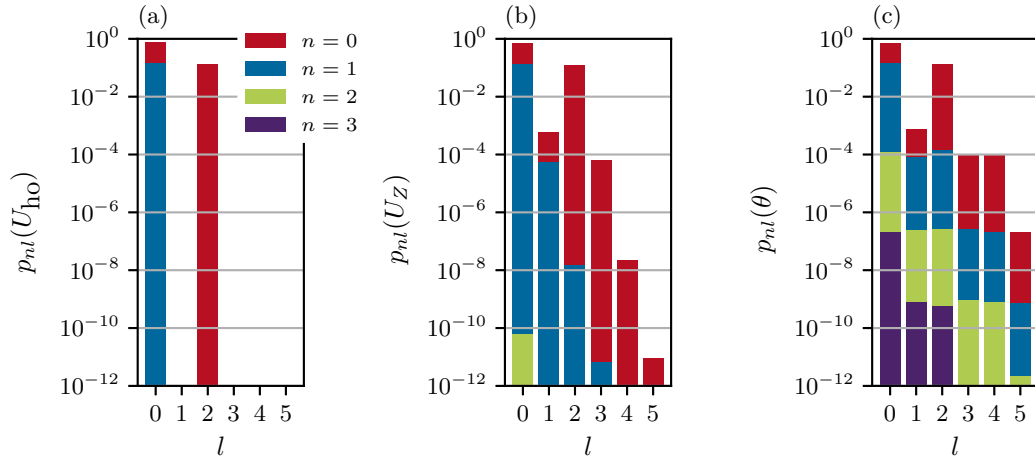


Figure 7.3: Multipole expansion of the magnetic chip trap potential. Relative powers $p_{nl}(U)$ versus angular momentum l of the Zeeman potential shown in Fig. 7.2. Different principle numbers: red $n = 0$, blue $n = 1$, green $n = 2$, purple $n = 3$. (a) harmonic approximation $p_{nl}(U_{ho})$, (b) Zeeman potential $p_{nl}(U_z)$, (c) cumulant $p_{nl}(\theta)$. We used $R = 40 \mu\text{m}$ and $n_{\text{max}} = 3$, $l_{\text{max}} = 5$ in equation (7.6), (7.4), and (7.9).

and the anisotropy $\alpha^2 = w_0^2/(2z_R)$ depending on the ratio of the minimal waist and the Rayleigh length.

We evaluate the relative powers for the optical dipole potential of a single Laguerre-Gaussian (cf. figure 7.1), in figure 7.4. We compare the harmonic approximation $p_{nl}(U_{ho})$ (7.21) (a), the dipole potential $p_{nl}(U_D)$ (7.1) (b) and the cumulant $p_{nl}(\theta)$ in equation (7.2) (c). In contrast to the Zeeman potential of the atom chip, the expansion of the cumulant is much more efficient than the multipole expansion of the potential (compare subfigures 7.4 (b) and 7.4 (c)). As the considered Rayleigh length $z_R \gg R$ is much larger than the regarded length scale, the spatial dependence of the exponent $\theta(\mathbf{r})$ almost matches the harmonic approximation 7.4.2, which is shown in subfigures 7.4 (a) and (c). Additional corrections to the harmonic potential in higher angular momentum components $l > 2$ are of the order 10^{-9} and smaller.

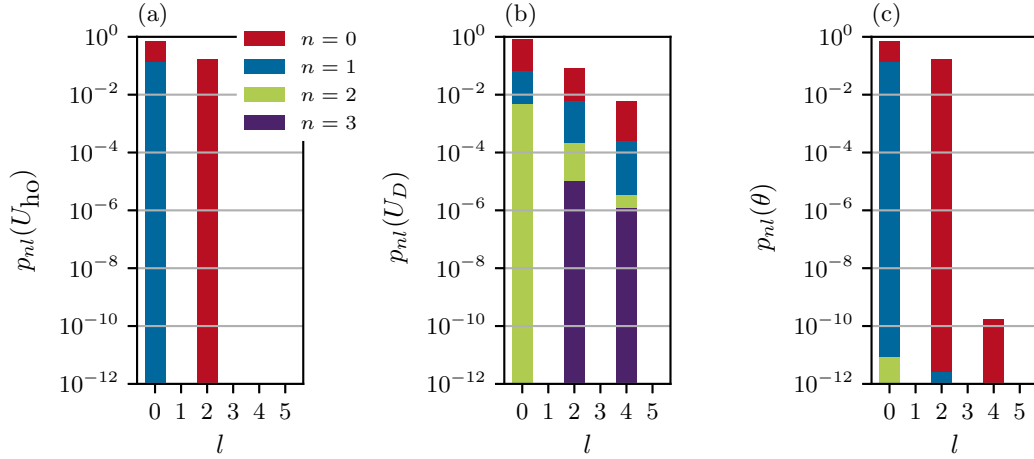


Figure 7.4: Multipole expansion of the optical dipole potential for a single Laguerre-Gaussian beam shown in figure 7.1. Relative powers $p_{nl}(U)$ versus angular momentum l . Different principle numbers: red $n = 0$, blue $n = 1$, green $n = 2$, purple $n = 3$. (a) harmonic approximation $p_{nl}(U_{ho})$, (b) optical dipole potential $p_{nl}(U_D)$, (c) cumulant $p_{nl}(\theta)$. We used $R = 40 \mu\text{m}$ and $n_{\max} = 3$, $l_{\max} = 5$ in equation (7.6), (7.4), and (7.9).

7.5 GROUND STATE DENSITY DISTRIBUTIONS

Besides the external trapping potentials, we are also interested in an efficient representation of a three-dimensional Bose-Einstein condensate. Therefore, we study the multipole expansion for ground-state density distributions

$$n(\mathbf{r}) = \sum_{n=0}^{\infty} \sum_{l=0}^{\infty} \sum_{m=-l}^l n_{nlm} \langle \mathbf{r} | nlm \rangle, \quad (7.37)$$

in some of the trapping potentials discussed in the previous section. Thereby, we discuss the strongly interacting Thomas-Fermi regime (4.39) as well as the exact numerical solution of the stationary Gross-Pitaevskii equation (4.37), that also covers the weakly interacting regime. For the Thomas-Fermi density, we expect an exact interpolation by the Stringaris, if the potential is of polynomial form.

Setting the interaction strength to $g = 0$ and considering a harmonic oscillator potential, one obtains a Gaussian distribution as the harmonic oscillator ground state [93]

$$n(\mathbf{r}) = n_0 e^{-\theta(\mathbf{r})}, \quad \theta(\mathbf{r}) = \sum_{j=1}^3 \frac{r_j^2}{2\sigma_j^2}. \quad (7.38)$$

The widths of the Gaussian correspond to the harmonic oscillator lengths $\sigma_j = \sqrt{\hbar/(M\omega_j)}$, $j = 1, 2, 3$ for the three spatial directions. For the latter, the cumulant expansion

$$\theta(\mathbf{r}) = -\log \frac{n(\mathbf{r})}{n_0} = \sum_{n=0}^{\infty} \sum_{l=0}^{\infty} \sum_{m=-l}^l \theta_{nlm} \langle \mathbf{r} | nlm \rangle, \quad (7.39)$$

is always of quadratic form which we have already covered in the previous section for the optical dipole potential of a single Laguerre-Gaussian beam.

We should note that in principle the Stringari as polynomials can exhibit negative values which is nonphysical when regarding positive-valued atomic densities. In order to avoid this anomaly, the Stringari polynomials should just be considered in the interval for coordinates such as $0 \leq r \leq R$ and for $n(\mathbf{r}) \geq 0$ in equation (7.37).

7.5.1 3D ISOTROPIC HARMONIC OSCILLATOR POTENTIAL

We consider the atomic density distributions in an isotropic harmonic oscillator potential (7.18). As the symmetry of the external potential determines the symmetry of the density, the condensate is interpolated by monopoles only. The efficiency of the interpolation with the Stringari polynomials depends on the actual radial shape $n(\mathbf{r}) = n(r)$, which will be determined by either the Thomas-Fermi density (4.39) or the stationary Gross-Pitaevskii equation (4.37). For the Gross-Pitaevskii density, we also evaluate the cumulant expansion to investigate the effect of different mean-field interactions.

THOMAS-FERMI DENSITY As the Thomas-Fermi density is directly proportional to the trapping potential, the interpolation is obtained by

$$n_{\text{TF}}(\mathbf{r}) = n_{000} \langle \mathbf{r} | 000 \rangle + n_{100} \langle \mathbf{r} | 100 \rangle, \quad (7.40)$$

two Stringari polynomials. Using the Thomas-Fermi approximation in its dimensionless form (cf. equation (4.44)) with $r' = r/r_{\text{TF}}$,

$$n_{\text{TF}}(\mathbf{r}) = \frac{15N}{8\pi} n'_{\text{TF}}(\mathbf{r}'), \quad (7.41)$$

we find for the three-dimensional inverted, isotropic Thomas-Fermi parabola

$$n'_{\text{TF}}(\mathbf{r}') = 1 - r'^2, \quad (7.42)$$

the dimensionless monopole coefficients

$$n'_{000} = \frac{4}{5} \sqrt{\frac{\pi}{3}}, \quad n'_{100} = \frac{4}{5} \sqrt{\frac{\pi}{7}}. \quad (7.43)$$

Figure 7.5 depicts the corresponding two relative angular powers $p_{n0}(n)$ which were obtained numerically. The benchmark test shows that errors in higher-order radial coefficients are of the order $< 10^{-12}$. Figure 7.6 presents the interpolation of the Thomas-Fermi density by the Stringari polynomials. As noted before, the polynomials are regarded within the region of interest for the position coordinates $\{\mathbf{r}_j\} \in V_{\text{TF}}$.

GROSS-PITAEVSKII DENSITY For the Gross-Pitaevskii density, we use different particle numbers to study the behavior of the radial expansion coefficients in different regimes. The n_{nlm} 's in equation (7.37) are obtained using the method of least-squares (7.15) replacing the target potential with the discrete Gross-Pitaevskii target density $n_t(\mathbf{r}_j)$. In contrast to the Thomas-Fermi density the radius R of the spherical integration volume in equation (7.6) is not known a priori. Therefore, we are minimizing the least-square error $\epsilon(R)$ with respect to a variable parameter R

$$\min \epsilon(R) = \|S(R)\mathbf{n} - \mathbf{n}_t\|^2, \quad (7.44)$$

for a fixed number of basis functions. The monopole coefficients p_{n0} for the isotropic Gross-Pitaevskii density are depicted in figure 7.7 on a semi-logarithmic scale for $n_{\text{max}} = 14$ basis functions. For small particle numbers 7.7 (a), the coefficients are declining exponentially for $n > 6$

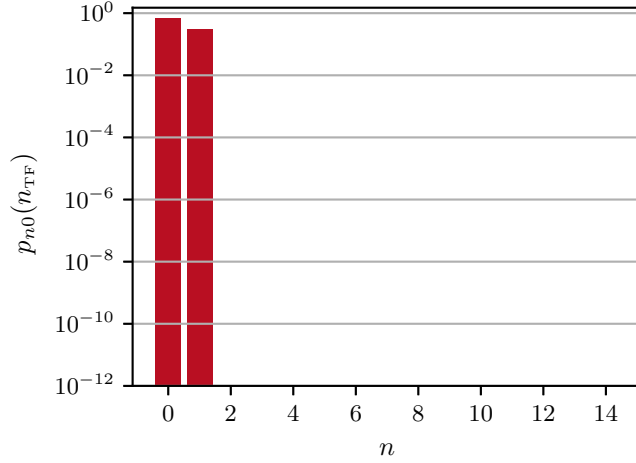


Figure 7.5: Monopole coefficients $p_{n0}(n_{\text{TF}})$ of the Thomas-Fermi density with $n_{\text{max}} = 14$ in an isotropic harmonic oscillator potential (7.18).

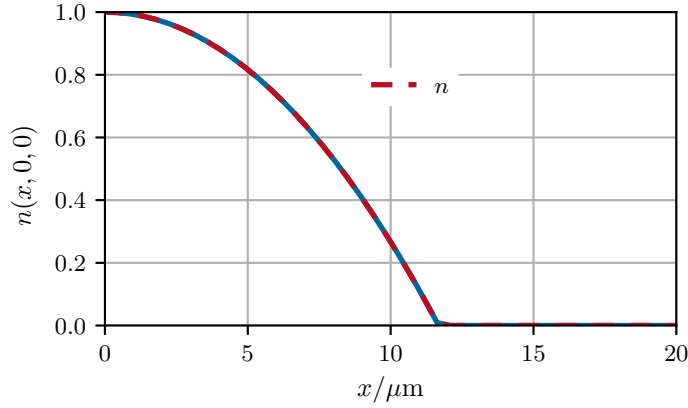


Figure 7.6: Cross-section of the scaled Thomas-Fermi density $n_{\text{TF}}(x, 0, 0)$ (blue —). Interpolation of the density with Stringari polynomials (red - -). Parameters: trap frequency $\nu = 22.1$ Hz, Thomas-Fermi radius $r_{\text{TF}} = 11.7 \mu\text{m}$, chemical potential $\mu_{\text{TF}}/h = 287$ Hz, particle number $N = 10^5$.

whereas the magnitude of the tenth coefficient is $p_{10,0} < 10^{-6}$. Entering the intermediate and strong interacting regime, the decline in magnitude becomes more irregular, as the Gaussian-like shape of the density is modified towards a polynomial shape. In (b), the most contributions to the polynomial expansion are within the first five coefficients, and in (c) within the first three. The latter reflects the transition to the pure quadratic Thomas-Fermi regime. However, we also recognize that the magnitude of the expansion coefficients does not converge to the same level as in the low interacting regime. In contrast to the Thomas-Fermi solution, the density also contains high-energetic modes at the Thomas-Fermi radius, whose interpolation requires a lot of Stringari polynomials. As we are interested in good interpolation in the region of significant density, we introduce a cutoff

$$p_c = \frac{|n_{nlm}|^2}{P(n)} = 10^{-6}, \quad P(n) = \sum_{nlm} |n_{nlm}|^2, \quad (7.45)$$

which disregards some of the highly energetic modes. In figure 7.8, we plot the corresponding expansion in terms of the polynomials which matches the Gross-Pitaevskii density quite well. We

also use the Stringari polynomials with a reduced number of basis functions, neglecting coefficients smaller than the chosen cutoff.

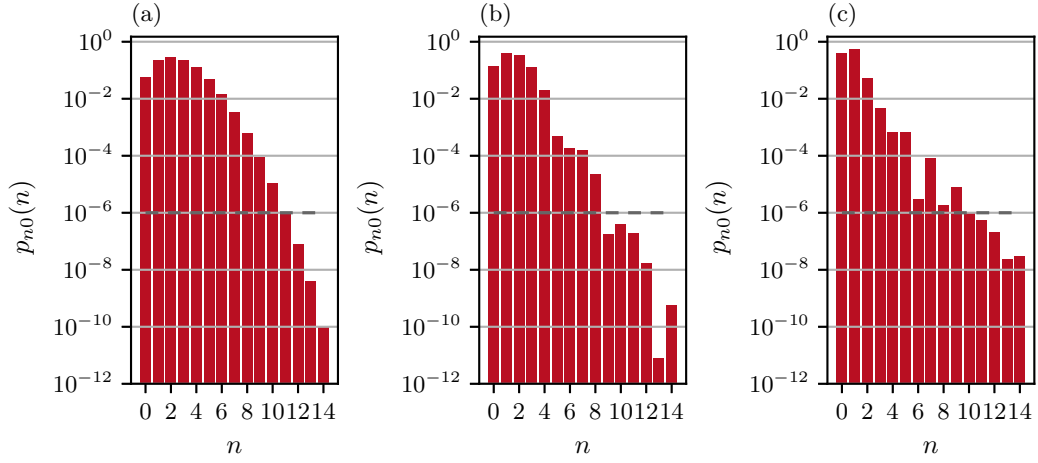


Figure 7.7: Multipole expansion of the Gross-Pitaevskii density $n(\mathbf{r})$ for the isotropic harmonic oscillator (7.18). Monopole coefficients $p_{n0}(n)$ versus principle number n up to $n_{\max} = 14$. Parameters: Trap frequency $\nu = 22.1$ Hz, particle number, chemical potential, aperture radius R : (a) $N = 10$, $\mu/h = 35.6$ Hz, $R = 9.21 \mu\text{m}$; (b) $N = 1000$, $\mu/h = 55.8$ Hz, $R = 8.95 \mu\text{m}$; (c) $N = 10^5$, $\mu/h = 289.2$ Hz, $R = 14.1 \mu\text{m}$. For the reconstruction of the density in figure 7.8 we mark the cutoff $p_c = 10^{-6}$ (gray - - -).

Besides the multipole coefficients for the density, we also look into the cumulant expansion, equation (7.9), for which we expect a faster convergence in the low-interacting limit. Figure 7.9 (a) confirms that the density distribution is more of Gaussian shape, as the cumulant expansion almost terminates for monopole powers $n > 3$. For larger particle numbers, subfigures (b) and (c), the cumulant expansion works quite efficiently as the polynomial series converges faster as in figure 7.7. Cross-sections of the cumulant and the interpolation by the Stringari polynomials are shown in figure 7.10.

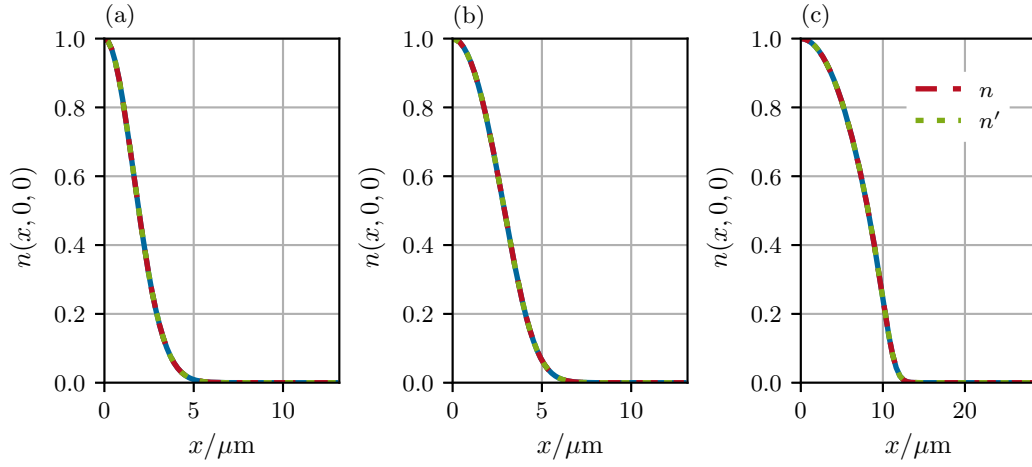


Figure 7.8: Cross-sections of the scaled Gross-Pitaevskii ground-state density distribution $n(x, 0, 0)$ versus Cartesian coordinate x in a three-dimensional isotropic harmonic oscillator potential. Gross-Pitaevskii solution (blue —). Interpolation of the density with Stringari polynomials $n(\mathbf{r})$ (7.37) (red - -) and alternatively with the cutoff $p_c = 10^{-6} n'(\mathbf{r})$ (green ····). Parameters as in figure 7.7.

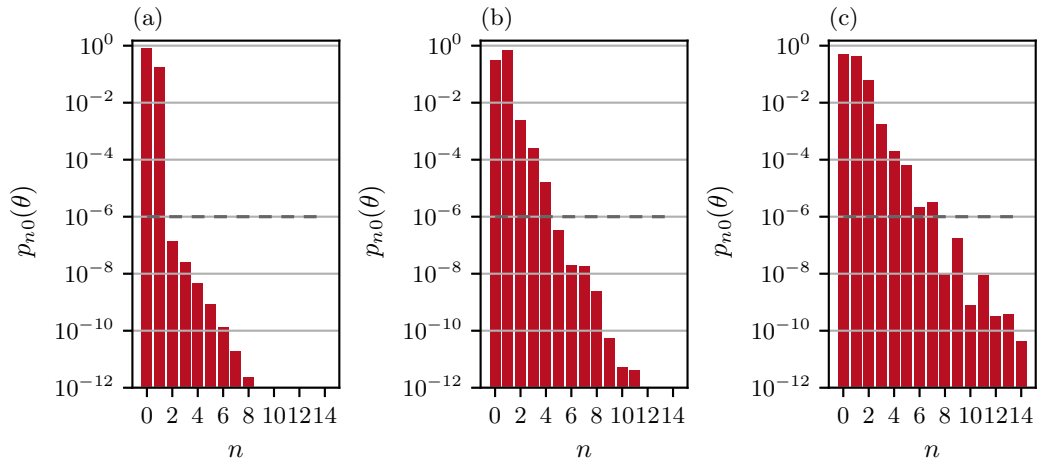


Figure 7.9: Multipole expansion of the isotropic Gross-Pitaevskii cumulant $\theta(\mathbf{r})$ (7.39). Monopole coefficients $p_{n0}(\theta)$ versus principle number n with $n_{\max} = 14$. For the reconstruction of the cumulant in figure 7.10 we mark the cutoff $p_c = 10^{-6}$ (gray - -). Parameters as in figure 7.7.

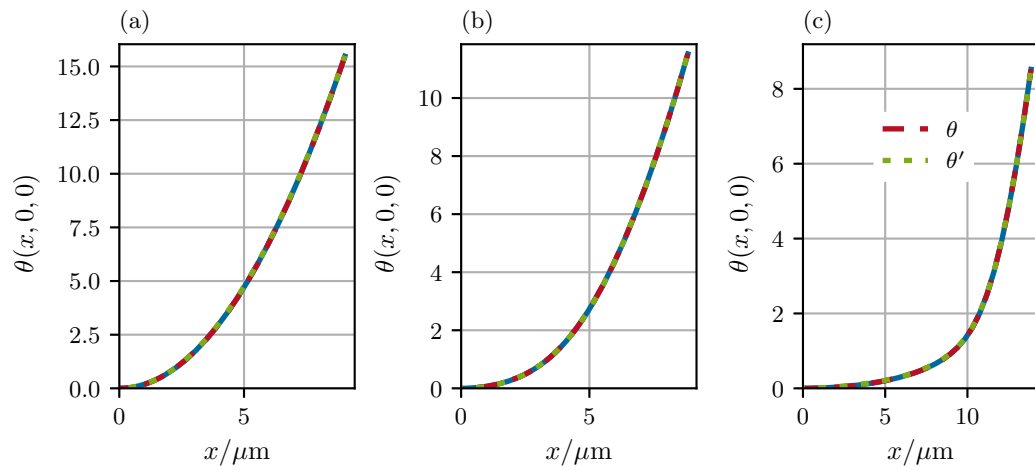


Figure 7.10: Cross-sections of the cumulant of the isotropic ground-state density distribution $\theta(x, 0, 0)$ versus Cartesian coordinate x in a three-dimensional harmonic oscillator potential. Cumulant evaluated up to the aperture radius R . Gross-Pitaevskii solution (blue —), interpolation of the cumulant with Stringari polynomials θ (red - -) and alternatively with the cutoff $p_c = 10^{-6}$ θ' (green ·····). Parameters as in figure 7.7.

7.5.2 3D ANISOTROPIC HARMONIC OSCILLATOR POTENTIAL

We face two major obstacles when interpolating an anisotropic density distribution by the Stringari polynomials. First, it is not clear what the optimal radius R in equation (7.6) is. Second, the density should be a positive valued function. To cover both problems as best as possible, we consider a coordinate transformation as in equation (4.42) that rescales Thomas-Fermi wave function to an isotropic s-wave.

For a non-Thomas-Fermi-like distribution, we evaluate the covariance matrix

$$\Sigma_{\mathbf{r}} = \langle (\mathbf{r} - \mathbf{r}_0) \otimes (\mathbf{r} - \mathbf{r}_0) \rangle, \quad \mathbf{r}_0 = \langle \mathbf{r} \rangle = \int \mathbf{r} n(\mathbf{r}) d^3r, \quad (7.46)$$

which contains the information of the quadrupole moments

$$n_{2m} = \int Y_{2m}^*(\vartheta, \varphi) n(\mathbf{r}) r^2 d^3r. \quad (7.47)$$

For the positive, semi-definite matrix $\Sigma_{\mathbf{r}}$ we do a Cholesky decomposition of the form

$$\Sigma_{\mathbf{r}} = \mathbf{C}\mathbf{C}^{\top}, \quad \mathbf{C} = \mathbf{Q}\sigma. \quad (7.48)$$

The matrices \mathbf{Q} and σ are defined by the eigenvalue equation

$$\Sigma\mathbf{Q} = \mathbf{Q}\sigma^2. \quad (7.49)$$

The matrix \mathbf{C} and the expectation value \mathbf{r}_0 define the required affine coordinate transformation

$$\boldsymbol{\zeta} = \mathbf{C}^{-1}(\mathbf{r} - \mathbf{r}_0), \quad (7.50)$$

that we use to evaluate a multipole expansion of the form

$$n(\mathbf{r}) = \sum_{n=0}^{\infty} \sum_{l=0}^{\infty} \sum_{m=-l}^l n_{nlm} S_{nlm}(\boldsymbol{\zeta}), \quad (7.51)$$

$$\theta(\mathbf{r}) = \sum_{n=0}^{\infty} \sum_{l=0}^{\infty} \sum_{m=-l}^l \Theta_{nlm} S_{nlm}(\boldsymbol{\zeta}), \quad (7.52)$$

where the Stringari polynomials are evaluated with respect to the new coordinates $\boldsymbol{\zeta}$ and new coefficients n_{nlm} , Θ_{nlm} . We define also the corresponding spectral powers

$$\mathfrak{p}_{nl}(n) = \sum_{m=-1}^l \frac{|n_{nlm}|^2}{\mathfrak{P}(n)}, \quad \mathfrak{P}(n) = \sum_{nlm} |n_{nlm}|^2, \quad (7.53)$$

$$\mathfrak{p}_{nl}(\theta) = \sum_{m=-1}^l \frac{|\Theta_{nlm}|^2}{\mathfrak{P}(\theta)}, \quad \mathfrak{P}(\theta) = \sum_{nlm} |\Theta_{nlm}|^2, \quad (7.54)$$

THOMAS-FERMI DENSITY As a benchmark test, we investigate the Thomas-Fermi density in an anisotropic oscillator with cylindrical symmetry, which we discussed in paragraph 7.4.2. For the anisotropy we use $\alpha = 2$. Applying the coordinate transformation in equation (4.42) or equation (7.50), we obtain the angular powers $\mathfrak{p}_{nl}(n_{\text{TF}})$ shown in figure 7.11. As the multipole expansion is performed in the scaled reference frame (7.51), where the ellipsoid is rescaled to a sphere, we expect only the monopoles that were presented in figure 7.5 and in equation (7.43). Indeed, we find good agreement with the isotropic Thomas-Fermi density as the quadrupoles are $\mathfrak{p}_{n2}(n_{\text{TF}}) < 10^{-9}$ as

displayed in figure 7.11. Using the monopoles n_{n00} and the quadrupoles within the transformation matrix \mathbf{C} , one can reconstruct the original oblate-shaped Thomas-Fermi density as depicted in figure 7.12.

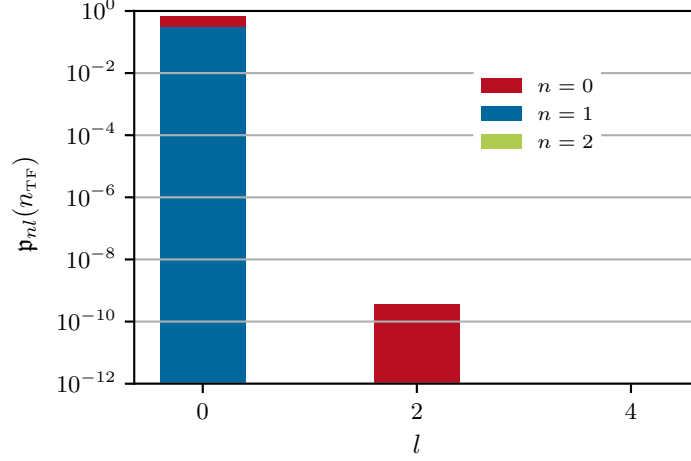


Figure 7.11: Multipole expansion of the scaled Thomas-Fermi density $n_{TF}(\mathbf{r})$ for the spheroidal harmonic oscillator (7.21) with anisotropy $\alpha = 2$. Relative angular powers $p_{nl}(n_{TF})$ versus principle number n . Different principle numbers: red $n = 0$, blue $n = 1$, green $n = 2$. $n_{\max} = 14$, $l_{\max} = 4$, $R = 6.6 \mu\text{m}$.

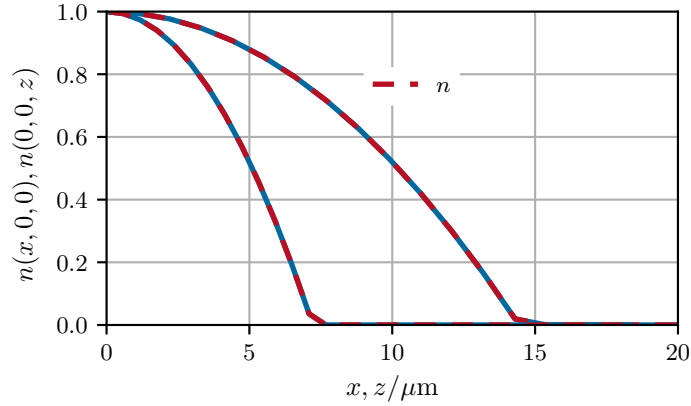


Figure 7.12: Cross-sections of the scaled Thomas-Fermi density $n_{TF}(x, 0, 0)$, $n_{TF}(0, 0, z)$ (blue —) versus Cartesian coordinates x , z in a spheroidal harmonic oscillator (7.21). Interpolation of the density with Stringari polynomials $n(\mathbf{r})$ (7.37) (red - - -). Parameters: $\alpha = 2$, Thomas-Fermi radii $x_{TF} = y_{TF} = 14.4 \mu\text{m}$, $z_{TF} = 7.2 \mu\text{m}$, particle number $N = 10^5$, chemical potential $\mu_{TF}/h = 304 \text{ Hz}$.

GROSS-PITAEVSKII DENSITY As in the previous section, we study the Gross-Pitaevskii density for different particle numbers. In addition, we compare the multipole expansion of the density with the multipole expansion of the cumulant. In both cases, the evaluated expansion coefficients are in the scaled reference frame defined by equation (7.51). In contrast to the ellipsoidal Thomas-Fermi density, we observe non-negligible quadrupole contributions in the relative angular powers for the low as well as for the high interacting regime, which is presented in figure 7.13. For low particle numbers, subfigure (a), the angular powers $\mathfrak{p}_{n0}(n)$, $\mathfrak{p}_{n2}(n)$, $\mathfrak{p}_{n4}(n)$ are decaying exponentially with respect to the principle number n as we already stated in the isotropic case. Increasing the angular momentum for a fixed value of n , the magnitudes of the $\mathfrak{p}_{nl}(n)$ decrease by roughly 1.5-2 orders of magnitude. The angular momentum dependence decreases for increasing interactions as shown in the subfigures 7.13 (b), (c). In particular, the powers $\mathfrak{p}_{n4}(n) < 10^{-6}$, are emphasizing the change of the Gross-Pitaevskii density towards the Thomas-Fermi shape. Moreover, the spectrum of the monopoles $\mathfrak{p}_{n0}(n)$ in the rescaled reference frame exhibits the same structure as in the isotropic case (cf. figure 7.7), reflecting again the high-energetic modes in the Gross-Pitaevskii density that require a large number of Stringari polynomials. Nevertheless, we are able

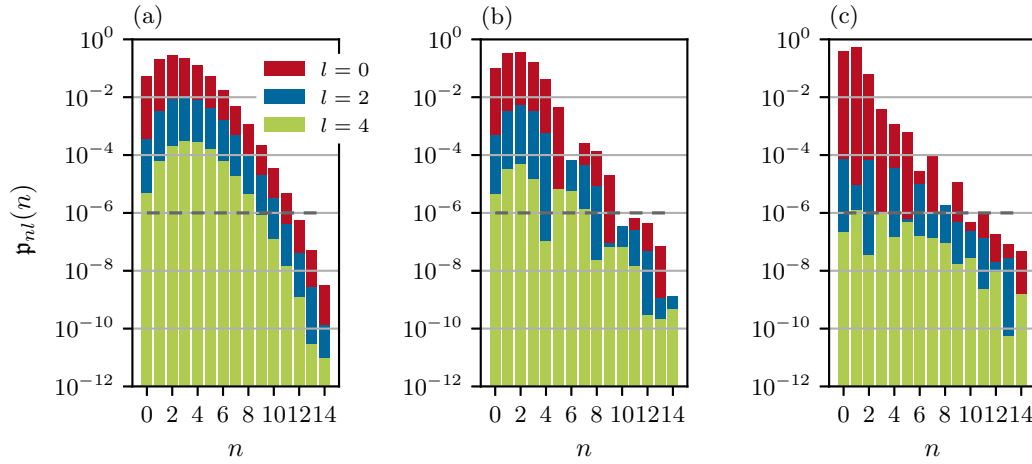


Figure 7.13: Multipole expansion of the scaled Gross-Pitaevskii density $n(\mathbf{r})$ for the spheroidal harmonic oscillator (7.21) with anisotropy $\alpha = 2$. Relative angular powers $\mathfrak{p}_{nl}(n)$ versus principle number n . Different angular momenta: red $l = 0$, blue $l = 2$, green $l = 4$ with $n_{\max} = 14$, $l_{\max} = 4$. For the reconstruction of the density in figure. 7.14 we mark the cutoff $p_c = 10^{-6}$. Particle number, chemical potential, aperture radius: Particle number, chemical potential, aperture radius: (a) $N = 10$, $\mu/h = 37.2$ Hz, $R = 11.6$ μm ; (b) $N = 1000$, $\mu/h = 60.6$ Hz, $R = 12.1$ μm ; (c) $N = 10^5$, $\mu/h = 307$ Hz, $R = 17.6$ μm .

to interpolate the ground-state density distributions also in the anisotropic harmonic oscillator as depicted in figure 7.14. In particular, we can neglect modes with $l = 4$ for the condensate with large particle numbers to obtain a good approximation with the Stringari polynomials. The results for the anisotropic cumulant expansion are presented in the figures 7.15 and 7.16. The monopoles $\mathfrak{p}_{n0}(\theta)$ exhibit again the same features as for the isotropic density, while the cumulant expansion works more efficiently describing the low-interacting regime. The latter is well described by just three multipole coefficients Θ_{000} , Θ_{020} and Θ_{200} , subfigure 7.15 (a). In contrast to the direct multipole expansion of the density, the cumulant expansion contains significant angular powers $\mathfrak{p}_{n4}(\theta)$ which needs to be considered for the polynomial interpolation.

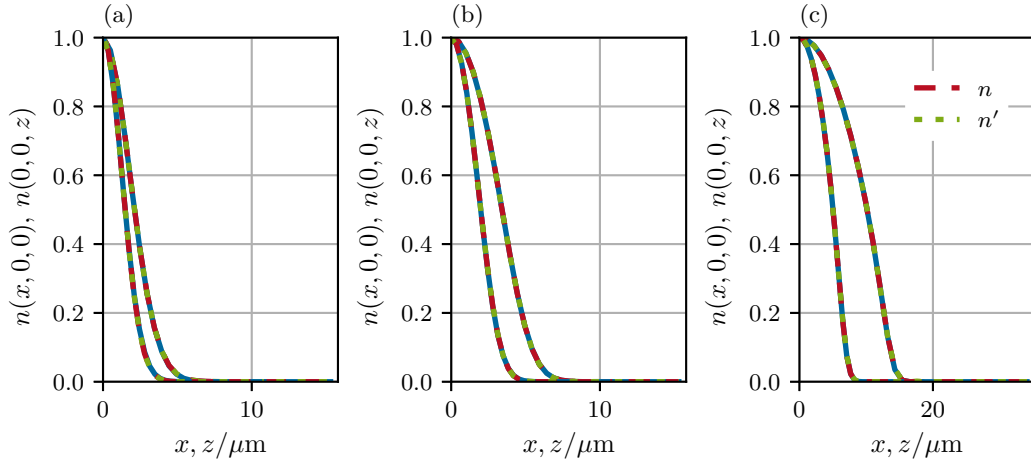


Figure 7.14: Cross-sections of the scaled ground-state density distributions $n(x, 0, 0)$, $n(0, 0, z)$ versus Cartesian coordinates x , z in a spheroidal harmonic oscillator (7.21). Gross-Pitaevskii solution (blue —). Interpolation of the density with Stringari polynomials $n(\mathbf{r})$ (7.37) (red - - -), alternatively with the cutoff $n'(\mathbf{r})$ at $p_c = 10^{-6}$ (green ····). Parameters as in figure 7.13.

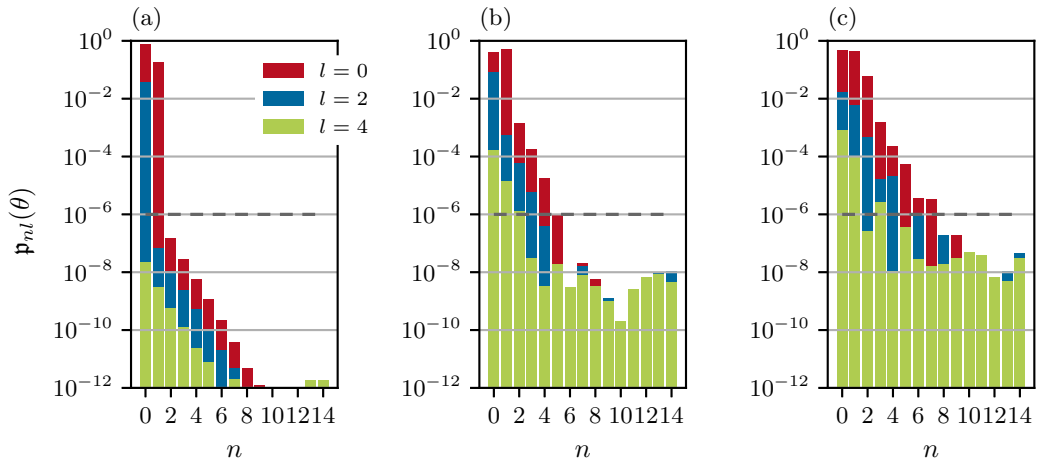


Figure 7.15: Multipole expansion of the Gross-Pitaevskii cumulant $\theta(\mathbf{r})$ (7.39) for the spheroidal harmonic oscillator (7.21) with anisotropy $\alpha = 2$. Relative angular powers $p_{nl}(\theta)$ versus principle number n . Different angular momenta: red $l = 0$, blue $l = 2$, green $l = 4$ with $n_{\max} = 14$, $l_{\max} = 4$. For the reconstruction of the cumulant in figure 7.16 we mark the cutoff $p_c = 10^{-6}$ (gray - - -). Parameters as in figure 7.13.

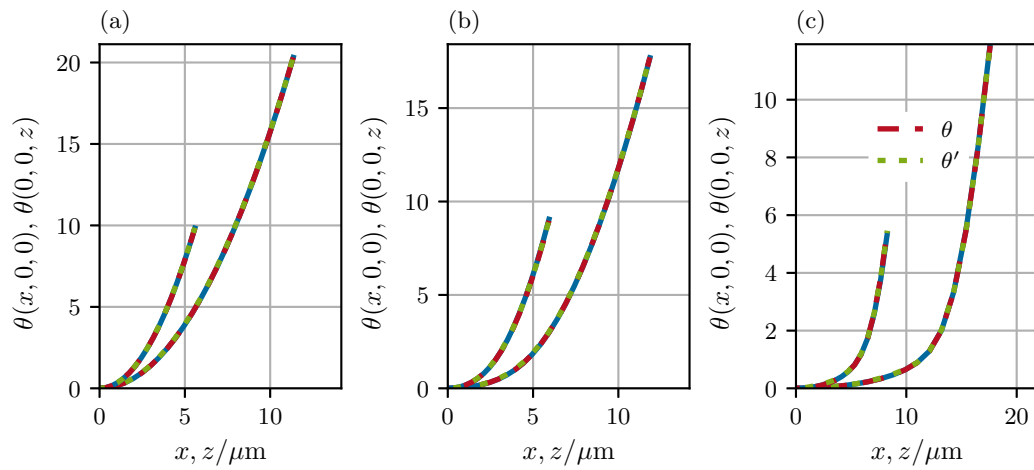


Figure 7.16: Cross-section of the cumulants $\theta(x, 0, 0)$, $\theta(0, 0, z)$ of the ground state density distribution versus Cartesian coordinates x , z in a spheroidal harmonic oscillator (7.21). Cumulant evaluated up to the aperture radius R . Gross-Pitaevskii solution (blue —). Interpolation of the cumulant with Stringari polynomials $\theta(\mathbf{r})$ (7.9) (red - - -), alternatively with the cutoff $\theta'(\mathbf{r})$ at $\mathfrak{p}_c = 10^{-6}$ (green ·····). Parameters as in figure 7.13.

8 COLDEST CLOUDS IN UNIVERSE

The method of delta-kick collimation limits [35] the spatial extent of a freely expanding Bose-Einstein condensate. Hence, it allows the detection of the atoms in the diluted gas even after several seconds in an interferometer. Analogous to ray optics with thin lenses in the paraxial approximation, a short-pulsed parabolic potential can act as a matter-wave lens in the time domain. An infinite focal length, also known as collimation, reduces the momentum width of the atomic cloud. In the drop tower ZARM [37] and on the ISS [33] the condensates were “cooled” to record temperatures in the pK regime, providing the best sources for atom-interferometry with long expansion times.

In this chapter, we analyze a delta-kick collimation sequence similar to the experiment in [37]. We use full (3+1)d Gross-Pitaevskii simulations in anharmonic chip trap potentials [138]. We compare these results to the ideal scaling approximation. Deviations are quantified by applying a multipole expansion to density variations, Bogoliubov excitations, and phases. For the latter, we can construct the Seidel diagram [4] for matter waves indicating the main aberrations of the optical system.

8.1 DELTA-KICK COLLIMATION USING ADAPTIVE SCALES

We start this chapter by illustrating the delta-kick collimation sequence using the scaling approximation in the Thomas-Fermi regime, which was introduced in chapter 4.4.1. The sequence in the time domain is sketched in figure 8.1. It consists of the first time of flight t_1 , the application of a

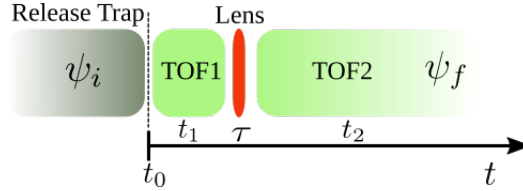


Figure 8.1: Illustration of delta-kick collimation sequence: Initial state in release trap, first time of flight t_1 , application of matter-wave lens τ , imaging after the second time of flight t_2 .

harmonic, parabolic lens τ , and the second time of flight t_2 . Within this sequence, one needs to solve the differential equations (4.72) for the scales $\Lambda(t) = \text{diag}(\lambda_1, \lambda_2, \lambda_3)$,

$$\ddot{\lambda}_i = \frac{\omega_i^2}{\lambda_i \lambda_1 \lambda_2 \lambda_3}, \quad 0 \leq t \leq t_1, \quad (8.1)$$

$$\ddot{\lambda}_i + \omega_{l,i}^2 \lambda_i = \frac{\omega_0^2}{\lambda_i \lambda_1 \lambda_2 \lambda_3}, \quad t_1 \leq t \leq t_1 + \tau, \quad (8.2)$$

$$\ddot{\lambda}_i = \frac{\omega_i^2}{\lambda_i \lambda_1 \lambda_2 \lambda_3}, \quad t_1 + \tau \leq t \leq t_2. \quad (8.3)$$

where we have assumed that the trapping matrix of the release trap $\Omega(0) = \text{diag}(\omega_1, \omega_2, \omega_3)$ and the trapping matrix of the lens $\Omega_l = \text{diag}(\omega_{l,1}, \omega_{l,2}, \omega_{l,3})$ are aligned to each other. Further, the lens is turned on and off immediately in form of a box-shaped pulse. Assuming that the lensing time τ is small, $\tau \omega_{l,i} \ll 1$, $\tau \ll t_1$, compared to the timescale of the angular frequencies of

the lens, and to the first time of flight, the right-hand side of equation (8.2) is approximately of constant value. During this impact approximation, the density of condensate is unaltered, while we change its superfluid velocity rapidly (4.71). Hence equation (8.2) simplifies to

$$\ddot{\lambda}_i + \omega_{i,l}^2 \lambda_i = c_i, \quad (8.4)$$

$$\dot{\lambda}_i(t) = \dot{\lambda}_{i,t_1} \cos(\omega_{l,i}t) - \omega_{l,i} \left(\lambda_{i,t_1} - \frac{c_i}{\omega_{l,i}^2} \right) \sin(\omega_{l,i}t), \quad (8.5)$$

a harmonic oscillator equation with $\lambda_i(t_1) = \lambda_{i,t_1}$, constant lens frequency $\omega_{l,i}$ and inhomogeneity $c_i = \omega_{i,0}^2 / (\lambda_i \lambda_1 \lambda_2 \lambda_3)$ that depends on the scales of the first time of flight and the angular frequencies of the release trap.

For optimal collimation, we like to reduce the velocity spread. In terms of the scaling solutions and the applied phase space transformation (3.32) that means that the velocities, $\dot{\lambda}_i = 0$, are vanishing (cf. equation (B.11)). The angular frequencies of the lens allow (2.4), collimation in just two spatial directions, $i = 2, 3$ (y, z). Hence, we look for minimizing the square of the velocity

$$\mathbf{v}^2(t) = \dot{\lambda}_2^2 + \dot{\lambda}_3^2, \quad (8.6)$$

with respect to time for an optimal lens time estimator. In figure 8.2, we show the evolution of the time-derivative $d\mathbf{v}^2/dt$ of the squared velocities (8.6) during the evolution in the harmonic oscillator potential. The root of the curve corresponds to the optimal lensing time. We use the angular frequencies for ^{87}Rb in the tables 2.2 and 2.4 for the initial release trap and the harmonic approximation of the lens. We estimate the lens time to be $\tau_\lambda = 2.716$ ms for a time of flight $t_1 = 80$ ms.

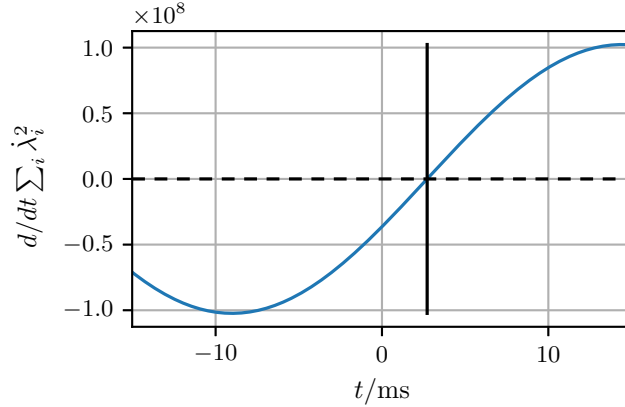


Figure 8.2: Lens time estimation using the scaling equations (8.1), (8.2) for cylindrical symmetric traps. The root of the function (8.6) corresponds to minimal velocity spread.

Figure 8.3 shows the time evolution of the Thomas-Fermi size $\mathbf{r}_{\text{TF}}(t) = \Lambda(t)\mathbf{r}_{\text{TF}}$ and the superfluid velocity \mathbf{v}_λ (4.71) evaluated at the Thomas-Fermi radius of the condensate during the whole delta-kick collimation sequence. When we apply the lens at $t = 80$ ms, the expansion in the y as well as in the z -direction is dramatically reduced. The velocity drops from $\mathbf{v}_{\lambda,\text{TF}} = (0.62, 1.42, 1.32)$ mm s $^{-1}$ to $\mathbf{v}_{\lambda,\text{TF}} = (0.55, 0.01, -0.003)$ mm s $^{-1}$ while the size just increases from $\mathbf{r}_{\text{TF}} = (70.9, 116.2, 108.8)$ μm to $\mathbf{r}_{\text{TF}} = (183.5, 119.8, 109.5)$ μm by $\approx 1 - 3$ μm during the second time of flight of $t_2 = 200$ ms in the lensed directions. Without the matter-wave lens, the size of the condensate would expand linearly in time as $\lambda_i(t) \approx a_i t$, constants a_i , for long expansion times, $t \rightarrow \infty$ [79]. The latter is shown in 8.4, where we depict the scaling solutions

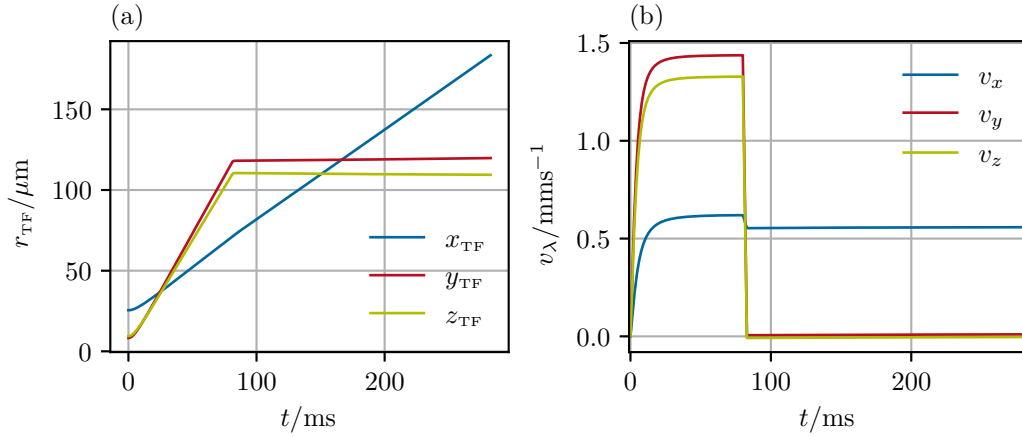


Figure 8.3: Delta-kick collimation shown for the Thomas-Fermi scaling approximation. (a) Initial size at t_0 , $\mathbf{r}_{\text{TF}} = (25.5, 8.3, 9.4) \mu\text{m}$. After time of flight $t_1 = 80$ ms, $\mathbf{r}_{\text{TF}} = (70.9, 116.2, 108.8) \mu\text{m}$. Final size after second time of flight $t_2 = 200$ ms, $\mathbf{r}_{\text{TF}} = (183.8, 119.8, 109.5) \mu\text{m}$. (b) Superfluid velocity \mathbf{v}_λ at $\mathbf{r} = \mathbf{r}_{\text{TF}}$ before matter-wave lens $\mathbf{v}_{\lambda, \text{TF}} = (0.62, 1.42, 1.32) \text{mm s}^{-1}$, after matter-wave lens $t_1 + \tau$, $\tau = 2.716$ ms, $\mathbf{v}_{\lambda, \text{TF}} = (0.55, 0.01, -0.003) \text{mm s}^{-1}$.

$\lambda_i(t)$ for ballistic expansion with $t_1 = 500$ ms. The double-logarithmic scales and the linear curve fitting with coefficients $\mathbf{a} = (0.84, 0.99, 0.98)$ confirm the linear time dependence.

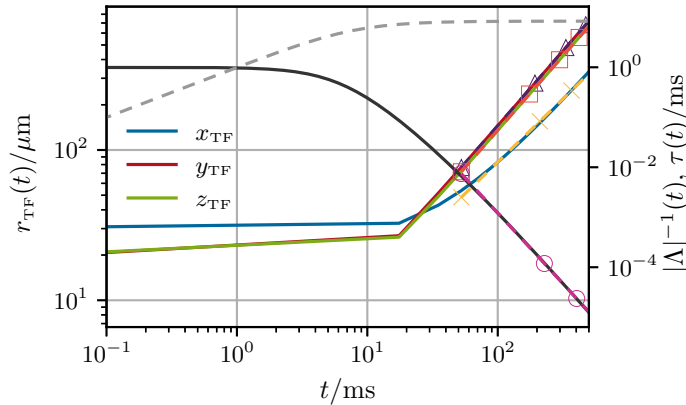


Figure 8.4: Time evolution of the Thomas-Fermi size \mathbf{r}_{TF} (red, blue, green —) for long expansion times. Results of the linear fit: $\mathbf{a} = (0.84, 0.99, 0.98)$, marked as - - - lines. We also display $|\Lambda(t)|^{-1}$ (black —) and the time $\tau(t)$ 6.21 (gray - - -).

We conclude this section by showing the wavefronts of the condensate during the delta-kick collimation protocol in figure 8.5. The wavefronts are surfaces of constant phase $\phi(\mathbf{r}, t) = \text{const.}$. According to equation (4.70), the Thomas-Fermi wavefronts are ellipsoids whose curvatures and orientations are determined by the matrix $\dot{\Lambda}^{-1}$. During the free expansion, the curvature gets more shallow. After the collimation when $\dot{\Lambda} \rightarrow 0$, one finds a planar surface with vanishing curvature analogous to classical (2+1)d ray optics.

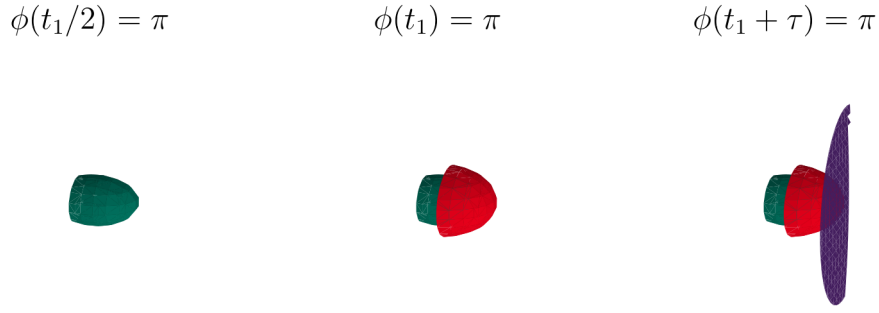


Figure 8.5: Isosurfaces of the three-dimensional wavefront $\phi(\mathbf{r}, t) = \pi$ during the free expansion of the condensate at $t = 40$ ms (green), $t = 80$ ms (red) and after delta-kick collimation (purple) (from left to right).

8.2 CONDENSATE IN THE RELEASE TRAP

In this section, we investigate the state of the condensate in the release trap (cf. section 2.4.4). From our multipole analysis in chapter 7, we have characterized the anharmonic contributions in the Zeeman potential in terms of different angular momentum states and radial polynomials, the Stringari (7.6) polynomials. Now, we focus on the physical impact on the condensates density distribution as well as on the collective excitations using the Bogoliubov theory from section 4.5. For all our three-dimensional simulations that do not exhibit any symmetries, we use a Fourier series representation and the method of Fast Fourier transform (FFT) on a discretized Cartesian grid. We provide the details about the Fourier representation of the fields and the numerical treatment of the Bogoliubov-de Gennes equation in the appendices F and H.2.

8.2.1 GROUND STATE DENSITY DISTRIBUTION

We obtain the ground state densities of the condensate by solving the stationary Gross-Pitaevskii equation (4.37) within the Zeeman potential U_z (2.18) of the release trap and its harmonic approximation (2.25). We choose a large condensate with $N = 10^5$ ^{87}Rb atoms which correspond to the experimental parameter used in the QUANTUS drop tower experiments [37, 38]. One- and two-dimensional cross-sections of the density $n(\mathbf{r})$ in the release trap are shown in figure 8.6. To study the stationary density deviations, we investigate the normalized, $\int n(\mathbf{r}) d^3r = 1$, equilibrium densities

$$\delta n(\mathbf{r}) = n(\mathbf{r}) - n_{\text{HO}}(\mathbf{r}), \quad (8.7)$$

in the release trap and the corresponding harmonic approximation. The density deviations are depicted in figure 8.7. Within the spatial extent of the atomic cloud, we find maximal deviations of $\max[\delta n(\mathbf{r})] \approx 0.01\%$. Moreover, we analyze the shape deviations in terms of our multipole analysis

$$\delta n(\mathbf{r}) = \sum_{n=0}^{\infty} \sum_{l=0}^{\infty} \sum_{m=-l}^l \delta n_{nlm} S_{nlm}(\zeta), \quad \zeta = C^{-1}(\mathbf{r} - \mathbf{r}_0). \quad (8.8)$$

If the anharmonicities of the trap were applied instantaneously, the Stringari polynomials would approximately describe the excited eigenmodes of the perturbation in the hydrodynamic regime (cf. sections 4.4.2 and 4.5) underlining the physical motivation of using these basis functions.

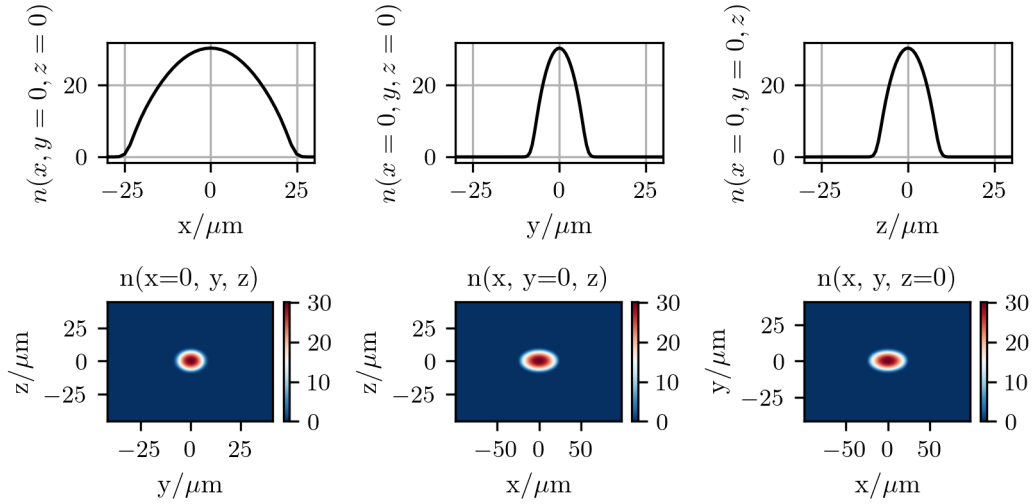


Figure 8.6: One -and two-dimensional cross sections of the ground state density distribution $n(\mathbf{r})$ in the release trap Zeeman potential 2.4.4. Particle number $N = 10^5$. Thomas-Fermi size $\mathbf{r}_{\text{TF}} = (25.5, 8.3, 9.4) \mu\text{m}$.

The parameters of the affine coordinate transformations \mathbf{C} , \mathbf{r}_0 and the radius of the spherical integration volume R are obtained from the anisotropic density $n(\mathbf{r})$ as explained in the section 7.5.2. We expect the multipole coefficients $\delta\mathbf{n}_{nlm}$ to reflect the anharmonic contributions in the potential which are now mapped onto the density distribution. The relative angular powers

$$p_{nl}(\delta n) = \sum_{m=-l}^l |\delta\mathbf{n}_{nlm}|^2 P^{-1}(\delta n), \quad P(\delta n) = \sum_{nlm} |\delta\mathbf{n}_{nlm}|^2, \quad (8.9)$$

are depicted in figure 8.8. As we regard the density difference, the angular momenta with odd parity are particularly prominent. Similar to the Zeeman potential in figure 7.3, the dominant non-harmonic coefficients are the dipole ($l = 1$) as well as the octupole ($l = 3$) powers.

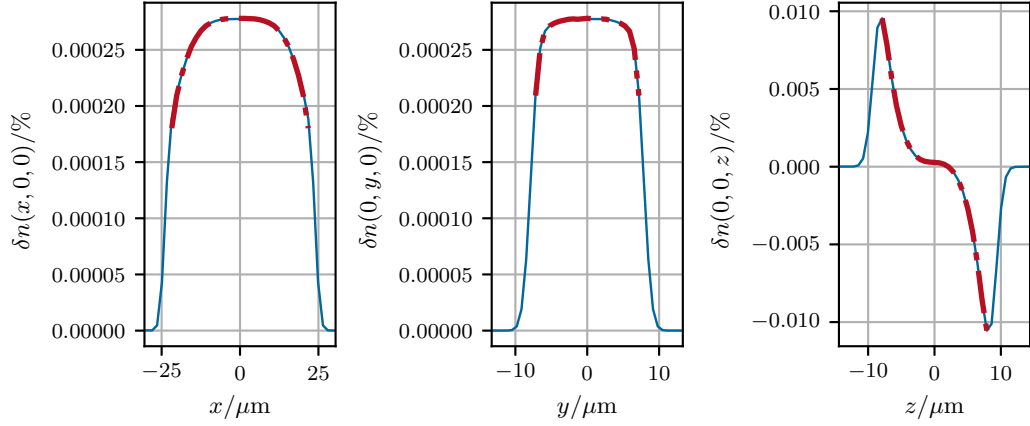


Figure 8.7: One-dimensional cross-sections of density deviations $\delta n(\mathbf{r})$ (8.7) of the equilibrium distributions in the release trap and its harmonic approximation. --- lines corresponds to Stringari interpolation (8.8) with $n_{\text{max}} = 9$, $l_{\text{max}} = 5$ up the Thomas-Fermi radii r_{TF} .

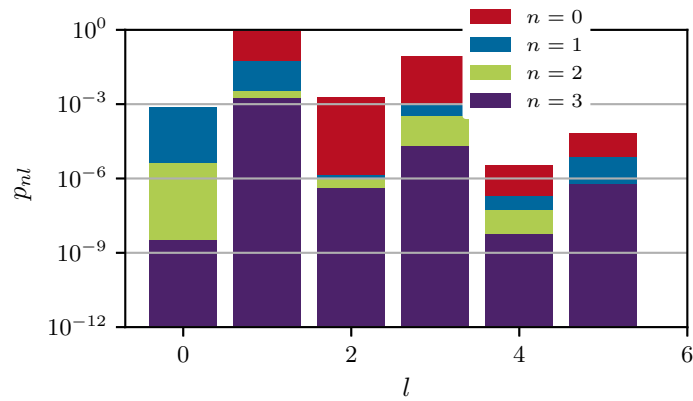


Figure 8.8: Multipole expansion of the density deviation $\delta n(\mathbf{r})$ (8.7) in the release trap. Relative angular powers $p_{nl}(\delta n)$ (8.9) versus l . Different principle numbers: red $n = 0$, blue $n = 1$, green $n = 2$, purple $n = 3$.

8.2.2 COLLECTIVE EXCITATIONS

Having determined the ground-state density distributions, we can compute the collective excitation inside the different trapping potentials in linear response by solving the Bogoliubov- de Gennes equations (4.91),

$$\Sigma^B W_k = E_k W_k, \quad E_k > 0, \quad (8.10)$$

numerically on a three-dimensional Cartesian grid (cf. appendix F and H.2). The excitation frequencies inside the release trap are relevant to control the center of mass motion as well as the quadrupole modes that are excited during the transport to the final trap [37, 73]. Because of the anharmonicities in the Zeeman potential, we expect violations of the harmonic potential theorem [127, 128] in the excitation spectrum that affects the center of mass oscillations in the trap. In particular, we find the absolute frequency shifts in the three Kohn modes, $\delta\nu = \nu - \nu_{\text{HO}}$,

$$\delta\nu_x = -7.2 \cdot 10^{-4} \text{ Hz}, \quad \delta\nu_y = -2.3 \cdot 10^{-3} \text{ Hz}, \quad \delta\nu_z = -1.5 \cdot 10^{-2} \text{ Hz}, \quad (8.11)$$

where $\nu = (9.08, 27.88, 24.61) \text{ Hz}$ (cf. table 2.2). The differences are in the mHz regime with lower excitation frequencies for the Zeeman potential. Cross-sections of the three-dimensional particle-hole mode functions, $u_k(\mathbf{r})$, $v_k(\mathbf{r})$, that correspond to the three symmetry broken Kohn modes in the release trap are shown in figure 8.9. More detailed figures as well as pictures of the first eleven Bogoliubov excitations are found in the appendix J.

The index k in the eigenvalue equation (8.10) labels the k -th eigenvalue obtained by the ARPACK eigenvalue solver [139] which are sorted by their magnitude in increasing order. We analyze the eigenfunctions of the Bogoliubov operator

$$W_k(\mathbf{r}) = \sum_{n=0}^{n_{\max}} \sum_{l=0}^{l_{\max}} \sum_{m=-l}^l \mathbf{w}_{nlm}^k S_{nlm}(\zeta), \quad (8.12)$$

$$W_k = (u_k, v_k)^\top, \quad \mathbf{w}_{nlm}^k = (\mathbf{u}_{nlm}^k, \mathbf{v}_{nlm}^k)^\top,$$

by our established partial wave expansion. If the physical system were spherical symmetric, the expansion in basis state, $\{|nlm\rangle\}$, could be used to construct the numerical eigenfunctions $W_{nlm}(\mathbf{r})$ of the angular momentum operators L^2 and L_z in the degenerate manifold (cf. appendix I). As the rotational symmetry of the condensate density in the release trap is broken, there is no exact one-to-one correspondence between the dipole coefficients, \mathbf{w}_{n1m}^k , in equation (8.12), and the Kohn modes in the harmonic trap. However within the rescaled coordinate system (7.50), we expect a strong overlap between the angular momentum eigenfunctions $Y_{lm}(\vartheta, \varphi)$ and the eigenfunctions $W_k(\mathbf{r})$ of the Bogoliubov operator. We also include the expanded Kohn modes to figure 8.9. With the help of the expansion coefficients \mathbf{w}_{nlm}^k we characterize the spectrum in terms of radial and angular momentum quantum numbers. In addition to the rotational symmetry, the Zeeman potential also breaks the space inversion symmetry

$$x \rightarrow -x, \quad y \rightarrow -y, \quad z \rightarrow -z, \quad (8.13)$$

of a three-dimensional harmonic oscillator potential. Hence, we expect coefficients with odd and even parities to appear in our multipole expansion (cf. figures 7.3 and 8.16). We depict the different angular angular powers for the mode $u_k(\mathbf{r})$,

$$p_{nl}^k(u_k) = \sum_{m=-l}^l \frac{|\mathbf{u}_{nlm}^k|^2}{P^k(u_k)}, \quad P^k(u_k) = \sum_{nlm} |\mathbf{u}_{nlm}^k|^2, \quad (8.14)$$

for the Zeeman as well as for the harmonic potential in the figures 8.10, 8.11, and 8.12. As the particle-hole functions are very similar in the low-energy regime, we restrict ourselves by just analyzing one of the modes. The angular powers $p_{nl}^k(u_k)$ for the exact Kohn modes in the harmonic trap exhibit strong contributions from the dipole ($l = 1$) and little contributions from the octupoles ($l = 3$). As the parity symmetry is preserved we just find multipole coefficients with odd symmetry. As the p_{nl}^k are rotational invariants, we can not distinguish between the preferred directions of the center of mass oscillations when comparing the bottom pictures in the figures 8.10, 8.11, and 8.12. In contrast to the exact Kohn modes, the spectrum of the multipole coefficients u_{nlm}^k in the Zeeman potential is much richer. Besides the prominent dipoles $p_{n1}^k(u_k)$, we find angular powers in all different angular momentum states. In figure 8.11, we note the additional appearance of different monopoles $p_{n0}^5(u_5)$ in the power spectrum. This hints towards an additional weak coupling mechanism of the $l = 1$ and $l = 0$ modes caused by the anharmonic potential.

Comparing the power spectra in the different figures, we conclude that the partial wave expansion of the eigenfunctions W_k in equation (8.12) is very sensitive to the shape of the external trapping potential. Even for small frequency shifts for the center of mass oscillations, we resolve the perturbations in the mode functions which corresponds to physical perturbations in the density as well as in the phase (cf. equation (4.100)). We can characterize the spectrum in terms of radial and angular momentum eigenfunctions $|nlm\rangle$, and identify non-trivial couplings in the anharmonic trap.

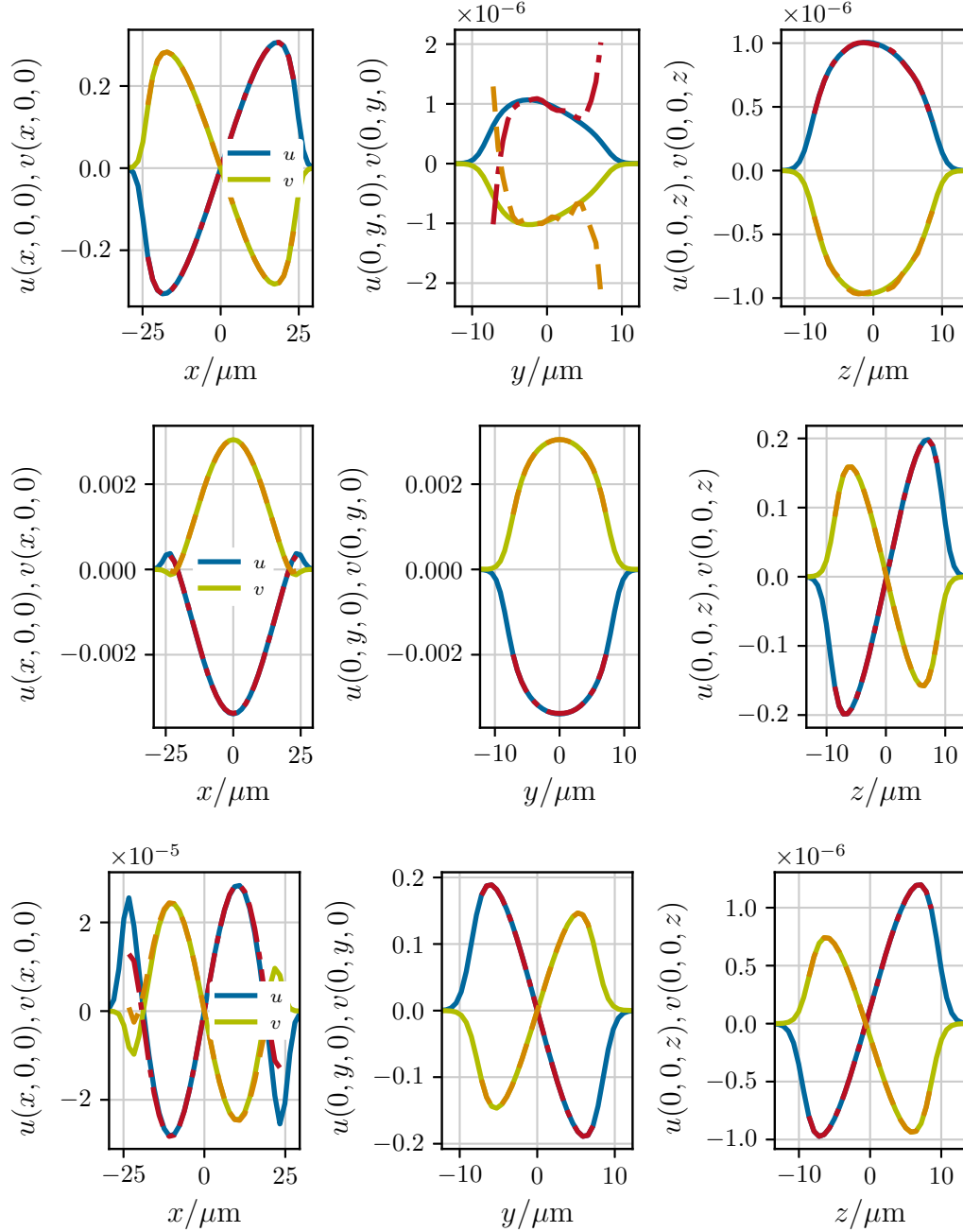


Figure 8.9: One-dimensional cross-sections of the particle-hole excitations, (u_k, v_k) (— lines), that corresponds to the symmetry broken Kohn modes in the Zeeman potential of the release trap. - - - lines corresponds to the Stringari interpolation (8.12) up the Thomas-Fermi radii r_{TF} . From top to bottom: angular excitation frequencies $\omega_1 = 9.08283$ Hz, $\omega_5 = 24.6014$ Hz, $\omega_7 = 27.8809$ Hz.

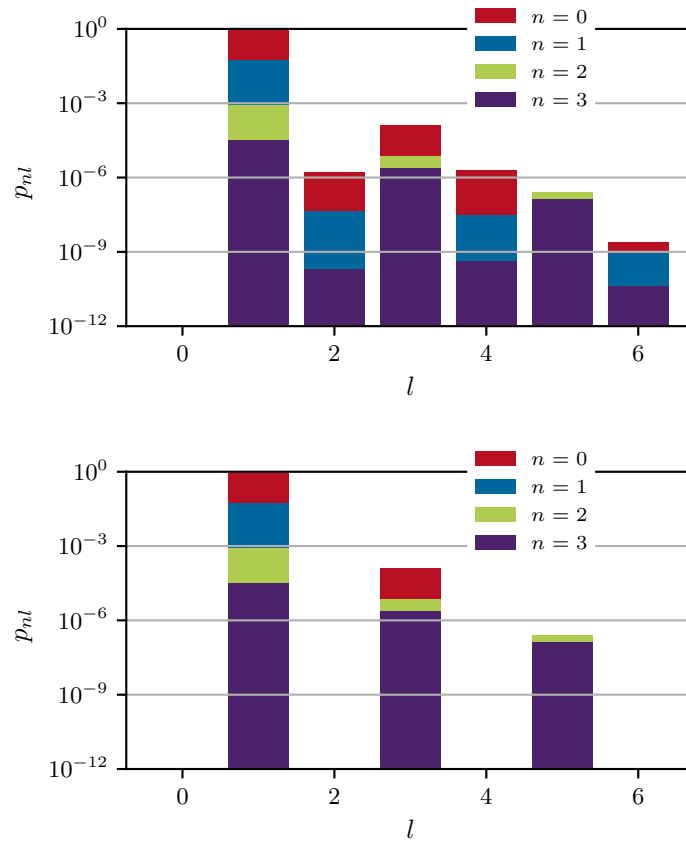


Figure 8.10: Multipole expansion of the Bogoliubov mode $u(\mathbf{r})$ that corresponds to the first Kohn mode ω_1 . First row in figure 8.9. Relative angular powers $p_{nl}^1(u_1)$ versus l . Different principle numbers: red $n = 0$, blue $n = 1$, green $n = 2$, purple $n = 3$. $n_{\max} = 5$, $l_{\max} = 6$. Top: Zeeman potential. Bottom: Harmonic potential.

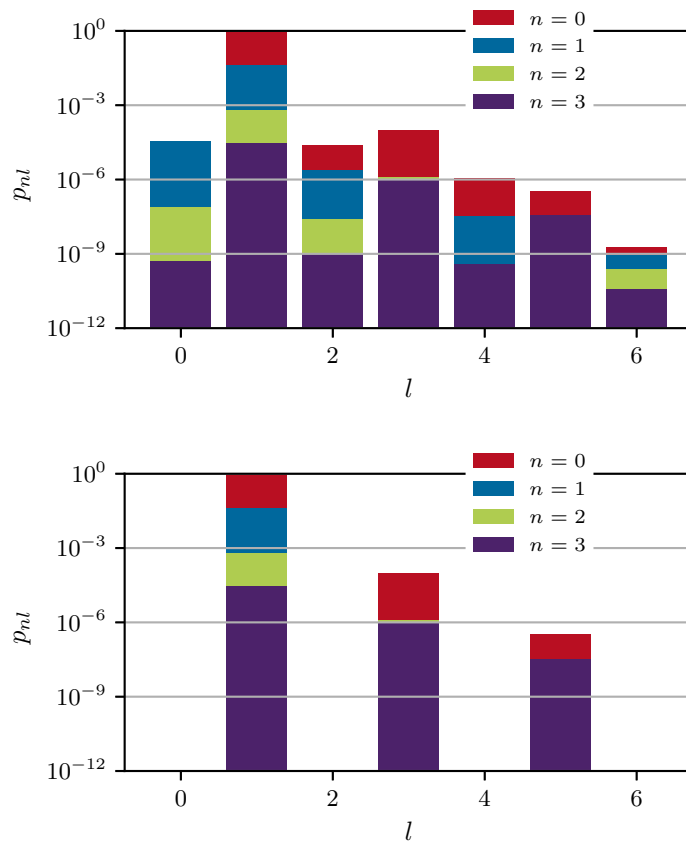


Figure 8.11: Multipole expansion of the Bogoliubov mode $u(\mathbf{r})$ that corresponds to the second Kohn mode ω_5 , second row in figure 8.9. Relative angular powers $p_{nl}^5(u_5)$ versus l . Different principle numbers: red $n = 0$, blue $n = 1$, green $n = 2$, purple $n = 3$. $n_{\max} = 5$, $l_{\max} = 6$. Top: Zeeman potential. Bottom: Harmonic potential.

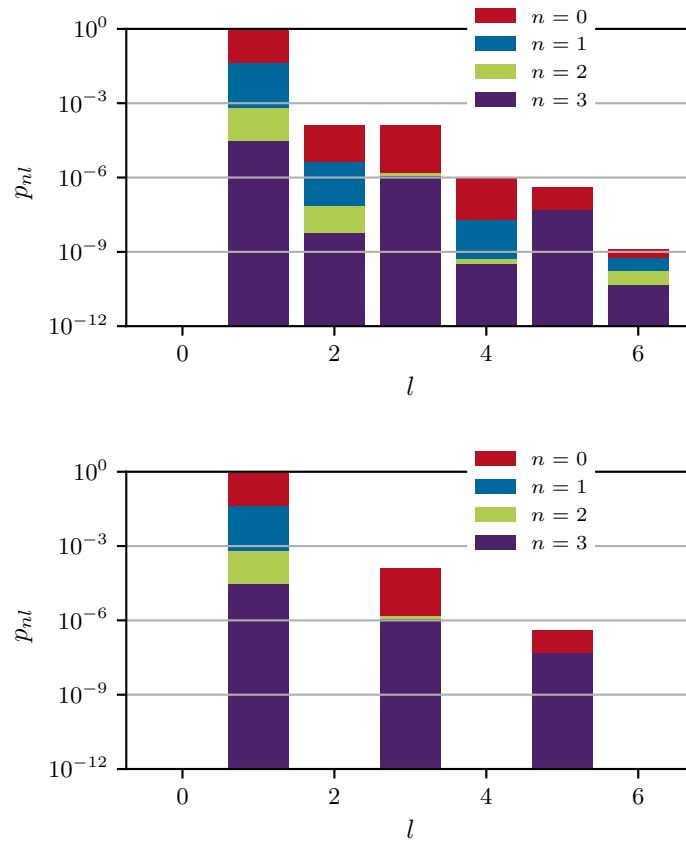


Figure 8.12: Multipole expansion of the Bogoliubov mode $u(\mathbf{r})$ that corresponds to the third Kohn mode ω_7 , second row in figure 8.9. Relative angular powers $p_{nl}^7(u_7)$ versus l . Different principle numbers: red $n = 0$, blue $n = 1$, green $n = 2$, purple $n = 3$. $n_{\max} = 5$, $l_{\max} = 6$. Top: Zeeman potential. Bottom: Harmonic potential.

8.3 BALLISTIC EXPANSION: PRE LENS

To perform atom interferometry with long interferometer times, one aims to reduce the mean-field pressure of the condensate before atomic lenses, beam splitter, and mirrors are applied to the condensate. In the previous section, we have characterized the ground state in the trap that we use as the initial state for the time evolution. As density variations are small, we assume that the initial state is characterized by its harmonic approximation. Hence, the release trap is purely characterized by its trapping matrix $\Omega(0) = \text{diag}(\omega_1, \omega_2, \omega_3)$. To verify our assumption we propagate both input states using the three-dimensional Gross-Pitaevskii equation in adaptive scales (6.3) with initial conditions

$$\Lambda(0) = \mathbb{1}, \quad \dot{\Lambda}(0) = 0, \quad \boldsymbol{\eta}(0) = \dot{\boldsymbol{\eta}}(0) = 0. \quad (8.15)$$

To solve the time-dependent Gross-Pitaevskii equation on adaptive scales $\Lambda(t)$, we use a 4th-order Runge-Kutta integrator (appendix L.1). For the numerical grid we chose the parameters as $N_x = N_y = 2^6 = 64$, $N_z = 2^7 = 128$, $L_x = 28.5$, $L_y = 11.9$, $L_z = 13.1$ and time step $dt = 5 \times 10^{-4}$ for the time evolution with numerical integrator.

During the time evolution, we monitor the fidelity

$$\mathcal{F}(t) = |\langle \Psi(t), \Psi_s(t) \rangle|^2 = \left| \int \Psi^*(\mathbf{r}, t) \Psi_s(\mathbf{r}, t) d^3r \right|^2, \quad (8.16)$$

with respect to the scaling approximation (6.11) which we present in figure 8.13. Indeed, we find tiny differences, $|\Delta\mathcal{F}| = 0.06\%$, in the fidelity for the simulation with large particle numbers, $N = 10^5$ atoms (cf. figure 8.13 (b)). Nevertheless, the total fidelity stays close to one, $\mathcal{F}(t_1) \approx 1$. For lower particle numbers, $N = 10$, $N = 1000$, we expect even fewer density deviations for the input states due to their smaller spatial extent. Therefore, differences in the fidelity are smaller compared to the former being less than 0.01% after the first time of flight. However, we need to consider significant deviations to the scaling approximation which decrease to $\mathcal{F}(t_1) = 0.95$ and $\mathcal{F}(t_1) = 0.83$ respectively. Non-quadratic deviations in the initial atomic density distribution

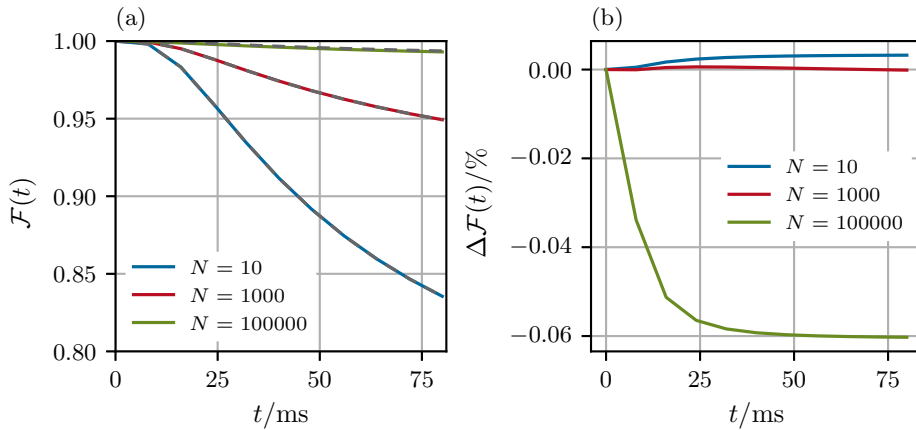


Figure 8.13: (a) Fidelity of the scaling approximation (8.16) during the ballistic expansion. Initial state in Zeeman potential (—). Initial state in harmonic potential approximation (- - -). (b) Difference in the fidelity for the different input states.

result in additional contributions to the quadratic Thomas-Fermi phase ϕ_0 (4.70). Beyond the

scaling solution, we also experience tiny phase terms that arise when the initial condensate is trapped in the anharmonic Zeeman potential. Hence, we find for the total phase

$$\begin{aligned}\phi(\boldsymbol{\xi}, t_1) &= \phi_0(\boldsymbol{\xi}, t_1) + \phi_1(\boldsymbol{\xi}, t_1) \\ &= \frac{M}{2\hbar} \boldsymbol{\xi}^\top \boldsymbol{\Lambda}^\top \dot{\boldsymbol{\Lambda}} \boldsymbol{\xi} + \phi_1(\boldsymbol{\xi}, t_1),\end{aligned}\quad (8.17)$$

after the first time of flight, where $\phi_1(\boldsymbol{\xi}, t)$ incorporates all non-quadratic parts of the total phase. We show $\phi(\boldsymbol{\xi}, t_1)$ (8.17) in figure 8.14 for the simulation with $N = 10^5$ atoms. To analyze the

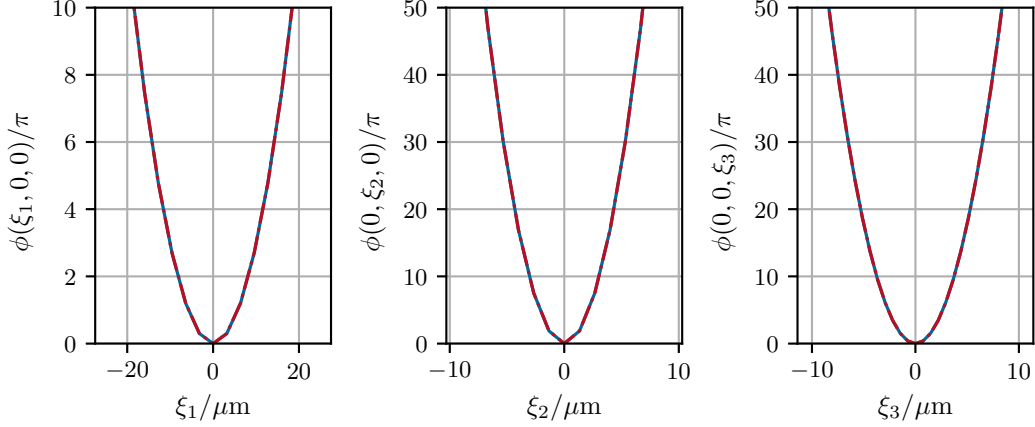


Figure 8.14: One-dimensional cross-sections of the $\phi(\boldsymbol{\xi}, t_1)$ (8.17) after the first time of flight $t_1 = 80$ ms. Phase of the condensate initially trapped in the release trap potential (blue —). Interpolation by Stringari polynomials (red - - -).

shape of the phase in detail, we perform the multipole expansion as

$$\phi(\boldsymbol{\xi}, t_1) = \sum_{n=0}^{n_{\max}} \sum_{l=0}^{l_{\max}} \sum_{m=-l}^l \phi_{nlm}(t_1) S_{nlm}(\boldsymbol{\xi}). \quad (8.18)$$

The relative angular powers $p_{nl}(\phi)$,

$$p_{nl}(\phi) = \sum_{m=-l}^l \frac{|\phi_{nlm}|^2}{P(\phi)}, \quad P(\phi) = \sum_{nlm} |\phi_{nlm}|^2, \quad (8.19)$$

are shown in figure 8.15. In the subfigures, we compare the phase of the condensate that was initially trapped in the Zeeman potential (a) to the condensate initially in the harmonic trap approximation (b). From the latter, we state that the next leading orders to the scaling approximation are of the form r^4 with spectral powers $p_{20}(\phi)$, $p_{12}(\phi)$, and $p_{04}(\phi)$. They are related to the kinetic energy perturbations H_3 in equation (6.18). In addition, we find that their values are approximately three orders of magnitude higher than the anharmonic corrections of the input state in the release trap.

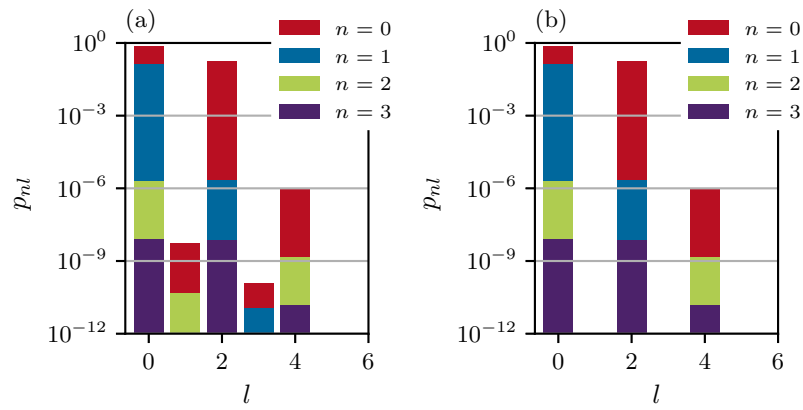


Figure 8.15: Multipole expansion of the phase $\phi(\xi, t_1)$ after a time of flight $t_1 = 80$ ms. Relative angular powers $p_{nl}(\phi)$ (8.19). Same parameter as in figure 8.6. (a) condensate initially trapped in the Zeeman potential (b) condensate initially trapped in the harmonic trap. Different principle numbers: red $n = 0$, blue $n = 1$, green $n = 2$, purple $n = 3$. $n_{\max} = 3$, $l_{\max} = 4$.

8.4 DELTA-KICK COLLIMATION WITH MAGNETIC CHIP TRAPS

8.4.1 CHARACTERIZATION OF THE MAGNETIC LENS

We have depicted the Zeeman potential of the magnetic lens in chapter 2 in the figures 2.9, 2.10. We decompose the potential of the magnetic lens in terms of the Stringari polynomials as we did for the release trap in chapter 7. Figure 8.16 depicts the angular powers $p_{nl}(U_z)$ for the Zeeman potential (7.34), the harmonic approximation, and the cumulant expansion (7.35). As the Zeeman potential of the lens is also obtained in a Z-wire configuration, the relative multipole components are very similar to the release trap that we presented in figure 7.3. In the following, we discuss the

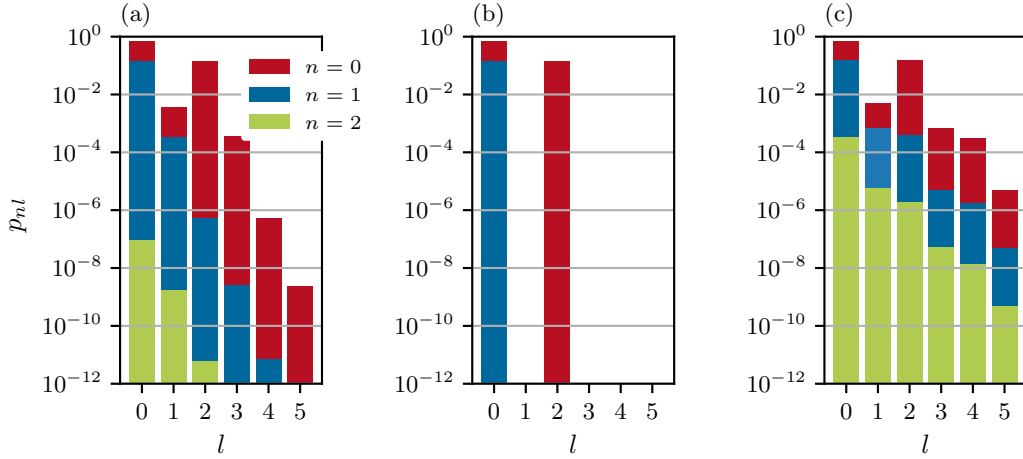


Figure 8.16: Multipole expansion of the magnetic lens. Relative angular powers $p_{nl}(U_z)$ versus angular momentum l . Different principle numbers: red $n = 0$, blue $n = 1$, green $n = 2$. (a) harmonic approximation, (b) multipoles of the Zeeman potential U_z , (c) multipoles of the cumulant. We used $R = 140 \mu\text{m}$ and $n_{\text{max}} = 2$, $l_{\text{max}} = 5$.

impact of the magnetic lens on the optimal lens time and the momentum width of the condensate using the full (3+1)d Gross-Pitaevskii equation in the magnetic lens potential. Afterward, we discuss the wavefront aberrations in terms of a “Seidel-diagram” for matter-wave optics and the momentum distribution of the condensate. The latter is imaged in the far-field zone after a second time of flight measurement.

8.4.2 OPTIMAL LENS TIME

In section 8.1 we have illustrated the delta-kick collimation protocol using the Thomas-Fermi scaling approximation. To include the realistic Zeeman potential of the chip model in our analysis, we need to solve the full (3+1)d Gross-Pitaevskii equation (6.3). First, we investigate the lens time as a function of different particle numbers. Further, we can study the influence of the non-harmonic potential on the momentum width of the condensate. In figure 8.17 we present the width in momentum space

$$|\Sigma_{\mathbf{k},ii}(t)|^{1/2} = \sigma_{k,i}(t), \quad i = 1, 2, 3, \quad (8.20)$$

for different spatial directions as a function of the lensing time τ . The widths during the application of the potential are normalized to the width after the first time of flight. As mentioned in section 8.1, the shape of the lens is most efficient in y - and z -direction where the velocity spread is reduced by almost 90%. For the third direction, one finds a reduction of $\approx 20\%$. During the application of the lens the widths are reduced linearly in the short time limit (cf figure 8.2), where the impact approximation is valid. Minimal values are found to be in good agreement with the result in

sections 8.1, $\tau = 2.716$ ms, even for smaller condensates with lower particle numbers (subfigures 8.17 (a), (b)). Moreover, the smaller extent of the atomic cloud is advantageous regarding the aberrations of the Zeeman potential as the magnetic lens does not affect either the momentum widths or the lensing time. In general, the harmonic approximation of the lens matches the result when we consider the full Zeeman potential. The impact of the anharmonic lens becomes visible

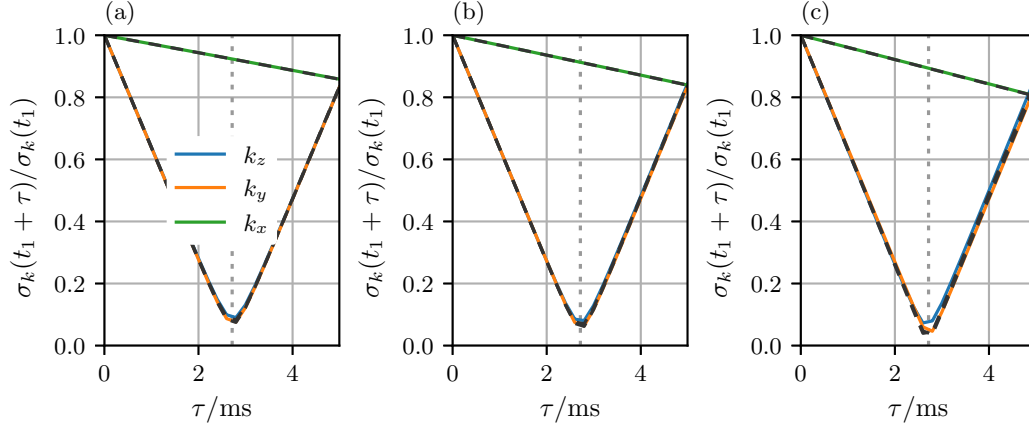


Figure 8.17: Normalized momentum widths σ_k as a function of lensing time τ . - - - lines correspond to harmonic lens approximation. Optimal lens time $\tau_\lambda = 2.716$ ms marked as $\cdots\cdots$ line. Particle numbers: (a) $N = 10$, (b) $N = 1000$, (c) $N = 10^5$.

in the momentum width in z -direction for large atom numbers which correspond to the subfigure 8.17 (c). It broadens the velocity distribution (cf. 8.4.5) without affecting the optimal lens time for infinite focal length, cf. figure 8.18.

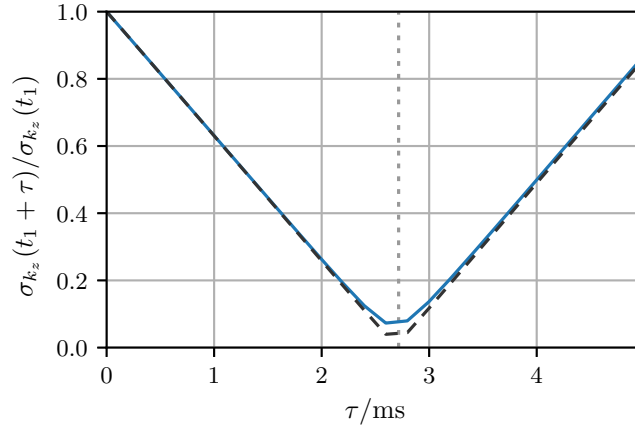


Figure 8.18: Normalized momentum width σ_{k_z} for different as function of lensing time. Particle number $N = 1 \times 10^5$, cf. figure 8.17 (c). - - - lines is the harmonic lens approximation. Optimal lens time $\tau_\lambda = 2.716$ ms marked as $\cdots\cdots$ line.

8.4.3 WAVEFRONT ABERRATIONS

To analyze the wavefront aberrations we solve the time-dependent Gross-Pitaevskii equation (6.3) in the Zeeman potential including all the anharmonic contributions for the estimated lens time τ_λ . We compare the result with the harmonic approximation of the potential. We show the phase for

both cases in figure 8.19. In addition, we depict the phase one finds using the phase imprinting where the total phase after the lens is of the form

$$\phi(\boldsymbol{\xi}, t_1 + \tau) = \phi(\boldsymbol{\xi}, t_1) - \tau[U_0(\Lambda\boldsymbol{\xi}) + U_1(\Lambda\boldsymbol{\xi})]/\hbar. \quad (8.21)$$

The first term on the right-hand side corresponds to the total phase before the lens from equation (8.17). U_0 denotes the harmonic, and U_1 the perturbation of the potential. The latter matches the full numerical solution quite well approving the thin lens presumption. To analyze the wavefront

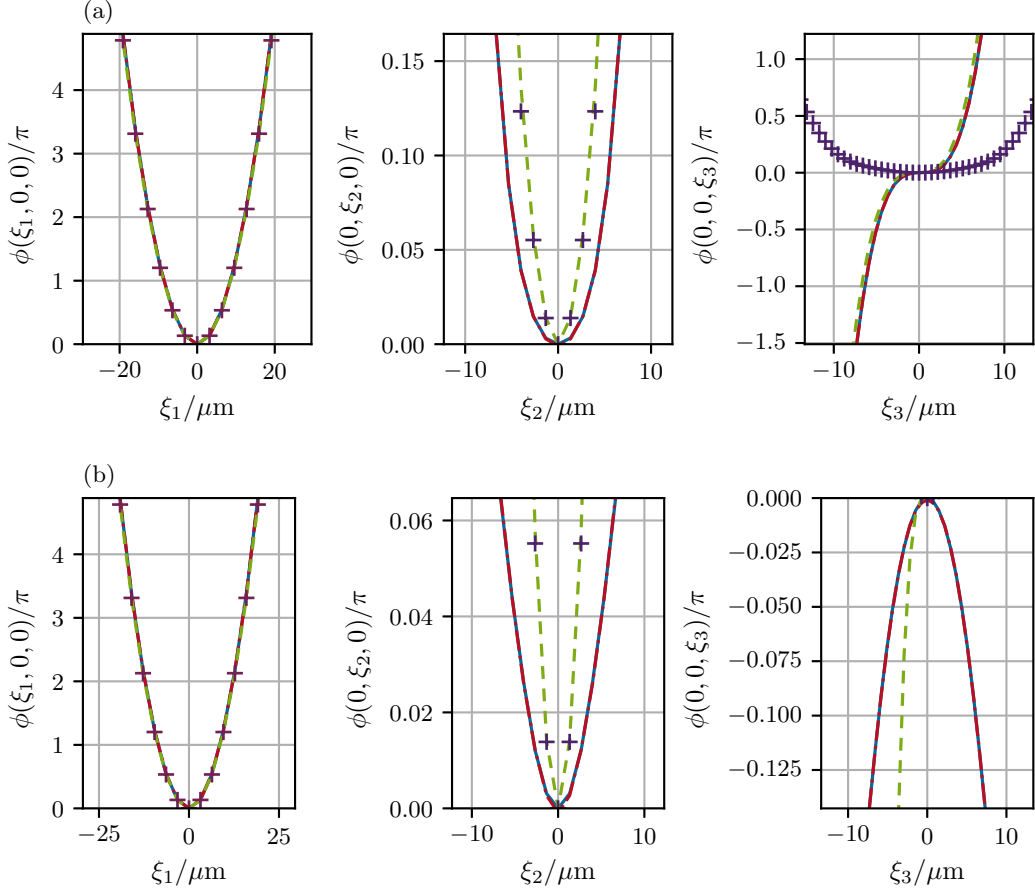


Figure 8.19: One-dimensional cross-sections of the phase $\phi(\boldsymbol{\xi}, t_1 + \tau)$ after the matter-wave lens. (a) Gross-Pitaevskii solution with anharmonic lens (blue —). Interpolation by Stringari polynomials (red - - -). Impact approximation anharmonic lens (green - - -). Impact approximation harmonic lens (purple +). (b) Gross-Pitaevskii solution with harmonic lens (blue —).

aberrations after the lens, we use again our polynomials expansion in equation 8.18. The coefficients in figure 8.20 in terms of the relative powers are now completely analogous to the famously known Seidel coefficients, that one uses to characterize the aberrations in optic design problems [4]. For perfect collimation, the wavefront becomes a planar surface and one expects all coefficients to be zero. As mentioned before, this matter-wave lens is not designed for collimation in x -direction. Hence, we see that quadratic coefficients are still present in figures 8.20 (a) and (b). Parts of the wavefront are still of parabolic shape in (cf. figure 8.19) and the orientation is encoded in the raw coefficient ϕ_{nlm} . Besides the quadratic expansion coefficients, we find the phase contributions that correspond to the first time of flight which are still present in the system. However, these aberrations are small compared to the other phase summands imprinted by the Zeeman potential. The main contributions in the spectrum are in the dipole ($l = 1$) as well as in the octupole ($l = 3$)

that we have already determined for the Zeeman potential in figure 8.16. The coefficients ϕ_{nlm} in equation (8.18) and the diagrams in figures 8.15 and 8.20 can be used for designing corrective optics in a multi-lens approach. The latter could be realized with painted potentials [132] or optical dipole potential shaped by digital micromirror devices [140].

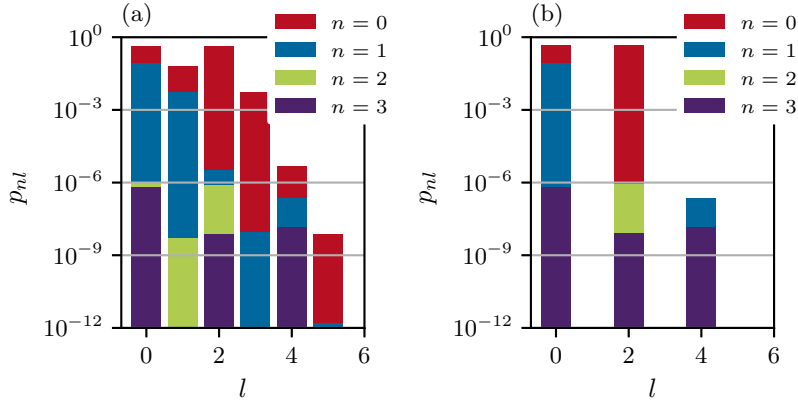


Figure 8.20: "Seidel-Diagram" in terms of relative angular powers $p_{nl}(\phi)$ versus angular momenta l for the phase after the lens $\phi(\boldsymbol{\xi}, t_1 + \tau)$ showing the wavefront aberrations after the matter-wave lens: (a) Zeeman potential, (b) Harmonic approximation. Different principle numbers: red $n = 0$, blue $n = 1$, green $n = 2$, purple $n = 3$. $n_{\max} = 3$, $l_{\max} = 5$.

8.4.4 MOMENTUM KICKS

The magnetic Zeeman potential exhibits multipole moments with odd symmetries. In particular, it has an existing dipole moment that leads to an additional momentum kick even when the potential minimum of the lens is aligned with the center of mass position of the atoms. The momentum distribution

$$\tilde{\psi}'(\boldsymbol{\kappa}, t) = \int \frac{e^{-i\boldsymbol{\kappa}^\top \boldsymbol{\xi}}}{(2\pi)^{3/2}} \psi(\boldsymbol{\xi}, t) d^3\xi, \quad \psi(\boldsymbol{\xi}, t) = \sqrt{n(\boldsymbol{\xi}, t)} e^{i\phi_1(\boldsymbol{\xi}, t)}, \quad (8.22)$$

$$\tilde{n}'(\boldsymbol{\kappa}, t) = |\tilde{\psi}'(\boldsymbol{\kappa}, t)|^2, \quad (8.23)$$

in the co-expanded frame with momenta $\boldsymbol{\kappa} = \Lambda^\top \mathbf{k}$ as defined in equation (A.10) is depicted in figure 8.21. The momentum expectation value in the impact approximation, assuming initial zero mean momentum, is given by

$$\langle \mathbf{k} \rangle = \int \frac{n(\boldsymbol{\xi}, t_1)}{|\Lambda|N} \Lambda^{-\top} \nabla_{\boldsymbol{\xi}} \left[\sum_{nlm} \phi_{nlm}(t_1 + \tau) S_{nlm}(\boldsymbol{\xi}) \right] d^3\xi, \quad (8.24)$$

where we used equation (B.8) to evaluate the momentum expectation value in the co-expanded reference frame. For further analysis, we assume from the Seidel diagram 8.20 that corrections of the quadratic phase are mostly determined by the multipole coefficients ϕ_{010} , ϕ_{110} , ϕ_{030} which correspond to a cubic phase aberration of the form

$$\phi_1(\boldsymbol{\xi}, t_1 + \tau) = \frac{\epsilon}{3} \xi_z^3. \quad (8.25)$$

Inserting the phase into equation (8.24), the additional momentum kick reads

$$\langle \mathbf{k} \rangle = \Lambda^{-\top} \mathbf{e}_z \epsilon \langle \xi_z^2 \rangle, \quad (8.26)$$

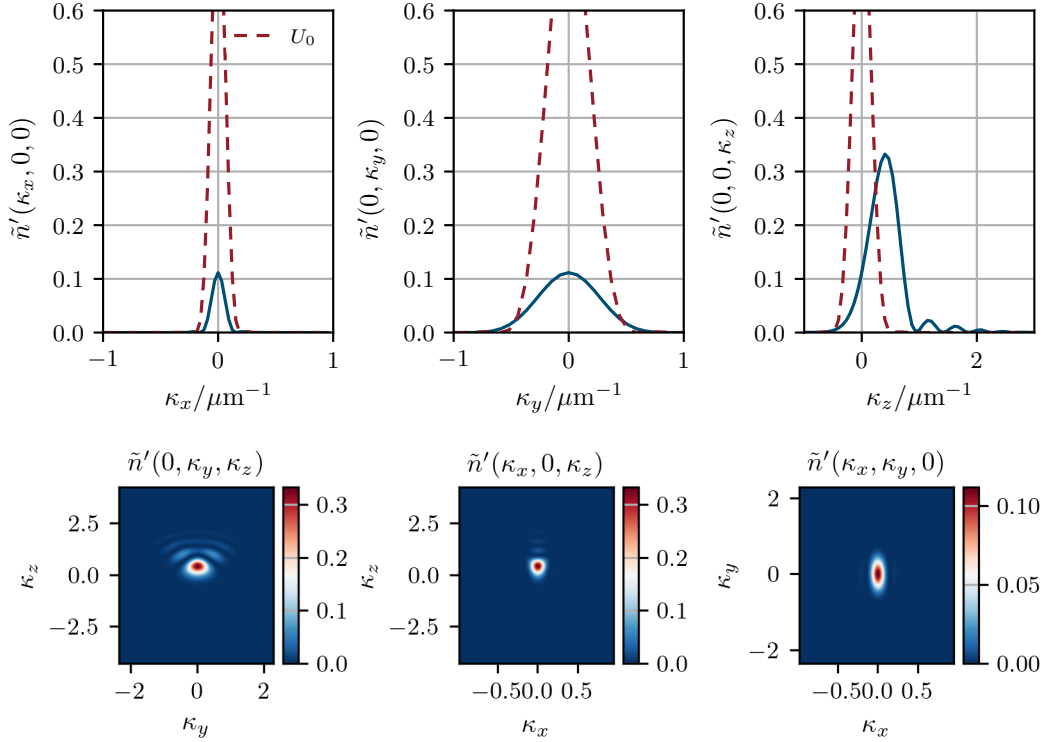


Figure 8.21: First row: One-dimensional cross-sections of the normalized, $\int \tilde{n}' d^3\boldsymbol{\kappa} = 1$, Fourier densities $\tilde{n}'(\boldsymbol{\kappa})$ (8.22) after Zeeman lens (blue —), after ideal lens (red - - -). Second row: Two-dimensional cross-sections of the Fourier densities $\tilde{n}'(\boldsymbol{\kappa})$ (8.22) after Zeeman lens.

which depends on the second moment of the initially trapped condensate. In figure 8.22 we evaluate the momentum kick $\langle \mathbf{k}(t) \rangle$ and the mean position $\langle \mathbf{r}(t) \rangle$ during the delta-kick collimation sequence for a second time of flight $t_2 = 2000$ ms. The kick in the k_z direction is displayed in subfigure (b), whereas the other momentum components are unaffected by the matter-wave lens. As the mean momentum is a constant of motion after the lens, the condensate's position in z -directions grows linearly in time with

$$\langle z(t) \rangle = \langle k_z \rangle t \Theta[t - (t_1 + \tau)], \quad (8.27)$$

as shown in subfigure (a), matching the numerical Gross-Pitaevskii solution exactly. After $t_2 = 2000$ ms, we find the z -position to be at $z = 73.9 \mu\text{m}$. One can balance the kick by re-positioning the trap minimum of the lens which adds a dipole moment to the phase in equation (8.24).

Besides the shift of the distribution along the positive κ_z -direction, one finds a wide-reaching oscillating momentum tail in the Fourier density which is caused by the higher order multipole moments in the condensate's phase. Due to the cubic phase perturbation (8.25), the momentum distribution is very similar to the intensity pattern of finite-energy Airy beams in (1+1)d and (2+1)d paraxial optics [141, 142].

8.4.5 MOMENTUM WIDTH

In section 8.4.2 we investigated the effect of the lens on the momentum width of the condensate. While the magnetic lens does not affect the optimal lens time, the Zeeman potential broadens the momentum width

$$\Sigma_{\mathbf{k}}(t) = \Sigma_{\mathbf{k},0}(t) + \Sigma_{\mathbf{k},1}(t), \quad (8.28)$$

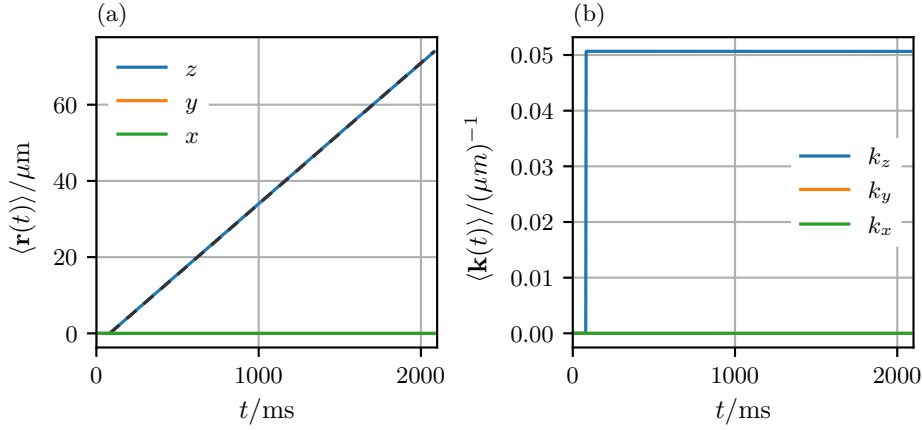


Figure 8.22: (a) mean position $\langle \mathbf{r}(t) \rangle$ of the condensate, (b) momentum kick $\langle \mathbf{k}(t) \rangle$ after the magnetic lens.

as shown in the figure 8.18. Here $\Sigma_{\mathbf{k},0}$ describes the covariance matrix for the unperturbed parabolic lens. Taking the same multipole moments as in the previous section, we can describe the additional width in the k_z -direction as

$$\Sigma_{\mathbf{k},1} = \epsilon^2 \text{tr} \{ \Lambda^{-1} \Lambda^{-\top} \mathbf{e}_z \otimes \mathbf{e}_z^\top \} \langle \xi_z^4 \rangle - \langle \xi_z^2 \rangle \mathbf{e}_z^\top \Lambda^{-1} \otimes \Lambda^{-\top} \mathbf{e}_z \langle \xi_z^2 \rangle, \quad (8.29)$$

where we used the expression in equation (B.11) to evaluate the covariance matrix in momentum space. Hence, the aberrational shift depends on the initial fourth central moment of the condensate.

8.5 BALLISTIC EXPANSION: POST LENS

In this section, we study the fidelity of the (3+1)d Gross-Pitaevskii dynamics with the scaling approximation (8.16) throughout the whole delta-kick collimation sequence. For the second time of flight after the matter-wave lens, we use very long expansion times that “images” the condensate density at $t_2 = 2$ s in the far field zone. Hereby, we investigate four different scenarios:

- 1) Gross-Pitaevskii propagation after the magnetic lens (U_z)
- 2) Gross-Pitaevskii propagation after the ideal lens (U_0)
- 3) “Schrödinger” propagation after the magnetic lens ($U_z, g = 0$)
- 4) “Schrödinger” propagation after the ideal lens ($U_0, g = 0$)

Cross-sections of the different densities at the end of the propagation are depicted in figure 8.23. As we know from the non-interacting wave packet expansion A.9, the position distribution of the diluted gas is mainly determined by its initial momentum distribution (cf. figure 8.21), analogous to the Fraunhofer diffraction limit [143]. Hence, we recover the oscillating tails in the density after the second time of flight for the condensates that passed the anharmonic lens.

The first scenario reflects the influence on the fidelity in the presence of the anharmonic lens. In contrast to the first time of flight sequence in section 8.3, we expect clear deviations to the scaling approach, when we consider the full (3+1)d Gross-Pitaevskii simulation in 1). For the Gross-Pitaevskii simulation with the harmonic lens 2), we check again the validity of the scaling approach during very long expansion times that can be accomplished in microgravity experiments. In the last two cases, 3) and 4), we study the effect of residual mean-field effects in the diluted gas.

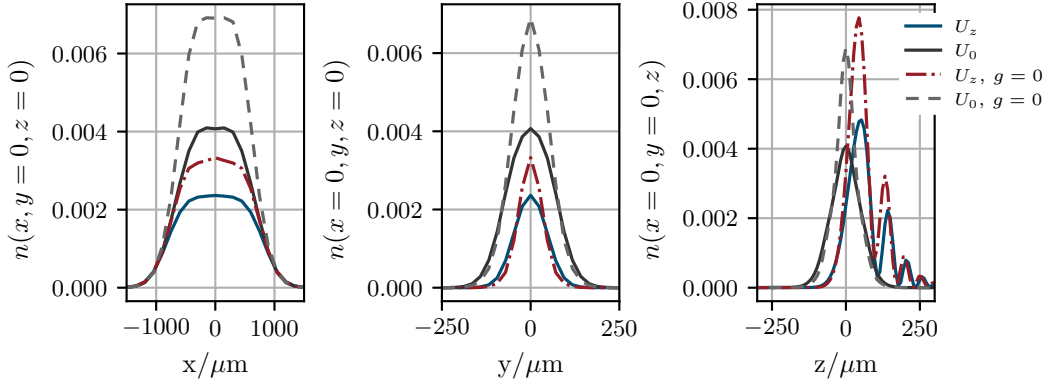


Figure 8.23: One-dimensional cross-sections of the condensate density $n(\mathbf{r})$ after second time of flight $t_2 = 2$ s. 1) blue —, 2) red - - -, 3) dark gray —, 4) gray - - -.

To do this, we turn off the interaction strength, $g = 0$, immediately after the lens and propagate the condensate wave function with the Schrödinger equation,

$$i\hbar\partial_t\psi(\boldsymbol{\xi}, t) = -\frac{\hbar^2}{2M}\nabla_{\boldsymbol{\xi}}^T\mathbf{M}^{-1}\nabla_{\boldsymbol{\xi}}\psi + \frac{1}{|\Lambda|}\left(\frac{M}{2}\boldsymbol{\xi}^T\Omega^2(0)\boldsymbol{\xi} - \mu\right)\psi, \quad t_1 + \tau < t < t_2. \quad (8.30)$$

Experimentally this could be realized using a Feshbach resonance [144] which tunes the s-wave scattering length by an external magnetic field.

We summarize the results for all different sequences in figure 8.24. As the scaling ansatz (6.1) just includes the time-dependent harmonic part of the external potential, the fidelity drops from $\mathcal{F}(t_1) = 0.99$ to $\mathcal{F}(t_1 + \tau) = 0.24$ in the scenarios 1) and 3), when we phase-imprint non-harmonic contributions to the condensate wave function. During the time evolution, we note an additional decrease in fidelity for the aberrated atomic cloud from $t = 82.7$ ms to $t \approx 1000$ ms, while the fidelity for the non-interacting cloud increase during approximately the same time interval. Regarding the pictures in appendix C, most of the density distortions that fractionate the condensate take place during this time interval. As both solutions differ in their non-linear interaction strength, we presume that mean-field interactions are still present and have a non-trivial impact on the condensate distribution after the magnetic lens.

In contrast to the first time of flight (cf. section 8.3) with intermediate expansion times ($t_1 \sim 80$ ms), we find discrepancies with respect to the pure scaling approximation of $\approx 7\%$ after $t_2 = 2$ s for the scenario 2). We obtain additional deviations when we disregard the residual mean-field interactions after the ideal lens, in 4), where the fidelity reads $\mathcal{F}(t_2) = 0.88$ at the end of the propagation compared to $\mathcal{F}(t_2) = 0.93$ for the interacting case in 2). As the effect of mean-field interactions on the interference pattern is currently investigated in different experiments [145, 146], we look into the evolved phases $\phi(\boldsymbol{\xi}, t_1 + \tau + t_2)$ after the delta-kick collimation sequence for the cases 2) and 4), disregarding the phase aberrations of the magnetic lens. Comparing the ‘‘Seidel’’-diagram in figure 8.26, we notice just subtle changes when interactions are turned off after the lens. In particular, we find an enhanced quadrupole moment, p_{22} , being proportional to r^6 as well as coefficients in the angular momentum $l = 4$.

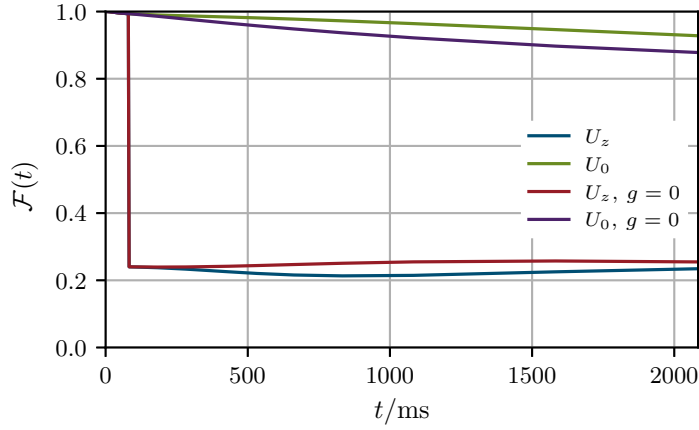


Figure 8.24: Fidelity of the Gross-Pitaevskii scaling solution (8.16) during the delta-kick collimation sequence: for Zeeman lens U_z (blue —), Zeeman lens zero interaction $U_z, g = 0$ (red —), harmonic lens U_0 (green —), harmonic lens zero interaction $U_0, g = 0$ (purple —).

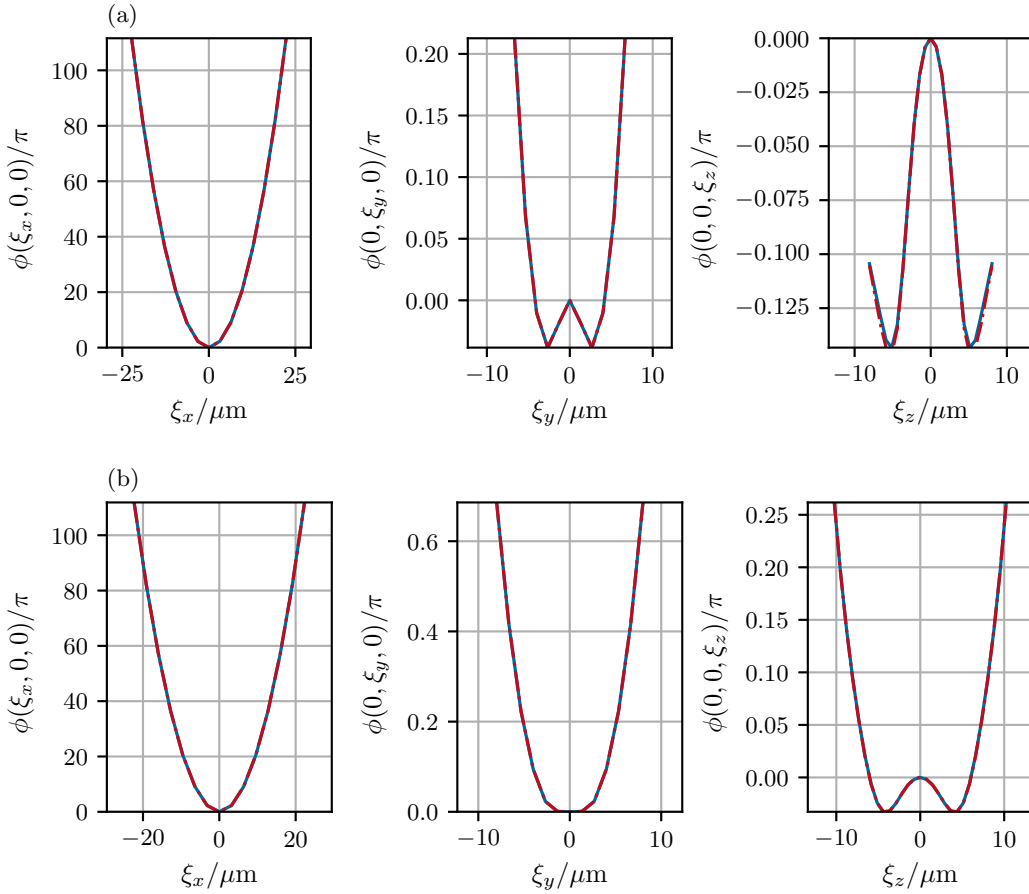


Figure 8.25: One-dimensional cross-sections of the phase, $\phi(\xi, t_1 + \tau + t_2)$, after the second time of flight $t_2 = 2$ s (blue —). (a) harmonic lens zero interaction $U_0, g = 0$, (b) harmonic lens U_0 . Interpolation by Stringari polynomials (red - - -).

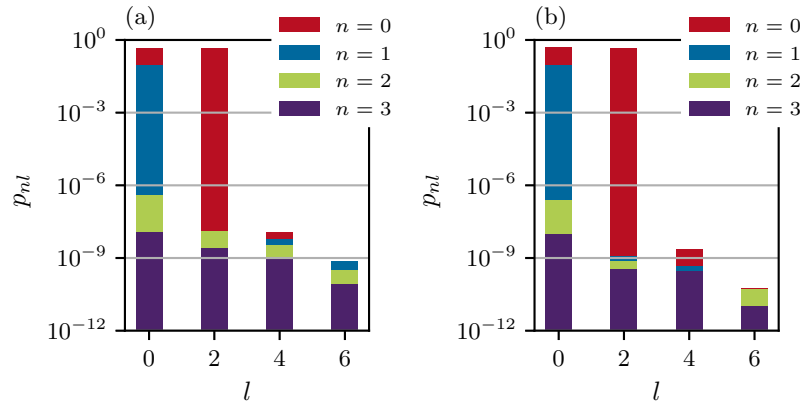


Figure 8.26: "Seidel-Diagram" in terms of relative angular powers $p_{nl}(\phi)$ versus angular momenta l showing the wavefront aberrations after the second time of flight $t_2 = 2$ s : (a) harmonic lens zero interaction $U_0, g = 0$, (b) harmonic lens U_0 . Different principle numbers: red $n = 0$, blue $n = 1$, green $n = 2$, purple $n = 3$. $n_{\max} = 8, l_{\max} = 6$.

9

TOPOLOGICAL DEFORMATION OF BOSE-EINSTEIN CONDENSATES IN OPTICAL DIPOLE TRAPS

In this chapter, we investigate the static and dynamical properties of a Bose-condensed gas in a toroidal ring geometry. Due to the properties of phase coherence as well as superfluidity, a ring geometry allows persistent flow and the measurement of rotations in a Sagnac interferometer scheme. Further, toroidal condensates may be regarded as a building block for atomtronic devices: circuits and networks of guided matter waves [44] that are built in analogy to their electronic counterpart. Ring-shaped geometries can be realized by magnetic as well as optical dipole trapping. Technical details of both methods are presented in [44] and the references therein.

This chapter is organized as follows: First, we briefly discuss the basic mechanisms of trapping neutral atoms using the optical dipole force. We present two methods to create ring geometries based on the effect of conical refraction and imaging optical potentials with digital micromirror devices. For the former, we look at the equilibrium properties of the three-dimensional condensate which is compared to experimental data. Afterward, we focus on the geometrical change in topology by investigating the collective excitations of a two-dimensional Bose-condensed gas. We conclude by introducing a feedback mechanism that damps the radial motion after the transformation toward a ring-shaped potential.

9.1 OPTICAL DIPOLE TRAPS

The first proposals of using the optical dipole force for atom manipulation were considered by [147] in 1962. In 1970 Arthur Ashkin demonstrated the acceleration and trapping of micron-sized particles using the radiation pressure and the optical dipole force [148]. In 2018 he won the Nobel Prize in physics for his invention of optical tweezers and their application to biological systems. With the invention of the laser, the advance in laser cooling and trapping [149] as well as the availability of different techniques of optical beam manipulation and shaping, optical dipole traps have become a great tool to generate a wide range of diverse potential landscapes for cold atoms [44, 131, 150]. In chapter 2 we have already discussed the basic physical concepts for trapping neutral atoms in a static magnetic field. In contrast to magnetic traps, optical dipole traps rely on the interaction of the atom's induced electric dipole moment with an external light field. The coupling to the intrinsic atomic energy levels induces two competing forces: the radiative and the conservative dipole force which we discuss in the following.

TWO-LEVEL SYSTEM The motion of a two-level atom in an electromagnetic field is one of the major problems in quantum optics and is treated in many textbooks [151, 152]. In the following, we briefly discuss the forces acting on the center of mass motion of a two-level atom $\{|g\rangle, |e\rangle\}$ which interacts with a classical laser and quantized vacuum field. The total Hamilton operator of the interacting system reads

$$\hat{H} = \hat{H}_A + \hat{H}_V + \hat{H}_{AL} + \hat{H}_{AV}, \quad (9.1)$$

where the atomic Hamilton operator

$$\hat{H}_A = \frac{\mathbf{P}^2}{2M} + \hbar\omega_e |e\rangle \langle e| + \hbar\omega_g |g\rangle \langle g|, \quad (9.2)$$

consists of the kinetic energy of the center of mass motion and the internal energies. The energy levels of the excited $|e\rangle$ and the ground state $|g\rangle$ are separated by the frequency $\omega_{eg} = \omega_e - \omega_g$. The interaction of the electric field with the atom is described within the dipole approximation

$$\hat{H}_{AL} = -\hat{\mathbf{d}} \cdot \mathbf{E}_L(\mathbf{R}, t), \quad (9.3)$$

as the wavelength for available laser systems is typically much larger than the extent of the atomic wave function. The electric field of the monochromatic laser is given by

$$\mathbf{E}_L(\mathbf{r}, t) = \mathcal{E}(\mathbf{r})\boldsymbol{\epsilon}(\mathbf{r}) \cos[\omega_L t - \Phi(\mathbf{r}, t)], \quad (9.4)$$

where $\boldsymbol{\epsilon}(\mathbf{r})$, $\mathcal{E}(\mathbf{r})$, $\Phi(\mathbf{r}, t)$, are the polarization, the amplitude, and the phase of the laser field. We denote the monochromatic laser frequency as ω_L which is detuned by $\Delta = \omega_L - \omega_{eg}$ towards the atomic resonance. The atomic electric dipole moment within the atomic basis states reads as

$$\hat{\mathbf{d}} = \mathbf{d}_{eg} |e\rangle \langle g| + \mathbf{d}_{ge} |g\rangle \langle e|, \quad \mathbf{d}_{ij} = \langle i|\hat{\mathbf{d}}|j\rangle. \quad (9.5)$$

Further, the atom interacts with the vacuum field \hat{H}_{AV} , which is responsible for the spontaneous emission of photons which is characterized by the natural lifetime Γ of the excited state $|e\rangle$. The Hamilton operator of the vacuum field H_V is regarded as a large reservoir with infinite degrees of freedom leading to fluctuations and damping in the system [153].

OPTICAL FORCES The force acting on the center of mass motion, described by the center of mass position \mathbf{R} and center of mass momentum \mathbf{P} , is given by the Heisenberg equation

$$\hat{\mathbf{F}} = \partial_t \hat{\mathbf{P}} = \frac{1}{i\hbar} [\hat{\mathbf{P}}, \hat{H}]. \quad (9.6)$$

The observable of interest is the force expectation value $\mathbf{F} = \text{tr}\{\hat{\mathbf{F}}\hat{\rho}\}$ where $\hat{\rho}$ is the density operator of the total system consisting of the atom and the vacuum field. Tracing out the dynamical degrees of freedom of the reservoir, one finds the mean force

$$\mathbf{F} = \text{tr}\{\hat{\mathbf{F}}\hat{\rho}\} \approx \mathbf{F}_{\text{dissp}} + \mathbf{F}_{\text{dip}} = 2\hbar|\Omega|^2 \Im\left(\frac{\rho_{eg}}{\Omega^*}\right) \nabla\Phi + \hbar\Re\left(\frac{\rho_{eg}}{\Omega^*}\right) \nabla|\Omega|^2, \quad (9.7)$$

with respect to the reduced density operator $\hat{\rho}$ of the atom [154]. ρ_{ij} are the off-diagonal matrix elements of the internal atomic density operator and $\Omega(\mathbf{r}) = -\mathbf{d}_{eg} \cdot \boldsymbol{\mathcal{E}}(\mathbf{r})/\hbar$ denotes the complex Rabi frequency. The first term $\mathbf{F}_{\text{dissp}}$ is related to a dissipative force caused by the radiation pressure when the atom is absorbing and emitting photons. It is proportional to the gradient of the laser phase and points into the direction of the local wave vector \mathbf{k}_L . The second term \mathbf{F}_{dip} is called optical dipole force. It points into the direction $\nabla|\Omega|^2 \propto \nabla I$ where I denotes the light intensity.

Essential for atom trapping in a conservative optical dipole potential is a laser light field that is far-detuned from the atomic resonance, $|\Delta| \gg |\Omega|, \Gamma$. In this case, the two competing forces in equation (9.7) simplify to

$$\mathbf{F}_{\text{dissp}} = \Gamma_{\text{sc}} \hbar \nabla\Phi, \quad \mathbf{F}_{\text{dip}} = -\frac{\hbar}{4\Delta} \nabla|\Omega|^2, \quad (9.8)$$

with the spatially-dependent photonic scattering rate

$$\Gamma_{\text{sc}}(\mathbf{r}) = \frac{3\pi c^2}{2\hbar\omega_{eg}} \left(\frac{\Gamma}{\Delta} \right)^2 I(\mathbf{r}). \quad (9.9)$$

As the force is the negative gradient of a potential, one finds for the optical dipole potential

$$U_{\text{dip}}(\mathbf{r}) = \frac{\hbar}{4\Delta} |\Omega(\mathbf{r})|^2 = \frac{3\pi c^2}{2\omega_{eg}^3} \frac{\Gamma}{\Delta} I(\mathbf{r}). \quad (9.10)$$

From equations (9.9) and (9.10), one finds that dipole potential scales with I/Δ , whereas the scattering rate scales as I/Δ^2 . Therefore, one tries to stay in the far-detuned regime, with high light intensities to limit the number of scattering events inside the trap. In addition, the optical dipole potential depends on the sign of the detuning Δ . Below the atomic resonance, $\Delta < 0$ (red-detuned), atoms are attracted into the light field and the potential minimum coincides with the maximum of intensity. For blue-detuned laser light $\Delta > 0$, the atoms are repelled by the light field and potential minima occur at the minima of the intensity [131, 153].

MULTILEVEL ATOMS For trapping alkali atoms (cf. section 2.2.2) in their atomic ground state, one needs to consider multiple atomic transitions as the optical dipole generally depends on the sub-state of the atom. Relevant energy scales are the fine and hyperfine-splittings of the ground state Δ_{hfs} as well as the excited states Δ'_{hfs} , Δ''_{hfs} (cf. figure 2.1). As long as all the light's detuning is much larger than all the hyperfine splittings, the hyperfine structure is not resolved and the optical dipole potential for linearly polarized light in the rotating wave approximation reads

$$U_{\text{dip}}(\mathbf{r}) = -\frac{3\pi c^2}{2} \left[\frac{2\Gamma_{D2}}{3\omega_{D2}^3} \left(\frac{1}{\omega_{D2} - \omega} \right) + \frac{\Gamma_{D1}}{3\omega_{D1}^3} \left(\frac{1}{\omega_{D1} - \omega} \right) \right] I(\mathbf{r}), \quad (9.11)$$

whereas $D1$ and $D2$ correspond to the optical transition from the $n^2S_{1/2}$ to $n^2P_{1/2}$, $n^2P_{3/2}$ manifolds [131].

9.2 RING GEOMETRIES WITH DIPOLE OPTICAL POTENTIAL

The optical dipole potential (9.10) is directly proportional to the light intensity. Hence, ring-shaped trapping geometries are obtained by creating light fields in ring-shaped optical patterns. For a Laguerre-Gaussian beam a toroidal intensity profile is obtained in the donut-like LG_{01} mode. Alternatively one can use so-called painted potential with a fast rotating focused laser beam that creates a time-averaged ring-shaped potential for the atoms [44]. In the ongoing chapter, we will discuss optical potentials that are created by using the effect of conical refraction in birefringent biaxial crystals and programmable potentials using digital micromirror devices.

9.2.1 CONICAL REFRACTION

The AG Birkl at TU Darmstadt has examined a new technique to create toroidal ring structures which are based on the effect of conical refraction [155, 156]. The effect of conical refraction occurs in biaxial crystals. A focused Gaussian beam with waist w_0 propagating along one of the optical axes of the crystal creates one or more concentric rings of light in the focal plane. If one is blue-detuned to the atomic resonance, atoms are trapped either in the dark focus of a single ring with radius R_0 , the so-called bottle-beam configuration, or in between two bright rings, resulting in a toroidal trap configuration. For ultra-cold atoms, trapping in dark traps is advantageous because the photonic scattering rate (9.9) is proportional to the light intensity, and decoherence processes

are minimized. One can vary between these two different distinct topological patterns by changing the beam size of the input laser beam which changes the waist of the focused beam in the focal plane. Quasi-two-dimensional trapping configuration and gravity compensation are achieved by using an additional attractive light sheet potential.

In the following, we will briefly discuss the light intensity distribution created by conical refraction. As in [155, 157], we consider a cylindrical symmetric input beam with transverse electrical field amplitude

$$\mathcal{E}(r) = \mathcal{E}_0 e^{-r^2/w_0^2}. \quad (9.12)$$

A paraxial solution for the output field is given in terms of the Belskii-Khapalyuk-Berry integrals

$$\begin{aligned} B_0(\rho, Z) &= \frac{1}{2\pi} \int_0^\infty \kappa a(\kappa) e^{-\frac{i}{2n}\kappa^2 Z} \cos(\kappa\rho_0) J_0(\kappa\rho) d\kappa, \\ B_1(\rho, Z) &= \frac{1}{2\pi} \int_0^\infty \kappa a(\kappa) e^{-\frac{i}{2n}\kappa^2 Z} \sin(\kappa\rho_0) J_1(\kappa\rho) d\kappa, \end{aligned} \quad (9.13)$$

with dimensionless wave vector $\kappa = kw_0$, coordinates $\rho = r/w_0$, $Z = z/z_R$, the mean refractive index of the crystal n and normalized ring radius $\rho_0 = R_0/w_0$. The function $a(\kappa) = 2\pi \int \mathcal{E}(r) J_0(r\kappa) r dr$ denotes the radial part of the two-dimensional Fourier transform of the electric input field and J_n is the n -th Bessel function of the first kind [158–160]. If the input field is circularly polarized, the output density distribution created by conical refraction is given by

$$I = |B_0|^2 + |B_1|^2. \quad (9.14)$$

As the light pattern of the conical refraction directly depends on the Fourier components $a(\kappa)$ of the focused laser beam, one can manipulate the output light field, e.g. using a digital micromirror device (DMD), in a very controllable fashion. Besides toroidal ring structures, bucket-like potential for atomic transport and acceleration, as well as periodic structures, might be generated with suitable DMD images [156].

CHANGE OF TOPOLOGY A change of topology in the optical potential was investigated in [156]. In this work, a DMD creates a variable circular aperture with radius R_A , which blocks the input light of a Gaussian laser beam for values $r > R_A$. In figure 9.1 we depict the optical potential in the focal plane $z = 0$ for three different aperture values for a circular polarized, cylinder symmetric Gaussian beam using equations (9.11), (9.13) and (9.14) for our simulation. The optical parameters and the atomic data of ^{87}Rb are summarized in table 9.1 The potential shape changes from simply

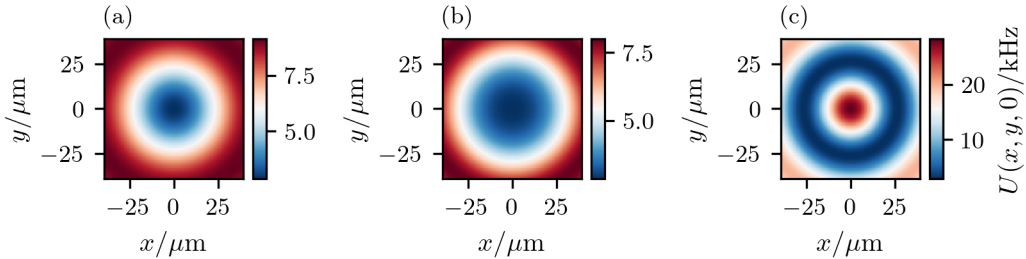


Figure 9.1: Optical dipole potential in the focal plane $U(x, y, 0)$ obtained by conical refraction. DMD aperture radii R_A : (a) 920 μm , (b) 1152 μm , (c) 1840 μm . Optical parameters as in table 9.1.

connected almost harmonic confinement to a multiple-connected ring-shaped confinement. For a maximal DMD aperture value of $R_A = 1840 \mu\text{m}$ the ring size is $\rho_0 \approx 25 \mu\text{m}$ with a radial trapping frequency of $\nu_\rho \approx 150 \text{ Hz}$ for ^{87}Rb (cf. figure 9.3 (b) and (c)).

For three-dimensional trapping, we consider a harmonic confinement created by an optical light sheet potential in the perpendicular direction. Hence the total three-dimensional potential reads

$$U_{\text{dip}}(\rho, z) = U_{\text{con}}(\rho) + \frac{M}{2}\omega_z^2 z^2. \quad (9.15)$$

For a given potential at a fixed DMD aperture and light sheet potential with frequency $\nu_z = 169$ Hz in the transverse directions, we have examined the equilibrium density distribution solving the stationary Gross-Pitaevskii equation for 17 000 ^{87}Rb atoms. The corresponding atomic densities in the focal plane $z = 0$ are presented in figure 9.2. The trapping frequencies in the radial direction,

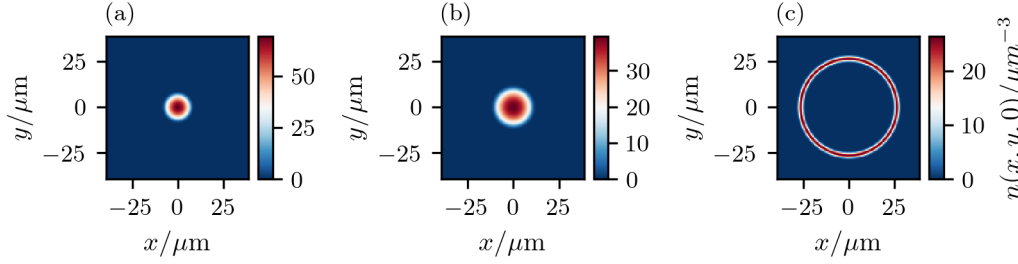


Figure 9.2: Ground state density distribution $n(x, y, 0)$ of a Bose-Einstein condensate in the optical dipole potential shown in figure 9.1. Parameters as in table 9.1

as well as the ring radii ρ_0 , are obtained numerically by a second-order Taylor expansion in the trap minimum. The results are summarized in figure 9.3 (b) and (c). From this, we can determine the chemical potentials in the Thomas-Fermi approximation for the three-dimensional harmonic oscillator (4.46) and for the three-dimensional toroidal trap [161]

$$\mu_{\text{TF}}^{3\text{d}} = \hbar\bar{\omega}\sqrt{\frac{2Na_s}{\pi\rho_0}}, \quad \bar{\omega} = \sqrt{\omega_\rho\omega_z}, \quad (9.16)$$

which we compare with the calculated chemical potential of the Gross-Pitaevskii simulations. The results are depicted in figure 9.3 (a). In the limits of the harmonic as well the in the toroidal ring

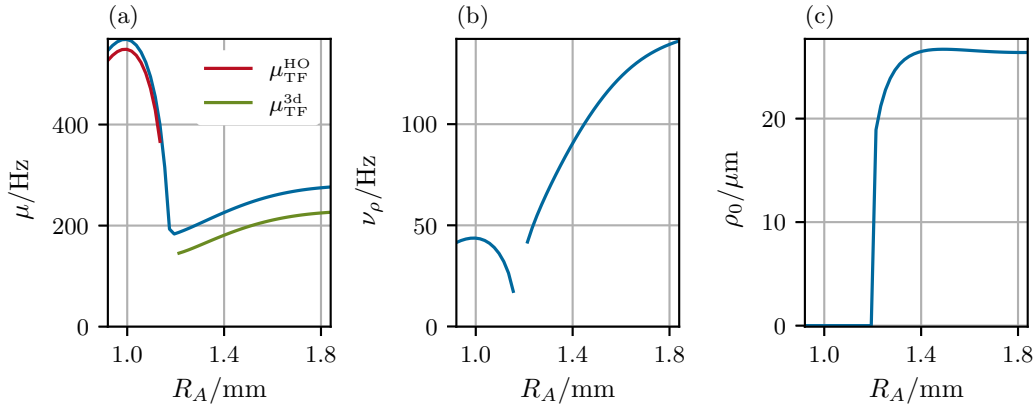


Figure 9.3: (a) chemical potential μ versus aperture radius R_A (blue). Thomas-Fermi approximation for the harmonic oscillator potential $\mu_{\text{TF}}^{\text{HO}}$ (red). Thomas-Fermi approximation for toroidal potential $\mu_{\text{TF}}^{3\text{d}}$ (9.16) (green). (b) radial frequency ν_ρ and (c) ring radius ρ_0 versus aperture radius R_A .

trap, the chemical potential describes the quantitative behavior quite well. The reduction of the trapping frequency, see figure 9.3 (b), leads to an increase of the effective volume $V_{\text{eff}} = N/n_{\text{max}}$

and a decrease of the chemical potential. As the trapping potential transforms towards a ring, and the radial trap frequency tends to zero, the chemical potential stops the monotonic decline and flattens as the chemical $\mu_{\text{TF}}^{3\text{d}} \propto \sqrt{\omega_\rho}$ for an almost constant ring radius (cf. figure 9.3 (c)). The drastic change in the behavior of the chemical potential may be regarded as one sign of the topological change in the trapping geometry. Moreover, we can use the chemical potential to determine the conditions for reaching a lower dimensional regime [162]. The reduction of spatial dimension has an impact on the coherence properties of the condensate as phase fluctuations become more relevant. In addition, new phases of matter such as the fermionization of Bosons in highly elongated one-dimensional [150] or the BKT transition [163, 164] in two-dimensional quantum gases may be studied [165]. The conditions for reaching a lower quasi-dimensional regime may be expressed in terms of the different energy scales of the Bose-condensed gas

$$\mu > \hbar\omega_z \text{ (3d)}, \quad \hbar\omega_\rho < \mu < \hbar\omega_z \text{ (2d)}, \quad \mu < \hbar\omega_\rho \text{ (1d)}, \quad (9.17)$$

and the external trapping energies [161]. Within the harmonic simply connected as well as in the multiple connected ring potential, the experimental setting stays in the three-dimensional regime as $\mu/h > 169$ Hz for all DMD aperture radii. A two-dimensional regime would require a modification of the light sheet potential that increases the harmonic confinement in z -direction.

EXPERIMENTAL DATA In the model for conical refraction, we have considered only a Gaussian beam with perfect circular polarization as an input state. Further, we did not assume any optical aberrations that change the intensity pattern in the focal plane nor any defects in the biaxial crystal that may affect the ring structure. The AG Birkl¹ provided us with recorded two-dimensional light field patterns in the focal plane which are shown in the figure 9.4 for comparable parameters as in table 9.1. We note that the measured intensities do not exhibit the azimuthal symmetry as in figure

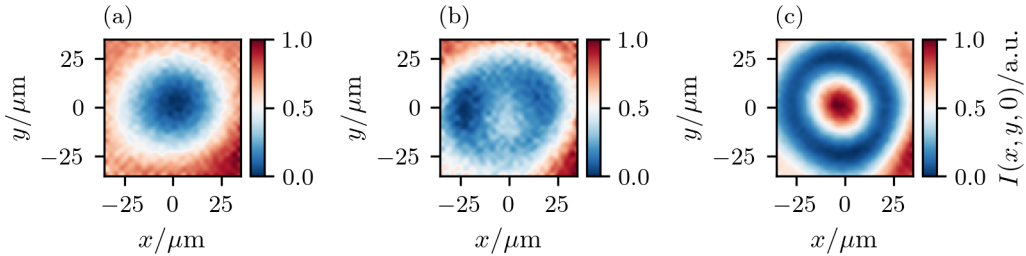


Figure 9.4: Measured light intensities for three different aperture values R_A : (a) 920 μm , (b) 1152 μm , (c) 1840 μm . As the laser light is blue-detuned towards the atomic resonance atoms are trapped in the local minima of the intensity.

9.1. In addition, they show inhomogeneities in the radial as well as in the azimuthal direction for all values of the DMD aperture. One finds that the most divergent configuration to the analytic model is close to the point where the topology of the light field should change to a ring-shaped geometry 9.4 (b). Instead of the emergence of one central bright spot, the light field fractionates into an intensity distribution with two distinct local minima.

From the light intensities, we have extracted the physical potentials: We normalize the central spot in the figure 9.4 (c) to the maximal potential energy obtained by the model for the conical refraction, $E_{\text{spot}}/h \approx 26.4$ kHz. The spatial extent of the optical dipole trap is obtained from the estimated pixel size 0.56 $\mu\text{m}/\text{pxl}$. In order to estimate the effect on the atomic distribution when applying different potentials to them, we display the stationary equilibrium density $n(x, y, 0)$, shown in figure 9.5, that we obtain from the extracted optical potential. While the density in figure

¹Experimental results by F. Schmalz. Data provided by D. Pfeiffer.

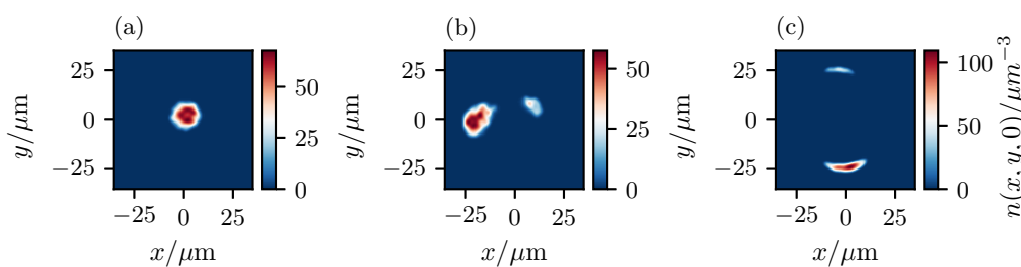


Figure 9.5: Equilibrium density distribution $n(x, y, 0)$ for the measured optical dipole potential (cf. figure 9.4).

9.5 (a) agrees qualitatively well with the distribution in figure 9.2 (a), the condensate separates into different pieces during the transformation into the ring potential 9.5 (b) and (c), as the chemical potential is lower than the intrinsic energetic barriers in the distorted potential. From the latter, we would expect a highly excited state with radial as well as azimuthal flow in the final ring configuration that would affect the coherence properties as well as the lifetime of the condensed atoms in the toroidal trap.

9.2.2 DIGITAL MICROMIRROR DEVICES

Instead of using a digital micromirror device (DMD) for manipulating the beam shape that propagates through the biaxial crystal, the desired light field may be generated on the DMD and imaged directly into the vacuum chamber. Hence, the DMD allows in principle a much better control of the external potential and therefore a better control of the dynamical degrees of freedom of the system. A digital micromirror device consists of up to millions of individually addressable mirrors that can be switched to either an on or an off state. One mirror is usually rectangular with an edge length of $\approx 10.8 \mu\text{m}$. Due to their small size and the grid-like arrangement, the DMD acts as a classical two-dimensional optical diffraction grating when all mirrors are in their on-state. Details on the image formation are found in [140, 166].

9.3 BOSE-EINSTEIN CONDENSATE IN A QUASI-TWO-DIMENSIONAL HARMONIC RING POTENTIAL

In this section, we focus on the quasi-two-dimensional ring potential. In particular, we study the collective excitations in a two-dimensional ring-shaped condensate. We provide an analytic approximation for the energy spectrum in thin rings within the hydrodynamic Thomas-Fermi regime. The result is compared to the numerical values obtained by the Bogoliubov-de Gennes equations. We use the latter to exploit the excitation spectrum during the topological transition from simply connected harmonic to multiply connected ring trap.

We represent the effective Gross-Pitaevskii equation (9.21) and the Bogoliubov-de Gennes operator (9.27) on radial Fourier grid F.4. The wave functions in section 9.5 are propagated in time using a 4th-order Kunge-Kutta integrator L.1.

Table 9.1: Symbols and values for the laser and the atom parameters.

Quantity	Symbol	Value
particle number in BEC	N	17 000
scattering length ^{87}Rb	a_s	5.23 nm
trapping frequency in z -direction	ω_z	$2\pi \cdot 169$ Hz
D1 decay rate	Γ_{D1}	$2\pi \cdot 5.74$ MHz
D2 decay rate	Γ_{D2}	$2\pi \cdot 6.07$ MHz
D1 transition frequency	ω_{D1}	$2\pi \cdot 377.1$ THz
D2 transition frequency	ω_{D2}	$2\pi \cdot 384.2$ THz
laser frequency	ω_L	$2\pi \cdot 377.6$ THz
laser wavelength	λ	793.95 nm
laser power	P	1.681 mW
DMD aperture radius	R_A	920 to 1840 μm
beam size before aperture	w'	1.39 mm
waist of focused beam	w_0	22.7 μm
mean index of refraction of the crystal	n	2
maximal height of the central spot	E_{max}	26.4 kHz

9.3.1 EFFECTIVE GROSS-PITAEVSKII EQUATION

We describe the Bose-condensed gas in the mean-field limit with the time-dependent Gross-Pitaevskii equation (4.36) within the harmonic approximation of the toroidal trap given by the external potential of the form

$$U(\mathbf{r}) = \frac{M}{2}\omega_0^2(\rho - \rho_0)^2 + \frac{M}{2}\omega_z^2 z^2, \quad (9.18)$$

with ring radius ρ_0 and harmonic trap frequencies ω_0 and ω_z in transverse and longitudinal directions. If the chemical potential satisfies the 2d condition for a lower dimension in equation (9.17), we can formulate an effective two-dimensional equation of motion. Assuming that the degrees of freedom in the longitudinal direction are frozen, that is $\omega_z \gg \omega_0$ the condensate wave function factorizes

$$\Psi(\mathbf{r}, t) = \psi(\rho, \varphi, t)\chi(z, t), \quad (9.19)$$

in the wave function $\psi(\rho, \varphi, t)$ depending on the radial and the azimuthal coordinates as well as in the ground state

$$\chi(z, t) = \pi^{-1/4} l_z^{-1/2} e^{-i\omega_z t/2} e^{-z^2/(2l_z^2)}, \quad l_z = \sqrt{\frac{\hbar}{M\omega_z}}, \quad \int |\chi(z, t)|^2 dz = 1, \quad (9.20)$$

of the one-dimensional harmonic oscillator potential. If not stated otherwise, we will use $\omega_z = 2\pi \cdot 500$ Hz in the ongoing chapter. After integrating equation (4.36) along the z -direction and introducing the harmonic oscillator length $l_0 = \sqrt{\hbar/(M\omega_0)}$ and the time $T = 2\pi/\omega_0$ as the natural units (cf. appendix G), one finds an effective dimensionless two-dimensional Gross-Pitaevskii equation

$$i\partial_t\psi(\rho, \varphi, t) = (h + \kappa|\psi|^2)\psi. \quad (9.21)$$

The coupling constant is $\kappa = \sqrt{8\pi}a_s/l_z$ and h denotes the Hamilton operator

$$h = -\frac{1}{2}\left[\partial_\rho^2 + \frac{\partial_\rho}{\rho} + \frac{\partial_\varphi^2}{\rho^2} - (\rho - \rho_0)^2\right], \quad (9.22)$$

consisting of the two-dimensional Laplace operator in polar coordinates and the harmonic ring potential. As the potential does not depend on the azimuthal angle, one finds stationary states of equation (9.21) for different angular momentum manifolds, $|m| \geq 0$, with the ansatz $\psi(\rho, \varphi, t) = \psi_m(\rho)e^{-i\mu t}e^{im\varphi}$,

$$\left[h^{(m)} + \kappa|\psi_m|^2 - \mu\right]\psi_m(\rho) = 0, \quad (9.23)$$

with the Hamilton operator

$$h^{(m)} = -\frac{1}{2}\left[\partial_\rho^2 + \frac{\partial_\rho}{\rho} - \frac{m^2}{\rho^2} - (\rho - \rho_0)^2\right], \quad (9.24)$$

for the angular momentum manifold $|m|$.

9.3.2 LINEAR RESPONSE ANALYSIS

After having introduced the equation of motion, we analyze the excitation spectrum of the Bose-Einstein condensate in the two-dimensional ring configuration in linear response. We formulate the corresponding radial Bogoliubov-de Gennes equations which are solved numerically. In addition, we find an analytic approximation for the collective excitations in the hydrodynamic Thomas-Fermi regime.

BOGOLIUBOV-DE GENNES EQUATION From the effective Gross-Pitaevskii equation (9.21), one can study the linear response to small external perturbations as described in section 4.5. We focus on perturbations $\psi_1(\rho, \varphi, t)$ around the non-rotational ground state $m = 0$, ψ_0 . As in equation (4.87) we use the following ansatz for the wave function in (9.21)

$$\psi(\rho, \varphi, t) = e^{-i\mu t}[\psi_0(\rho) + \psi_1(\rho, \varphi, t)], \quad (9.25)$$

with ψ_0 and μ being determined by the stationary equation (9.23) and

$$\psi_1(\rho, \varphi, t) = u_l(\rho)e^{-i(\varepsilon t - l\varphi)} + v_l^*(\rho)e^{i(\varepsilon t - l\varphi)}. \quad (9.26)$$

u_l, v_l are denoting the excitation modes for positive energies $\varepsilon > 0$ in the angular momentum manifold $|l| \geq 0$. In linear response, one finds the radial Bogoliubov-de Gennes eigenvalue problem for the rotational invariant system

$$\begin{pmatrix} \Sigma^{(l)} & \psi_0^2 \\ -\psi_0^{*2} & -\Sigma^{*(l)} \end{pmatrix} \begin{pmatrix} u_l \\ v_l \end{pmatrix} = \varepsilon \begin{pmatrix} u_l \\ v_l \end{pmatrix}, \quad (9.27)$$

with

$$\Sigma^{(l)} = h^{(l)} + 2\kappa|\psi_0|^2 - \mu. \quad (9.28)$$

The excitation spectrum for a rotating Bose-Einstein condensate in a ring trap has been also investigated in [167] and [168].

HYDRODYNAMIC SOUND WAVES IN THE THOMAS-FERMI LIMIT To get more insight into the excitation spectrum obtained by the Bogoliubov equation (9.27), we study the sound waves in the condensate using the hydrodynamic equations (4.76). Therein, we use the dimensionless Thomas-Fermi density in the harmonic ring potential

$$n_0^{\text{TF}}(\rho) = \left[\mu_{\text{TF}} - \frac{1}{2}(\rho - \rho_0)^2 \right] / \kappa, \quad (9.29)$$

with the radial Thomas-Fermi radius $\rho_{\text{TF}}/l_0 = \sqrt{2\mu_{\text{TF}}}$ and the chemical potential in units of $\hbar\omega_0$

$$\mu_{\text{TF}} = \zeta^{1/3} \left(\frac{3Na_s}{4\sqrt{\pi}\rho_0} \right)^{2/3}, \quad \zeta = \omega_z/\omega_0, \quad (9.30)$$

as well as the gradient $\nabla = \partial_\rho \mathbf{e}_\rho + \rho^{-1} \partial_\varphi \mathbf{e}_\varphi$ in polar coordinates.

In order to find the spectrum for the two-dimensional ring condensate, we look for solutions of equation (4.80) which reads explicitly

$$\omega^2 \bar{n}_1(\rho, \varphi) = -\mu \nabla \left[1 - \left(\frac{\rho - \rho_0}{\rho_{\text{TF}}} \right)^2 \right] \nabla \bar{n}_1. \quad (9.31)$$

We simplify equation (9.31) by introducing, $\bar{n}_1(\rho, \varphi) = D(u)e^{il\varphi}$, new radial functions $D(u)$ with argument $u = (\rho - \rho_0)/\rho_{\text{TF}}$, $-1 \leq u \leq 1$ and angular momentum eigenfunctions $e^{il\varphi}$. We find the following differential equation

$$(1 - u^2)D'' - 2uD' + \frac{1 - u^2}{u + \xi} D' - l^2 \frac{1 - u^2}{(u + \xi)^2} D = \lambda D, \quad (9.32)$$

with the ratio of the ring radius and the Thomas-Fermi size $\xi = \rho_0/\rho_{\text{TF}}$, eigenvalue $\lambda = -2\omega^2/\omega_0^2$ and $D' = dD/du$. For large ring radii and small Thomas-Fermi sizes $\xi \gg 1$, and relatively low angular momenta such that $l/\xi < 1$, we linearize equation (9.32) as

$$(L_0 + \xi^{-1}L_1 + \xi^{-2}L_2)D_n(u) = \lambda_n D_n(u), \quad (9.33)$$

$$L_0 = (1 - u^2) \frac{d^2}{du^2} - 2u \frac{d}{du}, \quad L_1 = (1 - u^2) \frac{d}{du}, \quad L_2 = -uL_1 - l^2(1 - u^2), \quad (9.34)$$

and study the eigenvalues

$$\lambda_n = \lambda_n^{(0)} + \xi^{-1}\lambda_n^{(1)} + \xi^{-2}\lambda_n^{(2)} + \mathcal{O}(\xi^{-3}), \quad (9.35)$$

in perturbation theory for the parameter ξ^{-1} .

For $\xi \rightarrow \infty$, that is either the infinitely large or infinitely thin ring limit, the equations (9.32) and (9.33), reduce to the Legendre's differential equation, $L_0 D_n^{(0)} = \lambda_n^{(0)} D_n^{(0)}$ [103]. Regular solutions are the normalized Legendre polynomials,

$$D_n^{(0)}(u) = \sqrt{\frac{2n+1}{2}} P_n(u), \quad \int_{-1}^1 D_n^{(0)}(u) D_{n'}^{(0)}(u) du = \delta_{nn'}, \quad (9.36)$$

with eigenvalues

$$\lambda_n^{(0)} = -n(n+1), \quad \omega^{(0)}(n) = \omega_0 \left[\frac{n(n+1)}{2} \right]^{1/2}. \quad (9.37)$$

Hence, the excitation frequencies in zeroth order are independent of the angular momentum quantum number l , and the energy spectrum is dominated by collective excitations in the radial direction. Indeed, one finds the same discrete dispersion relation for the Bose-condensed gas trapped in the one-dimensional harmonic oscillator [107]. For higher-order corrections in a thicker ring with a finite ring size, we find

$$\lambda_n^{(1)} = \langle D_n^{(0)} | L_1 | D_n^{(0)} \rangle = 0, \quad (9.38)$$

$$\begin{aligned} \lambda_n^{(2)} &= \sum_{m \neq n} \frac{|\langle D_n^{(0)} | L_1 | D_m^{(0)} \rangle|^2}{\lambda_n^{(0)} - \lambda_m^{(0)}} + \langle D_n^{(0)} | L_2 | D_n^{(0)} \rangle \\ &= -\frac{3n(n+1)}{2(2n+3)(2n-1)} - \frac{l^2}{2} \left[1 - \frac{1}{(2n+3)(2n-1)} \right]. \end{aligned} \quad (9.39)$$

For the evaluation of the matrix elements, we used the derivative of the Legendre polynomials

$$(1-u^2)P_n'(u) = n[P_{n-1}(u) - uP_n(u)], \quad (9.40)$$

and the integral of the triple product

$$\int_{-1}^1 P_{l_1}(u)P_{l_2}(u)P_{l_3}(u) du = 2 \begin{pmatrix} l_1 & l_2 & l_3 \\ 0 & 0 & 0 \end{pmatrix}^2, \quad (9.41)$$

where the expression in the bracket is the $3j$ -symbol [103]. Hence, the excitation spectrum in terms of the ring trap frequency is

$$\begin{aligned} \left(\frac{\omega_{nl}}{\omega_0} \right)^2 &= \frac{n(n+1)}{2} \left[1 + \frac{3\xi^{-2}}{2(2n+3)(2n-1)} \right] \\ &\quad + \frac{\xi^{-2}l^2}{4} \left[1 - \frac{1}{(2n+3)(2n-1)} \right]. \end{aligned} \quad (9.42)$$

From equation (9.42), one sees that the frequency spectrum has two well-separated energy scales for the radial and angular motion. The levels for different n are separated by $\mathcal{O}(\omega_0)$ defining a band structure for different angular momentum l separated by $\mathcal{O}(\xi^{-1}\omega_0)$. We note that similar results have been obtained for the collective excitations of thin three-dimensional, shell-shaped Bose-Einstein condensates [169] as they share the same topology with the two-dimensional ring condensate, having an inner and outer boundary. Therefore it is evident that the energetic spectrum of the collective excitations is dominated by the topology of the condensate.

In figure 9.6 we compare the analytic results (9.42) for the hydrodynamic collective excitation with the Bogoliubov spectrum for the quasi-two-dimensional Bose-Einstein in a ring potential (9.27). For the lowest energy states $\varepsilon_{nl} < 2\hbar\omega_0$, we find particularly very good agreement between these two solutions, as the modes behave more like sound-wave excitations. While the energy difference increases for higher radial excitations, equation (9.42) describes the qualitative behavior

quite well, as the frequencies show little dependence on the angular momentum l . For pure angular collective modes $n = 0$, one finds

$$\omega_{0l} = \omega_0 \xi^{-1} |l| / \sqrt{3}, \quad (9.43)$$

a linear dispersion relation. In contrast to the filled two-dimensional harmonic oscillator (cf. equation (9.48)), the ring-shaped condensate exhibits non-zero angular frequencies that are lower than the radial trap frequency.

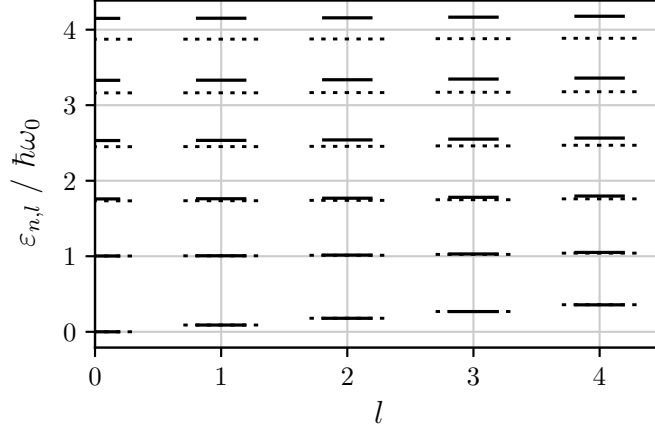


Figure 9.6: Excitation spectrum $\varepsilon_{nl} = \hbar\omega_{nl}$ of the quasi-two-dimensional BEC in a ring potential for the non-rotational ground state $m = 0$. Solid lines are the numerical solutions of the Bogoliubov-de Gennes equations (9.27) for different $l \geq 0$ manifolds. Dashed horizontal lines are referring to the hydrodynamic approximation (9.42) with $\xi = 6.44$ for $\rho_0 = 20 \mu\text{m}$ and $\rho_{\text{TF}} = 3.1 \mu\text{m}$. Parameters: $N = 17\,000$ ^{87}Rb atoms, $\nu_\rho = 100 \text{ Hz}$, $\nu_z = 500 \text{ Hz}$, $\mu_{\text{TF}}/h = 414 \text{ Hz}$.

9.4 COLLECTIVE EXCITATIONS DURING TOPOLOGY CHANGE

In section 9.2.1 we have discussed the topology change from the harmonic to the ring potential for the specific model of conical refraction. In doing so we noticed an abrupt change in the chemical potential as one signature for the transition to different geometry. In the following, we look into the change of the excitation spectrum for the trapped condensate for a model potential that allows a smooth loading of the ring trap potential. As we have seen in the previous section, the frequency spectrum of the collective excitations is strongly influenced by the actual topology of the condensate. As in the transition from filled to hollow sphere [169, 170], we expect a dip in the spectrum around the transition point towards the ring topology.

9.4.1 DEFINITION OF TRANSITION POTENTIAL

In order to describe a smooth transition from harmonic oscillator confinement to a ring geometry, we consider the following model potential

$$U_t(\rho) = \frac{M}{2} \omega^2 \rho^2 + v e^{-\rho^2/(2\sigma^2)}, \quad (9.44)$$

consisting of an outer harmonic confinement with frequency ω as well as a central Gaussian barrier characterized by the central height v and width σ . For $U_t(\rho)$, one finds the following harmonic approximation

$$U_{ho}(\rho) = \begin{cases} \frac{M}{2}\omega_{\perp}^2\rho^2, & \beta \geq 1, \\ \frac{M}{2}\omega_{\perp}^2(\rho - \rho_0)^2 & \beta < 1, \end{cases} \quad (9.45)$$

where we have introduced the dimensionless parameter $\beta = \tilde{\sigma}^2/\tilde{v}$ with $\tilde{\sigma} = \sigma/\sqrt{\hbar/(M\omega)}$, $\tilde{v} = v/(\hbar\omega)$. For the corresponding trapping frequencies one finds

$$\omega_{\perp} = \begin{cases} \omega(1 - \beta^{-1})^{1/2} & \beta \geq 1, \\ \omega(-2 \ln \beta)^{1/2} & \beta < 1, \end{cases} \quad (9.46)$$

whereas the ring radius in equation (9.45) is given by

$$\rho_0 = (-2\sigma^2 \ln \beta)^{1/2}. \quad (9.47)$$

Figure 9.7 depicts the potential (9.44) for different values of β including the initial harmonic oscillator for $\beta \gg 1$, ($\tilde{v} \rightarrow 0$), the transition regime at $\beta = 1$ ($\tilde{v} = 12.25$) as well the ring geometry $\beta = 6.125 \times 10^{-2}$ ($\tilde{v} = 200$).

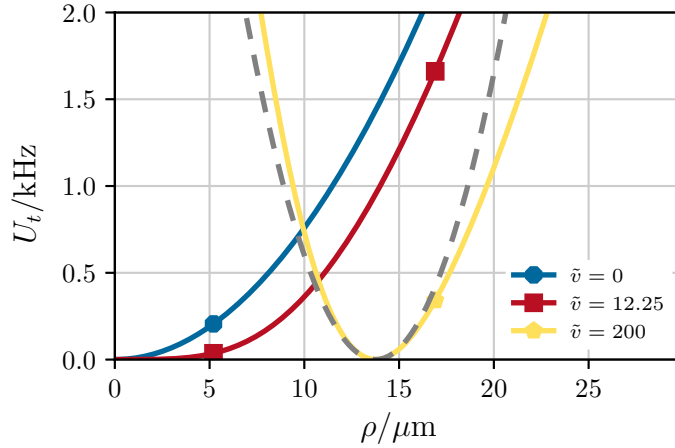


Figure 9.7: Radial symmetric model potential (9.44) for different values of $\tilde{v} = 0, 12.25$ and 200 . Trap parameters in equation (9.44): $\sigma = 5.8 \mu\text{m}$ and $\omega/(2\pi) = 42 \text{ Hz}$. Harmonic approximation (9.45) (grey - - -) with $\rho_0 = 13.8 \mu\text{m}$, $\omega_{\perp}/(2\pi) = 99.3 \text{ Hz}$.

9.4.2 DISCUSSION OF EXCITATION SPECTRUM

In order to investigate the spectrum from harmonic to ring trap we solve the radial Bogoliubov-de Gennes equation (9.27) for varying the potential height for 17 000 ^{87}Rb atoms. The outer harmonic confinement has a trapping frequency of $\omega = 2\pi \cdot 42 \text{ Hz}$ and the Gaussian barrier has a width of $\sigma = 5.8 \mu\text{m}$ as in figure 9.7. The radial excitation energies for the three lowest energy levels are shown in figure 9.8. For $\beta \gg 1$, the trap may be considered as a fully two-dimensional harmonic oscillator. In that case ($v = 0, \beta \rightarrow \infty$), one finds the exact hydrodynamic dispersion relation

$$\omega(n, l) = \omega_{\perp}[2n(n + l + 1) + l]^{1/2}, \quad (9.48)$$

within the Thomas-Fermi approximation [107]. The radial excitations of equation (9.48) are marked as pentagons in figure 9.8 showing good agreement with the numerical solutions of

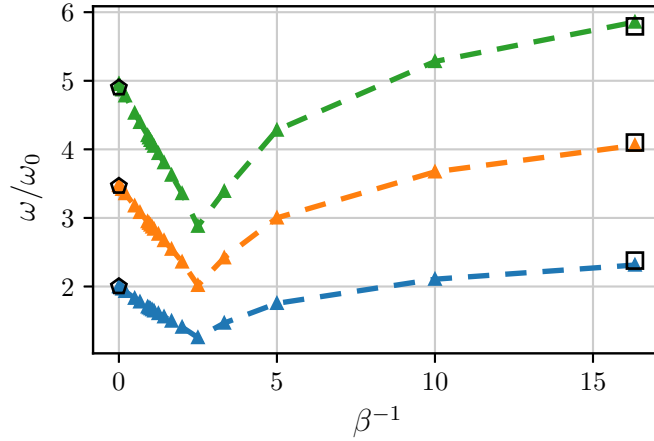


Figure 9.8: First radial excitation frequencies ($n = 1, n = 2, n = 3$) for $l = 0$ versus inverse transition parameter β . Pentagon markers at $\beta \rightarrow \infty$ refer to hydrodynamic approximations for the two-dimensional harmonic oscillator (9.48). Square markers at $\beta = 6.125 \times 10^{-2}$ referring to two-dimensional ring solution in equation (9.42) with $\xi = 4.9$.

equation (9.27). In the other limit, at $\beta = 6.125 \times 10^{-2}$, the squares are marking first radial excitations which are determined by equation (9.42).

As we have seen in the previous section, the frequency spectrum of the collective excitations is strongly influenced by the actual topology of the condensate. The frequency curves can be distinguished throughout the transition and do not cross each other. The topological change appears as a clear visible dip in the spectrum at $\beta^{-1} = 2.5$. That is where the radial density $n(0) \approx 0$ vanishes at the origin and forms an inner and outer boundary. Thus, the condensate's density has changed its topology from single to multiple connected. The same signature is observed in the hollowing transition from a three-dimensional filled sphere to a shell-shaped condensate [169, 170], stating that the spectrum is a feature of the topology change and does not depend on the details of the potential or the spatial dimension.

9.5 DAMPING WITH FEEDBACK

So far we have only discussed static properties of the toroidal Bose-Einstein condensate. In addition, we did not consider any mechanism of symmetry breaking in the external potential, which happens inevitably in a realistic experimental setting. As an outlook, we will briefly discuss the radial excitations of the condensate that occur during the loading of the ring trap and present a control mechanism to damp the motion close to the ground state of the system.

The dynamical transfer from the simply connected harmonic oscillator to the multiple connected toroidal trap configuration leads inevitably to excitations in the Bose-Einstein condensate. For the radial symmetric trap, we expect a radial center of mass oscillations around the new equilibrium positions. Further, a change in frequency in the different trap geometries will lead to quadrupole excitations changing the radial width of the condensate. The dynamics of the system is described by the time-dependent effective two-dimensional Gross-Pitaevskii equation (9.21) with the time-dependent Hamiltonian operator

$$h^{(0)}(t) = -\frac{1}{2} \left(\partial_\rho^2 + \frac{\partial_\rho}{\rho} \right) + U_t(\rho, t). \quad (9.49)$$

In the transition potential U_t (9.44) we consider for the sake of convenience just the height of the Gaussian barrier $v = v(t)$ to be time-dependent. For the barrier, we choose a smooth pulse shape in form of a Blackman time window

$$w(\tilde{t}) = \frac{1}{42\pi} [21(\pi + \tilde{t}) + 25 \sin(\tilde{t}) + 2 \sin(2\tilde{t})], \quad \tilde{t}(t) = \frac{2\pi}{t_{\max}} t - \pi. \quad (9.50)$$

For the time evolution, we have chosen the same initial trap parameters as in the previous section, with angular frequency $\omega = 2\pi \cdot 42$ Hz and width of the Gaussian barrier $\sigma = 5.8 \mu\text{m}$. The height of the Gaussian barrier is varied within 45 ms from $v = 0$ to $v = 200 \hbar\omega$ as shown in figure 9.9. We end in the final ring geometry displayed in figure 9.7 with ring radius $\rho_0 = 13.8 \mu\text{m}$

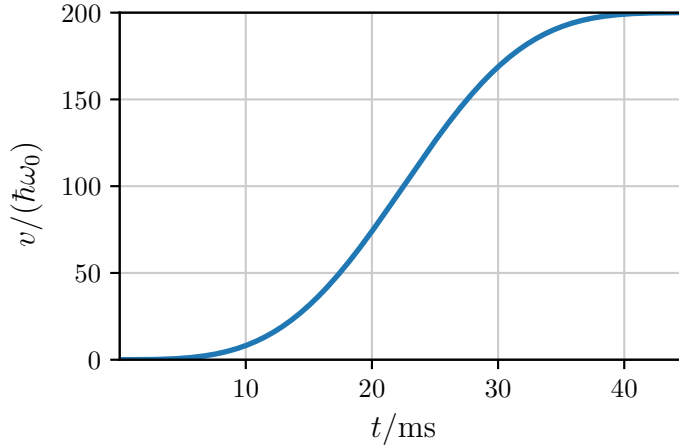


Figure 9.9: Central barrier $v(t)$ versus time t . Blackman pulse shape (9.50) with $t_{\max} = 45$ ms.

and trap frequency $\nu_{\perp} = 99.2$ Hz. Figure 9.10 shows the initial density n_0 at $t = 0$, the stationary equilibrium density distribution of the final trap n_f and the density $n(\rho, t)$ at $t = 80.81$ ms. We monitor the fidelity

$$\mathcal{F}(t) = |\langle \psi(t), \psi(t_e) \rangle|^2 = |2\pi \int \psi^*(\rho, t) \psi_0(\rho, t_e) \rho d\rho|^2, \quad (9.51)$$

with respect to the stationary state $\psi_0(t_e)$ in the final trap configuration as well as the first and second moments $\langle \rho^n(t) \rangle = 2\pi \int \rho^{n+1} |\psi(\rho, t)|^2 d\rho$ during the 45 ms transition and 55 ms holding time in the final ring trap.

Figure 9.11 depicts the mean radial position $\langle \rho(t) \rangle$, the radial width $\sigma_{\rho}(t) = \sqrt{\langle \rho^2 \rangle - \langle \rho \rangle^2}$ as well as the fidelity $\mathcal{F}(t)$ (9.51). $n(\rho, t)$ oscillates around the equilibrium position ρ_0 exhibiting additional periodic density perturbations which change the shape of density, (cf. figure 9.10), caused by the change of the frequency and the shape of the final potential which deviates from the harmonic approximation. To the oscillatory motions, we fit sinusoidal functions to obtain the excitation frequencies. For the radial oscillations, we find $\nu'_{\rho} = 96.5$ Hz and for the widths $\nu'_{\sigma} = 173.3$ Hz. In addition to the sinusoidal fit, we investigate the spectra $\tilde{\rho}(\omega), \tilde{\sigma}(\omega)$ shown in figure 9.12. The characteristic frequencies are visible as clear peaks in the spectrum. Moreover, we added the first Bogoliubov excitations ω_{n0} (cf. figure 9.8) which characterize the radial excitations as a “dipole” $n = 1$ and a “quadrupole” $n = 2$ mode.

In order to minimize radial excitations, one could implement methods of optimal control for a quasi-adiabatic transfer to the ground state of the system. In [171], they investigated the loading from a slightly elongated harmonic to a toroidal potential, using one frequency component of the harmonic trap and the Gaussian barrier as control parameters with fixed boundaries. Alternatively,

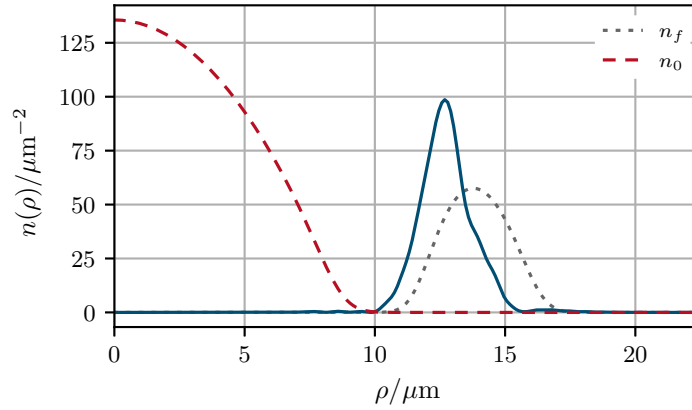


Figure 9.10: Radial density $n(\rho, t)$ at $t = 80.81$ ms after 45 ms transition from harmonic to ring potential (blue —). n_0 initial density in the harmonic oscillator potential (red - -). n_f is the ground state density in the final ring trap (grey ····).

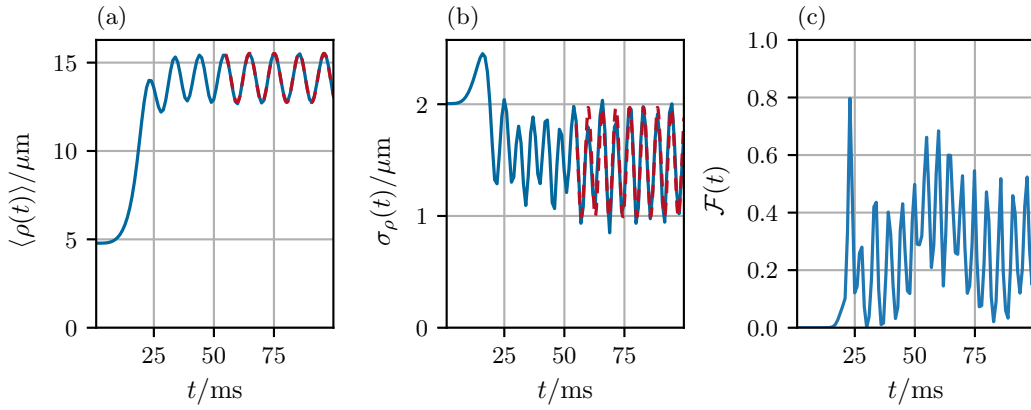


Figure 9.11: (a) mean radial position $\langle \rho(t) \rangle$, $\nu'_\rho = 96.5$ Hz, (b) mean radial width $\sigma_\rho(t)$, $\nu'_\sigma = 173.3$ Hz, (c) fidelity $\mathcal{F}(t)$ versus time. Fit of sinusoidal function $f(t) = a \sin(\omega't + \phi) + c$ (red - -). Sequence: transition $t = 45$ ms, hold $t = 55$ ms.

one could use shortcuts to adiabaticity which provide fast routes to the desired final state compared to the slow adiabatic changes of the control parameters [86]. In [172], they have implemented a scaling solution that solves approximately the hydrodynamic equations (4.66) and (4.67) for a Bose-Einstein condensate inside a toroidal potential. Within this approach, they have modeled the evolution of the condensate in an expanding harmonic ring potential [173]. Minimizing radial mode oscillations could be accomplished by solving the obtained differential equations for the scaling parameters with fixed boundary conditions.

We propose a method based on a feedback control as introduced in [174]. Therein external perturbations in the trap potential and changes in the interaction strengths were used to control the motion of a Bose-Einstein condensate in a one-dimensional harmonic oscillator potential. For an appropriate choice of controls, the feedback alters the initial state ψ_0 with energy E_0 to a state ψ_1 with energy E_1 , such that $E_1 < E_0$ when the feedback control is switched off.

We consider the following scheme to damp the motion in the final ring configuration: We solve the time-dependent Gross-Pitaevskii equation within the potential

$$U(\rho, t) = U_t(\rho, t_f) + \sum_i a_i(t) V_i(\rho). \quad (9.52)$$

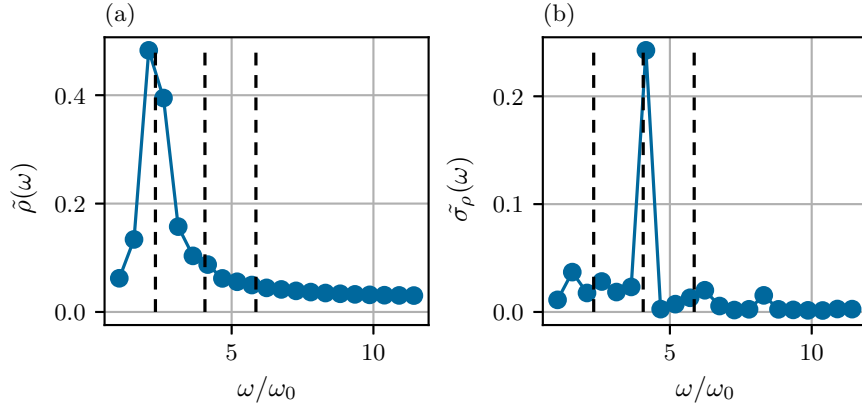


Figure 9.12: Frequency spectrum of the radial excitations in the final ring trap. (a) $\tilde{\rho}(\omega)$, (b) $\tilde{\sigma}_\rho(\omega)$. Dashed lines corresponds the first radial excitations ω_{n0} in the Bogoliubov spectrum in figure 9.8.

Here $U_t(\rho, t_f)$ denotes the final, desired trapping potential as discussed before (cf. figure 9.7). Further, we have now included the set of control potentials $\{V_i\}$ with time-dependent coefficients $\{a_i\}$. They serve as control parameters which are based on the oscillatory change in the first and second moments of the condensate. For damping the radial excitations, we choose the following external control potentials

$$V_1 = \rho, \quad a_1(t) = c_1 \frac{d}{dt} \langle \rho \rangle, \quad (9.53)$$

$$V_2 = \rho^2, \quad a_2(t) = c_2 \frac{d}{dt} \langle \rho^2 \rangle, \quad (9.54)$$

whereas the values of $\{c_i\}$ can be used to optimize the damping rate.

If $U(\rho, t_f)$ is well approximated by its quadratic approximation in equation (9.45), the Ehrenfest theorem for the non-interacting gas $\kappa = 0$ provides the equation of motion for the mean radial position

$$\begin{aligned} \frac{d^2}{dt^2} \langle \rho \rangle &= - \langle \rho \rangle [1 + 2a_2(t)] - a_1(t) + \rho_0 \\ &= - \langle \rho \rangle \bar{\omega}^2(t) - c_1 \frac{d}{dt} \langle \rho \rangle + \rho_0, \quad \bar{\omega}^2 = [1 + 2a_2(t)] \end{aligned} \quad (9.55)$$

which is a damped harmonic oscillator equation with time-dependent angular frequency. Critical damping of the oscillatory motion is achieved by choosing the coefficient as $c_1 = 2\sqrt{1 + 2a_2(t)}$. The results of the feedback damping for damping coefficients $c_2 = 0$ and $c_2 = 0.2$ are summarized in figure 9.13 and 9.15 respectively. In both cases, we have turned on the feedback for 70 ms, after a holding time for 10 ms in the final trap. In the first case ($c_2 = 0$), we have disregarded the coupling to the radial width of the condensate. While we see critical damping of the radial oscillations in $\langle \rho(t) \rangle$, the change in $\sigma_\rho(t)$ is not affected. However, the mean fidelity increases from $\mathcal{F} \approx 0.3$ to $\mathcal{F} > 0.8$ when we control the first moment $\langle \rho(t) \rangle$ of the condensate. The damping of the dipole mode becomes also visible in the spectra depicted in figure 9.14, where the amplitude of the first excited mode decreases by a factor of ≈ 10 , while the spectrum of $\tilde{\sigma}_\rho$ is almost unaffected after the feedback.

When we set $c_2 = 0.2$, we achieve exponential damping in the radial width and a fidelity close to $\mathcal{F} \approx 0.98$. As the center of mass motion is not decoupled from the relative motion in the anharmonic ring configuration, we recognize that the damping of $\sigma_\rho(t)$ affects the motion of the radial mean position $\langle \rho(t) \rangle$. The latter becomes clear when regarding the spectra in figure 9.16

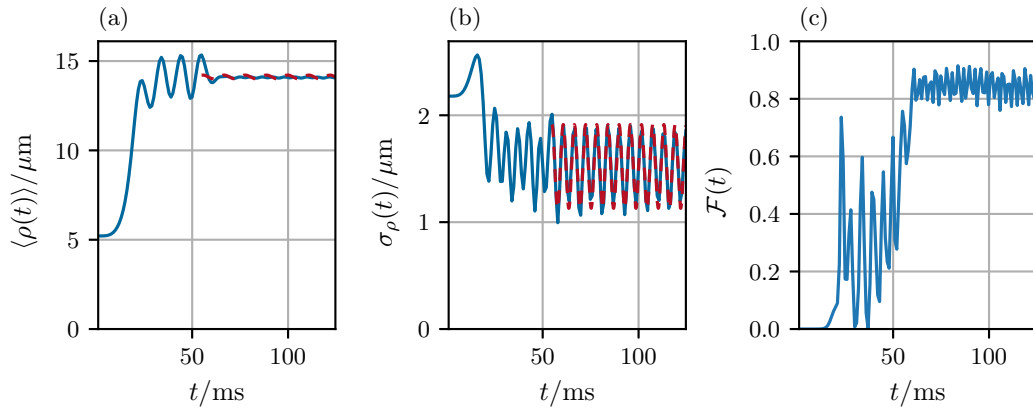


Figure 9.13: (a) mean radial position $\langle \rho(t) \rangle$, $\nu'_\rho = 90.6$ Hz, (b) mean radial width $\sigma_\rho(t)$, $\nu'_\sigma = 171.5$ Hz, (c) fidelity $\mathcal{F}(t)$ versus time. Control potentials turned on after 10 ms holding in final trap configuration. Control parameters: $c_1 = 2\sqrt{1 + 2a_2}$, $c_2 = 0$. Fit of sinusoidal function $f(t) = a \sin(\omega't + \phi) + c$ (red - - -). Sequence: transition $t = 45$ ms, hold $t = 10$ ms, feedback $t = 70$ ms.

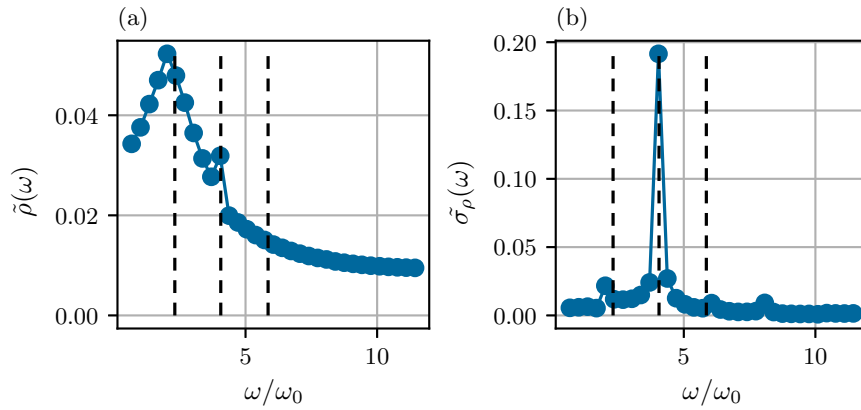


Figure 9.14: Frequency spectrum of the radial excitations in the final ring trap including the feedback damping. (a) $\tilde{\rho}(\omega)$, (b) $\tilde{\sigma}_\rho(\omega)$. Dashed lines correspond to the first radial excitations ω_{n0} in the Bogoliubov spectrum in figure 9.8.

(a) for $\tilde{\rho}$. The amplitude of the dipole mode is larger than in figure 9.14 when we considered pure radial damping. In addition, the spectrum now contains a second frequency that corresponds to the quadrupole excitation which is damped in the oscillatory motion of $\sigma_\rho(t)$. In general, the non-linearity in the Gross-Pitaevskii equation couples higher energetic modes to the controlled modes which leads to an inefficient damping process. Performance of the feedback damping might be increased using a non-linear control by tuning the interaction strength of the condensate via Feshbach resonances [144, 174].

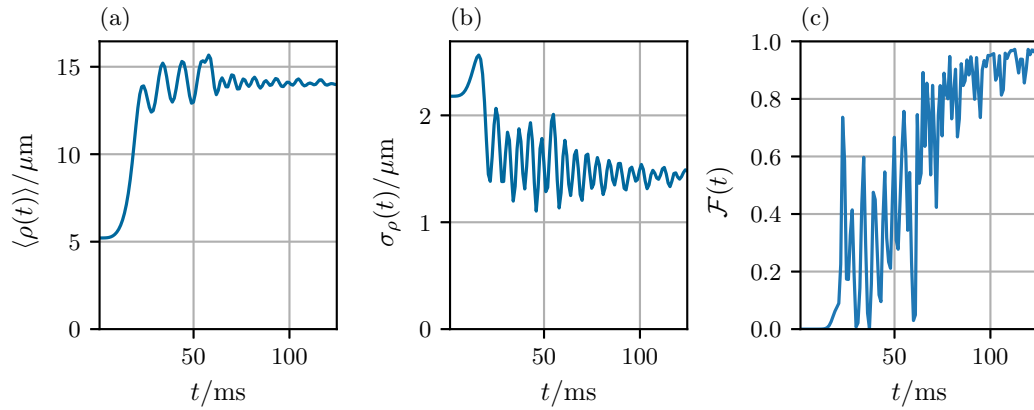


Figure 9.15: (a) mean radial position $\langle \rho(t) \rangle$, (b) mean radial width $\sigma_\rho(t)$, (c) fidelity $\mathcal{F}(t)$ versus time. Control potentials turned on after 10 ms holding in final trap configuration. Control parameters: $c_1 = 2\sqrt{1 + 2a_2}$, $c_2 = 0.2$. Sequence: transition $t = 45$ ms, hold $t = 10$ ms, feedback $t = 70$ ms.

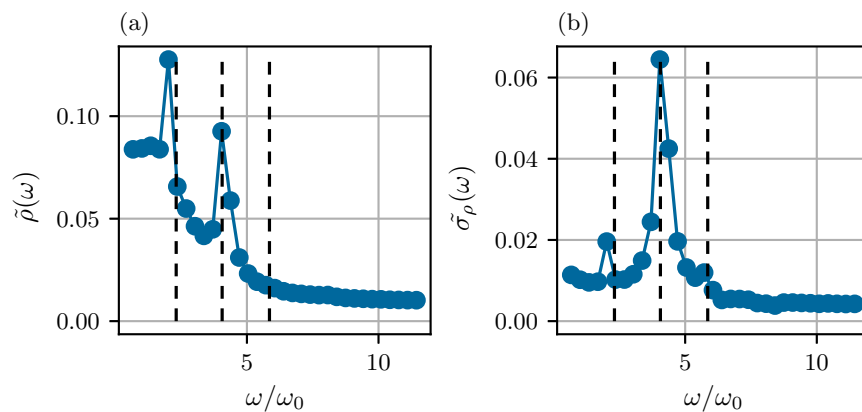


Figure 9.16: Frequency spectrum of the radial excitations in the final ring trap including the feedback damping. (a) $\tilde{\rho}(\omega)$, (b) $\tilde{\sigma}_\rho(\omega)$. Dashed lines correspond to the first radial excitations ω_{n0} in the Bogoliubov spectrum in figure 9.8.

10 CONCLUSION AND OUTLOOK

This thesis investigates aberrations in (3+1)d matter-wave optics adapting Zernike's approach from light optics using orthogonal basis functions to describe wavefront distortions in expanded and collimated Bose-Einstein condensates.

Microgravity platforms require a miniaturizing of the experimental setup utilizing magnetic chip traps for realizing versatile trapping potential. The chip model consists of a set of finite wires matching the geometry of its real-world copy. Based on magnetic field simulations, using the Biot-Savart law, we deduce the Zeeman potential and trapping parameters for a Bose-Einstein condensate of rubidium atoms.

For a theoretical description, we use the three-dimensional Gross-Pitaevskii equation without any symmetries. Numerical ground state solutions are obtained efficiently using a Newton optimization scheme that includes the second-order expansion of the Gross-Pitaevskii functional. Concerning the initial distribution, we have derived the Rayleigh widths in momentum space for an initial Thomas-Fermi distribution in an anisotropic d-dimensional harmonic oscillator [51]. Neglecting the quantum pressure, one finds an analytic solution of the Euler equation in the Thomas-Fermi approximation in terms of scaling equations. These scales define a canonical phase space transformation transforming the initial time-dependent quadratic Hamiltonian to a new time-independent Hamilton function with trivial dynamics. The latter can be used to solve the Liouville equation which governs the time evolution for a classical phase distribution.

For representing matter waves in phase space, one utilizes the Wigner function. In a semi-classical approximation, the Wigner function follows a phase flow on classical trajectories. As the Gaussian trial states disregard the mean-field interactions, we approximate the Thomas-Fermi coherence function to find an appropriate representation of the Thomas-Fermi Wigner function in a one-dimensional harmonic oscillator potential. As discussed in [51], a representation for the six-dimensional s-wave Wigner function is still an open question. Due to the rotational symmetry, it would be natural to expand the phase space distribution in terms of angular momentum states and radial functions depending on the magnitude of position and momentum coordinates.

To make (3+1)d Gross-Pitaevskii simulation with long expansion times feasible, one requires a co-expanding reference frame. Within the latter, we define the Gross-Pitaevskii scaling approximation as a reference state for aberration analysis that includes the non-quadratic time evolution, either generated by the kinetic energy perturbation or by anharmonic external potentials. For small perturbations, these aberrations are characterized by the Bogoliubov basis of the initially trapped condensate. We interpret the basis expansion coefficient as aberration coefficients for (3+1)d matter-wave optics with interacting Bose-Einstein coefficients.

While the Bogoliubov modes are the optimal basis function to describe the perturbations for an expanded Bose-Einstein condensate, we prefer to characterize density and phase aberrations in terms of known three-dimensional basis functions. For the Thomas-Fermi density in a three-dimensional spherical harmonic oscillator potential, density and phase fluctuations are given in terms of the Jacobi polynomials.

As external potentials are a main source of aberrations, we use these Stringari polynomials to characterize the shape of popular trapping potentials. In particular, we analyze the Zeeman potential of the magnetic chip trap that is obtained in the Z-wire configuration. For an optical dipole potential with Laguerre-Gaussian beam, the expansion of the cumulant is advantageous.

By comparing the results with the harmonic approximation, we find that our multipole expansion is very sensitive noting differences on machine precision level.

The polynomial approach opens up possibilities for efficient interpolation schemes for representing Bose-Einstein condensates. In the strongly interacting regime, the Thomas-Fermi approximation is directly proportional to the potential. Hence, our former results are directly applicable to represent the three-dimensional condensate. Considering the exact numerical Gross-Pitaevskii density, we regard different interaction strengths. Depending on the particle number, the expansion of the cumulant or the plain density is more suitable. The expansion for the Gross-Pitaevskii field in terms of Stringari polynomials is limited by the high-energetic density tails beyond the Thomas-Fermi radius.

With our multipole expansion, we characterize aberrations in a single-lens delta-kick collimation sequence with long expansion times. We look for deviations in the phase evolution of expanding Bose-Einstein condensates that are needed to describe matter wave interference. As the condensate probes different regions of the magnetic Zeeman potential, we find deviations of the quadratic phase during the ballistic time evolution as well as after the magnetic lens. Resolved in angular momentum states and radial polynomials, we present these wavefront aberrations in a “Seidel-diagram”. Further, the influence on the beam splitter performance as well as on the contrast of the inference pattern is required. Phase shifts in the interferometer due to mean-field interactions have been investigated in [145, 146], but just include the quadratic temporal evolution in the Thomas-Fermi regime [146]. For the latter, we found additional deviations for long expansion times that could be potentially investigated on microgravity platforms.

The topology change to toroidal condensates has a substantial impact on the excitation spectrum which has - to our knowledge - not been experimentally investigated yet. In this work, we have only investigated rings with spherical symmetry. For a more realistic description of current experiments, we need to take frequency shifts in symmetry-broken rings into account. Optical DMD potentials could be used to investigate different geometries systematically. DMD patterns are usually based on physical models and assumptions of the systems. As both pieces of information are limited, an optimization of the optical dipole potential with respect to the desired potential also requires experimental feedback measurements. Feedback optimization based on Iterative Learning Control information has been investigated in [175, 176], to shape one-dimensional potentials. Further, we have not discussed the feasibility of the feedback damping mechanism in current experiments.

A WAVE PACKET DYNAMICS

A.1 SCHRÖDINGER PROPAGATION

One can solve the free-particle Schrödinger equation directly in the momentum representation

$$\tilde{\Phi}(\mathbf{k}, t) = e^{-i\alpha\mathbf{k}^2/2}\tilde{\Phi}(\mathbf{k}, 0), \quad \alpha(t) = \frac{\hbar}{M}t, \quad (\text{A.1})$$

$$\Phi(\mathbf{r}, t) = \int \frac{e^{i\mathbf{k}\mathbf{r}}}{(2\pi)^{3/2}}\tilde{\Phi}(\mathbf{k}, t) d^3k. \quad (\text{A.2})$$

The time evolution in the position representation is recovered using the Fourier integral (A.2). In order to study the long-time solution, we rewrite equation (A.2) as a convolution integral

$$\Phi(\mathbf{r}, t_1) = \int G_0(\mathbf{r}, t_1; \mathbf{r}', t_0)\Phi(\mathbf{r}', t_0) d^3r', \quad (\text{A.3})$$

where

$$G_0(\mathbf{r}, t; \mathbf{r}, 0) = \int \frac{e^{i\mathbf{k}\mathbf{r}}}{(2\pi)^{3/2}}e^{-i\alpha\mathbf{k}^2/2} d^3k = \left(\frac{i}{\alpha}\right)^{3/2}e^{i\mathbf{r}^2/(2\alpha)}, \quad (\text{A.4})$$

is the Green's function for the free propagation of the Schrödinger equation evaluated at equal points in space.

GAUSSIAN WAVE PACKET We consider a Gaussian wave packet in position

$$\Phi(\mathbf{r}, 0) = e^{i\mathbf{k}_0(\mathbf{r}-\mathbf{r}_0)}e^{-\frac{1}{2}(\mathbf{r}-\mathbf{r}_0)(2\Sigma_r^{-1})(\mathbf{r}-\mathbf{r}_0)}, \quad (\text{A.5})$$

$$\tilde{\Phi}(\mathbf{k}, 0) = \sqrt{|2\Sigma_r|}e^{i\mathbf{k}\mathbf{r}_0}e^{-\frac{1}{2}(\mathbf{k}-\mathbf{k}_0)(2\Sigma_r)(\mathbf{k}-\mathbf{k}_0)}, \quad (\text{A.6})$$

as well as in Fourier space at the initial position \mathbf{r}_0 and with the initial momentum $\mathbf{k}_0 = \mathbf{p}_0/\hbar$. The orientation and width of the Gaussian in position space are determined by the symmetric covariance matrix $\Sigma_r = \langle(\mathbf{r} - \mathbf{r}_0) \otimes (\mathbf{r} - \mathbf{r}_0)\rangle$. One finds the free wave packet spreading

$$\Phi(\mathbf{r}, t) = \sqrt{\frac{|\Sigma_r|}{|\Sigma_r(t)|}}e^{i\mathbf{k}_0(\mathbf{r}-\mathbf{r}_0)}e^{-i\alpha\mathbf{k}_0^2/2}e^{-\frac{1}{2}[\mathbf{r}-\mathbf{r}(t)][2\Sigma_r(t)][\mathbf{r}-\mathbf{r}(t)]}, \quad (\text{A.7})$$

by inserting equation (A.6) into the free particle propagation (A.2) of the Schrödinger equation. The wave packet moves along the center of mass position $\mathbf{r}(t) = \mathbf{r}_0 + \mathbf{v}_0t$ with the group velocity $\mathbf{v}_0 = \hbar\mathbf{k}_0/M$. The time-dependent covariance matrix in equation (A.7) reads

$$\Sigma_r(t) = \Sigma_r + i\alpha/2. \quad (\text{A.8})$$

LONG-TIME EXPANSION To study the free-particle Schrodinger evolution for long expansion times, one can examine the convolution integral in equation (A.3). In the limit $t \rightarrow \infty$, only

values at wavenumbers $\mathbf{k} = \mathbf{r}/\alpha$ are contributing to the integral. Thus the wave function for in the far-field limit is given by

$$\Phi(\mathbf{r}, t) \simeq \left(\frac{i}{\alpha}\right)^{3/2} e^{i\mathbf{r}^2/(2\alpha)} \tilde{\Phi}(\mathbf{r}/\alpha), \quad (\text{A.9})$$

the Fourier transform of the initial state which corresponds to the Fraunhofer diffraction limit in optics.

A.2 GROSS-PITAEVSKII PROPAGATION

The ballistic expansion for a Bose-Einstein condensate which was initially trapped in a harmonic oscillator potential has been discussed in chapter 8. The ballistic expansion is already incorporated in the scaling approximation, where the adaptive scales follow equation (4.72).

The momentum distribution of the expanding Bose-Einstein condensate in the scaling approximation (6.11) is given by

$$\begin{aligned} \tilde{\Psi}(\mathbf{k}, t) &= \int \frac{e^{-i\mathbf{k}^\top \mathbf{r}}}{(2\pi)^{3/2}} \Psi_s(\mathbf{r}, t) d^3r = |\Lambda|^{1/2} \int \frac{e^{-i\boldsymbol{\kappa}^\top \boldsymbol{\xi}}}{(2\pi)^{3/2}} e^{iS(\boldsymbol{\xi}, t)/\hbar} \psi_0(\boldsymbol{\xi}) d^3\xi \\ &= |\Lambda|^{1/2} \tilde{\psi}_0(\boldsymbol{\kappa}, t), \quad \boldsymbol{\kappa} = \Lambda^\top \mathbf{k}. \end{aligned} \quad (\text{A.10})$$

In order to determine the momentum distribution for long expansion times, we are using again the convolution theorem. Disregarding the center mass motion, $\boldsymbol{\eta}(t) = \dot{\boldsymbol{\eta}}(t) = 0$, in the phase $S(\mathbf{r}, t)$, the equation above becomes

$$\tilde{\Psi}(\mathbf{k}, t) = \left(\frac{i\hbar}{M}\right)^{3/2} |\dot{\Lambda}|^{-1/2} e^{i\tilde{S}(\boldsymbol{\kappa}, t)} \int \frac{e^{i\boldsymbol{\xi}'^\top \boldsymbol{\kappa}'}}{(2\pi)^{3/2}} e^{-i\hbar M \boldsymbol{\kappa}'^\top \mathbf{A}^{-1} \boldsymbol{\kappa}'/2} \tilde{\psi}_0(\boldsymbol{\kappa}') d^3\boldsymbol{\kappa}', \quad (\text{A.11})$$

$$\tilde{S}(\boldsymbol{\kappa}, t) = e^{-i[\hbar \boldsymbol{\kappa}^\top \mathbf{A}^{-1} \boldsymbol{\kappa}/(2M) + \mu\tau/\hbar]}, \quad \boldsymbol{\xi}' = \dot{\Lambda}^{-1} \frac{\hbar \mathbf{k}}{M}, \quad (\text{A.12})$$

where we have introduced the new coordinate $\boldsymbol{\xi}'$. As $\mathbf{A}^{-1} = \dot{\Lambda}^{-1} \Lambda^{-\top}$, we expect the quadratic phase to decrease linearly in time for $t \rightarrow \infty$. Hence in the far-field zone, one obtains the following relation for the Gross-Pitaevskii wave function in momentum space

$$\tilde{\Psi}(\mathbf{k}, t) \simeq \left(\frac{i\hbar}{M}\right)^{3/2} |\dot{\Lambda}|^{-1/2} e^{i\tilde{S}(\boldsymbol{\kappa}, t)} \psi_0(\boldsymbol{\xi}'). \quad (\text{A.13})$$

Thus, in contrast to the Schrödinger propagation the momentum distribution for the condensate, depends on the initial distribution in position space.

THOMAS-FERMI LIMIT Within the scaling approximation, we can use the Thomas-Fermi field $\psi_0(\boldsymbol{\xi}') = \psi_{\text{TF}}(\boldsymbol{\xi}')$ as the initial wave function in equation (A.13). The orientation of the ellipsoid in k -space is then determined

$$\Sigma_k(t) = \dot{\Lambda} \left[\Omega(0)^2 \right]^{-1} \dot{\Lambda}^\top, \quad (\text{A.14})$$

by the dimensionless matrix Σ_k , which depends on the initial trapping matrix and the time-dependent scaling velocities $\dot{\Lambda}$. For the Thomas-Fermi density distribution $|\tilde{\Psi}_{\text{TF}}(\mathbf{k})|^2 = \tilde{n}_{\text{TF}}(\mathbf{k})$ in momentum space, one finds

$$\tilde{n}_{\text{TF}}(\mathbf{k}, t) = \frac{\hbar^3}{|\Lambda|gM^3} \left[\mu_{\text{TF}} - \frac{\hbar^2}{2M} \mathbf{k}^\top \Sigma_k^{-1}(t) \mathbf{k} \right], \quad (\text{A.15})$$

for large expansion times.

As the diffraction efficiency for an atomic beam splitter depends on the shape of the wave function in momentum space, the equations (A.13) and (A.15) provide an alternative description to the Gaussian state approximation [177]. For experimental observables along a particular spatial direction, we can use the integrated Thomas-Fermi distribution given in [79] to obtain the one-dimensional integrated momentum distribution

$$\begin{aligned} \tilde{n}_{\text{TF}}^{1d}(k_z, t) &= \int \int \tilde{n}_{\text{TF}}(\mathbf{k}, t) dk_x dk_y \\ &= \frac{\pi \hbar}{gM^2 \sqrt{\Sigma_{k,33}(t) |\Omega^2(0)|}} \left[\mu_{\text{TF}} - \frac{\hbar^2 k_z^2}{2M \Sigma_{k,33}(t)} \right]^2, \end{aligned} \quad (\text{A.16})$$

where $\Sigma_{k,33}$ is the matrix entry corresponding to the k_z direction at the third row and the third column position of the matrix Σ_k .

B OBSERVABLES IN SCALED REFERENCE FRAME

As the complex wave function is not a physical quantity that can be measured experimentally, we discuss the evaluation of different expectation values of some important operators. Of special significance are the first and second moments of the position and momentum. The central second moment is given by the covariance matrices

$$\Sigma_{\mathbf{r}} = \langle (\mathbf{r} - \mathbf{r}_0) \otimes (\mathbf{r} - \mathbf{r}_0) \rangle, \quad (\text{B.1})$$

and

$$\Sigma_{\mathbf{p}} = \langle (\mathbf{p} - \mathbf{p}_0) \otimes (\mathbf{p} - \mathbf{p}_0) \rangle. \quad (\text{B.2})$$

To make use of the numerical advantage of the adaptive scales $\Lambda(t)$, we require the canonical scaling transformation (3.32) that describes the relation between initial $\boldsymbol{\xi} = \mathbf{r}(0)$, $\boldsymbol{\pi} = \mathbf{p}(0)$, and rescaled coordinates in the original frame of reference.

Expectation value can be evaluated either using the evolved wave function $\psi(\boldsymbol{\xi}, t)$ using the time-dependent Gross-Pitaevskii equation (6.3) or using the scaling approximation (6.11) with the stationary solution $\psi_0(\boldsymbol{\xi})$. In the following, we assume that the condensate wave function is normalized as $\int |\Psi|^2 d^3r = \int |\psi|^2 d^3\xi = 1$ and expectation values in coordinate space read

$$\langle \boldsymbol{\xi} \rangle = \int \boldsymbol{\xi} |\psi(\boldsymbol{\xi}, t)|^2 d^3\xi, \quad \langle \boldsymbol{\pi} \rangle = -i\hbar \int \psi^*(\boldsymbol{\xi}, t) \nabla_{\boldsymbol{\xi}} \psi(\boldsymbol{\xi}, t) d^3\xi. \quad (\text{B.3})$$

B.1 POSITION

The expectation value for the position operator reads

$$\langle \mathbf{r} \rangle = \Lambda \langle \boldsymbol{\xi} \rangle + \boldsymbol{\eta}. \quad (\text{B.4})$$

The product is

$$\langle \mathbf{r} \rangle \otimes \langle \mathbf{r} \rangle = \langle \boldsymbol{\xi} \rangle \Lambda^T \otimes \Lambda \langle \boldsymbol{\xi} \rangle + \langle \boldsymbol{\xi} \rangle \Lambda^T \otimes \boldsymbol{\eta} + \boldsymbol{\eta} \otimes \Lambda \langle \boldsymbol{\xi} \rangle + \boldsymbol{\eta} \otimes \boldsymbol{\eta}. \quad (\text{B.5})$$

For the second moment, one finds

$$\begin{aligned} \langle \mathbf{r} \otimes \mathbf{r} \rangle &= \langle (\Lambda \boldsymbol{\xi} + \boldsymbol{\eta}) \otimes (\Lambda \boldsymbol{\xi} + \boldsymbol{\eta}) \rangle \\ &= \langle \boldsymbol{\xi} \Lambda^T \otimes \Lambda \boldsymbol{\xi} \rangle \\ &\quad + \langle \boldsymbol{\xi} \Lambda^T \otimes \boldsymbol{\eta} \rangle \\ &\quad + \langle \boldsymbol{\eta} \otimes \Lambda \boldsymbol{\xi} \rangle \\ &\quad + \boldsymbol{\eta} \otimes \boldsymbol{\eta}. \end{aligned} \quad (\text{B.6})$$

Therefore, we find the covariance matrix

$$\Sigma_{\mathbf{r}} = \langle \mathbf{r} \otimes \mathbf{r} \rangle - \langle \mathbf{r} \rangle \otimes \langle \mathbf{r} \rangle = \langle \boldsymbol{\xi} \Lambda^T \otimes \Lambda \boldsymbol{\xi} \rangle - \langle \boldsymbol{\xi} \rangle \Lambda^T \otimes \Lambda \langle \boldsymbol{\xi} \rangle. \quad (\text{B.7})$$

B.2 MOMENTUM

The expectation value for the momentum operator reads

$$\langle \mathbf{p} \rangle = \Lambda^{-\top} \langle \boldsymbol{\pi} \rangle + M \dot{\Lambda} \langle \boldsymbol{\xi} \rangle + M \dot{\boldsymbol{\eta}}. \quad (\text{B.8})$$

The product is

$$\begin{aligned} \langle \mathbf{p} \rangle \otimes \langle \mathbf{p} \rangle &= \langle \boldsymbol{\pi} \rangle \Lambda^{-1} \otimes \Lambda^{-\top} \langle \boldsymbol{\pi} \rangle \\ &+ \langle \boldsymbol{\pi} \rangle \Lambda^{-1} \otimes M \dot{\Lambda} \langle \boldsymbol{\xi} \rangle + \text{h.c.} \\ &+ \langle \boldsymbol{\pi} \rangle \Lambda^{-1} \otimes M \dot{\boldsymbol{\eta}} + \text{h.c.} \\ &+ M^2 \langle \boldsymbol{\xi} \rangle \dot{\Lambda}^\top \otimes \dot{\boldsymbol{\eta}} + \text{h.c.} \\ &+ M^2 \langle \boldsymbol{\xi} \rangle \dot{\Lambda}^\top \otimes \dot{\Lambda} \langle \boldsymbol{\xi} \rangle \\ &+ M^2 \dot{\boldsymbol{\eta}} \otimes \dot{\boldsymbol{\eta}}. \end{aligned} \quad (\text{B.9})$$

For the second moments we obtain

$$\begin{aligned} \langle \mathbf{p} \otimes \mathbf{p} \rangle &= \langle \boldsymbol{\pi} \Lambda^{-1} \otimes \Lambda^{-\top} \boldsymbol{\pi} \rangle \\ &+ M^2 \langle \boldsymbol{\xi} \dot{\Lambda}^\top \otimes \dot{\Lambda} \boldsymbol{\xi} \rangle \\ &+ M^2 \dot{\boldsymbol{\eta}} \otimes \dot{\boldsymbol{\eta}} \\ &+ M \langle \boldsymbol{\pi} \Lambda^{-1} \otimes \dot{\Lambda} \boldsymbol{\xi} \rangle + \text{h.c.} \\ &+ M \langle \boldsymbol{\pi} \rangle \Lambda^{-1} \otimes \dot{\boldsymbol{\eta}} + \text{h.c.} \\ &+ M^2 \langle \boldsymbol{\xi} \rangle \dot{\Lambda}^\top \otimes \dot{\boldsymbol{\eta}} + \text{h.c.} \end{aligned} \quad (\text{B.10})$$

For the covariance matrix, we find

$$\begin{aligned} \Sigma_{\mathbf{p}} &= \langle \mathbf{p} \otimes \mathbf{p} \rangle - \langle \mathbf{p} \rangle \otimes \langle \mathbf{p} \rangle = \langle \boldsymbol{\pi} \Lambda^{-1} \otimes \Lambda^{-\top} \boldsymbol{\pi} \rangle - \langle \boldsymbol{\pi} \rangle \Lambda^{-1} \otimes \Lambda^{-\top} \langle \boldsymbol{\pi} \rangle \\ &+ M^2 \langle \boldsymbol{\xi} \dot{\Lambda}^\top \otimes \dot{\Lambda} \boldsymbol{\xi} \rangle - M^2 \langle \boldsymbol{\xi} \rangle \dot{\Lambda}^\top \otimes \dot{\Lambda} \langle \boldsymbol{\xi} \rangle \\ &+ M \langle \boldsymbol{\pi} \Lambda^{-1} \otimes \dot{\Lambda} \boldsymbol{\xi} \rangle + \text{h.c.} \\ &- \langle \boldsymbol{\pi} \rangle \Lambda^{-1} \otimes M \dot{\Lambda} \langle \boldsymbol{\xi} \rangle - \text{h.c.} \end{aligned} \quad (\text{B.11})$$

B.3 CORRELATIONS

Using the results from the previous sections, we find the position and momentum correlation matrix

$$\begin{aligned} \Sigma_{\mathbf{r}\mathbf{p}} &= \langle \mathbf{r} \otimes \mathbf{p} \rangle - \langle \mathbf{r} \rangle \otimes \langle \mathbf{p} \rangle - i\hbar/2 \\ &= \langle \boldsymbol{\xi} \Lambda^\top \otimes \Lambda^{-\top} \boldsymbol{\pi} \rangle - \langle \boldsymbol{\xi} \rangle \Lambda^\top \otimes \Lambda^{-\top} \langle \boldsymbol{\pi} \rangle \\ &+ M \langle \boldsymbol{\xi} \Lambda^\top \otimes \dot{\Lambda} \boldsymbol{\xi} \rangle - M \langle \boldsymbol{\xi} \rangle \Lambda^\top \otimes \dot{\Lambda} \langle \boldsymbol{\xi} \rangle - i\hbar/2. \end{aligned} \quad (\text{B.12})$$

C TIME OF FLIGHT SERIES

We depict various atomic density distributions during the flight of flight after the anharmonic magnetic lens, from $t = 82.7$ ms to $t = 2082.7$ ms

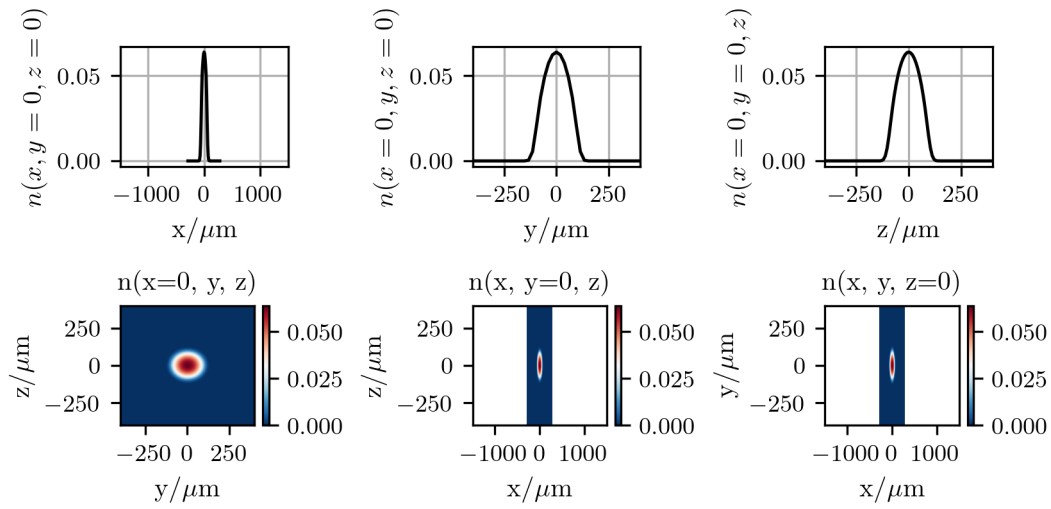


Figure C.1: $t = 82.7$ ms

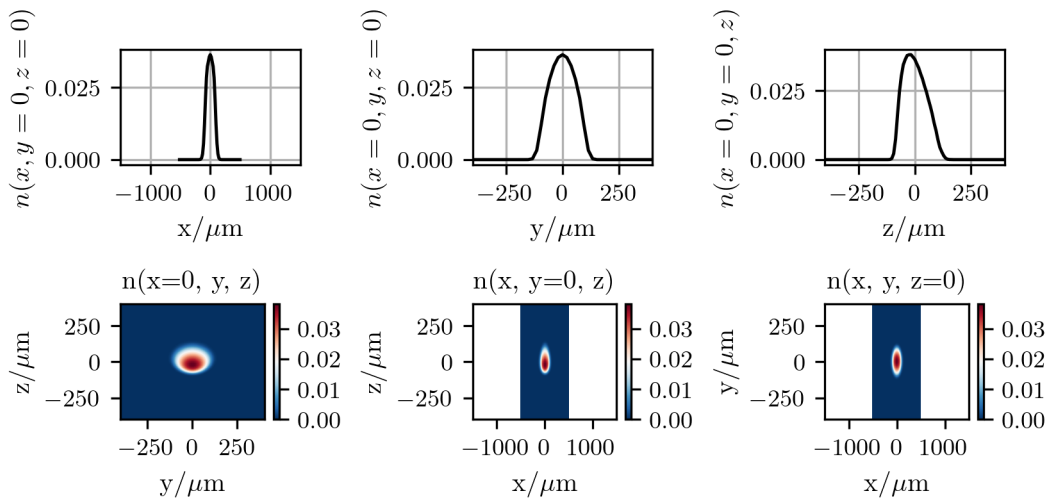


Figure C.2: $t = 182.7$ ms

C Time of flight series

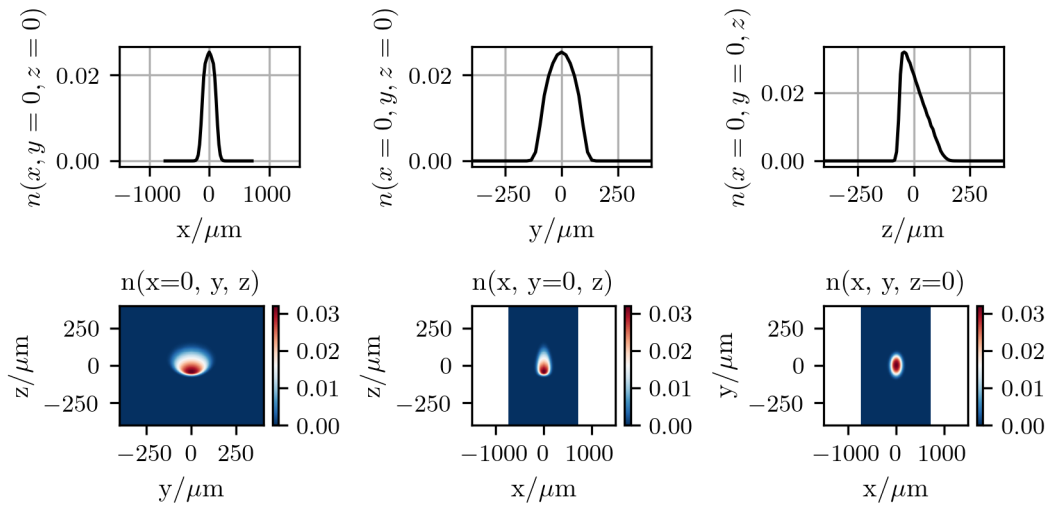


Figure C.3: $t = 282.7$ ms

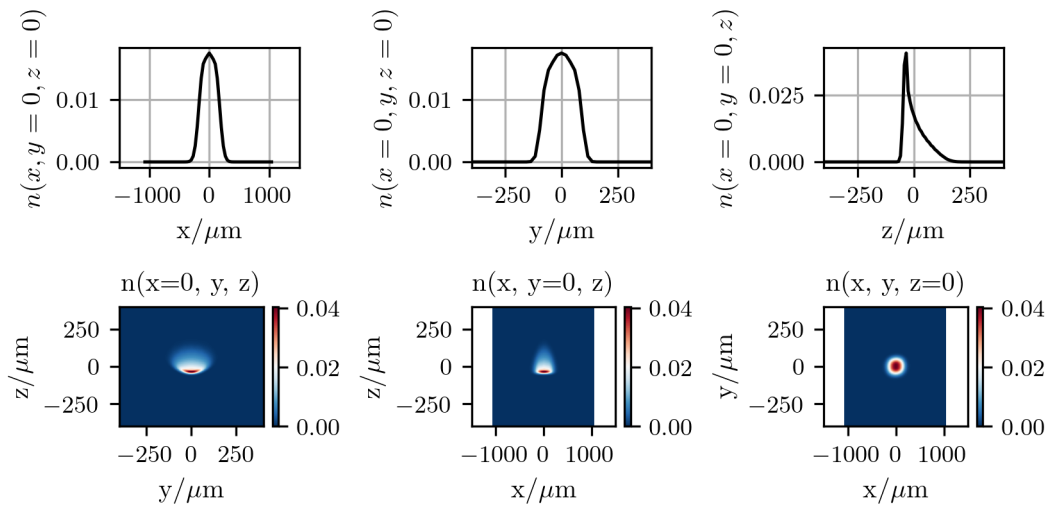


Figure C.4: $t = 432.7$ ms

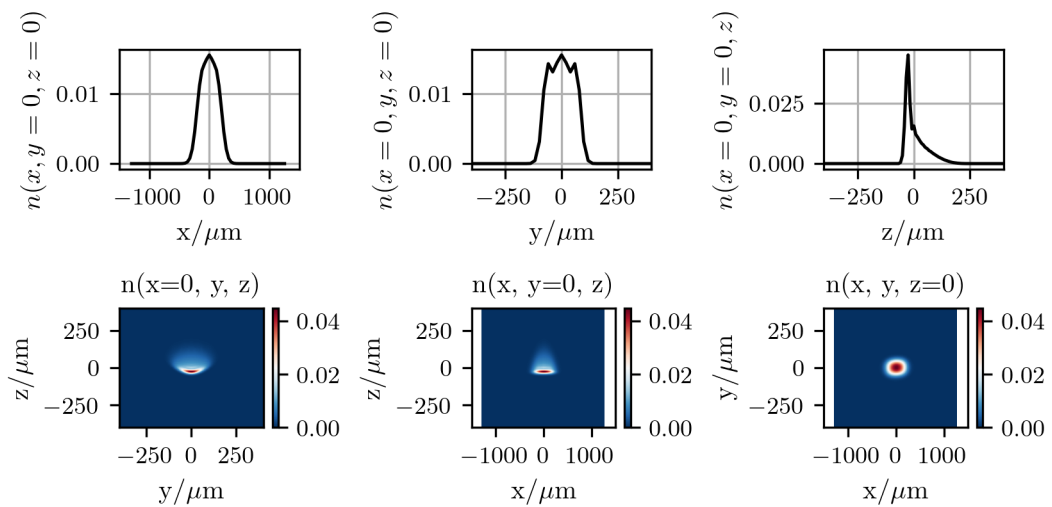


Figure C.5: $t = 532.7$ ms

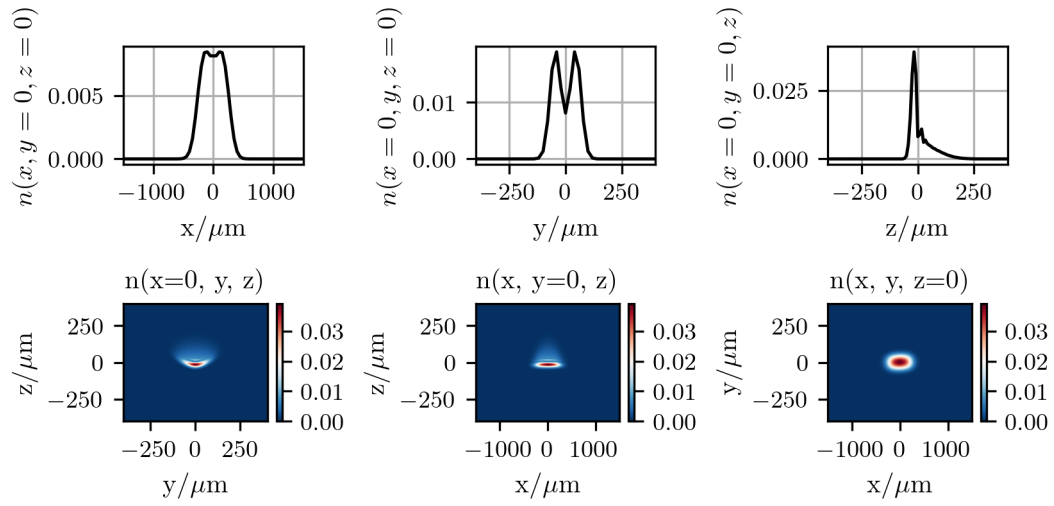


Figure C.6: $t = 662.7$ ms

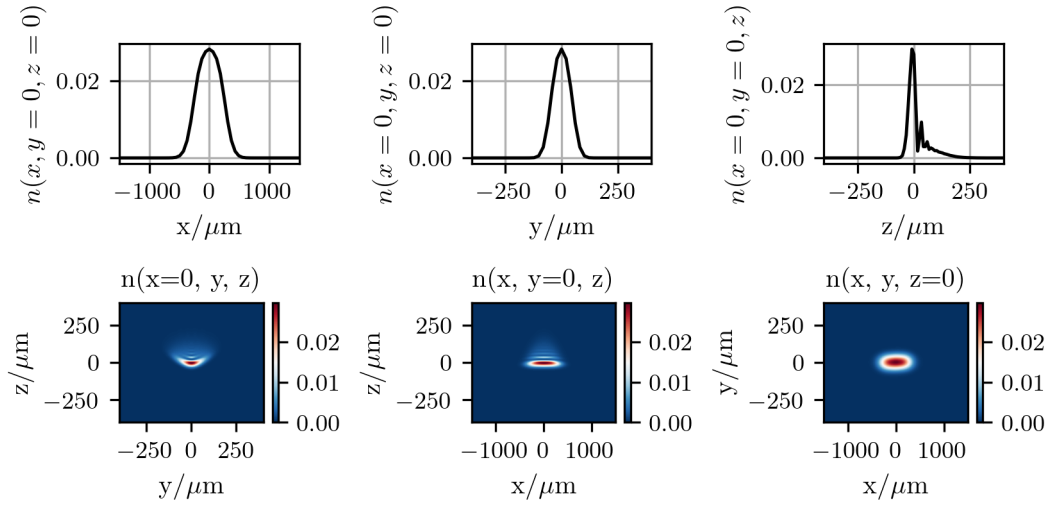


Figure C.7: $t = 832.7$ ms

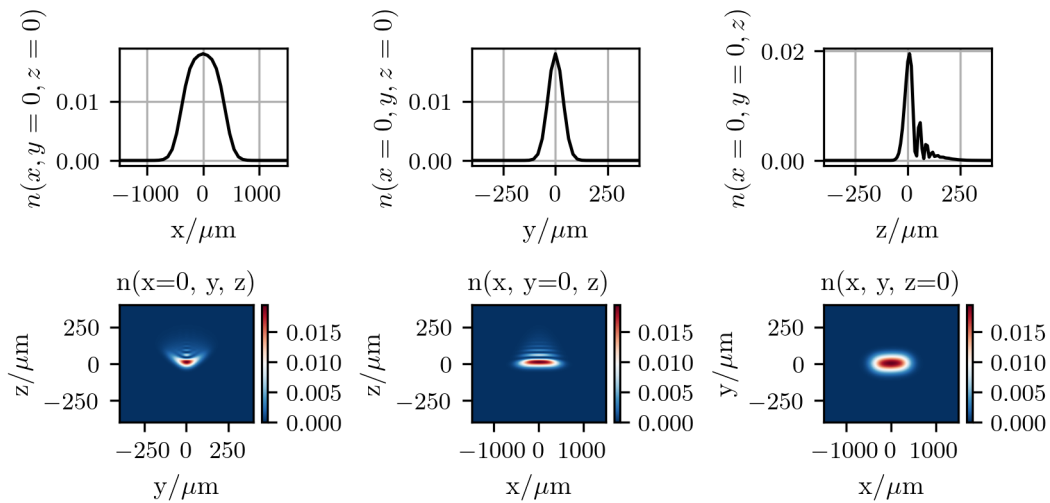


Figure C.8: $t = 1082.7$ ms

C Time of flight series

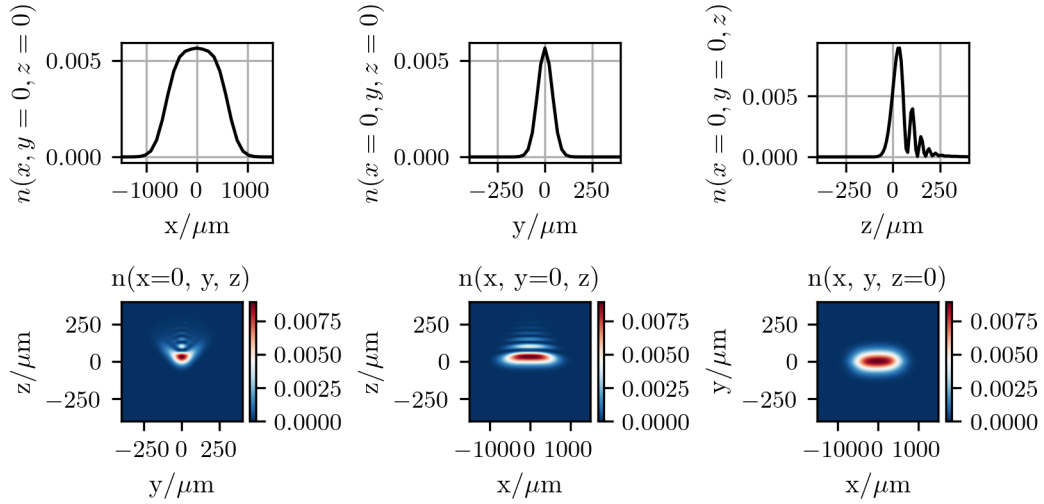


Figure C.9: $t = 1582.7$ ms

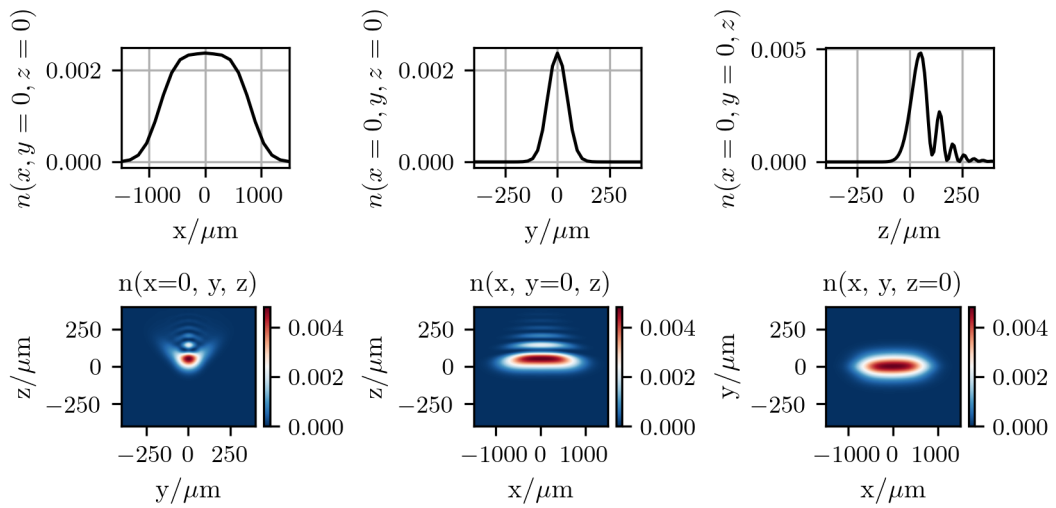


Figure C.10: $t = 2082.7$ ms

D PROPERTIES OF SPHERICAL HARMONICS

D.1 GENERAL RELATIONS

The spherical harmonics $Y_{lm}(\vartheta, \varphi)$ [103, 135] with non-negative integers l ($l \geq 0$) and integer m ($|m| \leq l$) form a complete set

$$\sum_{l=0}^{\infty} \sum_{m=-l}^l Y_{lm}^*(\vartheta, \varphi) Y_{lm}(\vartheta', \varphi') = \delta(\vartheta - \vartheta') \delta(\varphi - \varphi'). \quad (\text{D.1})$$

They are orthonormal

$$\int \int Y_{l'm'}^*(\vartheta, \varphi) Y_{lm}(\vartheta, \varphi) d^2\Omega = \delta_{ll'} \delta_{mm'}. \quad (\text{D.2})$$

The connection between the spherical harmonics and its complex conjugate is

$$Y_{lm}^*(\vartheta, \varphi) = (-1)^m Y_{l-m}(\vartheta, \varphi). \quad (\text{D.3})$$

D.2 MULTIPOLE EXPANSION

Any square-integrable function $f(\vartheta, \varphi)$ can be expanded into a series of angular momentum eigenfunctions,

$$f(\vartheta, \varphi) = \sum_{l=0}^{\infty} \sum_{m=-l}^l \langle \vartheta, \varphi | ml \rangle \langle lm | f \rangle \quad (\text{D.4})$$

$$= \sum_{l=0}^{\infty} \sum_{m=-l}^l f_{lm} Y_{lm}(\vartheta, \varphi), \quad (\text{D.5})$$

with

$$Y_{lm}(\vartheta, \varphi) = \langle \vartheta, \varphi | ml \rangle, \quad f(\vartheta, \varphi) = \langle \vartheta, \varphi | f \rangle, \quad f_{lm} = \langle lm | f \rangle. \quad (\text{D.6})$$

The series is also known as multipole expansion. The complex coefficients f_{lm} are found by

$$f_{lm} = \langle lm | f \rangle = \langle lm | \vartheta, \varphi \rangle \langle \vartheta, \varphi | f \rangle = \int \int Y_{lm}^*(\vartheta, \varphi) f(\vartheta, \varphi) d^2\Omega, \quad (\text{D.7})$$

projection from the continuous angle variables to the discrete variables l, m [135].

For a real-valued function $f(\vartheta, \varphi) = f^*(\vartheta, \varphi)$, one find the following relation between the complex expansion coefficients

$$f_{lm} = (-1)^m f_{l-m}^*. \quad (\text{D.8})$$

Hence, it is sufficient to compute coefficients with $m \geq 0$.

D.3 PRODUCTS OF SPHERICAL HARMONICS

A product of two spherical harmonics may be expanded in a Clebsch-Gordan series [135],

$$Y_{l_1 m_1}(\vartheta, \varphi) Y_{l_2 m_2}(\vartheta, \varphi) = \sum_{L=0}^{\infty} \sum_{M=-L}^L \sqrt{\frac{(2l_1+1)(2l_2+1)}{4\pi(2L+1)}} \times \quad (D.9)$$

$$C(l_1 l_2 L; 000) C(l_1 l_2 L; m_1 m_2 M) Y_{LM}(\vartheta, \varphi).$$

D.4 VISUAL REPRESENTATION

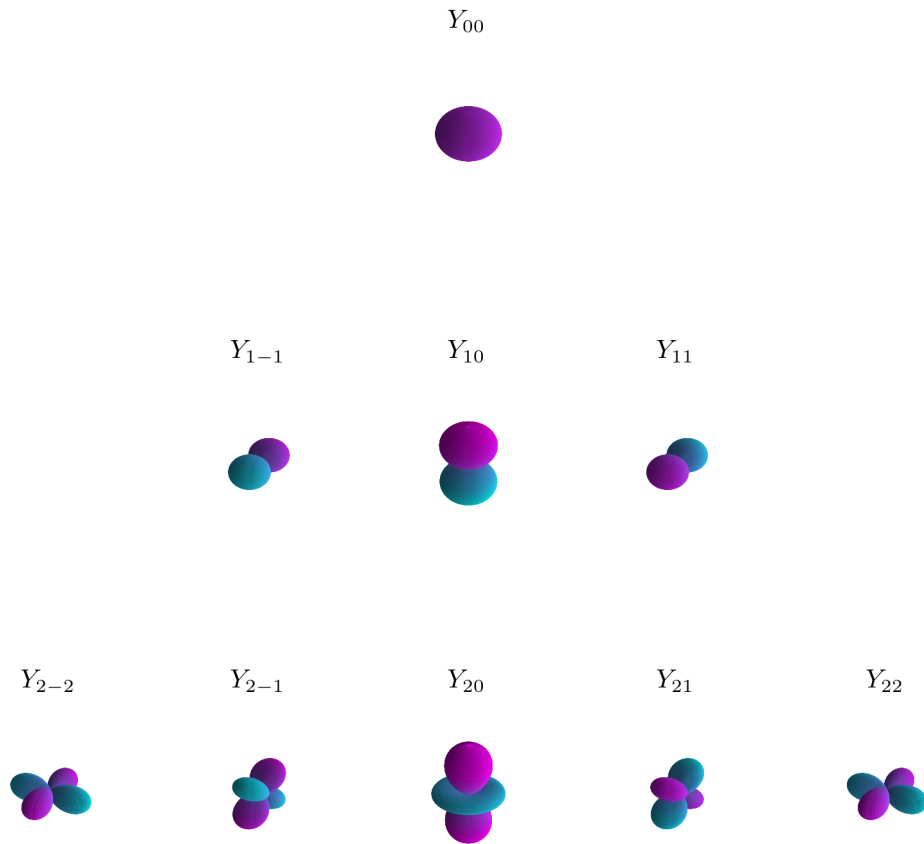


Figure D.1: Visual representation of the spherical harmonics $Y_{lm}(\vartheta, \varphi)$ for the first three angular momentum manifolds $l = 0, 1, 2$. Purple color indicates regions with a positive sign. Turquoise color indicates regions with a negative sign. Distance from the origin represents the absolute value.

E JACOBI POLYNOMIALS

The Jacobi polynomials are defined by a Gaussian hypergeometric function ${}_2F_1(a, \alpha, \beta)$ [103] for integer values $a = -n$,

$$J_n^{(\alpha, \beta)}(x) = \frac{(\alpha + 1)_n}{n!} {}_2F_1\left(-n, n + \alpha + \beta + 1; \alpha + 1; \frac{1-x}{2}\right). \quad (\text{E.1})$$

They are orthogonal on the interval $x \in [-1, 1]$,

$$\int_{-1}^1 w_{\alpha, \beta}(x) J_n^{(\alpha, \beta)}(x) J_m^{(\alpha, \beta)}(x) dx = \mathcal{A}_n \delta_{nm}, \quad (\text{E.2})$$

$$\mathcal{A}_n = \frac{2^{\alpha+\beta+1}}{2n + \alpha + \beta + 1} \frac{\Gamma(n + \alpha + 1)\Gamma(n + \beta + 1)}{\Gamma(n + \alpha + \beta + 1)n!}, \quad (\text{E.3})$$

with respect to the weight function

$$w_{\alpha, \beta}(x) = (1-x)^\alpha (1+x)^\beta. \quad (\text{E.4})$$

Different Jacobi polynomials with $\alpha = l + 1/2$, $\beta = 0$ are shown in figure E.1.

The Stringaris in equation (7.6) are shifted Jacobi polynomials with $\alpha = l + 1/2$ and $\beta = 0$ substituting the coordinate as $x = 1 - 2(r/R)^2$, $r \in [0, R]$. The orthogonality relation (E.2) becomes

$$\int_0^R r^2 S_{n'l}(r) S_{nl}(r) dr = \delta_{n, n'}, \quad (\text{E.5})$$

where the normalization constant \mathcal{N}_{nl} in equation (7.6) is obtained by using (E.3). Values into the radial direction are shown in figure E.2.

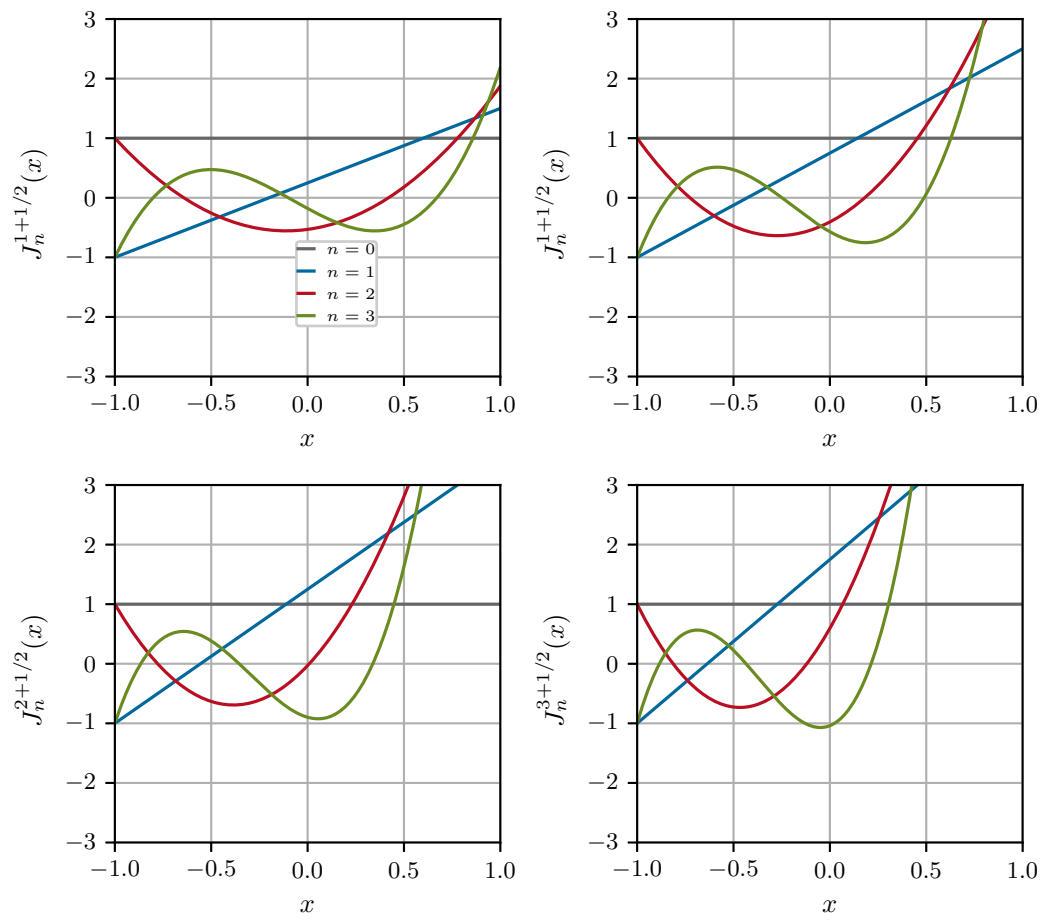


Figure E.1: Jacobi polynomials with $\alpha = l + 1/2$, $\beta = 0$ for different n and l .

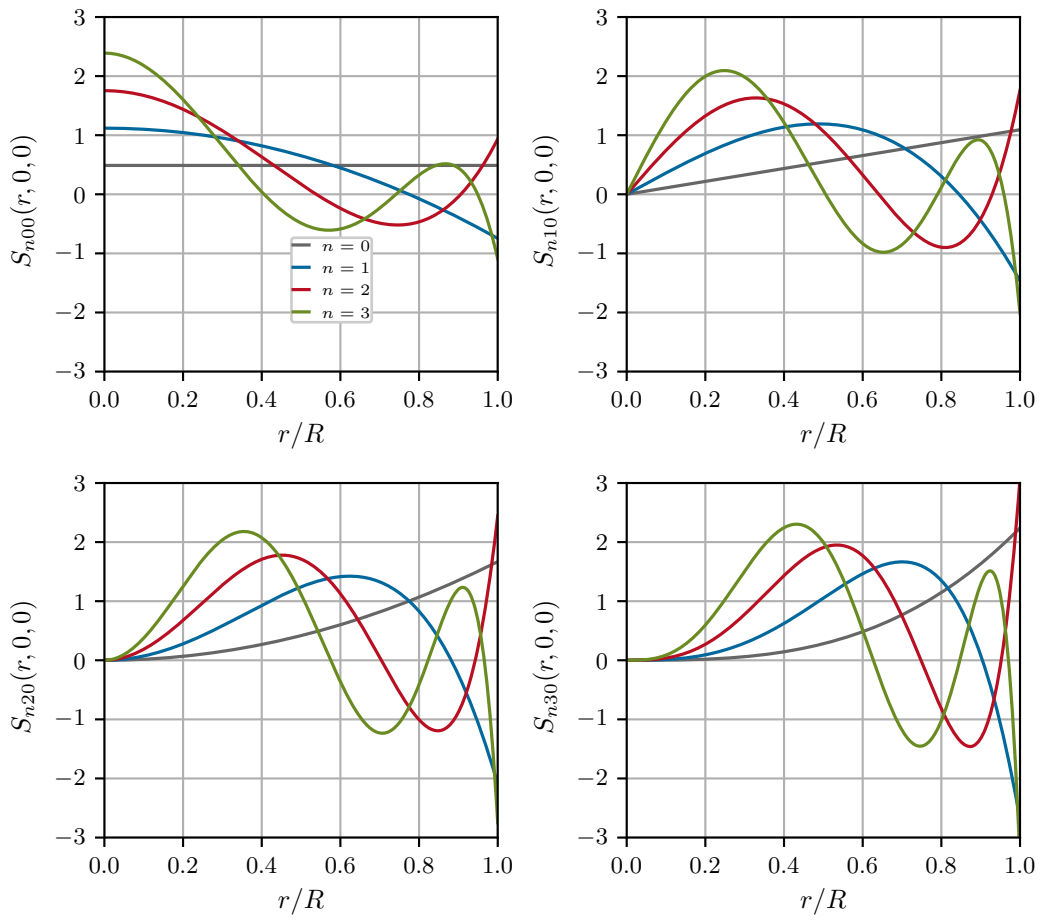


Figure E.2: Radial Stringari polynomials $S_{nl}(r, 0, 0)$ for different n and l .

F

FOURIER REPRESENTATION OF WAVE FUNCTIONS

Throughout this thesis we make heavily use of Fourier methods [171, 178–180]. In particular, we represent linear and non-linear operators as well as wave functions and fields by using discrete Fourier basis functions. Fourier discretization requires periodic boundary conditions

$$\psi(\mathbf{r}) = \psi(\mathbf{r} + 2L_i \mathbf{e}_i), \quad i = \{x, y, z\}. \quad (\text{F.1})$$

The size of the numerical box is

$$\mathcal{D} = [-L_x, L_x] \times [-L_y, L_y] \times [-L_z, L_z]. \quad (\text{F.2})$$

Within the domain \mathcal{D} , we discretize the position coordinates (x_j, y_k, z_l) as

$$x_j = 2L_x \left(-\frac{1}{2} + \frac{j}{N_x} \right), \quad 0 \leq j < N_x - 1, \quad \Delta x = \frac{2L_x}{N_x}, \quad (\text{F.3})$$

where $N_x = 2^{p_x}$, $p_x \in \mathbb{N}$. The discretization in the other spatial directions is analogous. The three-dimensional wave function in position space

$$\psi^{(i)}(x, y, z, t) = \psi^{(i)}(x_j, y_k, z_l, t) = \psi_{j,k,l}^{(i)}(t), \quad (\text{F.4})$$

is represented by a complex array where the additional index (i) may represent e.g. an internal level or another atomic species. The time variable is an attribute of the wave function object and is not stored in the complex array. The total dimension of the wave function is then

$$\dim \left[\psi_{j,k,l}^{(i)}(t) \right] = i \times N_x \times N_y \times N_z. \quad (\text{F.5})$$

F.1 DISCRETE FOURIER TRANSFORM

Having imposed periodic boundary conditions, the wave function may be decomposed in terms of the discrete Fourier basis $\{|u_m\rangle\}$,

$$\langle x_j | \psi \rangle = \sum_{m=0}^{N_x-1} \langle x_j | u_m \rangle \langle u_m | \psi \rangle, \quad (\text{F.6})$$

$$\langle x_j | u_m \rangle = \frac{1}{\sqrt{N_x}} e^{i(k_{x,m} - k_{x,0})(x_j - x_0)} = \frac{1}{\sqrt{N_x}} e^{i \frac{2\pi}{N_x} m j}, \quad (\text{F.7})$$

with discrete momenta

$$k_{x,m} = \frac{N_x \pi}{L_x} \left(-\frac{1}{2} + \frac{m}{N_x} \right), \quad 0 \leq m < N_x - 1, \quad \Delta k = \frac{\pi}{L_x}, \quad (\text{F.8})$$

F Fourier representation of wave functions

and maximal values at the boundary

$$x_0 = -L_x, \quad k_{x,0} = -\frac{N_x \pi}{2L_x}, \quad (\text{F.9})$$

such that $\langle x_j | \psi \rangle = \langle x_{j+N_x} | \psi \rangle$. The Fourier amplitudes are obtained by

$$\tilde{\psi}_n = \langle u_n | \psi \rangle = \sum_j \langle u_n | x_j \rangle \langle x_j | \psi \rangle. \quad (\text{F.10})$$

One can show, that the Fourier basis states are orthonormal

$$\langle u_l | u_m \rangle = \sum_{n=0}^{N_x-1} \langle u_l | x_n \rangle \langle x_n | u_m \rangle = \frac{1}{N_x} \sum_{n=0}^{N_x-1} e^{i \frac{2\pi}{N_x} (m-l)n} = \delta_{lm}, \quad (\text{F.11})$$

with respect to the discrete scalar product. In addition, the basis states are eigenfunctions of the momentum operator ($\hbar = 1$)

$$\langle x_j | \hat{p}_x | u_m \rangle = \bar{k}_{x,m} \langle x_j | u_m \rangle, \quad \bar{k}_{x,m} = k_{x,m} - k_{x,0}. \quad (\text{F.12})$$

The latter is particularly useful when evaluating the kinetic energy operator F.3.

F.2 REPRESENTATION OF THE 3D DISCRETE WAVE FUNCTION

The three-dimensional discrete wave function is represented by Fourier basis states (F.7) and amplitudes (F.10). For example, the value of the wave function at position (x_j, y_k, z_l) is

$$\psi^{(i)}(x_j, y_k, z_l, t) = \frac{1}{\sqrt{N_x}} \sum_{m=0}^{N_x-1} e^{i(k_{x,m} - k_{x,0})(x_j - x_0)} \tilde{\psi}_m^{(i)}(y_k, z_l, t). \quad (\text{F.13})$$

The Fourier amplitudes are given by

$$\tilde{\psi}_m^{(i)}(y_k, z_l, t) = \frac{1}{\sqrt{N_x}} \sum_{j=0}^{N_x-1} e^{-i(k_{x,m} - k_{x,0})(x_j - x_0)} \psi^{(i)}(x_j, y_k, z_l, t). \quad (\text{F.14})$$

F.3 EVALUATION OF THE KINETIC ENERGY

The kinetic energy $\hat{T} = \hat{\mathbf{p}}^2/2$ operator is separable in each spatial direction. Thus, we may write

$$\langle \mathbf{r} | \hat{p}_x^2 + \hat{p}_y^2 + \hat{p}_z^2 | \psi \rangle = \langle \mathbf{r} | \hat{p}_x^2 | \psi \rangle + \dots \quad (\text{F.15})$$

Using the eigenvalue relation in equation (F.12), one finds

$$\langle \mathbf{r} | \hat{p}_x^2 | \psi \rangle = \sum_{m=0}^{N_x-1} \langle x_j | \hat{p}_x^2 | u_m \rangle \tilde{\psi}_m(y_k, z_l) = \sum_{m=0}^{N_x-1} \bar{k}_{x,m}^2 \langle x_j | u_m \rangle \tilde{\psi}_m(y_k, z_l). \quad (\text{F.16})$$

Therefore, one evaluates the kinetic energy using a one-dimensional Fourier transform on the first axis, multiplying the amplitudes with $\bar{k}_{x,m}^2$ and transforming it back using an inverse Fourier transform. The other spatial directions are computed analogously.

The Fourier amplitudes in (F.10) are evaluated efficiently using the method of Fast Fourier transform (FFT) which reduces the computation cost from $\mathcal{O}(N_x^2)$ to $\mathcal{O}(N_x \log N_x)$ operations.

In most literature the algorithm is dedicated to J. W. Cooley and J. W. Tukey in 1965 [181] which made the discrete Fourier transform feasible for digital signal processing and numerical analysis. Nevertheless, the roots of the algorithm date back to C. F. Gauss in 1805 [182].

F.4 RADIAL FOURIER GRID

When the Hamilton operator commutes with the angular momentum operators \mathbf{L}^2, L_z , it is sufficient to solve radial differential equations for a given angular momentum manifold. In order to apply Fourier methods, we extend the radial coordinate negative values. Moreover, we shift the grid by $\Delta r/2$ to avoid the point at $r = 0$ which becomes singular when evaluating the Laplace operator in spherical or cylindrical coordinates. The equidistant grid for the radial coordinate is given by

$$r_j = \frac{2R_0}{N_r} \left(-\frac{1}{2} + \frac{1}{2N_r} + \frac{j-1}{N_r} \right), \quad 1 \leq j \leq N_r, \quad \Delta r = \frac{2R_0}{N_r}, \quad (\text{F.17})$$

where R_0 is the maximal radius and N_r denotes the number of grid points in the radial direction. The corresponding discrete momenta are

$$k_j = \frac{N_r \pi}{R_0} \left(-\frac{1}{2} + \frac{j-1}{N_r} \right), \quad 1 \leq j \leq N_r, \quad \Delta k = \frac{\pi}{R_0}. \quad (\text{F.18})$$

G GROSS-PITAEVSKII EQUATION IN DIMENSIONLESS UNITS

As the typical length scale for Bose-Einstein condensate is of the order of μm , it is convenient to work with dimensionless units when performing numerical simulations. The chosen length and timescales depend on the specific system. We introduce the dimensionless variables as

$$\begin{aligned} \mathbf{r} &= l\tilde{\mathbf{r}}, & t &= \frac{\tilde{t}}{\omega}, \\ U &= \hbar\omega\tilde{U}, & \Psi &= \tilde{\Psi}/\sqrt{l^3}, \end{aligned} \quad (\text{G.1})$$

with length scale l , timescale $1/\omega$ and energy scale $\hbar\omega$. Omitting the tildes, one finds the time-dependent Gross-Pitaevskii equation (4.36) with an external potential

$$i\partial_t\Psi = \left(-\frac{\hbar}{2M\omega l^2}\nabla^2 + U + \frac{4\pi\hbar a_s}{M\omega l^3}|\Psi|^2 \right)\Psi. \quad (\text{G.2})$$

A convenient choice for the angular frequency would be

$$\omega = \frac{\hbar}{Ml^2}, \quad (\text{G.3})$$

which simplifies equation (G.2) to

$$i\partial_t\Psi = \left(-\frac{1}{2}\nabla^2 + U + \bar{g}|\Psi|^2 \right)\Psi, \quad (\text{G.4})$$

where we have introduced the dimensionless coupling constant $\bar{g} = 4\pi a_s/l$.

HARMONIC OSCILLATOR UNITS If the external potential is well approximated by a harmonic oscillator potential, the natural length scales are the oscillator lengths, $l_i = \sqrt{\hbar/(M\omega_i)}$, $i = \{x, y, z\}$. Choosing l_x as a reference length scale, the harmonic oscillator potential in equation (G.4) has the following form

$$U(\mathbf{r}) = \frac{1}{2}(x^2 + \beta_y^2 y^2 + \beta_z^2 z^2), \quad (\text{G.5})$$

with anisotropies $\beta_y = \omega_y/\omega_x$, $\beta_z = \omega_z/\omega_x$.

H HARTREE-FOCK-BOGOLIUBOV-SELF-ENERGY OPERATOR

H.1 MATHEMATICAL PROPERTIES

The mathematical properties of a non-hermitian quadratic operator Σ are described in [97, 113]. The Bogoliubov operator (4.89) has the symmetry properties

$$\Sigma^{\text{B}} = -\sigma_1 \Sigma^{\text{B}*} \sigma_1, \quad \Sigma^{\text{B}\dagger} = \sigma_3 \Sigma^{\text{B}} \sigma_3, \quad (\text{H.1})$$

where σ_i are the Pauli matrices

$$\sigma_1 = \begin{pmatrix} 0 & 1 \\ 1 & 0 \end{pmatrix}, \quad \sigma_2 = \begin{pmatrix} 0 & -i \\ i & 0 \end{pmatrix}, \quad \sigma_3 = \begin{pmatrix} 1 & 0 \\ 0 & -1 \end{pmatrix}. \quad (\text{H.2})$$

Using the properties in equation (H.1), one finds that the energy spectrum is real-valued with pairs of positive and negative energies

$$\Sigma^{\text{B}} W_{k,\pm} = \pm E_k W_{k,\pm}, \quad E_k > 0. \quad (\text{H.3})$$

The eigenvectors are orthonormal with respect to the metric σ_3 ,

$$W_{k,\pm} \sigma_3 W_{k',\pm} = \pm \delta_{kk'}. \quad (\text{H.4})$$

Positive and negative eigenstates are connected by the relation

$$W_{k,-} = \sigma_1 W_{k,+}^*, \quad (\text{H.5})$$

In the linear response analysis of the Gross-Pitaevskii mean field, Σ has a doubly degenerate zero eigenvalue (gap-less spectrum). P denotes the eigenvector to zero energy

$$\Sigma^{\text{B}} P = 0. \quad (\text{H.6})$$

For a complete basis, one needs to introduce the additional quadrature vector Q which is defined by

$$\Sigma^{\text{B}} Q = -i \frac{P}{\mathfrak{M}}, \quad (\text{H.7})$$

where there real number \mathfrak{M} can be interpreted as an inertial mass parameter. The vectors are normalized as

$$Q^\dagger \sigma_3 P = i, \quad Q^\dagger \sigma_3 Q = P^\dagger \sigma_3 P = 0, \quad (\text{H.8})$$

and being orthogonal to the eigenstates $W_{k,\pm}$. Further, they satisfy

$$P = -\sigma_1 P^*, \quad Q = -\sigma_1 Q^*. \quad (\text{H.9})$$

The eigenvectors of non-zero energy and the linear combinations of the quadratures P, Q

$$W_{0,+} = \frac{1}{\sqrt{2}}(P + iQ), \quad W_{0,-} = \frac{-1}{\sqrt{2}}(P - iQ), \quad (\text{H.10})$$

form a basis $W = (W_{k,+}, W_{0,+}, W_{0,-}, W_{k,-})$ defining the following completeness relation

$$\begin{aligned} \mathbb{1} &= W \sigma_3^{(n)} W^\dagger \sigma_3^{(n)} = W' \sigma_3^{(n-1)} W'^\dagger \sigma_3^{(n-1)} + iQP^\dagger \sigma_3 - iPQ^\dagger \sigma_3 \\ &= \sum_{k>0} \left(W_{k,+} W_{k,+}^\dagger \sigma_3 - W_{k,-} W_{k,-}^\dagger \sigma_3 \right) + iQP^\dagger \sigma_3 - iPQ^\dagger \sigma_3, \end{aligned} \quad (\text{H.11})$$

where the Pauli matrices acting on subspaces with dimension $\dim[\sigma_3^{(l)}] = 2l \times 2l$ and W' are the eigenvectors for non-zero positive and negative energies

$$\Sigma^B W' = W' E'. \quad (\text{H.12})$$

The matrices in equation (H.12) have dimensions $\dim[\Sigma^B] = 2n \times 2n$, $\dim[W'] = 2n \times 2(n-1)$, $\dim[E'] = 2(n-1) \times 2(n-1)$.

H.2 NUMERICAL TREATMENT OF THE BOGOLIUBOV EQUATIONS

To solve the Bogoliubov-de Gennes eigenvalue problem numerically (4.91) it is convenient to make the change of variables

$$f_\pm = u \pm v, \quad (\text{H.13})$$

that transforms the linear equations to

$$\begin{pmatrix} 0 & H_0 \\ H_0 + 2g\Psi_0^2 & 0 \end{pmatrix} \begin{pmatrix} f_+ \\ f_- \end{pmatrix} = \varepsilon \begin{pmatrix} f_+ \\ f_- \end{pmatrix}, \quad (\text{H.14})$$

$$H_0 = -\frac{\hbar^2}{2M} \nabla^2 + U + g|\Psi_0|^2 - \mu, \quad (\text{H.15})$$

Equation (H.14) is decoupled by applying the operator twice which leads to the eigenvalue problem

$$L_\pm f_\pm = \varepsilon^2 f_\pm, \quad (\text{H.16})$$

where we have introduced the operators

$$L_+ = H_0(H_0 + 2g\Psi_0^2), \quad L_- = (H_0 + 2g\Psi_0^2)H_0. \quad (\text{H.17})$$

We solve (H.16) numerically by discretizing the operator L_+ in a Fourier basis (cf. appendix F) and using the *scipy.sparse.linalg.eigs* routine. The latter is a wrapper to ARPACK which utilizes the Implicitly Restarted Arnoldi Method to find eigenvalues and eigenvectors [139]. One obtains the second eigenvector, applying one of the equations in (H.14) to the state vectors f_+ or f_- respectively [171].

I ANGULAR MOMENTUM FILTERING ON CARTESIAN GRIDS

When solving the matrix-free eigenvalue problems for the operators H, L_+ eigenfunctions $\varphi_k(\mathbf{r})$ and eigenvalues ε_k are typically ordered from lowest to highest magnitude with label k . If the operators exhibit any symmetries, we find a set of energy degenerate solutions

$$H\varphi_k^{(d)}(\mathbf{r}) = \varepsilon_k\varphi_k^{(d)}(\mathbf{r}), \quad (\text{I.1})$$

where d denotes the level of degeneracy.

For an isotropic system, the Hamilton operator is invariant under rotations

$$[H, \mathbf{L}^2] = 0, \quad [H, L_z] = 0, \quad (\text{I.2})$$

and the operators $\{H, \mathbf{L}^2, L_z\}$ form a complete set of commuting operators with common basis states

$$H\psi_n(\mathbf{r}) = \varepsilon_n\psi_n(\mathbf{r}), \quad (\text{I.3})$$

$$\mathbf{L}^2\psi_{nl}(\mathbf{r}) = \hbar^2l(l+1)\psi_{nl}(\mathbf{r}), \quad (\text{I.4})$$

$$L_z\psi_{nlm}(\mathbf{r}) = m\hbar\psi_{nlm}(\mathbf{r}), \quad (\text{I.5})$$

where the three-dimensional eigenstates

$$\psi_{nlm}(\mathbf{r}) = R_n^l(r)Y_{lm}(\vartheta, \varphi), \quad (\text{I.6})$$

consist of usually unknown radial functions $R_n^l(r)$ and the well-known angular momentum eigenstates $Y_{lm}(\vartheta, \varphi)$.

Within a degenerate manifold, we can expand the given energy eigenfunctions

$$\varphi_n^{(d)}(\mathbf{r}) = \sum_{lm} \psi_{nlm}(\mathbf{r})C_l^{(dm)} = \sum_{lm} R_n^l(r)Y_{lm}(\vartheta, \varphi)C_l^{(dm)}, \quad (\text{I.7})$$

in terms of the basis states $\psi_{nlm}(\mathbf{r})$. The unknown expansion coefficients $C_l^{(dm)}$ are obtained by the projection of some known linear-independent basis functions, e.g. the regular solid harmonics $\mathcal{R}(\mathbf{r}) = r^l Y_{lm}(\vartheta, \varphi)$,

$$A_l^{(dm)} = \int \mathcal{R}^*(\mathbf{r})\varphi_n^{(d)}(\mathbf{r}) d^3r = c_l C_l^{(dm)}, \quad c_l = \int_0^\infty r^2 r^l R_l(r) dr. \quad (\text{I.8})$$

After inverting equation (I.7), one obtains the numerical eigenfunctions of H, \mathbf{L}^2, L_z .

J BOGOLIUBOV MODES QUANTUS II RELEASE TRAP

In the following, we show two- and one-dimensional cross-sections of the first 11 Bogoliubov modes for the QUANTUS II release trap potential (cf. section 2.4.4, table 2.2). We obtain the modes numerically as discussed in the appendices F and H.2. For our results in section 8.2.2 we use the following parameters: atom number 1×10^5 Rb, Fourier grid lengths $L_x = 27.81$, $L_y = 11.69$, $L_z = 11.82$, Fourier points $N_x = N_y = N_z = 2^7 = 128$. All length scales are in harmonic oscillator length $l_x = \sqrt{\hbar/(M\omega_x)} = 3.57 \mu\text{m}$. We sort the pictures with respect to their energy eigenvalue, including the mode $P = (\Psi_0, -\Psi_0)^\top$ with zero energy. All fields are real-valued $W_k \in \mathbb{R}$.

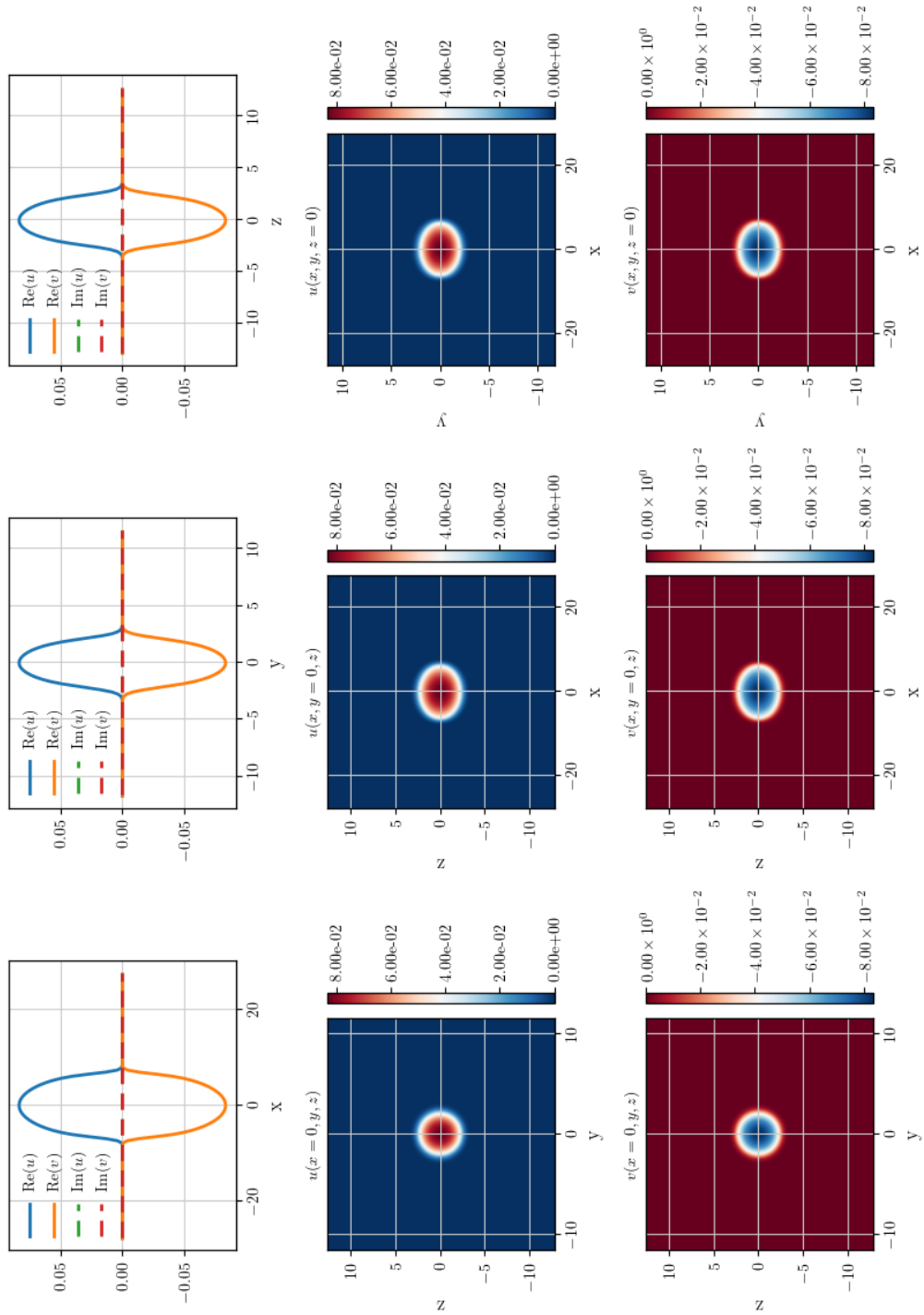


Figure J.1: $\omega_0 = 0$. Zero energy mode $P = (\Psi_0, -\Psi_0)^\top$.

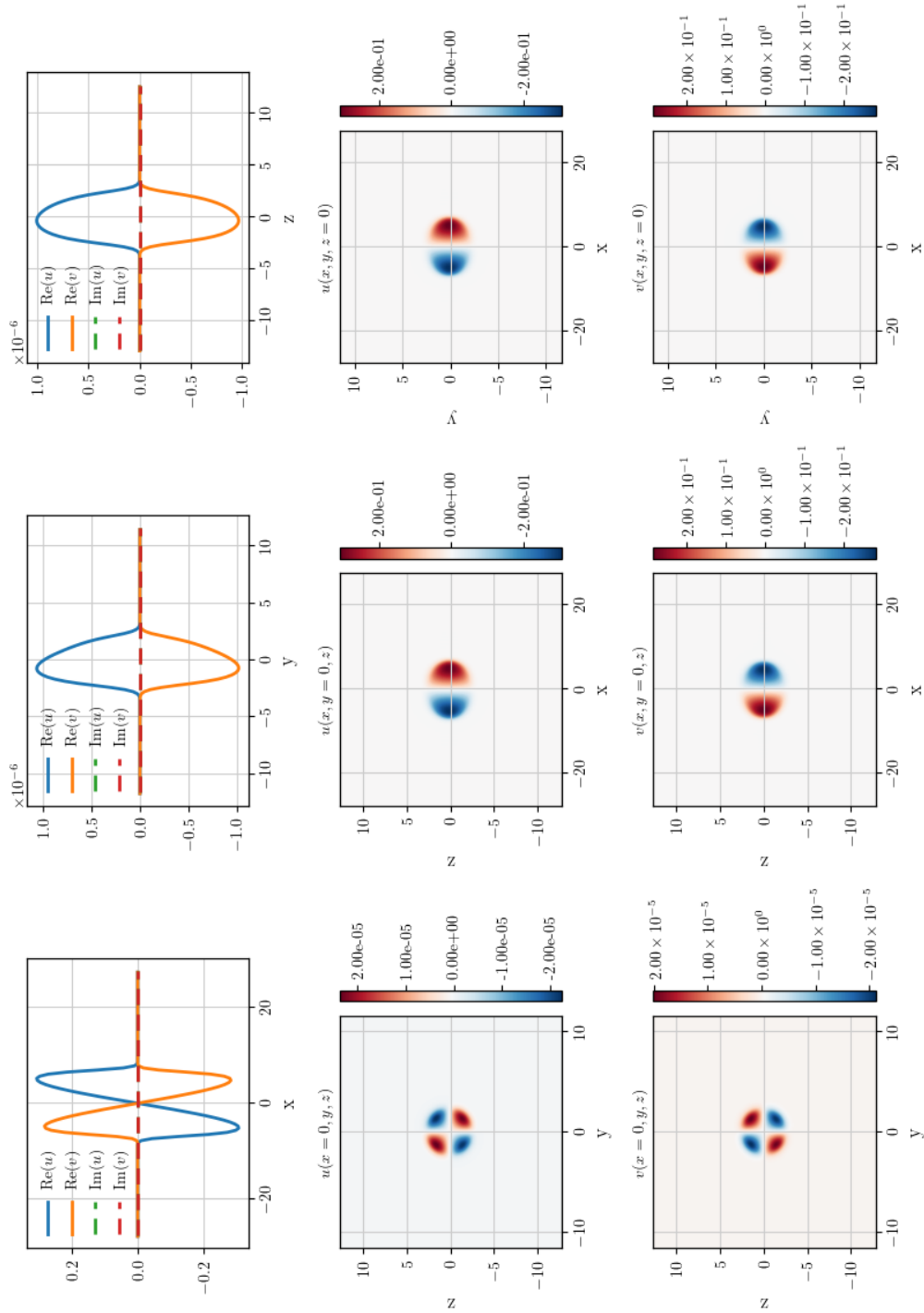


Figure J.2: $\omega_1/(2\pi) = 9.08$ Hz. First Kohn mode with the center of mass oscillation in x -direction.

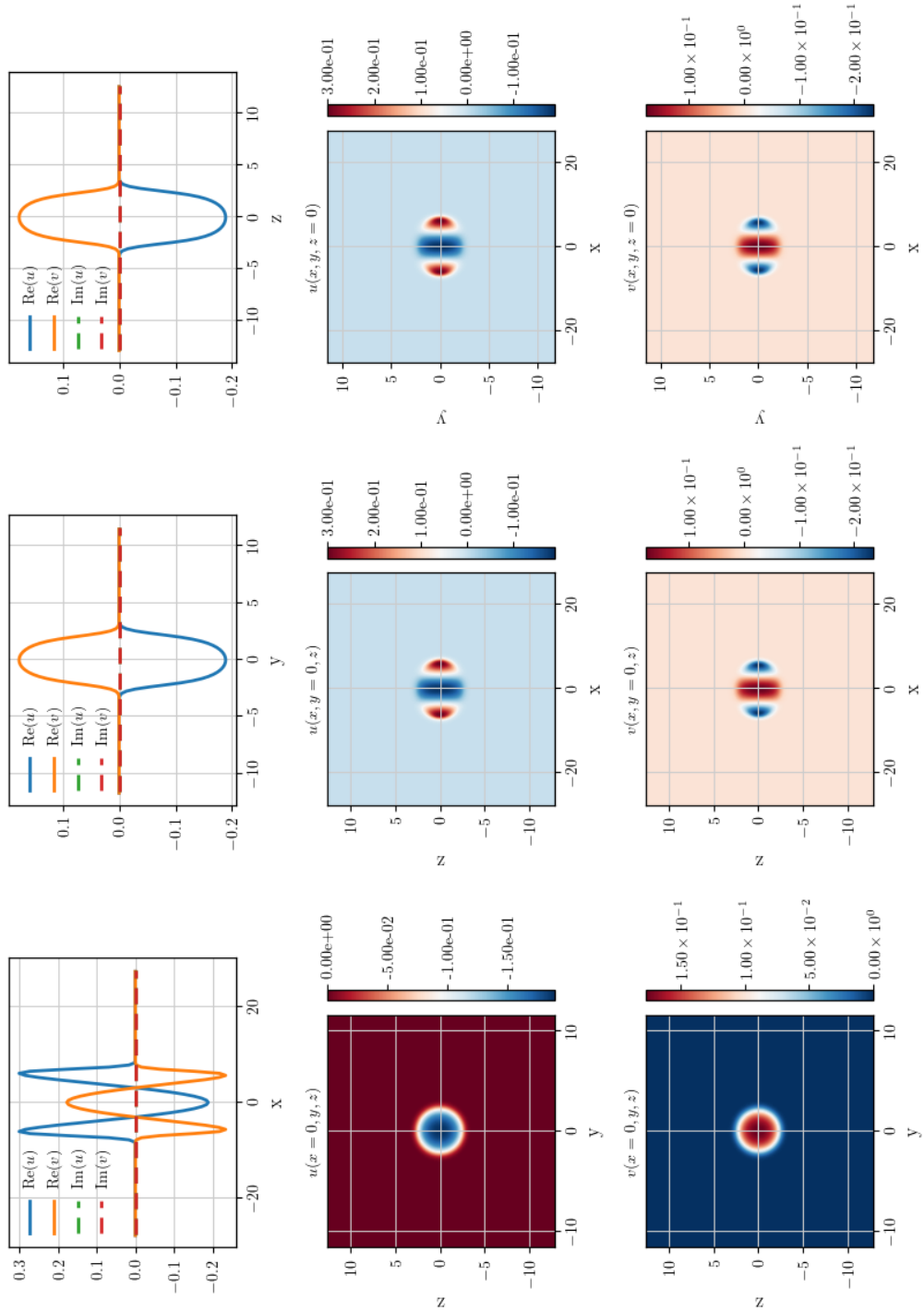


Figure J.3: $\omega_2/(2\pi) = 14.3$ Hz.

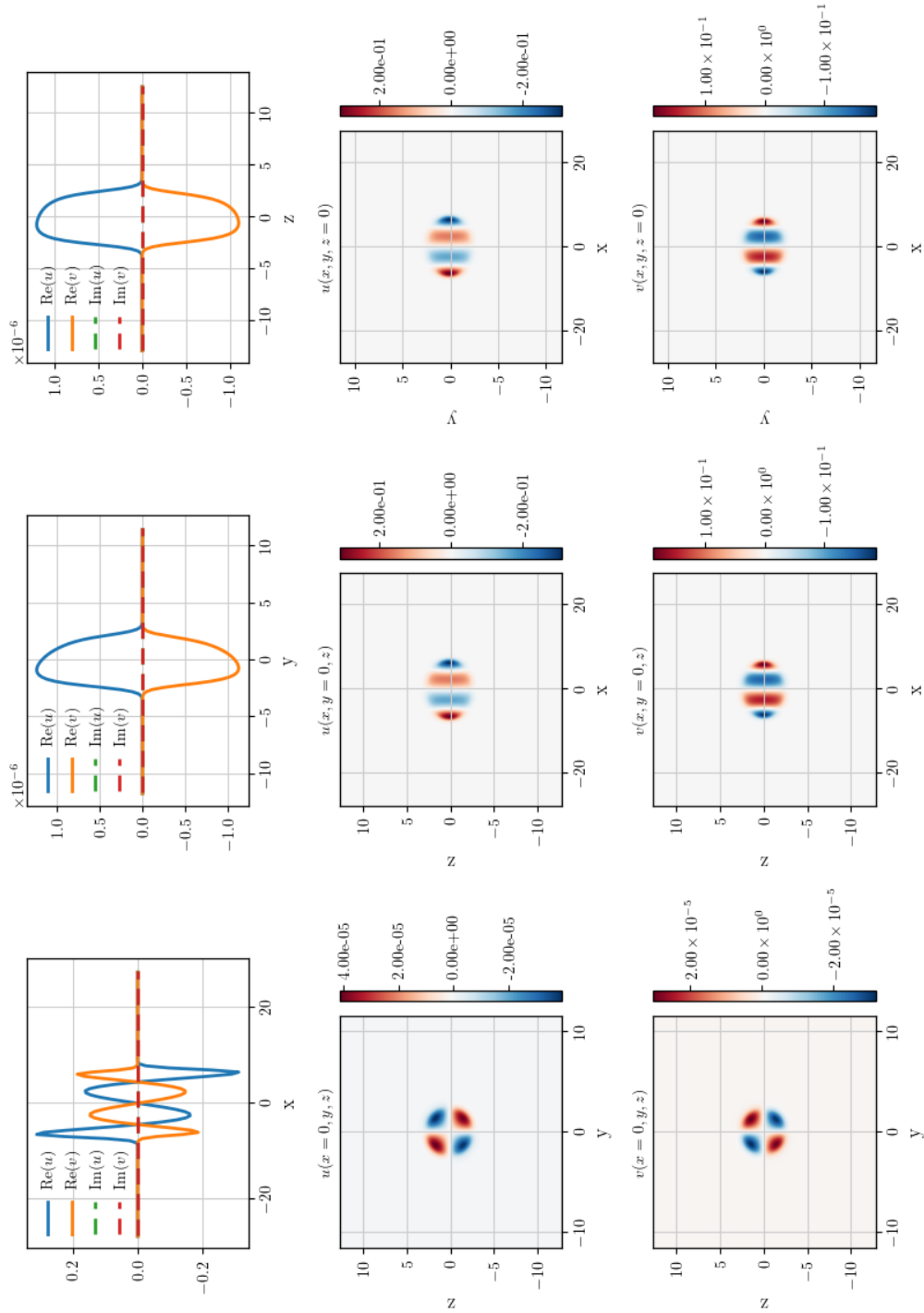


Figure J.4: $\omega_3/(2\pi) = 19.3$ Hz.

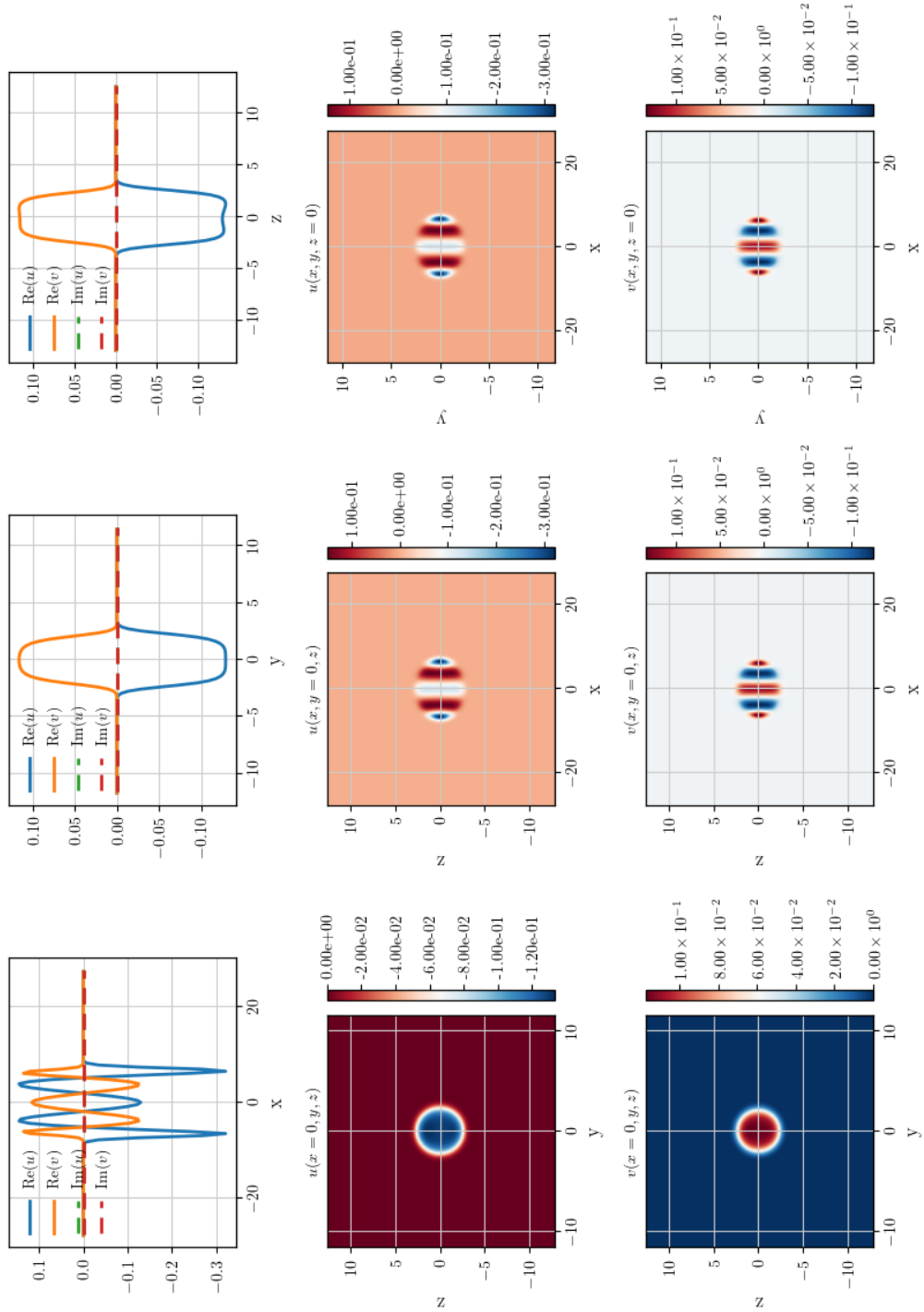


Figure J.5: $\omega_4/(2\pi) = 24.1$ Hz.

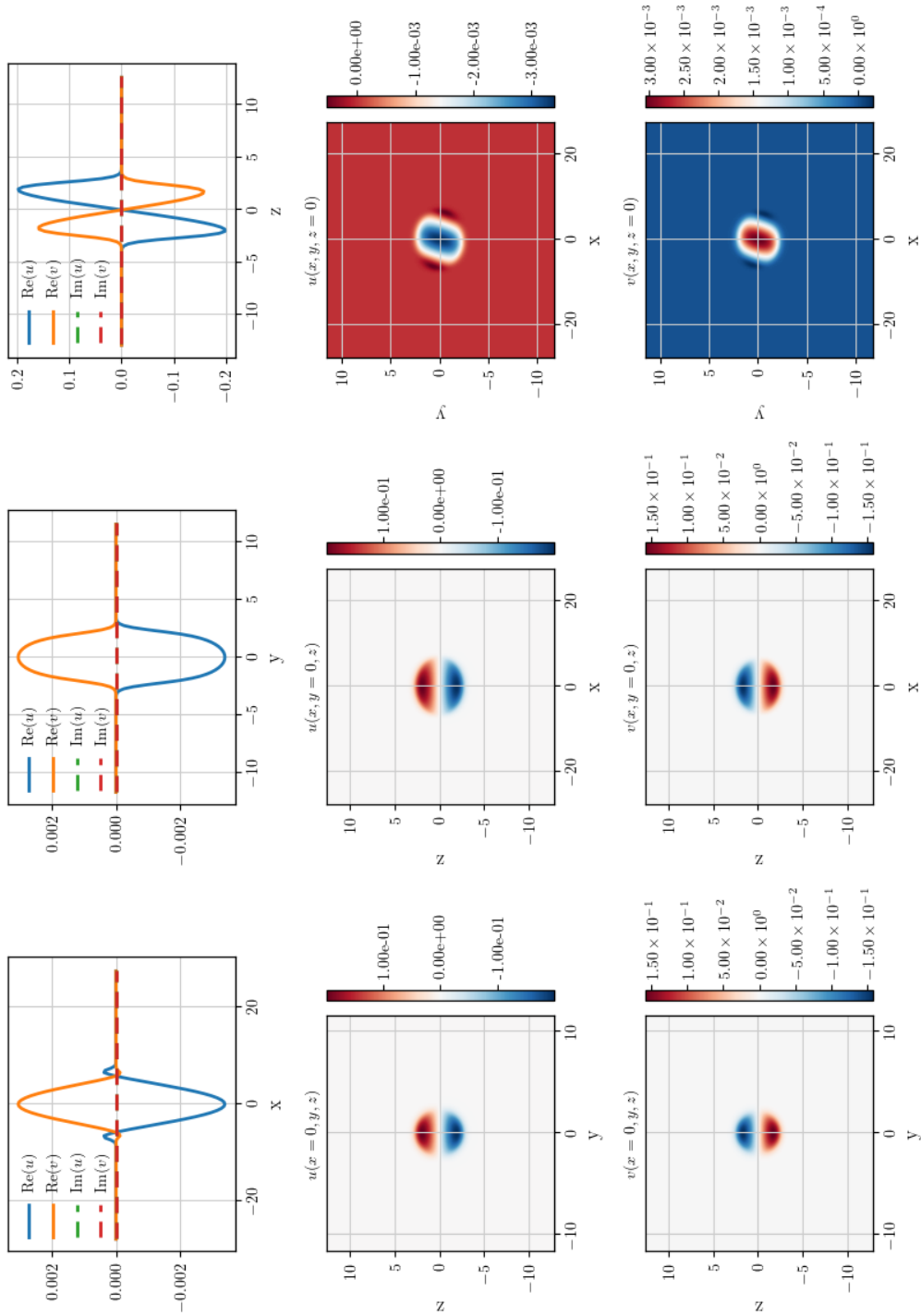


Figure J.6: $\omega_5/(2\pi) = 24.6$ Hz. Second Kohn mode with the center of mass oscillations in z -direction.

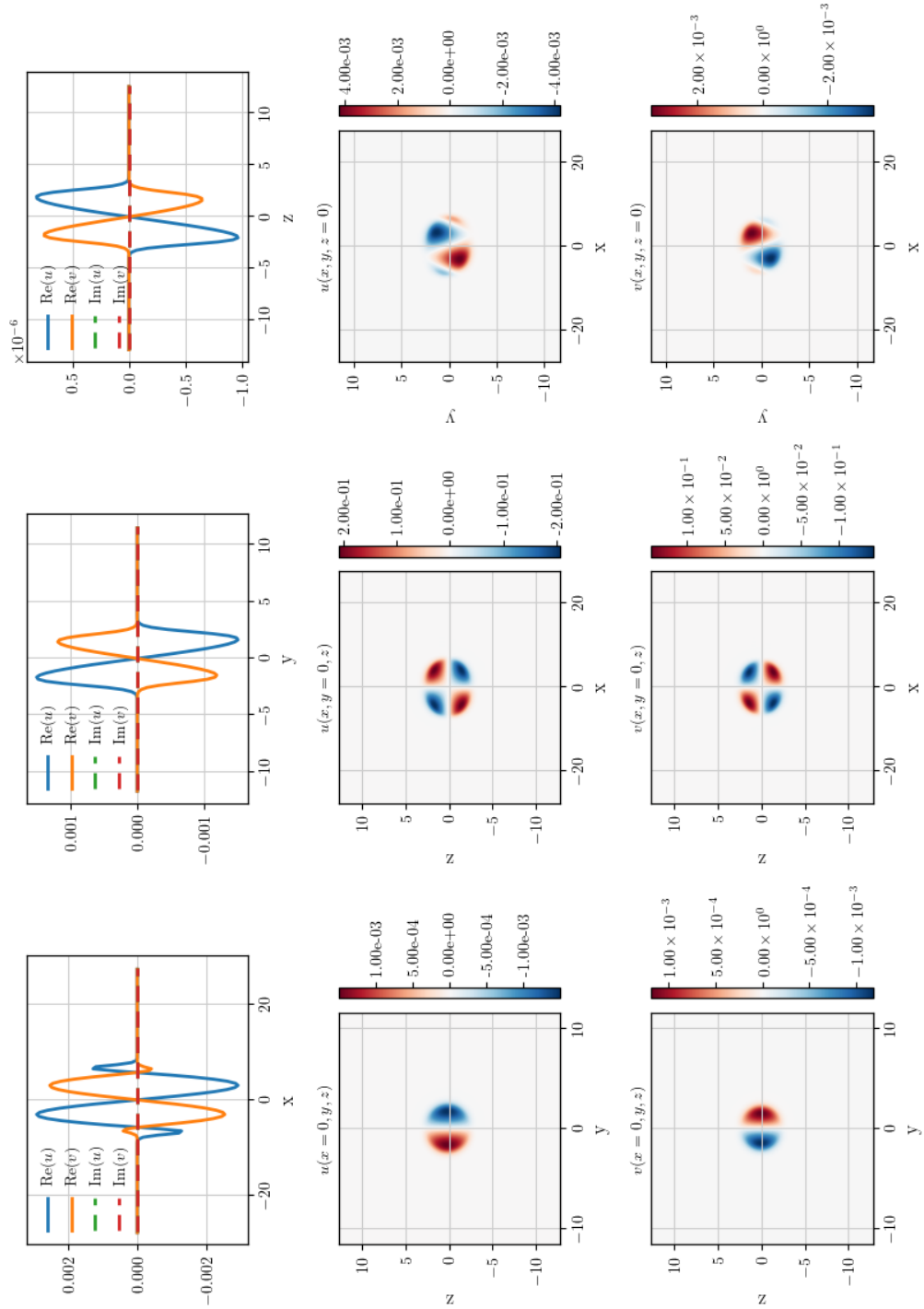


Figure J.7: $\omega_6/(2\pi) = 26.4$ Hz.

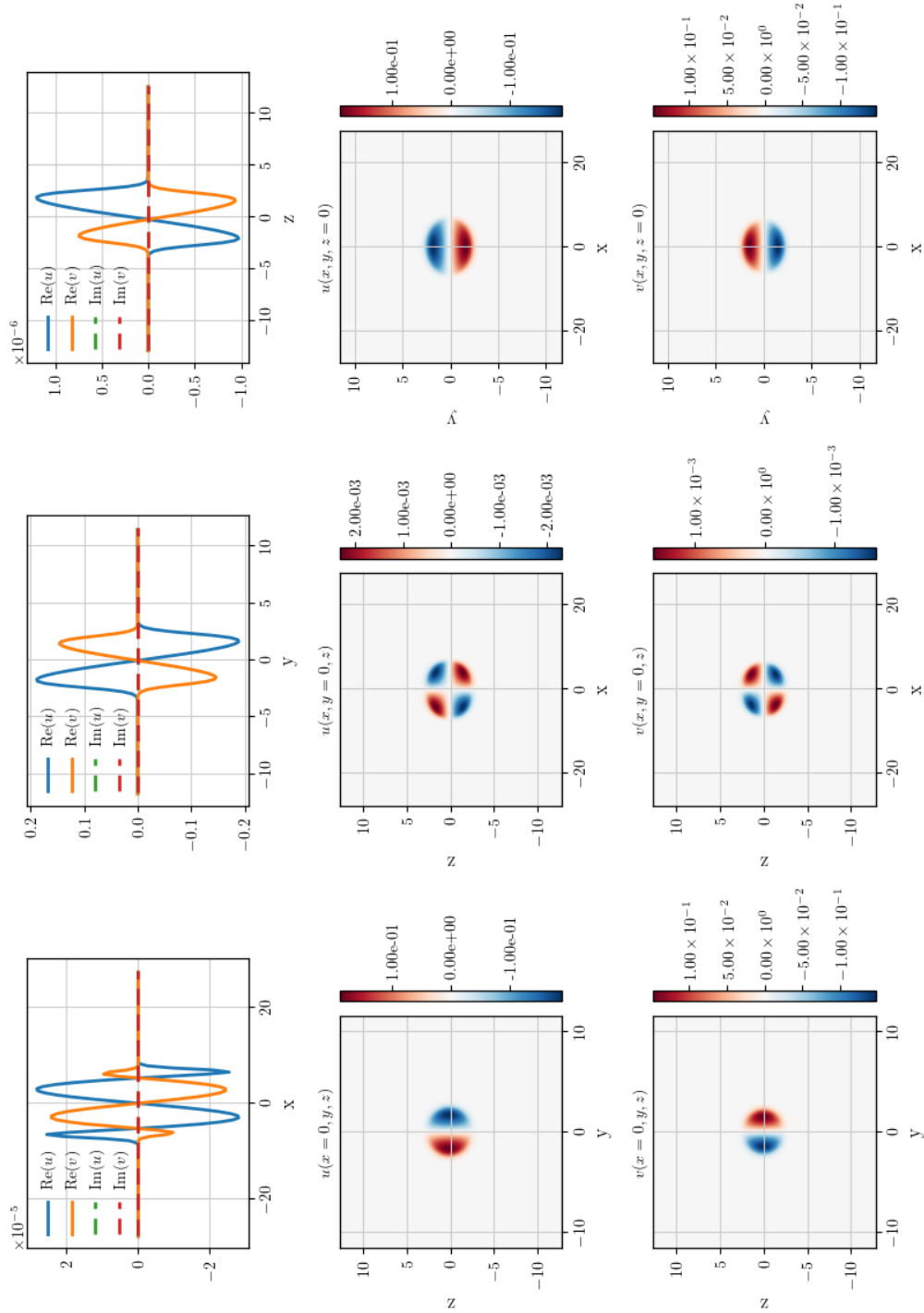


Figure J.8: $\omega_7/(2\pi) = 27.9$ Hz. Third Kohn mode with the center of mass oscillations in y -direction.

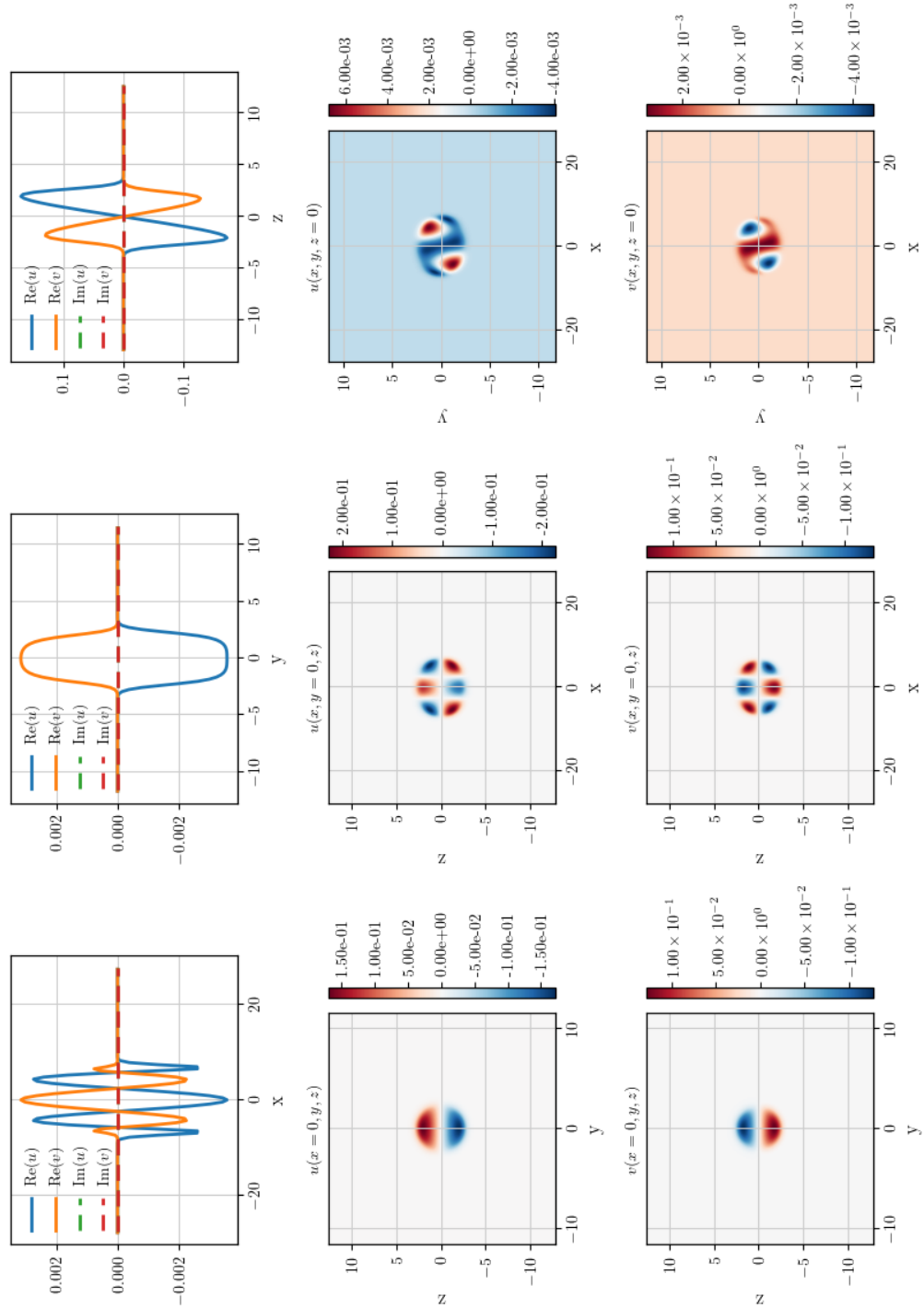


Figure J.9: $\omega_8/(2\pi) = 28.7$ Hz.

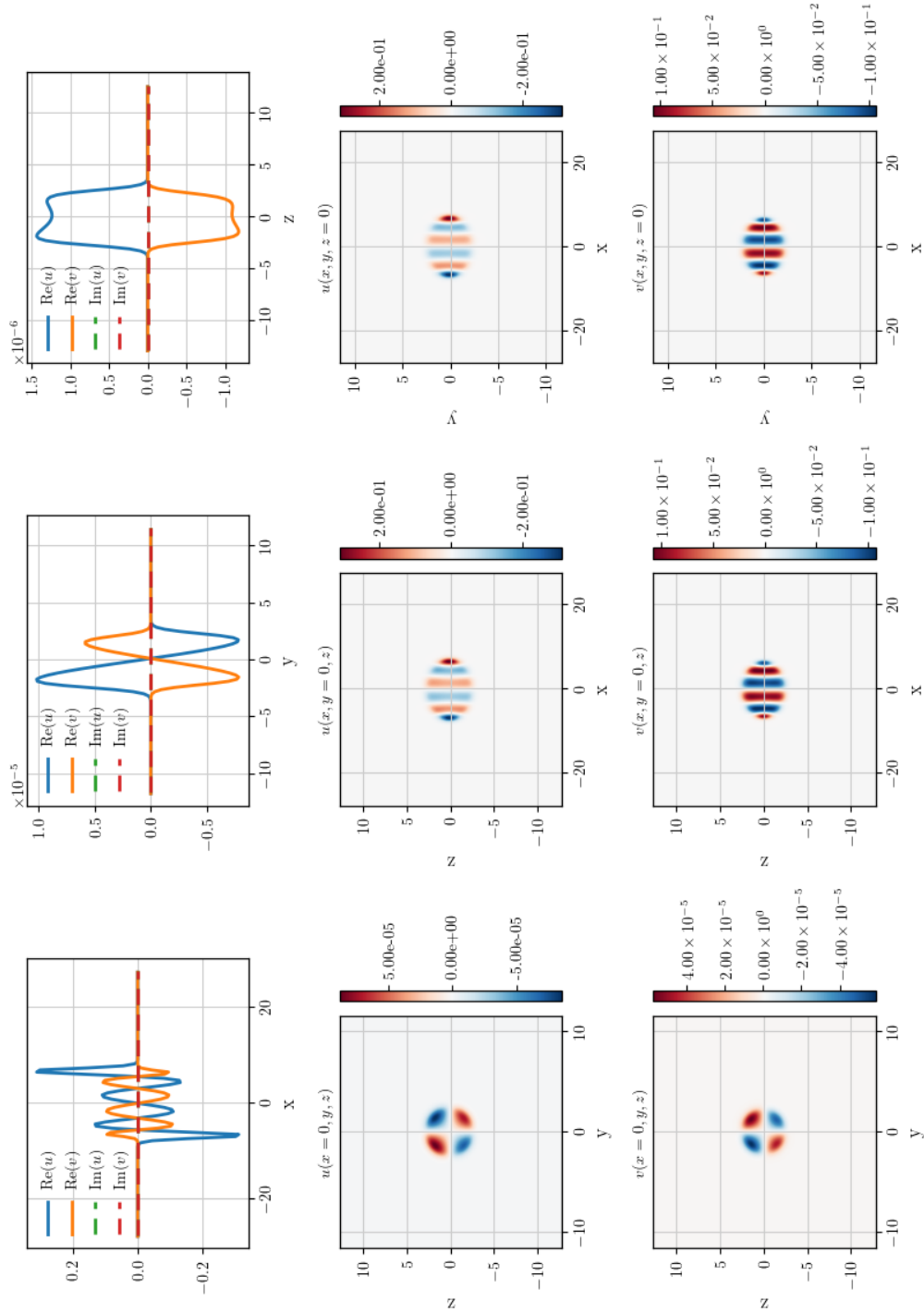


Figure J.10: $\omega_9/(2\pi) = 28.9$ Hz

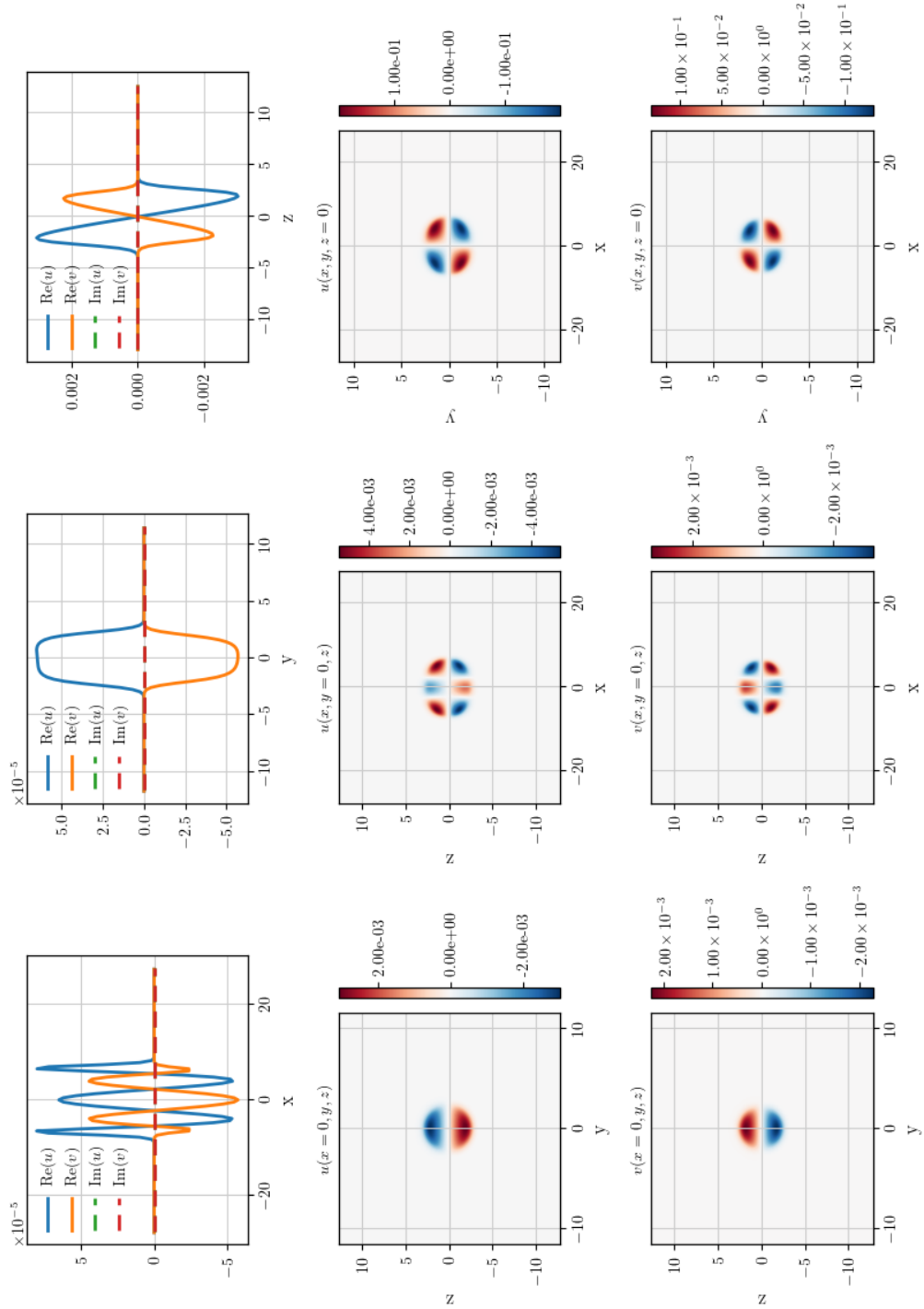


Figure J.11: $\omega_{10}/(2\pi) = 29.4$ Hz

K STATIONARY STATES IN EXTERNAL POTENTIALS

Imaginary-time propagation is a standard technique to find the ground state of the non-linear Gross-Pitaevskii equation. As long as the Euler step is small enough, the iterations will always converge to the ground state. One can extend the methods of steepest descent by computing the Newton direction of the Gross-Pitaevskii functional. The Newton method is particularly useful for three-dimensional calculations as the convergence efficiency is dramatically improved [71].

K.1 NON-ROTATIONAL SINGLE-COMPONENT BEC

In order to find the ground state numerically, one needs to find an iterative scheme for the wave function Ψ_k , converging to a solution

$$F[\Psi_0] > F[\Psi_1] > \dots, \quad (\text{K.1})$$

with minimal free energy Gross-Pitaevskii energy functional

$$F[\Psi] = \int \left(\frac{\hbar^2}{2M} |\nabla \Psi|^2 + U |\Psi|^2 + \frac{g}{2} |\Psi|^4 \right) d^3r - \mu \int |\Psi|^2 d^3r. \quad (\text{K.2})$$

To find a descent direction of the free energy functional, it is convenient to approximate F to second order with respect to a trial state Ψ_0 .

$$Q[\Psi] = F[\Psi_0] + \langle H, \Psi - \Psi_0 \rangle + \frac{1}{2} \langle \Psi - \Psi_0, \Sigma(\Psi - \Psi_0) \rangle, \quad (\text{K.3})$$

where the gradient, $H = \delta F / \delta \Psi$, is defined as the functional derivative with respect to the field. For the free energy of the single-component Gross-Pitaevskii equation one finds for real-valued fields $\Psi = \Psi^*$,

$$H = \frac{\delta F}{\delta \Psi} = 2 \left(-\frac{\nabla^2 \Psi_0}{2} + U \Psi_0 + g \Psi_0^3 - \mu \Psi_0 \right). \quad (\text{K.4})$$

The Hessian is given by

$$\Sigma = \frac{\delta^2 F}{\delta \Psi \delta \Psi'} = 2 \left(-\frac{\nabla^2}{2} + U + 3g \Psi_0^2 - \mu \right). \quad (\text{K.5})$$

An extremal point of the quadratic approximation requires a vanishing gradient

$$\frac{\delta Q}{\delta \Psi} = 0 = H + \Sigma(\Psi - \Psi_0), \quad (\text{K.6})$$

$$\Rightarrow \Psi = \Psi_0 - \Sigma^{-1} H. \quad (\text{K.7})$$

The stationary point is a minimum as long as the Hessian is positive definite. Equation (K.7) may be regarded as in iterative scheme to minimize the free energy functional

$$\begin{aligned}\Psi_{k+1} &= \Psi_k - \Sigma_k^{-1} H_k, \\ \Psi_{k+1} &= \Psi_k - \delta\Psi_k.\end{aligned}\tag{K.8}$$

The iteration scheme is called Newton's method for optimization. It is the preferred method for running three-dimensional calculations, as it dramatically improves the converge to the ground state solution. However, there are some issues to keep in mind. First, the propagation is not unitary and therefore the wave function needs to be renormalized to ensure the particle number conservation. Second, the direct inversion of the operator might not be accessible. Hence, it is better to solve the linear equation

$$\Sigma_k \delta\Psi_k = H_k,\tag{K.9}$$

to have at least a very good approximation of the update step $\delta\Psi_k$. Third, the Hessian might not be positive definite and the Newton method does not converge to the ground state solution. Then, it is easy to adopt the iteration scheme to the method of steepest descent (gradient descent)

$$\Psi_{k+1} = \Psi_k - \tau H_k,\tag{K.10}$$

with a fixed step size τ . It is also known as imaginary time propagation because it may be regarded as an Euler step of the time-dependent Gross-Pitaevskii equation replacing the time $t \rightarrow -i\tau$ [179].

K.2 NON-ROTATIONAL MULTI-COMPONENT BEC

The iterative scheme for minimizing the free energy functional (K.8) can also be applied for two-component Bose-Einstein condensates, replacing H and Σ with the corresponding gradient and Hesse matrix of the two-component Gross-Pitaevskii fields [46]

$$\mathbf{H} = \begin{pmatrix} H_1 - \mu_1 & 0 \\ 0 & H_2 - \mu_2 \end{pmatrix}, \quad \Sigma = \begin{pmatrix} \Sigma_{11} + g_{12}\psi_2^2 & 2g_{12}\psi_1\psi_2 \\ 2g_{12}\psi_1\psi_2 & \Sigma_{22} + g_{12}\psi_1^2 \end{pmatrix},\tag{K.11}$$

$$H_i\psi_i = \left(-\frac{\hbar^2}{2m_i} \nabla^2 + U_i + g_{ii}|\psi_i|^2 + g_{ij}|\psi_j|^2 \right) \psi_i,\tag{K.12}$$

$$\Sigma_{ii} = -\frac{\hbar^2}{2m_i} \nabla^2 + U_i + 3g_{ii}|\psi_i|^2 - \mu_i,\tag{K.13}$$

with $i \neq j$, $g_{ij} = 2\pi\hbar^2 a_{ij}/m_{ij}$, reduced mass $m_{ij} = m_i m_j / (m_i + m_j)$ and coupling constants $g_{12} = g_{21}$.

L TIME-EVOLUTION OF WAVE FUNCTION

For propagating wave function in time we have implemented a standard 4th-order Runge-Kutta integrator which is a convenient method for solving differential equations. Taking into account that the time-evolution is usually generated by a Hamilton operator, it is advantageous to use symplectic integrators which preserve the phase space geometry. We discuss both methods briefly in the following sections. More details and other numerical methods are found in [178, 180, 183] and references therein.

L.1 RUNGE-KUTTA INTEGRATOR

Consider the ordinary first-order differential equation

$$\frac{d}{dt}y(t) = f(t, y), \quad (\text{L.1})$$

with initial condition $y(t_0) = y_0$. Since dy/dt is just the slope of the function $f(t, y)$, we may write the left hand side of equation (L.1) as a difference quotient

$$\frac{y(t+h) - y(t)}{h} \approx f(t, y), \quad (\text{L.2})$$

or

$$y(t+h) \approx y(t) + hf(t, y), \quad (\text{L.3})$$

for a step width $h \neq 0$. Equation (L.3) defines a step-by-step iteration scheme, known as the forward Euler method, which should give a good approximation for small values of h . Nevertheless, the Euler method is not recommended because of its low accuracy and instability. However, we can use the step (cf. equation (L.3)) as a trial step to generate methods of higher order. A widely used formula is the fourth-order Runge-Kutta algorithm,

$$y_{n+1} = y_n + \frac{1}{6}(k_1 + 2k_2 + 2k_3 + k_4), \quad t_{n+1} = t_n + h, \quad (\text{L.4})$$

with weights

$$\begin{aligned} k_1 &= hf(t_n, y_n), \\ k_2 &= hf\left(t_n + \frac{1}{2}h, y_n + \frac{1}{2}k_1\right), \\ k_3 &= hf\left(t_n + \frac{1}{2}h, y_n + \frac{1}{2}k_2\right), \\ k_4 &= hf(t_n + h, y_n + k_3), \end{aligned} \quad (\text{L.5})$$

that are used to give a good approximation for y_{n+1} . To calculate the weights, $f(t, y)$ has to be evaluated once at the initial point applying a full Euler step, twice at trail midpoints, and once at a trail endpoint (figure L.1).

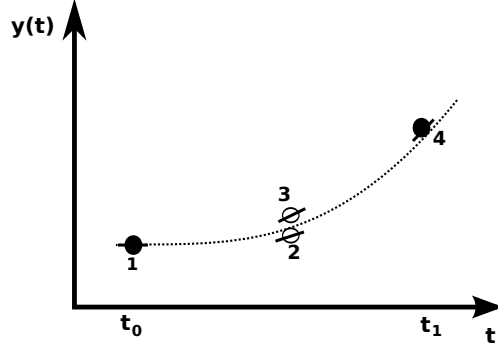


Figure L.1: Fourth order Runge-Kutta. In each iteration step the function is evaluated four times: once at the initial point, twice at trial midpoints, and once at a trial endpoint.

L.2 SPLIT OPERATOR

The split operator method is a symplectic integration method [184]. When the dynamic is generated by a Hamilton operator a symplectic integrator preserves the geometry of phase space. Therefore, observables such as norm, energy, or angular momentum are conserved.

The formal solution of the time-dependent (non-linear) Schrödinger equation is given by

$$\psi(t) = U(t)\psi(0), \quad (\text{L.6})$$

with the time-evolution operator

$$U(t) = \mathcal{T}e^{-i\int_0^t dt' H(t')}, \quad U(0) = \mathbb{1}, \quad (\text{L.7})$$

where \mathcal{T} denotes the time-ordering operator which is required when the Hamilton operator $H(t) = T + U(t)$ depends explicitly on time. If H is time-independent [184], we can approximate the time evolution operator in equation (L.7) as

$$U = e^{\tau(T+U)} = \prod_i^k e^{c_i T \tau} e^{d_i U \tau} + \mathcal{O}(\tau^{n+1}), \quad (\text{L.8})$$

to the order $n + 1$. The real numbers c_i, d_i depend on the splitting scheme and can be computed using the Baker-Campbell Hausdorff formula. Typical splittings schemes are [178, 184]:

FIRST ORDER SPLITTING

$$U_1 = e^{T\tau} e^{U\tau}. \quad (\text{L.9})$$

SECOND ORDER SPLITTING

$$U_2 = e^{T\tau/2} e^{U\tau} e^{T\tau/2}. \quad (\text{L.10})$$

FOURTH ORDER SPLITTING

$$U_4 = e^{\theta T \tau} e^{2\theta U \tau} e^{(\theta-0.5)T \tau} e^{(1-4\theta)U \tau} e^{(\theta-0.5)T \tau} e^{2\theta U \tau} e^{\theta T \tau}, \quad (\text{L.11})$$

with [178],

$$\theta = \frac{1}{6} \left(2 + 2^{1/3} + 2^{-1/3} \right). \quad (\text{L.12})$$

If the external potential depends explicitly on time $U = U(t)$, the integral in equation (L.7) needs to be approximated. For small time steps, we have

$$U(t + \Delta t, t) \approx e^{-i \int_t^{t+\Delta t} [T+U(t')] dt'}. \quad (\text{L.13})$$

The integral may be evaluated using different integration schemes, for example, the midpoint or Simpson's rule [185],

$$\int_t^{t+\Delta t} U(t') dt' = \frac{\Delta t}{6} [U(t) + 4U(t + \Delta t/2) + U(t + \Delta t)] + \mathcal{O}(\Delta t^5). \quad (\text{L.14})$$

M COORDINATE SYSTEMS

M.1 ROTATION MATRICES

Arbitrary rotations of coordinates are represented by a sequence of elementary rotation matrices. In three-dimensional space, these are 3×3 rotation matrices, which rotate the system around one coordinate axes with a given angle,

$$R_z(\gamma) = \begin{pmatrix} \cos \gamma & -\sin \gamma & 0 \\ \sin \gamma & \cos \gamma & 0 \\ 0 & 0 & 1 \end{pmatrix}, \quad (\text{M.1})$$

$$R_y(\beta) = \begin{pmatrix} \cos \beta & 0 & \sin \beta \\ 0 & 1 & 0 \\ -\sin \beta & 0 & \cos \beta \end{pmatrix}, \quad (\text{M.2})$$

$$R_x(\alpha) = \begin{pmatrix} 1 & 0 & 0 \\ 0 & \cos \alpha & -\sin \alpha \\ 0 & \sin \alpha & \cos \alpha \end{pmatrix}. \quad (\text{M.3})$$

There are six different combinations of matrices to obtain the desired coordinate transformation with two different conventions each [186]. In the Euler convention, the first and the last rotation are about the same axis, while in the Tait-Bryan angle convention, one uses three distinct rotation axes. Moreover, one differs between extrinsic (rotations in a fixed coordinate system) and intrinsic rotations (rotations about the rotated axis). For a composition of three extrinsic rotations about the axes z, y, x , with angles γ, β, α one finds the total rotation matrix

$$R_x(\alpha)R_y(\beta)R_z(\gamma) = \begin{pmatrix} c_\beta c_\gamma & -c_\beta s_\gamma & s_\beta \\ c_\alpha s_\gamma + s_\alpha s_\beta c_\gamma & c_\alpha c_\gamma - s_\alpha s_\beta s_\gamma & -s_\alpha c_\beta \\ s_\alpha s_\gamma - c_\alpha s_\beta c_\gamma & s_\alpha c_\gamma + c_\alpha s_\beta s_\gamma & c_\alpha s_\beta \end{pmatrix}, \quad (\text{M.4})$$

$$c_\theta = \cos \theta, \quad s_\theta = \sin \theta.$$

The Tait-Bryan angles are given by

$$\begin{aligned} \alpha &= \arctan_2(-R_{23}, R_{33}), \\ \beta &= \arcsin R_{13}, \\ \gamma &= \arctan_2(-R_{12}, R_{11}), \end{aligned} \quad (\text{M.5})$$

where $\arctan_2(y, x)$ is the element wise $\arctan(y/x)$ of y/x choosing the correct quadrant [186].

M.2 FINITE ROTATIONS

Euler rotations [136] in fixed coordinate system are obtained by the action of the operator (z - y - z convention)

$$\hat{R}(\alpha, \beta, \gamma) = e^{-i\alpha\hat{J}_z} e^{-i\beta\hat{J}_y} e^{-i\gamma\hat{J}_z}. \quad (\text{M.6})$$

The action on a ket state reads

$$|\psi'\rangle = \hat{R}(\alpha, \beta, \gamma) |\psi\rangle. \quad (\text{M.7})$$

For scalar field in coordinate space, one finds

$$\psi'(\mathbf{r}) = \langle \mathbf{r} | \hat{R} | \psi \rangle = \langle \mathbf{R}^{-1} \mathbf{r} | \psi \rangle = \psi(\mathbf{R}^{-1} \mathbf{r}). \quad (\text{M.8})$$

Hence the action of the operator \hat{R} on a position eigenstate reads

$$\hat{R}^\dagger |\mathbf{r}\rangle = |\mathbf{R}^{-1} \mathbf{r}\rangle. \quad (\text{M.9})$$

M.3 ROTATION OF ANGULAR MOMENTUM STATES

The action of the operator $\hat{R}(\alpha, \beta, \gamma)$ on angular momentum eigenstates $|lm\rangle$ is,

$$\hat{R}(\alpha, \beta, \gamma) |lm\rangle = \sum_{l'm'} |l'm'\rangle \langle l'm' | \hat{R}(\alpha, \beta, \gamma) |lm\rangle = \sum_{m'} |lm'\rangle D_{m'm}^{(l)}(\alpha, \beta, \gamma), \quad (\text{M.10})$$

where $D_{m'm}^{(l)}$ are the Wigner D-matrices representing the rotation operator in angular momentum basis states

$$\langle l'm' | \hat{R}(\alpha, \beta, \gamma) |lm\rangle = \delta_{l'l} D_{m'm}^{(l)}(\alpha, \beta, \gamma). \quad (\text{M.11})$$

The matrix is diagonal in l' , l as the rotation operator commutes with \hat{L}^2 ,

$$D_{m'm}^{(l)}(\alpha, \beta, \gamma) = e^{-i(\alpha m' + \gamma m)} d_{m'm}^{(l)}(\beta), \quad (\text{M.12})$$

$$d_{m'm}^{(l)}(\beta) = \langle lm' | e^{-i\beta\hat{J}_y} |lm\rangle, \quad (\text{M.13})$$

and unitary

$$\delta_{m,m'} = \sum_k D_{km}^{(l)*}(\mathbf{R}) D_{km'}^{(l)}(\mathbf{R}). \quad (\text{M.14})$$

M.4 ROTATION OF MULTIPOLE COEFFICIENTS

Having introduced the Wigner D-matrices and the action of the rotation operator on position eigenstates, one finds the following relation between the multipole coefficients in equation (7.4),

$$\begin{aligned} \langle \mathbf{r} | U \rangle &= \langle \mathbf{r}' | U' \rangle = \langle \mathbf{r}' | \hat{R} | U \rangle \\ &= \sum_{nlm} \langle \mathbf{r}' | \hat{R} | nlm \rangle U_{nlm} = \sum_{nlm} \sum_{m'=-l}^l \langle \mathbf{r}' | nlm' \rangle D_{m'm}^{(l)}(\alpha, \beta, \gamma) U_{nlm} \\ &= \sum_{nlm'} \langle \mathbf{r}' | nlm' \rangle U'_{nlm'}. \end{aligned} \quad (\text{M.15})$$

Therefore, one finds the rotated expansion coefficients

$$U'_{nlm'} = \sum_{m=-l}^l D_{m'm}^{(l)}(\alpha, \beta, \gamma) U_{nlm}, \quad (\text{M.16})$$

as a matrix multiplication with the Wigner D-matrices in the angular momentum manifold l .

BIBLIOGRAPHY

1. F. Zernike, “Beugungstheorie des Schneidenverfahrens und seiner verbesserten Form, der Phasenkontrastmethode”, *Physica* **1**:7-12, 689–704 (1934) (cited on page 1).
2. F. Zernike, “Das Phasenkontrastverfahren bei der mikroskopischen Beobachtung”, *Z. techn. Physik* **16**, 454–457 (1935) (cited on page 1).
3. H. Gross, editor, *Handbook of Optical Systems: Volume 1: Fundamentals of Technical Optics*, 1st edition, Wiley, 2005 (cited on page 1).
4. H. Gross, H. Zügge, M. Peschka, et al., editors, *Handbook of Optical Systems: Volume 3: Aberration Theory and Correction of Optical Systems*, Wiley-VCH Verlag GmbH & Co. KGaA, Weinheim, Germany, 2006 (cited on pages 1, 75, 92).
5. M. Haider, S. Uhlemann, E. Schwan, et al., “Electron microscopy image enhanced”, *Nature* **392**:6678, 768–769 (1998) (cited on page 1).
6. P. E. Batson, N. Dellby, and O. L. Krivanek, “Sub-ångstrom resolution using aberration corrected electron optics”, *Nature* **418**:6898, 617–620 (2002) (cited on page 1).
7. D. A. Muller, L. F. Kourkoutis, M. Murfitt, et al., “Atomic-Scale Chemical Imaging of Composition and Bonding by Aberration-Corrected Microscopy”, *Science* **319**:5866, 1073–1076 (2008) (cited on page 1).
8. A. D. Cronin, J. Schmiedmayer, and D. E. Pritchard, “Optics and interferometry with atoms and molecules”, *Rev. Mod. Phys.* **81**:3, 1051–1129 (2009) (cited on page 1).
9. L. De Broglie, “Recherches sur la théorie des Quanta”, *Ann. Phys.* **10**:3, 22–128 (1925) (cited on pages 1, 25, 33).
10. C. Bordé, “Atomic interferometry with internal state labelling”, *Physics Letters A* **140**:1-2, 10–12 (1989) (cited on page 1).
11. D. W. Keith, C. R. Ekstrom, Q. A. Turchette, et al., “An interferometer for atoms”, *Phys. Rev. Lett.* **66**:21, 2693–2696 (1991) (cited on page 1).
12. D. Schlippert, J. Hartwig, H. Albers, et al., “Quantum Test of the Universality of Free Fall”, *Phys. Rev. Lett.* **112**:20, 203002 (2014) (cited on page 1).
13. T. Kovachy, P. Asenbaum, C. Overstreet, et al., “Quantum superposition at the half-metre scale”, *Nature* **528**:7583, 530–533 (2015) (cited on pages 1–2).
14. Y. A. El-Neaj, C. Alpigiani, S. Amairi-Pyka, et al., “AEDGE: Atomic Experiment for Dark Matter and Gravity Exploration in Space”, *EPJ Quantum Technol.* **7**:1, 6 (2020) (cited on page 1).
15. S. Dimopoulos, P. W. Graham, J. M. Hogan, et al., “Gravitational wave detection with atom interferometry”, *Physics Letters B* **678**:1, 37–40 (2009) (cited on page 1).
16. G. M. Tino, A. Bassi, G. Bianco, et al., “SAGE: A proposal for a space atomic gravity explorer”, *Eur. Phys. J. D* **73**:11, 228 (2019) (cited on page 1).
17. K. Bongs, M. Holynski, J. Vovrosh, et al., “Taking atom interferometric quantum sensors from the laboratory to real-world applications”, *Nat Rev Phys* **1**:12, 731–739 (2019) (cited on page 1).

Bibliography

18. M. Kasevich and S. Chu, “Measurement of the gravitational acceleration of an atom with a light-pulse atom interferometer”, *Appl. Phys. B* **54**:5, 321–332 (1992) (cited on page 1).
19. P. Martin, B. Oldaker, A. Miklich, et al., “Bragg scattering of atoms from a standing light wave”, *Phys. Rev. Lett.* **60**:6, 515–518 (1988) (cited on page 1).
20. D. M. Giltner, R. W. McGowan, and S. A. Lee, “Atom Interferometer Based on Bragg Scattering from Standing Light Waves”, *Phys. Rev. Lett.* **75**:14, 2638–2641 (1995) (cited on page 1).
21. M. K. Oberthaler, R. Abfalterer, S. Bernet, et al., “Atom Waves in Crystals of Light”, *Phys. Rev. Lett.* **77**:25, 4980–4983 (1996) (cited on page 1).
22. E. Giese, A. Roura, G. Tackmann, et al., “Double Bragg diffraction: A tool for atom optics”, *Phys. Rev. A*, **23** (2013) (cited on page 1).
23. M. Kasevich, D. S. Weiss, E. Riis, et al., “Atomic velocity selection using stimulated Raman transitions”, *Phys. Rev. Lett.* **66**:18, 2297–2300 (1991) (cited on page 1).
24. S. Abend, B. Allard, A. S. Arnold, et al., “Technology roadmap for cold-atoms based quantum inertial sensor in space”, *AVS Quantum Sci.* **5**:1, 019201 (2023) (cited on page 1).
25. S. M. Dickerson, J. M. Hogan, A. Sugarbaker, et al., “Multiaxis Inertial Sensing with Long-Time Point Source Atom Interferometry”, *Phys. Rev. Lett.* **111**:8, 083001 (2013) (cited on page 2).
26. T. van Zoest, N. Gaaloul, Y. Singh, et al., “Bose-Einstein Condensation in Microgravity”, *Science* **328**:5985, 1540–1543 (2010) (cited on pages 2, 5, 9, 53).
27. H. Müntinga, H. Ahlers, M. Krutzik, et al., “Interferometry with Bose-Einstein Condensates in Microgravity”, *Phys. Rev. Lett.* **110**:9, 093602 (2013) (cited on pages 2, 5, 9, 53).
28. R. Geiger, V. Ménotet, G. Stern, et al., “Detecting inertial effects with airborne matter-wave interferometry”, *Nat Commun* **2**:1, 474 (2011) (cited on page 2).
29. B. Barrett, L. Antoni-Micollier, L. Chichet, et al., “Dual matter-wave inertial sensors in weightlessness”, *Nat Commun* **7**:1, 13786 (2016) (cited on page 2).
30. A. D. Carli, C. D. Colquhoun, S. Kuhr, et al., “Interferometric measurement of micro-g acceleration with levitated atoms”, *New J. Phys.* **21**:5, 053028 (2019) (cited on page 2).
31. D. Becker, M. D. Lachmann, S. T. Seidel, et al., “Space-borne Bose–Einstein condensation for precision interferometry”, *Nature* **562**:7727, 391–395 (2018) (cited on page 2).
32. M. D. Lachmann, H. Ahlers, D. Becker, et al., “Ultracold atom interferometry in space”, *Nat Commun* **12**:1, 1317 (2021) (cited on page 2).
33. D. C. Aveline, J. R. Williams, E. R. Elliott, et al., “Observation of Bose–Einstein condensates in an Earth-orbiting research lab”, *Nature* **582**:7811, 193–197 (2020) (cited on pages 2, 75).
34. K. Frye, S. Abend, W. Bartosch, et al., “The Bose-Einstein Condensate and Cold Atom Laboratory”, *EPJ Quantum Technol.* **8**:1, 1 (2021) (cited on pages 2, 5).
35. H. Ammann and N. Christensen, “Delta Kick Cooling: A New Method for Cooling Atoms”, *Phys. Rev. Lett.* **78**:11, 2088–2091 (1997) (cited on pages 2, 75).
36. T. Kovachy, J. M. Hogan, A. Sugarbaker, et al., “Matter Wave Lensing to Picokelvin Temperatures”, *Phys. Rev. Lett.* **114**:14, 143004 (2015) (cited on page 2).
37. C. Deppner, W. Herr, M. Cornelius, et al., “Collective-Mode Enhanced Matter-Wave Optics”, *Phys. Rev. Lett.* **127**:10, 100401 (2021) (cited on pages 2, 12, 15, 75, 78, 81).

38. M. Cornelius, “Atom interferometry with picokelvin ensembles in microgravity”, PhD thesis (Universität Bremen, 2022) (cited on pages 2, 15, 78).
39. A. Vogel, M. Schmidt, K. Sengstock, et al., “Bose–Einstein condensates in microgravity”, *Appl. Phys. B* **84**:4, 663–671 (2006) (cited on page 2).
40. M. Pfalz, “Forschung im Fallturm”, *Physik Journal* **21**:10 (2022) (cited on page 2).
41. K. Bongs, S. Burger, S. Dettmer, et al., “Waveguide for Bose-Einstein condensates”, *Phys. Rev. A* **63**:3, 031602 (2001) (cited on page 2).
42. T. Berrada, S. van Frank, R. Bücker, et al., “Integrated Mach–Zehnder interferometer for Bose–Einstein condensates”, *Nat Commun* **4**:1, 2077 (2013) (cited on page 2).
43. C. Ryu and M. G. Boshier, “Integrated coherent matter wave circuits”, *New J. Phys.* **17**:9, 092002 (2015) (cited on page 2).
44. L. Amico, M. Boshier, G. Birkl, et al., “Roadmap on Atomtronics: State of the art and perspective”, *AVS Quantum Sci.* **3**:3, 039201 (2021) (cited on pages 2, 99, 101).
45. F. Dalfovo and S. Giorgini, “Theory of Bose-Einstein condensation in trapped gases”, *Rev. Mod. Phys.* **71**:3, 50 (1999) (cited on pages 2, 30).
46. C. J. Pethick and H. Smith, *Bose–Einstein Condensation in Dilute Gases*, 2nd edition, Cambridge University Press, 2008 (cited on pages 2, 38, 160).
47. C. Ryu, M. Andersen, P. Cladé, et al., “Observation of Persistent Flow of a Bose-Einstein Condensate in a Toroidal Trap”, *Phys. Rev. Lett.* **99**:26, 260401 (2007) (cited on page 2).
48. N. Bazhan, A. Svetlichnyi, D. Pfeiffer, et al., “Generation of Josephson vortices in stacked toroidal Bose-Einstein condensates”, *Phys. Rev. A* **106**:4, 043305 (2022) (cited on page 2).
49. Y. Castin and R. Dum, “Bose-Einstein Condensates in Time Dependent Traps”, *Phys. Rev. Lett.* **77**:27, 5315–5319 (1996) (cited on pages 2, 17, 35–36, 51).
50. Y. Kagan, E. L. Surkov, and G. V. Shlyapnikov, “Evolution of a Bose-condensed gas under variations of the confining potential”, *Phys. Rev. A* **54**:3, R1753–R1756 (1996) (cited on pages 2, 17, 35, 51).
51. J. Teske, M. R. Besbes, B. Okhrimenko, et al., “Mean-field Wigner function of Bose–Einstein condensates in the Thomas–Fermi limit”, *Phys. Scr.* **93**:12, 124004 (2018) (cited on pages 3, 25, 30, 48–49, 119).
52. J. D. Jackson, “Electrodynamics, Classical”, in *Digital Encyclopedia of Applied Physics*, edited by Wiley-VCH Verlag GmbH & Co. KGaA, Wiley-VCH Verlag GmbH & Co. KGaA, Weinheim, Germany, 2003, eap109 (cited on page 5).
53. C. Cohen-Tannoudji, B. Diu, and F. Laloë, “Band 2 Quantenmechanik”, in *Band 2*, De Gruyter, Berlin, Boston, 2019, pages V–VI (cited on pages 5–7).
54. P. Zeeman, “On the Influence of Magnetism on the Nature of the Light Emitted by a Substance.”, *The Astrophysical Journal* **5**, 332 (1897) (cited on page 5).
55. W. Herr, “Eine kompakte Quelle quantenentarteter Gase hohen Flusses für die Atominterferometrie unter Schwerelosigkeit”, PhD thesis (Gottfried Wilhelm Leibniz Universität Hannover, 2013) (cited on pages 5, 9).
56. J. Rudolph, W. Herr, C. Grzeschik, et al., “A high-flux BEC source for mobile atom interferometers”, *New J. Phys.* **17**:6, 065001 (2015) (cited on pages 5, 9).
57. S. Earnshaw, “On the nature of the molecular forces which regulate the constitution of the luminiferous ether”, *Transactions of the Cambridge Philosophical Society* **7**, 97 (1848) (cited on page 5).

Bibliography

58. W. H. Wing, “On neutral particle trapping in quasistatic electromagnetic fields”, *Progress in Quantum Electronics* **8**:3-4, 181–199 (1984) (cited on page 6).
59. W. Ketterle and D. E. Pritchard, “Trapping and focusing ground state atoms with static fields”, *Appl. Phys. B* **54**:5, 403–406 (1992) (cited on page 6).
60. G. Breit and I. I. Rabi, “Measurement of Nuclear Spin”, *Phys. Rev.* **38**:11, 2082–2083 (1931) (cited on page 7).
61. D. A. Steck, <https://steck.us/alkalidata/> (cited on page 7).
62. D. A. Steck, *Rubidium 87 D Line Data*, 2021 (cited on page 7).
63. T. Tiecke, *Properties of Potassium*, 2019 (cited on page 7).
64. E. Majorana, “Atomi orientati in campo magnetico variabile”, *Nuovo Cim* **9**:2, 43–50 (1932) (cited on page 8).
65. J. Fortágh and C. Zimmermann, “Magnetic microtraps for ultracold atoms”, *Rev. Mod. Phys.* **79**:1, 235–289 (2007) (cited on page 8).
66. M. Keil, O. Amit, S. Zhou, et al., “Fifteen years of cold matter on the atom chip: promise, realizations, and prospects”, *Journal of Modern Optics* **63**:18, 1840–1885 (2016) (cited on page 8).
67. J. Reichel, W. Hänsel, and T. W. Hänsch, “Atomic Micromanipulation with Magnetic Surface Traps”, *Phys. Rev. Lett.* **83**:17, 3398–3401 (1999) (cited on page 9).
68. R. Folman, P. Krüger, D. Cassettari, et al., “Controlling Cold Atoms using Nanofabricated Surfaces: Atom Chips”, *Phys. Rev. Lett.* **84**:20, 4749–4752 (2000) (cited on page 9).
69. D. Cassettari, A. Chenet, R. Folman, et al., “Micromanipulation of neutral atoms with nanofabricated structures”, *Appl Phys B* **70**:5, 721–730 (2000) (cited on page 9).
70. A. Haase, D. Cassettari, B. Hessmo, et al., “Trapping neutral atoms with a wire”, *Phys. Rev. A* **64**:4, 043405 (2001) (cited on page 9).
71. J. Nocedal and S. Wright, *Numerical Optimization*, Springer Series in Operations Research and Financial Engineering, Springer New York, 2006 (cited on pages 11, 58, 159).
72. R. Corgier, S. Amri, W. Herr, et al., “Fast manipulation of Bose–Einstein condensates with an atom chip”, *New J. Phys.* **20**:5, 055002 (2018) (cited on page 12).
73. T. Sternke, “An ultracold high-flux source for matter-wave interferometry in microgravity”, PhD thesis (Universität Oldenburg, 2018) (cited on pages 15, 81).
74. R. Balescu, *Equilibrium and non-equilibrium statistical mechanics*, A Wiley Interscience Publication, Wiley, 1975 (cited on page 17).
75. W. P. Schleich, *Quantum Optics in Phase Space*, 1st edition, Wiley, 2001 (cited on pages 17, 41–42).
76. H. Goldstein, C. Poole, and J. Safko, *Classical Mechanics*, Addison-Wesley Series in Physics, Addison Wesley, 2002 (cited on page 17).
77. V. Arnold, *Mathematical Methods of Classical Mechanics*, Graduate Texts in Mathematics, Springer New York, 2013 (cited on page 17).
78. L. Landau and E. Lifshitz, *Mechanics: Volume 1*, Bd. 1, Elsevier Science, 1982 (cited on page 17).
79. M. Meister, S. Arnold, D. Moll, et al., “Efficient Description of Bose–Einstein Condensates in Time-Dependent Rotating Traps”, in *Advances In Atomic, Molecular, and Optical Physics*, Vol. 66, Elsevier, 2017, pages 375–438 (cited on pages 17, 35, 51, 53, 76, 123).

80. A. H. Nayfeh, *Perturbation Methods*, 1st edition, Wiley, 2000 (cited on page 20).
81. G. Nandi, R. Walser, E. Kajari, et al., “Dropping cold quantum gases on Earth over long times and large distances”, *Phys. Rev. A* **76**:6, 063617 (2007) (cited on page 20).
82. J. Schwinger, *Quantum Mechanics: Symbolism of Atomic Measurements*, edited by B.-G. Englert, Springer Berlin Heidelberg, Berlin, Heidelberg, 2001 (cited on page 21).
83. M. Boudjema-Bouloudenine, T. Boudjedaa, and A. Makhlof, “Schwinger action principle via linear quantum canonical transformations”, *Eur. Phys. J. C* **46**:3, 807–816 (2006) (cited on page 21).
84. H. R. Lewis and W. B. Riesenfeld, “An Exact Quantum Theory of the Time-Dependent Harmonic Oscillator and of a Charged Particle in a Time-Dependent Electromagnetic Field”, *Journal of Mathematical Physics* **10**:8, 1458–1473 (1969) (cited on pages 21, 23).
85. D. Schuch, *Quantum Theory from a Nonlinear Perspective*, Vol. 191, Fundamental Theories of Physics, Springer International Publishing, Cham, 2018 (cited on pages 21, 23).
86. D. Guéry-Odelin, A. Ruschhaupt, A. Kiely, et al., “Shortcuts to adiabaticity: Concepts, methods, and applications”, *Rev. Mod. Phys.* **91**:4, 045001 (2019) (cited on pages 21, 114).
87. V. Ermakov, *Univ. Izv. Kiev* **20** (1880) (cited on pages 23, 47).
88. E. Pinney, “The nonlinear differential equation $y'' + p(x)y + cy^{-3} = 0$ ”, *Proc. Amer. Math. Soc.* **1**:5, 681 (1950) (cited on pages 23, 47).
89. W. Ketterle, “Nobel lecture: When atoms behave as waves: Bose-Einstein condensation and the atom laser”, *Rev. Mod. Phys.* **74**:4, 1131–1151 (2002) (cited on page 25).
90. J. T. M. Walraven, *Quantum Gases lectures University of Amsterdam*, 2019 (cited on pages 25, 27–28).
91. R. G. Newton, *Scattering Theory of Waves and Particles*, Springer Berlin Heidelberg, Berlin, Heidelberg, 1982 (cited on page 26).
92. J. R. Taylor and H. Uberall, “*Scattering Theory: The Quantum Theory of Nonrelativistic Collisions*”, *Physics Today* **26**:5, 55–56 (1973) (cited on page 26).
93. A. Galindo and P. Pascual, *Quantum Mechanics I*, Springer Berlin Heidelberg, Berlin, Heidelberg, 1990 (cited on pages 26, 58, 60, 63).
94. Y. Castin, “Bose-Einstein Condensates in Atomic Gases: Simple Theoretical Results”, in *Coherent atomic matter waves*, Vol. 72, edited by R. Kaiser, C. Westbrook, and F. David, Springer Berlin Heidelberg, Berlin, Heidelberg, 2001, pages 1–136 (cited on page 28).
95. K. Huang, *Introduction to Statistical Physics*, 0th edition, Chapman and Hall/CRC, 2009 (cited on page 28).
96. E. Fermi, “Sul moto dei neutroni nelle sostanze idrogenate”, *Ricerca scientifica* **7**:2, 13–52 (1936) (cited on page 28).
97. J. Blaizot and G. Ripka, *Quantum theory of finite systems*, MIT Press, 1986 (cited on pages 29, 38, 143).
98. T. Lancaster and S. J. Blundell, *Quantum Field Theory for the Gifted Amateur*, Oxford University Press, 2014 (cited on page 29).
99. L. H. Thomas, “The calculation of atomic fields”, *Mathematical Proceedings of the Cambridge Philosophical Society* **23**:5, 542–548 (1927) (cited on page 30).
100. E. Fermi, “Eine statistische Methode zur Bestimmung einiger Eigenschaften des Atoms und ihre Anwendung auf die Theorie des periodischen Systems der Elemente”, *Zeitschrift für Physik* **48**:1-2, 73–79 (1928) (cited on page 30).

Bibliography

101. G. Baym and C.J. Pethick, “Ground-State Properties of Magnetically Trapped Bose-Condensed Rubidium Gas”, *Phys. Rev. Lett.* **76**:1, 6–9 (1996) (cited on pages 30, 33).
102. J. P. Dahl, G. Süssmann, A. Wolf, et al., “Adventures in s-waves”, *Laser Physics* **15**, 18–36 (2005) (cited on page 31).
103. F. W. Olver, D. W. Lozier, R. F. Boisvert, et al., *NIST handbook of mathematical functions*, 1st, Cambridge University Press, USA, 2010 (cited on pages 32, 37, 46, 108–109, 131, 133).
104. G. B. Folland and A. Sitaram, “The uncertainty principle: A mathematical survey”, *The Journal of Fourier Analysis and Applications* **3**:3, 207–238 (1997) (cited on page 33).
105. F. Dalfovo, C. Minniti, S. Stringari, et al., “Nonlinear dynamics of a Bose condensed gas”, *Physics Letters A* **227**:3-4, 259–264 (1997) (cited on page 35).
106. P. Storey and M. Olshanii, “Closed class of hydrodynamical solutions for the collective excitations of a Bose-Einstein condensate”, *Phys. Rev. A* **62**:3, 033604 (2000) (cited on page 36).
107. T.-L. Ho and M. Ma, “Quasi 1 and 2d Dilute Bose Gas in Magnetic Traps: Existence of Off-Diagonal Order and Anomalous Quantum Fluctuations”, *Journal of Low Temperature Physics* **115**:1, 61–70 (1999) (cited on pages 36–37, 109, 111).
108. M. J. Bijlsma and H. T. C. Stoof, “Collisionless modes of a trapped Bose gas”, *Phys. Rev. A* **60**:5, 3973–3981 (1999) (cited on page 36).
109. S. Stringari, “Collective Excitations of a Trapped Bose-Condensed Gas”, *Phys. Rev. Lett.* **77**:12, 2360–2363 (1996) (cited on pages 37, 57).
110. P. Öhberg, E. L. Surkov, I. Tittonen, et al., “Low-energy elementary excitations of a trapped Bose-condensed gas”, *Phys. Rev. A* **56**:5, R3346–R3349 (1997) (cited on page 37).
111. M. Fliesser, A. Csordás, P. Szépfalusy, et al., “Hydrodynamic excitations of Bose condensates in anisotropic traps”, *Phys. Rev. A* **56**:4, R2533–R2536 (1997) (cited on page 37).
112. A. Csordás and R. Graham, “Collective excitations in Bose-Einstein condensates in triaxially anisotropic parabolic traps”, *Phys. Rev. A* **59**:2, 1477–1487 (1999) (cited on page 37).
113. R. Walser, “Ground state correlations in a trapped quasi one-dimensional Bose gas”, *Optics Communications*, **23** (2004) (cited on pages 38, 54, 143).
114. N. N. Bogolyubov, “On the theory of superfluidity”, *J. Phys. (USSR)* **11**, 23–32 (1947) (cited on page 38).
115. P. G. De Gennes, *Superconductivity of Metals and Alloys*, 1st edition, CRC Press, 2018 (cited on page 38).
116. E. Wigner, “On the Quantum Correction For Thermodynamic Equilibrium”, *Phys. Rev.* **40**:5, 749–759 (1932) (cited on page 41).
117. M. Naraschewski and R. J. Glauber, “Spatial coherence and density correlations of trapped Bose gases”, *Phys. Rev. A* **59**:6, 4595–4607 (1999) (cited on page 41).
118. A. Sinatra, C. Lobo, and Y. Castin, “The truncated Wigner method for Bose-condensed gases: limits of validity and applications”, *J. Phys. B: At. Mol. Opt. Phys.* **35**:17, 3599–3631 (2002) (cited on page 42).
119. F. Impens and D. Guéry-Odelin, “Classical phase-space approach for coherent matter waves”, *Phys. Rev. A* **81**:6, 065602 (2010) (cited on page 42).
120. G. Condon, A. Fortun, J. Billy, et al., “Phase-space manipulations of many-body wave functions”, *Phys. Rev. A* **90**:6, 063616 (2014) (cited on pages 47–48).

121. J. P. Dahl, S. Varro, A. Wolf, et al., “Wigner functions of s waves”, *Phys. Rev. A* **75**:5, 052107 (2007) (cited on page 48).
122. S. Stringari, “Dynamics of Bose-Einstein condensed gases in highly deformed traps”, *Phys. Rev. A* **58**:3, 2385–2388 (1998) (cited on page 51).
123. D. Hellweg, S. Dettmer, P. Ryytty, et al., “Phase fluctuations in Bose–Einstein condensates”, *Appl Phys B* **73**:8, 781–789 (2001) (cited on page 51).
124. S. Dettmer, D. Hellweg, P. Ryytty, et al., “Observation of Phase Fluctuations in Elongated Bose-Einstein Condensates”, *Phys. Rev. Lett.* **87**:16, 160406 (2001) (cited on page 51).
125. D. S. Petrov, G. V. Shlyapnikov, and J. T. M. Walraven, “Phase-Fluctuating 3D Bose-Einstein Condensates in Elongated Traps”, *Phys. Rev. Lett.* **87**:5, 050404 (2001) (cited on page 51).
126. H. Kreuzmann, A. Sanpera, L. Santos, et al., “Characterization and control of phase fluctuations in elongated Bose-Einstein condensates”, *Applied Physics B: Lasers and Optics* **76**:2, 165–172 (2003) (cited on page 51).
127. W. Kohn, “Cyclotron Resonance and de Haas-van Alphen Oscillations of an Interacting Electron Gas”, *Phys. Rev.* **123**:4, 1242–1244 (1961) (cited on pages 52, 81).
128. J. F. Dobson, “Harmonic-Potential Theorem: Implications for Approximate Many-Body Theories”, *Phys. Rev. Lett.* **73**:16, 2244–2247 (1994) (cited on pages 52, 81).
129. H. Römer, *Theoretical Optics: An Introduction*, 1st edition, Wiley, 2004 (cited on page 53).
130. E. Dobrek, M. Gajda, M. Lewenstein, et al., “Optical generation of vortices in trapped Bose-Einstein condensates”, *Phys. Rev. A* **60**:5, R3381–R3384 (1999) (cited on page 55).
131. R. Grimm, M. Weidemüller, and Y. B. Ovchinnikov, “Optical Dipole Traps for Neutral Atoms”, in *Advances In Atomic, Molecular, and Optical Physics*, Vol. 42, Elsevier, 2000, pages 95–170 (cited on pages 55, 99, 101).
132. S. Kanthak, M. Gebbe, M. Gersemann, et al., “Time-domain optics for atomic quantum matter”, *New J. Phys.* **23**:9, 093002 (2021) (cited on pages 55–56, 93).
133. P. Öhberg, E. L. Surkov, I. Tittonen, et al., “Low-energy elementary excitations of a trapped Bose-condensed gas”, *Phys. Rev. A* **56**:5, R3346–R3349 (1997) (cited on page 57).
134. C. W. Gardiner, *Handbook of Stochastic Methods for Physics, Chemistry, and the Natural Sciences*, Springer, 1985 (cited on page 57).
135. D. A. Varshalovich, A. N. Moskalev, and V. K. Khersonskii, *Quantum Theory of Angular Momentum*, WORLD SCIENTIFIC, 1988 (cited on pages 58, 131–132).
136. L. E. Ballentine, *Quantum Mechanics: A Modern Development*, 2nd edition, WORLD SCIENTIFIC, 2014 (cited on pages 58, 166).
137. A. R. Edmonds, *Angular Momentum in Quantum Mechanics*, Princeton University Press, 1957 (cited on page 60).
138. W. Zeller, “The impact of wave-packet dynamics in long-time atom interferometry”, PhD thesis (Universität Ulm, 2016) (cited on page 75).
139. R. B. Lehoucq, D. C. Sorensen, and C. Yang, *ARPACK users’ guide*, Society for Industrial and Applied Mathematics, 1998 (cited on pages 81, 144).
140. G. Gauthier, T. A. Bell, A. B. Stilgoe, et al., “Dynamic high-resolution optical trapping of ultracold atoms”, in *Advances In Atomic, Molecular, and Optical Physics*, Vol. 70, Elsevier, 2021, pages 1–101 (cited on pages 93, 105).
141. M. V. Berry and N. L. Balazs, “Nonspreading wave packets”, *American Journal of Physics* **47**:3, 264–267 (1979) (cited on page 94).

Bibliography

142. G. A. Siviloglou, J. Broky, A. Dogariu, et al., “Observation of Accelerating Airy Beams”, *Phys. Rev. Lett.* **99**:21, 213901 (2007) (cited on page 94).
143. M. Born, E. Wolf, A. B. Bhatia, et al., *Principles of Optics: Electromagnetic Theory of Propagation, Interference and Diffraction of Light*, 7th edition, Cambridge University Press, 1999 (cited on page 95).
144. C. Chin, R. Grimm, P. Julienne, et al., “Feshbach resonances in ultracold gases”, *Rev. Mod. Phys.* **82**:2, 62 (2010) (cited on pages 96, 116).
145. A. Burchianti, C. D’Errico, L. Marconi, et al., “Effect of interactions in the interference pattern of Bose-Einstein condensates”, *Phys. Rev. A* **102**:4, 043314 (2020) (cited on pages 96, 120).
146. Z. Yao, C. Solaro, C. Carrez, et al., “Local phase shift due to interactions in an atom interferometer”, *Phys. Rev. A* **106**:4, 043312 (2022) (cited on pages 96, 120).
147. G. A. Askaryan, “Effects of the Gradient of a Strong Electromagnetic Beam on Electrons and Atoms”, *Zhur. Eksptl. i Teoret. Fiz.* **42** (1962) (cited on page 99).
148. A. Ashkin, “Acceleration and Trapping of Particles by Radiation Pressure”, *Phys. Rev. Lett.* **24**:4, 156–159 (1970) (cited on page 99).
149. H. J. Metcalf and P. van der Straten, *Laser Cooling and Trapping*, edited by R. S. Berry, J. L. Birman, J. W. Lynn, et al., Graduate Texts in Contemporary Physics, Springer New York, New York, NY, 1999 (cited on page 99).
150. T. Kinoshita, T. Wenger, and D. S. Weiss, “Observation of a One-Dimensional Tonks-Girardeau Gas”, *Science* **305**:5687, 1125–1128 (2004) (cited on pages 99, 104).
151. M. O. Scully and M. S. Zubairy, *Quantum Optics*, 1st edition, Cambridge University Press, 1997 (cited on page 99).
152. C. Cohen-Tannoudji, J. Dupont-Roc, and G. Grynberg, *Atom—Photon Interactions: Basic Process and Applications*, 1st edition, Wiley, 1998 (cited on page 99).
153. C. Cohen-Tannoudji, “Fundamental systems in quantum optics”, *Proc. Les Houches Summer School*, 1992 (1992) (cited on pages 100–101).
154. J. P. Gordon and A. Ashkin, “Motion of atoms in a radiation trap”, *Phys. Rev. A* **21**:5, 1606–1617 (1980) (cited on page 100).
155. F. Schmaltz, J. Küber, A. Turpin, et al., “Trapping of Bose-Einstein condensates in a three-dimensional dark focus generated by conical refraction”, DOI: 10.48550/ARXIV.1705.02425 (2017) (cited on pages 101–102).
156. F. Schmaltz, “Bose-Einstein-Kondensate in dynamischen Dipolpotentialen aus konischer Refraktion”, PhD thesis (Technische Universität Darmstadt, 2018) (cited on pages 101–102).
157. A. Turpin, J. Polo, Y. V. Loiko, et al., “Blue-detuned optical ring trap for Bose-Einstein condensates based on conical refraction”, *Opt. Express* **23**:2, 1638 (2015) (cited on page 102).
158. A. M. Belskii and A. P. Khapalyuk, “Internal conical refraction of bounded light beams in biaxial crystals”, *Optics and Spectroscopy* **44**:4, 436–439 (1978) (cited on page 102).
159. M. V. Berry, “Conical diffraction asymptotics: fine structure of Poggendorff rings and axial spike”, *J. Opt. A: Pure Appl. Opt.* **6**:5 (2004) (cited on page 102).
160. A. Turpin, Y. V. Loiko, T. K. Kalkandjiev, et al., “Light propagation in biaxial crystals”, *J. Opt.* **17**:6, 065603 (2015) (cited on page 102).

161. O. Morizot, Y. Colombe, V. Lorent, et al., “Ring trap for ultracold atoms”, *Phys. Rev. A* **74**:2, 023617 (2006) (cited on pages 103–104).
162. S. I. Mistakidis, A. G. Volosniev, R. E. Barfknecht, et al., “Cold atoms in low dimensions – a laboratory for quantum dynamics”, DOI: 10.48550/ARXIV.2202.11071 (2022) (cited on page 104).
163. V. L. Berezinsky, “Destruction of long-range order in one-dimensional and two-dimensional systems possessing a continuous symmetry group. II. Quantum systems.”, *Sov. Phys. JETP* **34**:3, 610 (1972) (cited on page 104).
164. J. M. Kosterlitz and D. J. Thouless, “Ordering, metastability and phase transitions in two-dimensional systems”, *J. Phys. C: Solid State Phys.* **6**:7, 1181–1203 (1973) (cited on page 104).
165. Z. Hadzibabic, P. Krüger, M. Cheneau, et al., “Berezinskii–Kosterlitz–Thouless crossover in a trapped atomic gas”, *Nature* **441**:7097, 1118–1121 (2006) (cited on page 104).
166. Y.-X. Ren, R.-D. Lu, and L. Gong, “Tailoring light with a digital micromirror device: Tailoring light with a digital micromirror device”, *ANNALEN DER PHYSIK* **527**:7-8, 447–470 (2015) (cited on page 105).
167. R. Dubessy, T. Liennard, P. Pedri, et al., “Critical rotation of an annular superfluid Bose-Einstein condensate”, *Phys. Rev. A* **86**:1, 011602 (2012) (cited on page 108).
168. A. I. Yakimenko, K. O. Isaieva, S. I. Vilchinskii, et al., “Vortex excitation in a stirred toroidal Bose-Einstein condensate”, *Phys. Rev. A* **91**:2, 023607 (2015) (cited on page 108).
169. K. Sun, K. Padavić, F. Yang, et al., “Static and dynamic properties of shell-shaped condensates”, *Phys. Rev. A* **98**:1, 013609 (2018) (cited on pages 109–110, 112).
170. A. Wolf, P. Boegel, M. Meister, et al., “Shell-shaped Bose-Einstein condensates based on dual-species mixtures”, *Phys. Rev. A* **106**:1, 013309 (2022) (cited on pages 110, 112).
171. J.-F. Mennemann, D. Matthes, R.-M. Weishäupl, et al., “Optimal control of Bose–Einstein condensates in three dimensions”, *New J. Phys.* **17**:11, 113027 (2015) (cited on pages 113, 137, 144).
172. J. M. Gomez Llorente and J. Plata, “Expanding ring-shaped Bose-Einstein condensates as analogs of cosmological models: Analytical characterization of the inflationary dynamics”, *Phys. Rev. A* **100**:4, 043613 (2019) (cited on page 114).
173. S. Eckel, A. Kumar, T. Jacobson, et al., “A Rapidly Expanding Bose-Einstein Condensate: An Expanding Universe in the Lab”, *Phys. Rev. X* **8**:2, 021021 (2018) (cited on page 114).
174. S. A. Haine, A. J. Ferris, J. D. Close, et al., “Control of an atom laser using feedback”, *Phys. Rev. A* **69**:1, 013605 (2004) (cited on pages 114, 116).
175. A. Deutschmann-Olek, M. Tajik, M. Calzavara, et al., “Iterative shaping of optical potentials for one-dimensional Bose-Einstein condensates”, in *2022 IEEE 61st Conference on Decision and Control (CDC)* (2022), pages 5801–5806 (cited on page 120).
176. M. Calzavara, Y. Kuriatnikov, A. Deutschmann-Olek, et al., “Optimizing optical potentials with physics-inspired learning algorithms”, DOI: 10.48550/ARXIV.2210.07776 (2022) (cited on page 120).
177. A. Neumann, M. Gebbe, and R. Walser, “Aberrations in (3+1)-dimensional Bragg diffraction using pulsed Laguerre-Gaussian laser beams”, *Phys. Rev. A* **103**:4, 043306 (2021) (cited on page 123).
178. W. Bao and Y. Cai, “Mathematical theory and numerical methods for Bose-Einstein condensation”, *Kinetic & Related Models* **6**:1, 1–135 (2013) (cited on pages 137, 161–162).

Bibliography

179. X. Antoine and R. Duboscq, “GPELab, a Matlab toolbox to solve Gross–Pitaevskii equations I: Computation of stationary solutions”, *Computer Physics Communications* **185**:11, 2969–2991 (2014) (cited on pages 137, 160).
180. X. Antoine and R. Duboscq, “GPELab, a Matlab toolbox to solve Gross–Pitaevskii equations II: Dynamics and stochastic simulations”, *Computer Physics Communications* **193**, 95–117 (2015) (cited on pages 137, 161).
181. J. W. Cooley and J. W. Tukey, “An algorithm for the machine calculation of complex Fourier series”, *Math. Comp.* **19**:90, 297–301 (1965) (cited on page 139).
182. M. Heideman, D. Johnson, and C. Burrus, “Gauss and the history of the fast fourier transform”, *IEEE ASSP Mag.* **1**:4, 14–21 (1984) (cited on page 139).
183. C. M. Dion, A. Hashemloo, and G. Rahali, “Program for quantum wave-packet dynamics with time-dependent potentials”, *Computer Physics Communications* **185**:1, 407–414 (2014) (cited on page 161).
184. H. Yoshida, “Construction of higher order symplectic integrators”, *Physics Letters A* **150**:5-7, 262–268 (1990) (cited on page 162).
185. K. Atkinson, *An Introduction to Numerical Analysis*, Wiley India Pvt. Limited, 2008 (cited on page 163).
186. D. M. Henderson, “Euler angles, quaternions, and transformation matrices for space shuttle analysis”, in (1977) (cited on pages 165–166).

LIST OF PUBLICATIONS

- J. Teske, M. R. Besbes, B. Okhrimenko, R. Walser
Mean-field Wigner function of Bose–Einstein condensates in the Thomas–Fermi limit
Phys. Scr. **93** (2018) 124004
[10.1088/1402-4896/aae516](https://doi.org/10.1088/1402-4896/aae516)
- J. Teske, R. Walser
Efficient multipole representation for matter-wave optics
In preparation
- J. Teske, R. Walser
Delta-kick collimation with atomic chip trap potentials
In preparation
- J. Teske, D. Pfeiffer, L. Lind, O. V. Marchukov, F. Schmaltz, G. Birkl and R. Walser
Topological deformation of Bose-Einstein condensates in optical dipole traps
In preparation

CONFERENCE CONTRIBUTIONS

- **Talk**
Efficient aberration analysis of Bose-Einstein condensates
DPG Frühjahrstagung, Erlangen, Germany (2022)
- **Talk + Poster**
Wave front aberrations of expanding Bose-Einstein condensates
Quantum Optics X, Torun, Polen (2021)
- **Poster**
Delta-kick collimation with atomic chip trap potentials
Quantum Matter out of Equilibrium, Granada, Spanien (2020)
- **Talk**
Wigner representation of interacting BECs in the Thomas-Fermi limit
69th International Astronautical Congress, Bremen Germany (2018)
- **Poster**
Wigner representation of BECs in the Thomas-Fermi limit
Frontiers of Matter Wave Optics, Archanes and Kolymbari, Kreta, Griechenland (2018)
- **Poster**
Wigner representation of BECs in the Thomas-Fermi limit
DPG Frühjahrstagung, Erlangen, Germany (2018)
- **Poster**
Lens Design for Coherent Matter Waves
Ecole de Physique des Houches – Cold atoms and quantum transport (2017)
- **Poster**
Cold quantum gases in real magnetic chip traps
DPG Frühjahrstagung, Mainz, Germany (2017)
- **Poster**
Matter wave optics in μ -gravity with Bose-Einstein condensates
DPG Frühjahrstagung, Hannover, Germany (2016)

DANKSAGUNG

Als Autor dieser Arbeit möchte ich dem verehrten Leser und der verehrten Leserin noch mitteilen, dass diese Arbeit nicht ohne die Hilfe von vielen wunderbaren Menschen zu Stande gekommen wäre.

An erster Stelle gilt mein Dank meinem Doktorvater Prof. Dr. Reinhold Walser für die Betreuung dieser Arbeit und Ihren Einsatz als wahrer Hochschullehrer, der sich viel Zeit für seine Studierenden nimmt. Danke, dass Sie mir viele Reisen auf Konferenzen und Workshops auf der ganzen Welt ermöglicht haben. Auch wenn am Ende wahrscheinlich doch alles – oder viel – Gutes aus Tirol kommt.

Ich danke meinem Buddy Paula für unsere bisherige gemeinsame Reise und die großartige Unterstützung in den letzten Monaten. Auch wenn du dich vielleicht etwas Hilflos gefühlt, ohne dich hätte ich es wahrscheinlich nicht geschafft. Ich freue mich auf viele neue Erlebnisse mit dir und unserem kleinen Sohn! Gruß auch an Mr Chackles, auch wenn er nun wirklich absolut gar nichts gemacht hat.

Vielen Dank an all meine tollen Freunde, die ich hier in Darmstadt kennenlernen durfte. Ubbi, Jochen, Ralph, Philipp, Tim, ohne euch wäre ich bestimmt nicht so unbeschwert durch die Studiensemester geschritten. Also besten Dank, Ubbi, dass du mich damals an der Straßenbahnhaltestelle belästigt hast.

Thanks to Dr Marchukov. I enjoyed all our evenings during the new normal. I'll never forget the Karaoke nights in der Krone - Bohemian Rhapsody what a performance! I'm admiring you, how you kept yourself together when the shit hit the fan continuously. Thank you for all your support and proof reading. Slava Ukraïni!

Ja, ich schreibe Deutsch. Liebe Grüße an die wahren Mitarbeiter und Mitarbeiterinnen des Monats im Hobbit. Ihr habt unsere Selbsthilfegruppe stets gut versorgt und schöne Abende mitgestaltet.

Vielen Dank daher auch an Dominik. Für physikalische und kaffetechnische Expertise. Ich hoffe, wir sehen uns bald wieder in den Bergen. Genauso hoffe ich dort auch Andi demnächst dort wieder begrüßen zu können. Danke mein Freund für deinen Support. Ich freue mich deine Kehrseite wieder beim Wandern bewundern zu dürfen.

Zuletzt gilt besonderer Dank meinen Eltern, die mich all die Jahre während meines Studiums unterstützt haben. Ihr habt mir bei all meinen Entscheidungen euer Vertrauen entgegengebracht und mir immer Bedingungslos geholfen, wenn gerade Not am Mann war.

Diese Arbeit wurde unterstützt durch das Zentrum für Luft- und Raumfahrt (DLR), mit Geldmitteln bereitgestellt vom Bundesministerium für Wirtschaft und Energie (BMWi) unter den Förderkennzeichen 50WM1957 und 50WM2250E.

ERKLÄRUNGEN LAUT PROMOTIONSORDNUNG

§8 ABS. 1 LIT. C PROMO

Ich versichere hiermit, dass die elektronische Version meiner Dissertation mit der schriftlichen Version übereinstimmt.

§8 ABS. 1 LIT. D PROMO

Ich versichere hiermit, dass zu einem vorherigen Zeitpunkt noch keine Promotion versucht wurde. In diesem Fall sind nähere Angaben über Zeitpunkt, Hochschule, Dissertationsthema und Ergebnis dieses Versuchs mitzuteilen

§9 ABS. 1 PROMO

Ich versichere hiermit, dass die vorliegende Dissertation selbstständig und nur unter Verwendung der angegebenen Quellen verfasst wurde.

§9 ABS. 2 PROMO

Die Arbeit hat bisher noch nicht zu Prüfungszwecken gedient.

Darmstadt, 12. April 2023

Jan Teske